A FRACTURE MECHANICS-BASED APPROACH FOR MODELING DELAMINATION OF SPRAY-APPLIED FIRE-RESISTIVE MATERIALS FROM STEEL STRUCTURES

By

Amir Arablouei

A DISSERTATION

Submitted to
Michigan State University
in partial fulfilment of the requirements
for the degree of

Civil Engineering-Doctor of Philosophy

2015

ABSTRACT

A FRACTURE MECHANICS-BASED APPROACH FOR MODELING DELAMINATION OF SPRAY-APPLIED FIRE-RESISTIVE MATERIALS FROM STEEL STRUCTURES

By

Amir Arablouei

Steel structures exhibit lower fire-resistance due to high thermal conductivity of steel and rapid deterioration of strength and stiffness properties of steel with temperature. Therefore, steel structures are to be provided with fire insulation to achieve required fire resistance. This is often achieved through spray applied fire resistive materials (SFRM) that are externally applied on steel surface. The main function of SFRM is to delay temperature rise in steel, and thus slow down the degradation of stiffness and strength properties of steel when exposed to fire.

Delamination of fire insulation can occur during service life of the structure due to exposure to harsh environmental conditions or due to poor bond properties at the interface of steel and SFRM. Further, high deformation levels in structural members due to extreme loading conditions such as earthquake, impact or explosion can lead to delamination of fire insulation from steel structures. Fire that can develop as a secondary event following an earthquake, explosion or impact (primary events) can cause significant damage and destruction to the steel structure if SFRM applied on the steel members experience fire insulation loss during primary events. For instance, combined effects of impact or blast and ensuing fire could lead to the progressive collapse of structure as in the case of the terrorist attacks on the World Trade Center buildings (NIST, 2005) and collapse of Piper Alpha platform in North Sea (1988).

In this research, an experimental-numerical approach is adopted to investigate delamination of fire insulation from steel structures subjected to static loading and also extreme loading

conditions such as seismic, impact and blast loading. The cohesive zone behavior at the interface of SFRM and steel is determined through static fracture tests conducted for three types of SFRM namely, mineral fiber-based, gypsum-based and Portland cement-based SFRM. Subsequently, dynamic impact tests are carried out on beams insulated with above three types of SFRM to assess performance of SFRM under dynamic loading and also to assess the effect of strain rate on cohesive zone properties.

A fracture mechanics-based numerical model, that can simulate crack initiation and propagation at the interface of steel and fire insulation, is developed in ANSYS and LS-DYNA for low and high strain rate loading conditions, respectively. The numerical approach is validated against both material and structural level tests. The validated numerical model is subsequently applied to quantify the effect of critical factors governing delamination phenomenon namely, fracture energy, elastic modulus and thickness of SFRM.

Results from parametric studies under static loading were utilized to identify the critical factors governing delamination of fire insulation from steel structures. Further, these results formed the basis for defining a delamination characteristic parameter that incorporates material-related governing factors in a single parameter and maintains interdependency between them. Results obtained from parametric study under impact loading is also utilized to estimate the dynamic increase factor (DIF) on fracture energy at the interface of steel and SFRM. Eventually, the delamination characteristic parameter is modified to capture differences in the nature of seismic and blast loading conditions, i.e. the way the stresses are transferred to the interface of steel and SFRM.

This research is dedicated to my beloved wife, Khadijeh and beautiful daughter, Hannah. Without their emotional support I would not have been able to accomplish this research.

ACKNOWLEDGEMENTS

I would like to especially appreciate my advisor, Professor Venkatesh Kodur for his supports during the course of my study at Michigan State University. His continuous supports and understanding helped me to overcome many obstacles I encountered with, over the past years. Undoubtedly, the training I received at Michigan State University under his supervision will remain a life-time treasure for me. I would also like to appreciate my PhD committee members, Prof. Parviz Soroushian, Prof. Alejandro Diaz and Prof. Nizar Lajnef for their time and providing valuable guidance on improving this research.

For her boundless support, love, and encouragement, I am thankful to my wife Khadijeh Rostami. She thoughtfully accompanied me along this journey.

My ultimate regards goes to Mr. Siavosh Ravanbakhsh for his unlimited and astonishing supports during the experimental program in this research.

I would like to extend my thanks to Ms. Margaret Conner, Ms. Laura Post, Ms. Mary Mroz and Ms. Laura Taylor for all the help they provided.

I am very much thankful to Prof. Emin Kutay for providing the high speed camera.

I would like to thank my friends Ata Babazadeh, Anuj Shakya, Sudhir Varma, Ankit Agrawal and Esam Aziz for helping me during the impact experiments.

The experiments presented in this thesis are partially supported through AISC Faculty Fellowship from American Institute of Steel Construction to Prof. Kodur and Michigan State University. Any opinions, findings, and conclusions or recommendations expressed in this paper are those of the authors and do not necessarily reflect the views of the sponsors.

TABLE OF CONTENTS

LIST OF TABLES x

LIST OF FIGURES xi

KEY TO ABBREVIATIONS xxiv

CHAPTER 1 1
1 INTRODUCTION 1
1.1 General 1
1.2 Role of SFRM in Fire Performance of Steel Structures 2
1.3 SFRM Categories and its Performance under Applied Loading 5
1.4 Potential Loading Scenarios Leading to Delamination of SFRM from Steel Structures . 9
1.5 Mechanisms of Fracture and Delamination of SFRM 12
1.6 Consequences of Fire Insulation Delamination 15
1.7 Research Objectives 16
1.8 Anticipated Research Impact 18
1.9 Scope and Outline 19

CHAPTER 2 20
2 STATE-OF-THE-ART REVIEW 20
2.1 General 20
2.2 Experimental Studies 21
2.2.1 Material Level Tests 21
2.2.2 Structural Level Tests 27
2.3 Numerical Studies 30
2.4 Codes of Practice 42
2.5 Knowledge Gaps 47

CHAPTER 3 50
3 EXPERIMENTAL STUDY 50
3.1 General 50
3.2 Determination of Fracture Process Zone Properties for SFRM 51
3.2.1 Test Procedures to Evaluate Cohesive Laws over FPZ 51
3.2.2 Materials and Specimen Geometry 53
3.2.3 Experimental Setup for Fracture Mode-I 54
3.2.4 Experimental Setup for Fracture Mode-II 56
3.2.5 Elastic Modulus Tests 58
3.3 Results from Fracture Tests 58
3.4 Drop Mass Impact Test 69
3.4.1 Selection of Experimental Approach 69

3.4.2 Impact Test Set-up 70
3.4.3 Test Specimens 72
3.5 Results from Impact Tests 74
3.5.1 Impact Force 75
3.5.2 Displacement 78
3.5.3 Extent of Delamination of Fire Insulation 80
3.6 Summary 84

CHAPTER 4 85
4 NUMERICAL MODELING 85
4.1 General 85
4.2 Fracture Mechanics-Based Numerical Model 86
4.2.1 Characterizing SFRM Delamination using Fracture Mechanics 86
4.2.2 Implementation of Fracture Mechanics in Finite Element Model 87
4.2.3 Modeling Delamination of SFRM during Seismic Loading 89
4.2.3.1 Finite Element Discretization 90
4.2.3.2 Contact Interaction 95
4.2.3.3 Material Constitutive Model 96
4.2.3.4 Material Properties 100
4.2.3.5 Mesh Size 100
4.2.3.6 Nonlinear Solution Predicaments 101
4.2.4 Modeling Delamination of SFRM during Impact and Blast Loading 102
4.2.4.1 Finite Element Discretization 102
4.2.4.2 Contact Interaction 103
4.2.4.3 Material Constitutive Model 104
4.2.4.4 Material Properties 106
4.2.4.5 Mesh Size 107
4.2.4.6 Pitfalls in Explicit Solution 107
4.3 Thermal-Structural Numerical Model 108
4.3.1 Structural Analysis 109
4.3.2 Thermal Analysis 110
4.3.3 Material Constitutive Model 113
4.3.4 Temperature-Dependent Material Properties 114
4.3.5 Fire Scenario 119
4.4 Validation of Numerical Model 119
4.4.1 Validation of Fracture Mechanics-Based Numerical Model 120
4.4.1.1 Direct Fracture Tests 120
4.4.1.2 Indirect Fracture Tests 127
4.4.1.3 Steel plate-SFRM Assembly under Tension 130
4.4.1.4 Cantilever Column Subjected Quasi-Static Loading 133
4.4.1.5 Beam-Column Assembly Subjected to Seismic Loading 138
4.4.1.6 Beam Subjected to Impact Loading 146
4.4.1.6.1 Insulated Beam Behavior 146
4.4.1.6.2 Non-insulated Beam Behavior 155

4.4.1.6.3 Effect of Boundary Conditions ... 157
4.4.1.7 Beam-Column Subjected to Blast Loading ... 160
4.4.2 Validation of Thermal-Structural Numerical Model ... 163
4.5 Summary ... 168

CHAPTER 5 ... 170
5 PARAMETRIC STUDY ... 170
5.1 General ... 170
5.2 Factors Governing Delamination of SFRM from Steel Structures ... 171
5.3 Delamination of Fire Insulation from Slender Steel Truss ... 172
5.3.1 Analysis Details ... 173
5.3.2 Effect of Type of SFRM on Delamination ... 174
5.3.3 Effect of Variation in Cohesive Zone Parameters on Delamination ... 180
5.3.4 Effect of Variation in SFRM Elastic Modulus ... 189
5.3.5 Effect of Variation in SFRM Thickness ... 192
5.3.6 Parameter for Characterizing Delamination of SFRM ... 194
5.4 Delamination of Fire Insulation from Steel Beam-Column Assembly under Seismic Loading ... 197
5.4.1 Analysis Details ... 199
5.4.2 Effect of Type of SFRM ... 200
5.4.3 Effect of Cohesive Strength and Fracture Energy ... 201
5.4.4 Effect of Elastic Modulus of Insulation ... 211
5.4.5 Effect of Insulation Thickness ... 213
5.4.6 Additional Sensitivity Analysis ... 216
5.4.7 Delamination Characteristic Parameter for Seismic Loading ... 218
5.5 Delamination of Fire Insulation from a Beam under Impact Loading ... 220
5.5.1 Analysis Details ... 221
5.5.2 Approach for Predicting Dynamic Increase Factor on Fracture Energy of SFRM 222
5.5.3 Numerical Predicaments ... 222
5.5.4 Quantified Dynamic Increase Factors ... 224
5.6 Delamination of Fire Insulation from Steel Beam-Column Assembly under Blast Loading ... 229
5.6.1 Analysis Details ... 230
5.6.2 Dynamic Response of the Beam-Column to Blast Load ... 232
5.6.3 Effect of Blast Overpressure ... 234
5.6.4 Effect of Elastic Modulus ... 237
5.6.5 Effect of Fracture Energy ... 240
5.6.6 Parameter for Characterizing Delamination of Fire Insulation under Blast Loading 242
5.7 Summary ... 244

CHAPTER 6 ... 247
6 CONSEQUENCES OF FIRE INSULATION DELAMINATION ... 247

6.1 General 247
6.2 Post-earthquake Fire Response of a Moment-Resisting Frame 248
6.2.1 Analysis Procedure to Obtain Load-Displacement Relationship 248
6.2.2 Analysis Procedure to Quantify Time to Failure 260
6.3 Post-Blast Fire Response of a Beam-Column 266
6.4 Strategies to Overcome Consequences of Delamination 280
6.5 Summary 280

CHAPTER 7 282
7 CONCLUSIONS AND RECOMMENDATIONS 282
7.1 General 282
7.2 Key Findings 283
7.3 Research Impact and Practical Implications 287
7.4 Recommendations for Future Research 288

REFERENCES 291

LIST OF TABLES

Table 1.1 Material ingredients of CAFCO300 and CAFCO400 13

Table 3.1 Three type of SFRM utilized in experiments.. 54

Table 3.2 Cohesive zone model parameters obtained in experiment for three types of SFRM ... 58

Table 3.3 Fire insulated steel specimens and test variables... 74

Table 4.1 Material properties used for verification of thermal-structural model 164

Table 5.1 Cohesive zone model parameters obtained in experiments for three types of SFRM 177

LIST OF FIGURES

Figure 1.1 SFRM applied on steel structural elements 6

Figure 1.2 Delamination of fire insulation from steel structures (observed in World Trade Center) 8

Figure 1.3 Illustration of stress build up in moment resisting frame subjected to cyclic loading 10

Figure 1.4 Blast load on long steel truss and beam-column members 12

Figure 1.5 Progression of cracks leading to delamination of SFRM from steel surface (Development of fracture process zone) 14

Figure 2.1 Normal and shear bond experiments carried out by Chen et al. (2010) 22

Figure 2.2 Normal bond experiments performed by Braxtan and Pessiki (2011a) 24

Figure 2.3 Experimental setup designed by NIST to measure fracture energy at steel-SFRM interface (Tan et al. (2011)) 25

Figure 2.4 Load-displacement curves for different initial crack size measured by Tan et al. (2011) in their fracture tests 26

Figure 2.5 Test setup of an exterior beam-column assembly to measure delamination of SFRM (Braxtan and Pessiki (2011b) 28

Figure 2.6 Delamination of SFRM type Blaze Shield-II from bottom flange of the beam-column assembly tested by Braxtan and Pessiki (2011b) 29

Figure 2.7 Test set-up for fire insulated column test (Wang et al. (2013)) 29

Figure 2.8 Debonding and fracture of SFRM from steel column at high levels of quasi-static load (Wang et al. (2013)) 30

Figure 2.9 Effect of partial loss of fire insulation on fire resistance of steel columns (Tomecek and Milke (1993)) 32

Figure 2.10 Effect of partial loss of fire insulation on fire resistance of steel columns (Ryder et al. (2002)) 33

Figure 2.11 Temperature distribution over the cross section of steel column as a consequence of missing fire insulation from flange (Kwon et al. (2006)) 36

Figure 2.12 Capacity reduction of the column versus fire duration (Kwon et al. (2006))........... 37

Figure 2.13 Effect of fire insulation damage on fire resistance of a moment resisting frame (Gu and Kodur, (2011))... 38

Figure 2.14 Effect of fire insulation damage on fire resistance of a steel column (Dwaikat and Kodur, (2012)) 39

Figure 2.15 Effect of fire insulation damage on moment-rotation response of beam-column connection (Dwaikat and Kodur, (2012a)) 40

Figure 2.16 Numerical modeling of fire insulation delamination from steel surface (Dwaikat and Kodur, (2011)) 41

Figure 2.17 Normal bonding test between steel and fire insulation based on ASTM E736 (2011) 44

Figure 2.18 Drop mass test for measuring durability of fire insulation under accidental impact loading based on ASTM E760 (2011) 45

Figure 2.19 Point load test for measuring durability of fire insulation under service loading conditions based on ASTM E759 (2011).. 45

Figure 3.1 Test plate geometry for measuring fracture parameters 55

Figure 3.2 Schematic of test assembly for determination of CZM parameters 56

Figure 3.3 Test set up designed for measuring CZM parameters at steel-SFRM......................... 57

Figure 3.4 Normal force-displacement relationship (fracture mode-I).. 60

Figure 3.5 Shear force-displacement relationship (fracture mode-II) 60

Figure 3.6 Fracture at steel-SFRM interface observed in the experiments................................. 62

Figure 3.7 Interfacial cohesive strength for three types of SFRM.. 66

Figure 3.8 Interfacial critical fracture energy for three types of SFRM 66

Figure 3.9 Determination of bilinear cohesive law based on experimental results 67

Figure 3.10 Bilinear cohesive law for fracture mode-I determined from experiments 68

Figure 3.11 Bilinear cohesive law for fracture mode-II determined from experiments 68

Figure 3.12 Schematic view of drop weight impact test set-up 71

Figure 3.13 Schematic view of specimen 73

Figure 3.14 Force-time history recorded during impact tests on the beams insulated with different types of SFRM 76

Figure 3.15 Vertical displacement time history recorded during impact tests at the end of the beams insulated with different types of SFRM.. 79

Figure 3.16 Extent of delamination of different types of SFRM from bottom flange of the I-beams subjected to impact loading 82

Figure 3.17 Illustration of high speed camera snapshots during impact on steel beams insulated with different types of SFRM (v=8.05 m/sec) 82

Figure 4.1 Cohesive zone constitutive model for SFRM... 99

Figure 4.2 True stress-true strain relationship for A992-Gr. 50 steel.. 107

Figure 4.3 Time-dependent engineering stress-strain relationship for S350 steel (EC3, 2005). 115

Figure 4.4 Time-dependent modulus of elasticity for structural steel (EC3, 2005) 116

Figure 4.5 Time-dependent thermal strain for structural steel (carbon steel) (EC3, 2005)........ 116

Figure 4.6 Variation of thermal conductivity with temperature for structural steel (carbon steel) (EC3, 2005).. 117

Figure 4.7 Variation of Specific heat with temperature for structural steel (carbon steel) (EC3, 2005) 117

Figure 4.8 Variation of thermal conductivity with temperature for gypsum-based SFRM (Kodur and Shakya, 2013 118

Figure 4.9 Variation of specific heat with temperature for gypsum-based SFRM (Kodur and Shakya, 2013)........ 118

Figure 4.10 Finite element model of SFRM-steel assembly in mode-I fracture experiments.... 121

Figure 4.11 Finite element model of SFRM-steel assembly in mode-II fracture experiments... 122

Figure 4.12 Comparison of force-displacement relationship predicted from numerical model with measured values from experiments for gypsum-based SFRM........ 124

Figure 4.13 Comparison of force-displacement relationship predicted from numerical model with measured values from experiments for Portland cement-based SFRM........ 125

Figure 4.14 Comparison of force-displacement relationship predicted from numerical model with measured values from experiments for mineral fiber-based SFRM........ 126

Figure 4.15 Experimental setup for fracture tests carried out by NIST to measure fracture energy of SFRM........ 128

Figure 4.16 Finite element model for fracture test conducted by NIST........ 128

Figure 4.17 Measured and predicted force-displacement response at the steel-insulation interface for material level tests conducted at NIST........ 129

Figure 4.18 Experimental setup for plate covered with mineral fiber-based SFRM (Braxtan and Pessiki, 2011a)........ 130

Figure 4.19 Finite element model for plate covered with mineral fiber-based SFRM........ 131

Figure 4.20 Delamination length predicted and measured on a plate covered with mineral fiber-based SFRM........ 132

Figure 4.21 Experimental set-up for quasi-static loading of a cantilever column insulated with SFRM (Wang et al., 2013)........ 134

Figure 4.22 Finite element model for quasi-static loading of a cantilever column insulated with SFRM........ 135

Figure 4.23 Load-displacement response of the insulated steel column tested by Wang et al. (2013)........ 136

Figure 4.24 Delamination and fracture of SFRM from steel column at high levels of static load 137

Figure 4.25 Test setup of an exterior moment frame assembly to measure delamination of SFRM (Braxtan and Pessiki (2011b)... 140

Figure 4.26 Finite element model of beam-column assembly tested by Braxtan and Pessiki (2011b).. 141

Figure 4.27 Cyclic displacements applied at beam tip for validation of SFRM delamination... 142

Figure 4.28 Comparison of predicted and measured load versus percent drift in insulated beam-column assembly.. 143

Figure 4.29 Comparison of predicted and measured extent of delamination in beam-column assembly insulated with gypsum-based SFRM 144

Figure 4.30 Comparison of predicted and measured extent of delamination in beam-column assembly insulated with mineral fiber-based SFRM 145

Figure 4.31 Numerical model of experimental setup for fire insulated beams in drop mass impact test 147

Figure 4.32 Comparison of experimental and predicted impact force for beams insulated with mineral fiber-based SFRM subjected to two different impact velocities 149

Figure 4.33 Comparison of experimental and predicted impact force for beams insulated with gypsum-based SFRM subject to two different impact velocities 150

Figure 4.34 Comparison of experimental and predicted impact force for beams insulated with Portland cement-based SFRM subject to two different impact velocities................................. 151

Figure 4.35 Comparison of experimental and predicted vertical deflection at one end of beams insulated with mineral fiber-based SFRM and subjected to two different impact velocities 152

Figure 4.36 Comparison of experimental and predicted vertical deflection at one end of beams insulated with gypsum-based SFRM and subjected to two different impact velocities 153

Figure 4.37 Comparison of experimental and predicted vertical deflection at one end of beams insulated with Portland cement-based SFRM and subjected to two different impact velocities 154

Figure 4.38 Comparison of experimental and predicted responses for a steel beam without insulation 156

Figure 4.39 Numerical models created for evaluating the effect of supports on beam behavior in drop 158

Figure 4.40 Effect of including support details in numerical predictions 159

Figure 4.41 Schematic view of blast tests on steel beam-column conducted by Nassr et al. (2011) 160

Figure 4.42 Finite element model of beam-column tested by Nassr et al. (2011) 161

Figure 4.43 Comparison between numerical prediction and experimentally measured deflection at mid-span of the beam-column under blast loading 162

Figure 4.44 Location of thermocouples in cross section of the concrete filled column SQ24 ... 164

Figure 4.45 Finite element Model for concrete filled steel column 165

Figure 4.46 Temperature prediction 166

Figure 4.47 Temperature (°K) distribution at cross section 167

Figure 4.48 Axial deformation of the column 168

Figure 5.1 Progression of crack at the interface of steel and SFRM (based on cohesive zone model concept) 174

Figure 5.2 Finite element model of bottom chord of truss encapsulated with SFRM 175

Figure 5.3 Percentage of delamination progression on outer sides of truss chord with respect to average axial strain developed in truss member 176

Figure 5.4 Crack propagation pattern at the interface of steel and gypsum-based SFRM at different strain levels 178

Figure 5.5 Fracture energies released during delamination for gypsum 179

Figure 5.6 Schematic view of various analyses cases for studying the sensitivity of delamination progression to CZM parameters 181

Figure 5.7 Effect of fracture energy of gypsum-based SFRM on initiation and progression of delamination in truss member under tension 183

Figure 5.8 Effect of fracture energy of Portland cement-based SFRM on initiation and progression of delamination in truss member under tension 184

Figure 5.9 Effect of fracture energy of Mineral fiber-based SFRM on initiation and progression of delamination in truss member under tension 185

Figure 5.10 Effect of cohesive strength of gypsum-based SFRM on initiation and progression of delamination in truss member under tension 186

Figure 5.11 Effect of cohesive strength of Portland cement-based SFRM on initiation and progression of delamination in truss member under tension 187

Figure 5.12 Effect of cohesive strength of Mineral fiber-based SFRM on initiation and progression of delamination in truss member under tension 188

Figure 5.13 Effect of SFRM elastic modulus on initiation and progression of delamination in truss member under tension (Gypsum-based SFRM) 190

Figure 5.14 Effect of SFRM elastic modulus on initiation and progression of delamination in truss member under tension (Portland cement-based SFRM) 190

Figure 5.15 Effect of SFRM elastic modulus on initiation and progression of delamination in truss member under tension (Mineral fiber-based SFRM) 191

Figure 5.16 Effect of SFRM thickness on initiation and progression of delamination in truss member under tension (Gypsum-based SFRM) 192

Figure 5.17 Effect of SFRM thickness on initiation and progression of delamination in truss member under tension (Portland cement-based SFRM) 193

Figure 5.18 Effect of SFRM thickness on initiation and progression of delamination in truss member under tension (Mineral fiber-based SFRM) 193

Figure 5.19 Strain ductility demand of steel at delamination initiation versus delamination parameter 196

Figure 5.20 Strain ductility demand of steel at complete delamination versus delamination parameter 196

Figure 5.21 Finite element model of beam-column assembly used for parametric study under seismic........ 198

Figure 5.22 Cyclic displacements applied at beam tip for parametric study........ 199

Figure 5.23 Percentage of delamination of three types of SFRM applied on the beam in a beam column assembly subjected to seismic loading........ 201

Figure 5.24 Effect of fracture energy of gypsum-based SFRM on delamination progression on the beam of beam-column assembly subjected to seismic loading........ 203

Figure 5.25 Effect of fracture energy of Portland cement-based SFRM on delamination progression on the beam of beam-column assembly subjected to seismic loading........ 204

Figure 5.26 Effect of fracture energy of mineral fiber-based SFRM on delamination progression on the beam of beam-column assembly subjected to seismic loading........ 205

Figure 5.27 Effect of cohesive strength of gypsum-based SFRM on delamination progression on the beam of beam-column assembly subjected to seismic loading........ 207

Figure 5.28 Effect of cohesive strength of Portland cement-based SFRM on delamination progression on the beam of beam-column assembly subjected to seismic loading........ 208

Figure 5.29 Effect of cohesive strength of mineral fiber-based SFRM on delamination progression on the beam of beam-column assembly subjected to seismic loading........ 209

Figure 5.30 Effect of elastic modulus of gypsum-based SFRM on delamination progression on the beam of beam-column assembly subjected to seismic loading........ 212

Figure 5.31 Effect of elastic modulus of Portland cement-based SFRM on delamination progression on the beam of beam-column assembly subjected to seismic loading........ 212

Figure 5.32 Effect of elastic modulus of mineral fiber-based SFRM on delamination progression on the beam of beam-column assembly subjected to seismic loading........ 213

Figure 5.33 Effect of thickness of gypsum-based SFRM on delamination progression on the beam of beam-column assembly subjected to seismic loading........ 215

Figure 5.34 Effect of thickness of Portland cement-based SFRM on delamination progression on the beam of beam-column assembly subjected to seismic loading........ 215

Figure 5.35 Effect of thickness of mineral fiber-based SFRM on delamination progression on the beam of beam-column assembly subjected to seismic loading 216

Figure 5.36 Effect of change in material properties of gypsum-based SFRM on delamination progression on the beam of beam-column assembly subjected to seismic loading.................... 217

Figure 5.37 Effect of change in material properties of Portland cement-based SFRM on delamination progression on the beam of beam-column assembly subjected to seismic loading 218

Figure 5.38 Extent of delamination as a function of parameter E.t/G_c 220

Figure 5.39 Extent of delamination ratio versus dynamic increase factor for CZM properties of mineral fiber-based SFRM.. 225

Figure 5.40 Extent of delamination ratio versus dynamic increase factor for CZM properties of gypsum-based SFRM.. 226

Figure 5.41 Extent of delamination ratio versus dynamic increase factor for CZM properties of Portland cement-based SFRM 226

Figure 5.42 Numerical and experimental illustration of extent of delamination in beam insulated with Mineral fiber-based SFRM (DIF=1.00).. 227

Figure 5.43 Numerical and experimental illustration of extent of delamination in beam insulated with Gypsum-based SFRM (DIF=1.41) 228

Figure 5.44 Numerical and experimental illustration of extent of delamination in beam insulated with Portland cement-based SFRM (DIF=2.32).. 229

Figure 5.45 Finite element model of beam-column insulated with SFRM utilized in parametric study under blast loading 231

Figure 5.46 Mid-span deflection of the beam-column insulated with SFRM under different blast overpressure level 233

Figure 5.47 Illustration of delamination of mineral fiber-based SFRM from steel beam-column over the first 10 ms of the blast scenario 234

Figure 5.48 Extent of delamination on steel column as a function of blast overpressure for mineral fiber-based SFRM.. 235

Figure 5.49 Extent of delamination on steel column as a function of blast overpressure for gypsum-based SFRM 236

Figure 5.50 Extent of delamination on steel column as a function of blast overpressure for Portland cement-based SFRM 236

Figure 5.51 Extent of delamination on steel column as a function of elastic modulus for mineral fiber-based SFRM 238

Figure 5.52 Extent of delamination on steel column as a function of elastic modulus for gypsum-based SFRM 239

Figure 5.53 Extent of delamination on steel column as a function of elastic modulus for Portland cement-based SFRM 239

Figure 5.54 Extent of delamination on steel column as a function of fracture energy for mineral fiber-based SFRM 241

Figure 5.55 Extent of delamination on steel column as a function of fracture energy for gypsum-based SFRM 241

Figure 5.56 Extent of delamination on steel column as a function of fracture energy for Portland cement-based SFRM 242

Figure 5.57 Extent of delamination on steel beam-column under blast loading as a function of delamination characteristic parameter 244

Figure 6.1 Finite element model of thermal analysis carried out to compute temperature time history of beam-column 249

Figure 6.2 Temperature (K) distribution in the beam insulated with gypsum-based SFRM exposed to standard fire (ASTM E119) 251

Figure 6.3 Temperature evolution in the beam and column subjected to standard fire (ASTM E119) 252

Figure 6.4 Finite element model of beam-column assembly used for studying effect of temperature rise on capacity reduction of moment connection due to loss of fire insulation during seismic loading 253

Figure 6.5 Effect of temperature on load-displacement relationship of beam-column assembly endured 25% delamination over the plastic hinge region on the beam 254

Figure 6.6 Effect of temperature on load-displacement relationship of beam-column assembly endured 50% delamination over the plastic hinge region on the beam 254

Figure 6.7 Effect of temperature on load-displacement relationship of beam-column assembly endured 75% delamination over the plastic hinge region on the beam 255

Figure 6.8 Effect of temperature on load-displacement relationship of beam-column assembly endured 100% delamination over the plastic hinge region on the beam 255

Figure 6.9 Effect of delamination percentage over the plastic hinge region of the beam on load-displacement relationship of beam-column assembly at temperature of 200 °C........................ 256

Figure 6.10 Effect of percentage of delamination over the plastic hinge region of the beam on load-displacement relationship of beam-column assembly at temperature of 400 °C 256

Figure 6.11 Effect of percentage of delamination over the plastic hinge region of the beam on load-displacement relationship of beam-column assembly at temperature of 600 °C 257

Figure 6.12 Effect of percentage of delamination over the plastic hinge region of the beam on load-displacement relationship of beam-column assembly at temperature of 800 °C 257

Figure 6.13 Effect of percentage of delamination over the plastic hinge region of the beam on load-displacement relationship of beam-column assembly at temperature of 1000 °C 258

Figure 6.14 Plastic strain distribution in beam-column assembly at T=200 °C with 25% delamination over the plastic hinge region 258

Figure 6.15 Plastic strain distribution in beam-column assembly at T=400 °C with 50% delamination over the plastic hinge region 259

Figure 6.16 Plastic strain distribution in beam-column assembly at T=600 °C with 75% delamination over the plastic hinge region 259

Figure 6.17 Plastic strain distribution in beam-column assembly at T=800 °C with 100% delamination over the plastic hinge region 260

Figure 6.18 Finite element model of beam-column assembly used for quantifying failure time during fire following earthquake 261

Figure 6.19 Displacement of the beam during fire following an earthquake that has undergone insulation damage during seismic loading 262

Figure 6.20 Displacement of the beam during fire following an earthquake that has undergone insulation damage during seismic loading 262

Figure 6.21 Plastic strain distribution in beam-column assembly at the time of failure (0% delamination of SFRM over the plastic hinge region) 264

Figure 6.22 Plastic strain distribution in beam-column assembly at the time of failure (25% delamination of SFRM over the plastic hinge region) 264

Figure 6.23 Plastic strain distribution in beam-column assembly at the time of failure (50% delamination of SFRM over the plastic hinge region) 265

Figure 6.24 Plastic strain distribution in beam-column assembly at the time of failure (75% delamination of SFRM over the plastic hinge region) 265

Figure 6.25 Plastic strain distribution in beam-column assembly at the time of failure (100% delamination of SFRM over the plastic hinge region) 266

Figure 6.26 Finite element model of cross section of column for thermal analysis 267

Figure 6.27 Temperature distribution (°K) in the cross section of column with full SFRM after 2 hours of exposure to standard fire (ASTM E119) 269

Figure 6.28 Temperature distribution (°K) in the cross section of column with 25% delamination of SFRM after 2 hours of exposure to standard fire (ASTM E119) 269

Figure 6.29 Temperature distribution (°K) in the cross section of column with 50% delamination of SFRM after 2 hours of exposure to standard fire (ASTM E119) 270

Figure 6.30 Temperature distribution (°K) in the cross section of column with 75% delamination of SFRM after 2 hours of exposure to standard fire (ASTM E119) 270

Figure 6.31 Temperature distribution (°K) in the cross section of column with 100% delamination of SFRM after 2 hours of exposure to standard fire (ASTM E119) 271

Figure 6.32 Finite element of the column to simulate effect of temperature rise after blast loading on structural response of the column 271

Figure 6.33 Vertical displacement of the column during fire following blast 273

Figure 6.34 Time to failure of the column exposed to fire following blast as a function of percentage delamination occurred during blast loading 273

Figure 6.35 Axial force developed in the column during fire following blast 275

Figure 6.36 Effect of axial restraint on vertical expansion of column exposed to fire following blast (100% delamination) 275

Figure 6.37 Displacement vector (mm) of column endured 25% delamination during fire following blast loading 276

Figure 6.38 Displacement vector (mm) of column endured 50% delamination during fire following blast loading 276

Figure 6.39 Displacement vector (mm) of column endured 75% delamination during fire following blast loading 277

Figure 6.40 Displacement vector (mm) of column endured 100% delamination during fire following blast loading 277

Figure 6.41 Plastic strain distribution over the column undergone 25% delamination of fire insulation and subjected to fire following blast loading 278

Figure 6.42 Plastic strain distribution over the column undergone 50% delamination of fire insulation and subjected to fire following blast loading 278

Figure 6.43 Plastic strain distribution over the column undergone 75% delamination of fire insulation and subjected to fire following blast loading 279

Figure 6.44 Plastic strain distribution over the column undergone 100% delamination of fire insulation and subjected to fire following blast loading 279

KEY TO ABBREVIATIONS

FPZ: Fracture Process Zone

CZM: Cohesive Zone Model

VCCT: Virtual Crack Closure Technique

LEFM: Linear Elastic Fracture Mechanics

CTOD: Crack Tip Opening Displacement

SFRM: Sprayed Applied Fire Resistive Material

LVDT: Linear Variable Differential Transformer

DIF: Dynamic Increase Factor

I_1 : First invariant of stress tensor

J_2: Second invariant of stress deviator tensor

φ: Internal friction angle

G_{nc}: Critical fracture energy at normal mode

G_{tc}: Critical fracture energy at tangential mode

σ_c: Normal cohesive strength

τ_c: Tangential cohesive strength

$\delta_{n,c}$: Normal failure displacement

$\delta_{t,c}$ Tangential failure displacement

Δ: Total mixed-mode relative displacement

δ_n: Separation in normal direction

δ_t: Separation in tangential direction

$\delta_{n,o}$: Normal separation at normal cohesive strength

$\delta_{t,o}$: Tangential separation at tangential cohesive strength

ρ: Density

q: heat flux

Q: Heat source

k: Thermal conductivity

h_f: Film coefficient

T_B: bulk temperature of adjacent fluid (air)

T_f: Fire temperature

σ: Stefan-Boltzman constant

CHAPTER 1

1 INTRODUCTION

1.1 General

Steel is one of the primary materials used in structural framing of buildings due to numerous advantages steel offers such as high strength-to-weight ratio, high level of ductility and ease in fabrication and construction process. However, steel structures do not exhibit good fire-resistance due to high thermal conductivity of steel and rapid deterioration of strength and stiffness properties of steel with temperature. Hence, to maintain stability and integrity of steel structures during fire, steel structures are to be provided with fire insulation to achieve required fire resistance. This is often achieved through spray applied fire resistive materials (SFRM) that are externally applied on steel surface. SFRM is widely used as fire insulation material due to number of advantages it offers over other insulation materials, including low thermal conductivity, light weight, cost-effectiveness and ease of application (Kodur and Shakya, 2013). The main function of SFRM is to delay the temperature rise in steel, and thus slow down the degradation of stiffness and strength properties of steel when exposed to fire.

1.2 Role of SFRM in Fire Performance of Steel Structures

Fire performance of a steel structure during normal loading conditions strongly relies on the quality of SFRM, equipment, workmanship and the application process. Delamination of fire insulation can occur during service life of the structure due to exposure to harsh environmental conditions, deterioration in material properties over the time or due to poor initial bond properties at the interface of steel and SFRM. Further, any change in functionality of structure can consequently increase the load level on fire insulated structural member and hence can be a potential factor for inducing cracking and delamination of SFRM during service life. Therefore, to achieve good performance from SFRM during a fire event, the delamination of SFRM under service loading conditions should be minimized. This entails utilizing SFRM with high fracture resistance, controlling the quality of application, and monitoring the condition of SFRM on structural members on a regular basis.

Fire can not only occur during normal loading condition, but also can develop following an extreme loading condition that strikes the structure. Fire following an earthquake is one of the possible scenarios to be accounted for in the design of structural systems (Mousavi et al. 2008). Post-earthquake fires caused numerous fatalities and high fire losses in many previous earthquakes. As an example, in the aftermath of Hyougoken-Nambu earthquake (Kobe, Japan, 1995) 7000 buildings were destroyed by post-earthquake fires alone (Faggiano, 2007).

Further, explosion and impact are the other possible loading scenarios to be considered in the design of critical steel structures such as tall buildings, petrochemical facilities and offshore platforms. Fire that can develop as a secondary event following an explosion or impact (primary events) can cause significant damage and destruction to the structure. The combined effects of impact or blast and ensuing fire could lead to the progressive failure of structure as in the case of the terrorist attack on the World Trade Center buildings (NIST, 2005) and collapse of Piper Alpha platform in North Sea (1988).

These impactful events have shown that, although explosion, impact, earthquake and subsequent fires are rare events in structures, their ramifications can be disastrous which include, but not limited to personnel casualties, environmental damage and considerable property losses. Consequently, post-earthquake, post-impact and post-blast fire consideration has been drawing attention over the past few past years as part of an emerging trend towards enhancing structural resiliency under multi-hazard scenarios.

Substantial inelastic actions in structures during an earthquake, impact and blast can impose large deformation in structural and non-structural elements. During such extreme loading events, there is therefore a high possibility that active fire protection systems get compromised by ruptured water supply piping system and delayed response for firefighting (Mousavi et al. 2008). In such scenarios, adequate fire resistance of structure is the only line of defense for overcoming the damage or collapse of structural systems. In other words, the fire performance of steel structures relies entirely on the effectiveness of fire insulation applied on structural members.

Given the fact that the fire performance of steel structures relies entirely on the effectiveness of fire insulation applied on structural members, a crucial question that can be raised is whether the fire insulation will remain in-place after massive energy transfer to structure during seismic, blast or impact loading. The answer to this question is negative since the role of SFRM, as a protective layer during fire following above extreme loading conditions, can be compromised if the energy transferred to the structure by seismic, impact and blast loading, can cause fracture and delamination of fire insulation from steel surface. Both experiments and field observations have shown that SFRM can delaminate under static, cyclic and blast loading (Braxtan and Pessiki, 2011b; Wang et al., 2013; NIST 2005).

Under seismic, impact and blast loading, dynamic interfacial stresses developed at the SFRM-steel interface in the highly stressed zones of structural elements can open the cracks that are inevitably left over from SFRM application process. Once initiated, theses cracks can rapidly propagate along the interface of steel and SFRM leading to delamination of SFRM from steel surface. Therefore, efficiency of SFRM during fire following earthquake, blast and impact, entails assuring stable dynamic fracture resistance at steel-SFRM interface such that SFRM would not delaminate during these impulsive loading events or at least the extent of delamination would be minimal.

An additional key question is that whether the SFRM types, currently utilized in steel construction, possess enough fracture toughness to resist against fracture and delamination under the action of seismic, impact and blast loading conditions. Further, if the current SFRM types are vulnerable and hence can be dislodged from steel surface, what types of material properties would be required to avoid the delamination of fire insulation from steel structures. Owing to the lack of answers to above questions, current fire safety provisions do not address the effect of multiple hazards such as fire following earthquake or impact, or blast on fire resistance of structures.

For evaluating post-earthquake, post-blast and post-impact fire performance of steel structures, it is of crucial importance to have comprehensive knowledge regarding the extent of SFRM damage during primary event of earthquake, impact and blast loading. In current practice, it is assumed that the SFRM will not debond or disintegrate and will continue to maintain its integrity throughout the fire following earthquake, impact or blast. In fire resistance analysis, thermal response of steel structures is evaluated by assuming SFRM to be perfectly intact during the fire exposure. This serious shortcoming in current provisions necessitates developing a robust approach to predict the delamination of SFRM from steel surface under the action of extreme loading events on a structure. Developing such knowledge is one of the imperative steps towards rational design and assessment of post-earthquake, post-impact and post-blast fire performance of steel structures.

1.3 SFRM Categories and its Performance under Applied Loading

Spray-applied fire-resistive material (SFRM) is commercially available in cementitious and mineral fiber-based forms. Cementitious-based SFRM is further grouped under two categories; gypsum-based SFRM that comprises gypsum and vermiculite, and Portland-cement based SFRM that is composed of Portland cement and vermiculite. Mineral fiber-based fire insulation comprises of Portland cement and mineral wool fiber mixture. Cementitious and mineral-fiber-based SFRM are delivered to the construction site as wet-mix and dry-mix, respectively. Figure 1.1 shows SFRM applied on steel structural elements.

There are number of factors that can influence the decision of building owners on choosing what type of SFRM should be used in a specific building. Fire engineers in close collaboration with structural engineers determine the thickness and type of SFRM to be applied on the steel structure to provide the desired protection against fire. However, this decision is mainly made based on the fire-ratings prescribed in current codes and standards. Fire-rating for beams and columns are affected by only thermal properties (i.e. thermal conductivity and specific heat) of SFRM, hence the mechanical properties (i.e. elastic modulus and fracture energy) of SFRM are not given any consideration when designing the fire protection. Therefore, the final decision may not necessarily lead to selection of SFRM with high bonding properties.

a) Gypsum-based SFRM applied on beams and columns in a moment-resisting frame

b) Mineral fiber-based SFRM applied on trusses in a floor assembly

Figure 1.1 SFRM applied on steel structural elements

Mechanical performance of SFRM is highly dependent upon its integrity, constitutive ingredients, and the manner in which insulation is prepared and applied to the steel surface. During application of SFRM on steel structural members, microscopic cracks can develop within bulk SFRM itself, and also at the interface between steel and SFRM, mainly due to high shrinkage and low tensile strength of SFRM. Poorly bonded SFRM can be dislodged under combination of permanent dead loads and frequently applied loading-unloading cycles of live loads. For instance, Figure 1.2 illustrates delamination of fire insulation from steel beam and truss elements under service loading conditions, which were observed in World Trade Center towers during inspection by Port Authority of New York in 1993.

Even in case of a good bond conditions, SFRM may experience some level of delamination from steel surface due to the fact that steel structures undergo high level of deformations under extreme loading conditions. As a result of such large strains developed in steel, strain compatibility can no longer be held at steel-SFRM interface. Consequently, existing microcracks within SFRM can widen and propagate to the steel-SFRM interface leading to partial or full delamination of fire insulation.

a) Delamination of insulation from steel beam (source: Fire Protection Engineering Magazine)

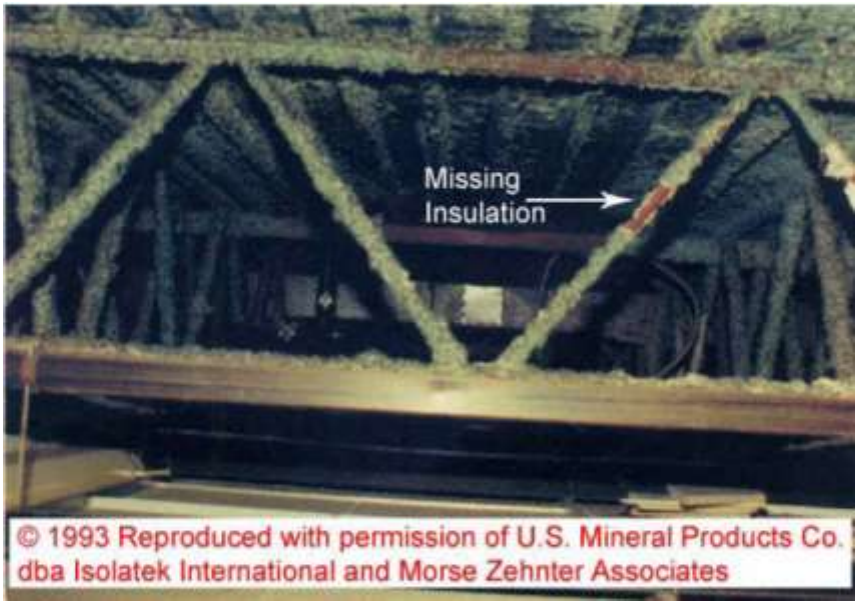

b) Delamination of insulation from truss system in floor assembly

Figure 1.2 Delamination of fire insulation from steel structures (observed in World Trade Center)

1.4 Potential Loading Scenarios Leading to Delamination of SFRM from Steel Structures

Special steel moment-resisting frames, which have gained vast attention in earthquake prone regions, are assigned the highest response modification factor (R) (NEHERP, 2009) and thus are expected to experience very large deformations. In steel moment frames subjected to earthquake loading, as shown in Figure 1.3, plastic hinges are formed in beams at the vicinity of columns, as well as at bottom of the columns, thereby the nonlinear actions in the structure is accommodated. Owing to large cyclic strains that develop in steel resulting from its high ductility demands during earthquake loading cycles, strain compatibility can no longer be maintained at the interface of steel and SFRM, as mentioned before. Since significant amount of strain energy is dissipated in the plastic hinge region and the beam cross section is highly distorted due to likely flange and web local buckling, considerable amount of energy also gets released at the interface of steel and applied SFRM. Further, effect of local buckling in flange and web on the extent of delamination are therefore expected to be quite significant.

However, in practice, regardless of the ductility demands anticipated to develop in the plastic hinge zones of the structure, SFRM with same properties and thickness is applied on the entire structural frame. This is applied by neglecting the fact that the level of strains developed at the steel-SFRM interface can vary over a broad range along the beam span. In other words, SFRM applied to plastic hinge region of a beam (in the vicinity of supports) will demand quite high level of fracture properties in order to remain in-place during cyclic loading. Under the action of seismic loading, crack tips are frequently subjected to tensile and shear stresses arising from steel deformations, either due to plastification or sudden deformation because of local buckling. Consequently, the damage accumulation during each loading cycle can substantially affect the extent of delamination in plastic hinge zones.

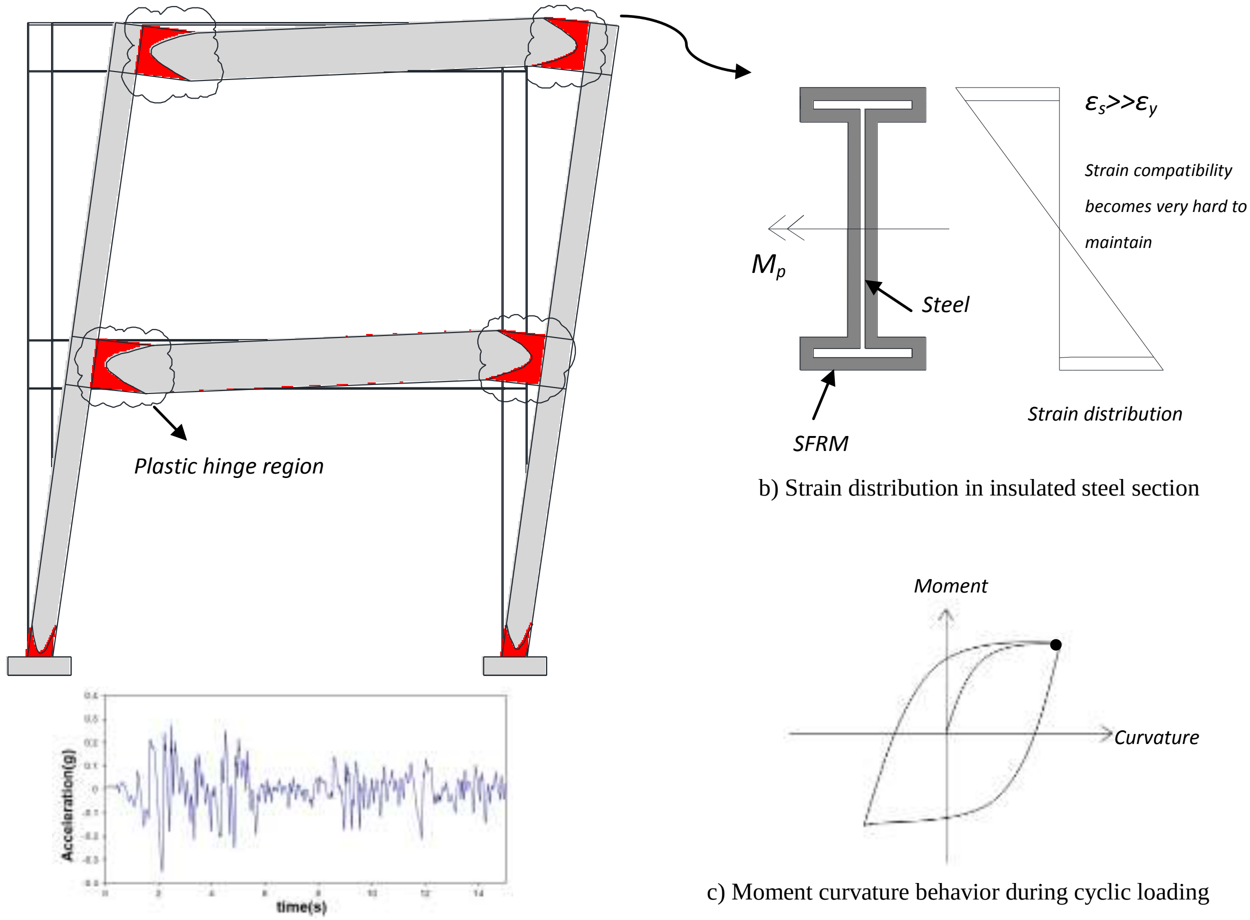

a) Steel moment frame subjected to seismic excitation

b) Strain distribution in insulated steel section

c) Moment curvature behavior during cyclic loading

Figure 1.3 Illustration of stress build up in moment resisting frame subjected to cyclic loading

Moment-resisting frames encapsulated with SFRM can also be subjected to debris impact as a result of an internal or external explosion or blast overpressure applied on the surface of the structural elements. Direct debris impact can locally damage the insulation applied on the members. Further, the impact kinetic energy, depending on the mass and velocity of debris, can cause delamination on the unexposed areas of the member due to stress wave propagation throughout the impacted member. The blast pressure generated during an explosion can affect both insulated beams and columns by imposing direct pressure on the SFRM applied on the steel surface. This type of loading can lead to significant local damage to SFRM as well as plastic deformation at both ends and mid-span of the member causing further indirect delamination from the members.

In modern high-rise buildings, not only the beams and beam-columns are prone to experience fire insulation damage, but also long steel truss systems are susceptible to encounter insulation damage due to direct debris impact or blast overpressure. Long span steel trusses are commonly utilized in the floor assemblies of high-rise buildings thereby accommodating large open spaces without any interruption from columns. These floors, while supporting their self-weight along with dead and live loads, provide lateral stability to the exterior walls and columns and distribute wind load among the exterior walls. The steel truss members are usually encapsulated with SFRM to achieve required fire resistance in floor systems. The truss members, due to high slenderness and small cross sectional sizes, are flimsy and thus are more vulnerable to insulation damage as compared to heavy steel sections utilized for columns and beams. Further, a truss system covers a larger area than columns and beams, hence the probability of debris impact on truss members during explosion or impact scenarios are higher than that in columns and beams. In the event of explosion, as illustrated in **Error! Reference source not found.**, generated blast overpressure can substantially increase the internal strains in truss members endangering the integrity of SFRM applied on truss members. In addition, under the action of impact loading, numerous trusses can completely fail leaving adjoining trusses heavily overloaded.

The above explained loading scenarios will be considered in studying delamination of SFRM from steel structures in this research. The fracture and delamination of SFRM will be investigated on steel moment-resisting frames subjected to seismic loading on flimsy truss members subjected to extreme deformation, on beams subjected to impact loading and on beam-columns subjected to blast overpressure.

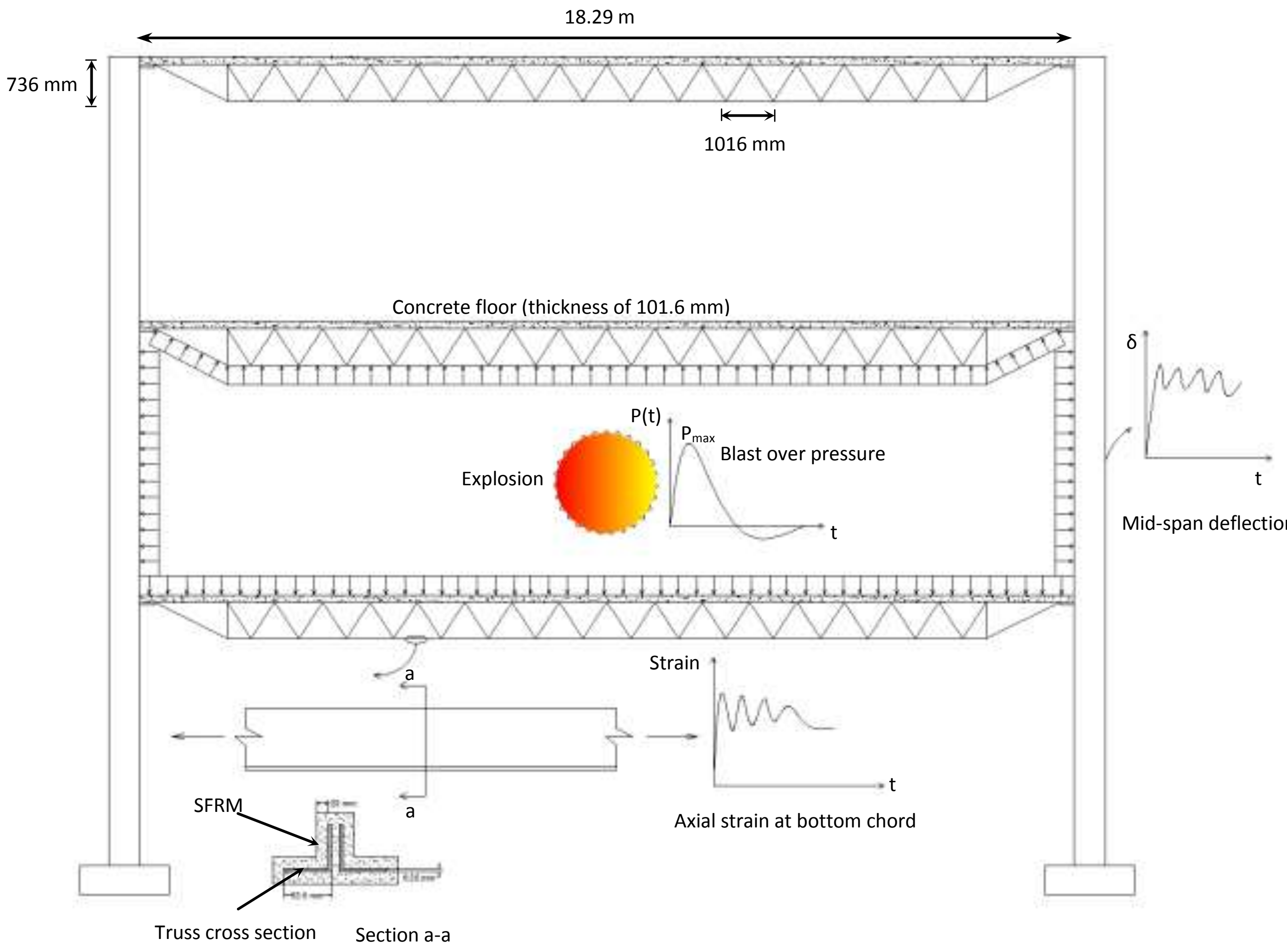

Figure 1.4 Blast load on long steel truss and beam-column members

1.5 Mechanisms of Fracture and Delamination of SFRM

Spray applied fire resistive materials, as cementitious materials, can be considered as two-phase composites comprising of a homogeneous phase and a particle phase (Modeer, 1979). Hence, in cementitious SFRM, the matrix (homogeneous phase) is composed of hydrated cement gels or gypsum paste, and the vermiculite particles (particle phase) form the reinforcement. This way the fracture properties of SFRM can be taken to be the average of individual properties of the two phases and the interfacial bond between the phases (Cotterell and Mai, 1996). Close examination of material constituents of SFRM reveals that nearly 70 percent of SFRM is composed of gypsum or cement, both of which are cementitious materials. Therefore, static and dynamic fracture mechanics of SFRM is expected to be analogous to the one developed for a cementitious material. For example, ingredients of a frequently utilized gypsum-based SFRM, which is known as CAFCO300, are provided in Table 1.1. Also, composition of a frequently utilized Portland cement-based SFRM, known as CAFCO400, is listed in Table 1.1.

Table 1.1 Material ingredients of CAFCO300 and CAFCO400

Chemical name	**Weight %**	
	CAFCO300	**CAFCO400**
Portland cement	-	40-70
Calcium Sulfate, Hemihydrate	50-75	-
Vermiculite	15-35	15-40
Cellulose	1-10	-
Calcium Carbonate	1-10	10-30
Quartz	0-5	<1

The loading scenarios illustrated in Figure 1.3 and Figure 1.4 can lead to crack initiation and propagation at the interface of SFRM and steel. This crack initiation and propagation phenomenon can be explained using fracture mechanics principles developed for cementitious materials (Cotterell and Mai, 1996). Figure 1.5 depicts a typical vicinity of crack at steel-SFRM interface and associated fracture process zone (FPZ) developed at the crack tip. Within the FPZ, microcracking and debonding between the homogeneous phase and the particle phase occurs causing strain-softening behavior in this zone. Delamination is initiated when the cohesive stress at the SFRM-steel interface reaches cohesive strength (σ_c) and subsequently progresses until the cohesive stress reaches zero value, the point at which delamination is completed. It should be noted that, stress-displacement relationship (cohesive laws) over the FPZ is one of the essential input to fracture mechanics-based numerical models. Hence, determination of theses cohesive laws (i.e. the stress-displacement relationships over FPZ) is one of the primary objectives in this research.

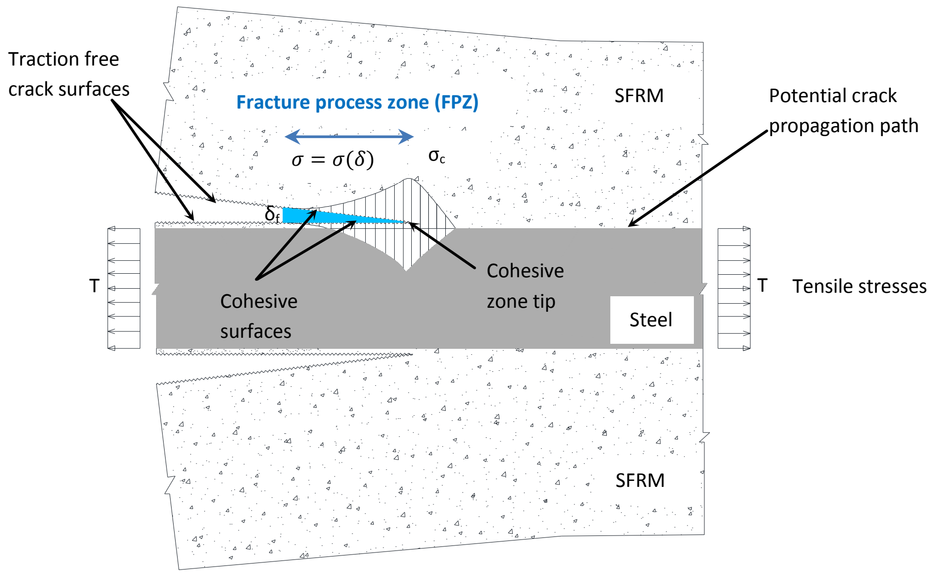

Figure 1.5 Progression of cracks leading to delamination of SFRM from steel surface (Development of fracture process zone)

During dynamic impulsive loading conditions (blast or impact), two additional factors play a crucial role on the crack formation and its development within the bulk SFRM, as well as at the interface of SFRM and steel (i.e. over the FPZ). These factors are so-called, strain rate dependency of material behavior and structural inertia forces. The effect of former factor is related to rate dependency of initiation and propagation of micro-cracks in SFRM and can be explained using fracture kinetics theory (Krausz and Krausz, 1988), whereas, influence of latter factor is associated with significant variations in state of strains and stresses in the material. According to fracture kinetics theory, micro-crack growth is dominated by activation energy. For an inherent micro-crack at SFRM-steel interface, even when the structure is at rest (no load applied), bond-breaking and bond-healing processes occur at atomic level resulting in forward and backward movement of crack-tip line, respectively. However, at macroscopic level, no net change in the crack size is observed since crack-tip progression and shrinkage occur at the same frequency.

When the structure is subjected to loading, the number of bond-breaking steps surpasses the number of bond-healing steps due to external energy supply, leading to crack progression in macro scale. If the load is applied within a very short time (as in the cases of impact or blast), since the number of bond-breaking phases is assumed to be constant in time for a given material, the total number of excessive bond-breaking phases will be smaller than the case when the applied load is quasi-static. As a result, the apparent cohesive strength as well as cohesive critical fracture energy of material (SFRM) will be higher (Krausz and Krausz, 1988).That means, during high strain rate loading conditions the fracture properties of steel-SFRM interface is expected to enhance. However, the enhancements observed in the material fracture properties owing to the effects of rate-dependency of material should always be distinguished from the effect of inertial forces on the increase in fracture load (Ožbolt et al., 2011; Ožbolt et al., 2014).

In this research, it is attempted to characterize the cohesive stress-displacement relationship over the FPZ developed at steel-SFRM interface, and also estimate the effect of high loading rate on these fracture properties. Developing this knowledge will make it possible to explore the delamination of fire insulation from steel structures subjected to various loading scenarios.

1.6 Consequences of Fire Insulation Delamination

The consequences of SFRM delamination from steel structural elements can be significantly severe. In moment-resisting frames subjected to seismic loading, damage to fire insulation over the plastic hinge zone in beams can lead to high heat transfer to beam and significantly diminish the beam capacity, which can result in excessive deformation of beam. More importantly, delamination of fire insulation on beams opens a path for heat to be transferred to adjacent columns, which otherwise would remain less prone to heat penetration. This can significantly affect the column capacity during post-earthquake fire (Braxtan and Pessiki, 2011b). Further, beams and beam-columns in steel frames, when subjected to blast overpressure, can undergo extreme deformations. Consequently, lack of fire insulation on these structural elements during fire following the explosion, can accelerate the adverse effect of fire and thereby extremely jeopardize the structural stability of building. Beams can suffer very high deformation leading to centenary action and horizontal pull-in in columns. Global buckling in beam-columns is thus accelerated as a result of horizontal force applied from beams and also due to direct effect of temperature rise.

In high-rise buildings, the floor assembly can experience large deformations due to softening in steel truss over a very short time. This can jeopardize the stability of adjacent columns through centenary action in floor assembly and eventually the entire structural stability of building can be compromised. For instance, the progressive collapse of WTC twin towers was partially attributed to loss of fire insulation resulting from high impact and blast loads (FEMA 2002, NIST 2005). This incident has led to a major debate with respect to the role of fire insulation on structural integrity and resiliency of high-rise buildings under extreme loading events (NIST, 2005).

1.7 Research Objectives

Based on above discussion, it is clear that there is lack of understanding on the initiation and propagation of damage and delamination in fire insulation applied on steel structures during static, cyclic and impulsive loading as encountered during service conditions, earthquake, impact and explosion, respectively. The main aim of this research is to develop fundamental understanding on the fracture mechanics and delamination of fire insulation from steel structures. The knowledge gap described in the previous section will be filled by pursuing following objectives:

- Carry out detailed state-out-the-art review on the delamination of fire insulation from steel structures and the consequences this phenomenon can impose on structures.
- Conduct material level experiments to determine fracture properties at the interface of steel and fire insulation. In particular, develop cohesive stress-displacement relationship over the fracture process zone at steel-SFRM interface. The results of these experiments will provide essential material property input for numerical models.
- Perform drop weight impact tests on fire insulated beams to characterize the delamination of different types of fire insulation from steel members subjected to impulsive loads causing high stain rate. Using an experimental-numerical approach estimate the effect of high loading rate on the fracture properties over the fracture process zone at steel-SFRM interface.
- Develop a fracture mechanics-based numerical approach for modeling crack initiation and propagation at the interface of fire insulation and steel structures. Subsequently, validate the developed numerical model by comparing the model predictions against test data at both material and structural levels.
- Carry out a set of parametric studies to identify critical factors governing delamination of fire insulation from steel structures subjected to seismic and blast loading. In doing so, quantify the extent of delamination over the structural members as a function of the governing factors.

- Define a new delamination characteristic parameter for fire insulation, which can account for all critical factors governing delamination through one parameter. Thereafter, relate delamination initiation limits and delamination extent on the structural members to this parameter.
- Develop a thermal-structural numerical model that can simulate effect of SFRM delamination on fire performance of steel structures during fire following earthquake, impact and blast loading scenarios.

1.8 Anticipated Research Impact

Current approach is unable to rationally assess post-earthquake, post-impact and post-blast fire performance of steel structures, partly due to limited knowledge on delamination of fire insulation from steel structures subjected to such loading scenarios. Further, the performance of fire insulation in terms of its adhesion to steel surface is only evaluated based upon normal bonding stress. The proposed Ph.D. research aims to produce two main results. First, the proposed experimental-numerical approach initiates the application of fracture mechanics in evaluating delamination of fire insulation from steel structures in a practical scale. Second, since proposed study aims to identify the critical factors governing delamination phenomenon at steel-SFRM interface, the outcomes of research can also be useful for those researchers who are attempting to rectify the drawbacks associated with current fire insulation by developing new fire insulation materials. Further, by relating the delamination initiation limits and extent of delamination at the critical locations of structural elements to the new parameter, a more rational approach of differentiating among different fire insulation products and their application in different situations will be possible for practicing engineers.

1.9 Scope and Outline

The current research is carried out to achieve the above objectives, results of which are presented in seven chapters in this dissertation. Chapter 1 provides the basic background with respect to issue of delamination of fire insulation from steel structures and its consequences. Chapter 2 details the state-of-the-art research on the fracture and delamination of fire insulation from steel structures where both experimental and numerical research results, as well as current code provisions are compiled and the knowledge gaps are underlined. Experimental program, encompassing static fracture tests and drop mass impact tests, are detailed in Chapter 3 and the outcomes are discussed. The fracture mechanics-based numerical model and its validation are outlined in Chapter 4 where implementation of fracture mechanics into the finite element model is outlined. In validation section of Chapter 4, predictions from the numerical model are compared against data from experiments conducted in this research, as well as other studies. Chapter 5 deals with performance of three types of SFRM, widely utilized in steel construction, under static and dynamic loading. The parametric study, in terms of critical factors governing delamination, is presented in Chapter 5. Chapter 6 addresses the consequences of fire insulation damage and delamination from steel structures. Results obtained from thermal-structural analysis, when the structure is exposed to fire following extreme loading events, are detailed in this chapter. Eventually, Chapter 7 summarizes the major outcomes form this research and outlines the future potential research areas.

CHAPTER 2

2 STATE-OF-THE-ART REVIEW

2.1 General

In current provisions, there is no methodology to account for the effect of delamination of fire insulation delamination on performance of steel structures during fire following earthquake, impact and blast. This is mainly because of limited studies carried out, both at material and structural levels, on delamination and fracture mechanisms of fire insulation and its role on fire performance of steel structures. After collapse of world trade center in 2001 there were some initial studies on fracture properties of SFRM and ever since limited research results has been published. At material level, experiments have been focused on measuring normal bond strength, which is usually reported in material specifications. At structural level, the results have been limited to measuring extent of delamination over the structural elements (i.e. beam and column) subjected to quasi-static cyclic loading. There has been no numerical model developed for modeling delamination of SFRM from steel surface on a practical scale. Further, there is no research, either experimental or numerical, on delamination of fire insulation from steel structures during impact and blast loading. This section provides a state-of-the-art review on experimental and numerical studies with respect to delamination of fire insulation from steel structures. The current provisions in codes and standard are also reviewed.

2.2 Experimental Studies

The limited experimental studies carried out on fracture performance of fire insulation materials can be divided into two groups; tests carried out at material level and experiments conducted at structural level.

2.2.1 Material Level Tests

At material level, Chen et al. (2010) carried out tests to evaluate mechanical and interfacial properties of one type of SFRM, namely YC3, including compressive strength, tensile strength, normal bond strength and shear bond strength. However, they did not measure load-displacement response at SFRM-steel interface and reported only maximum strength attained at fracture. The authors also carried out static tests on small scale specimens insulated with SFRM, namely tensile, compression and bending tests. Their results showed delamination of SFRM from steel surface under the applied loading. Figure 2.1 shows the experimental setup adopted by Chen et al. (2010) to measure the normal and shear bond strength at the interface of SFRM type YC3 and steel substrate.

In test set-up for normal bonding strength, the SFRM was applied on a short T-shaped steel specimen, while another T-shape steel profile with the same size was glued on the top face of the SFRM. The specimen was positioned in the material testing machine while being clamped by upper and lower jaws of the machine and load was applied through the bottom jaw as is depicted in **Error! Reference source not found.**a. The normal bond strength was defined as the maximum load attained during failure divided by the SFRM-steel interface area subjected to tensile stresses. In shear bond tests, a steel plate is sandwiched by two sets of SFRM-steel plate assembly which were glued to the central plate as shown in **Error! Reference source not found.**b. The load was applied on the central plate and the shear bond strength was defined as maximum load carried by the system divided by the SFRM-steel interface area subjected to shear stresses. The measured normal and shear bonding strength for this type of SFRM are 40 kPa and 70 kPa, respectively. The measured mechanical properties including density, elastic modulus, compressive strength and tensile strength were 550 kg/m^3, 32.43 MPa, 590 kPa and 50 kPa, respectively.

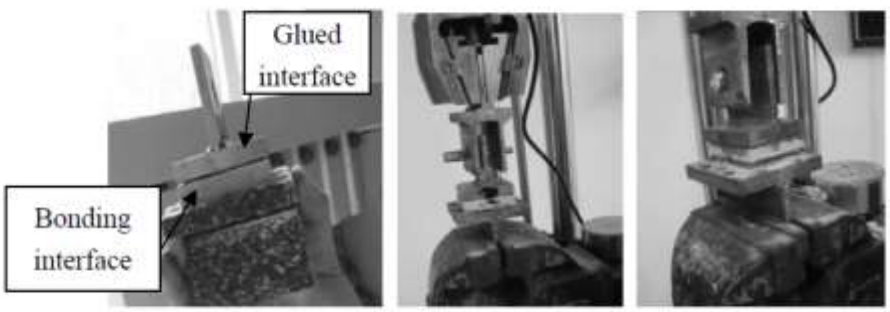

a) Normal bonding test

b) Shear bonding test

Figure 2.1 Normal and shear bond experiments carried out by Chen et al. (2010)

Braxtan and Pessiki (2011a) evaluated normal bond strength of SFRM types Cafco300 (wet-mix) and Blaze Shield II (dry-mix) through tests on small scale steel coupons. The steel plates, insulated with SFRM, were subjected to tensile yielding at various strain ductility demands. Once a certain strain level was attained, the plates were unloaded. Subsequently, normal bond tests were performed on the SFRM, and thereby degradation of the bond strength at SFRM-steel interface as a function of tensile yielding in steel was evaluated. They also studied the effect of surface mill finish of steel on normal bond performance. However, they did not provide any load-displacement response at SFRM-steel interface. The experimental set up used by Braxtan and Pessiki (2011a) and the relationship between average normal bond strength versus average strain on plate is illustrated in Figure 2.2.

Based on these tests, Braxtan and Pessiki (2011a) reported that when SFRM is applied on steel that has mill scale, the adhesive strength of the SFRM degrades rapidly once the steel yields. They attributed the rapid degradation of the adhesive strength to the debonding of the mill scale from the steel as the steel yields. They concluded that the normal bond strength is three times higher for Cafco300 than the normal bond strength for Blaze Shield II. Also, in tensile tests carried out on steel plates covered with fire insulation, they found that SFRM can detach from the steel plate after loading beyond yield. Further, delamination of SFRM was more prevalent in the plates sprayed with Blaze Shield II than in the plates sprayed with Cafco300.

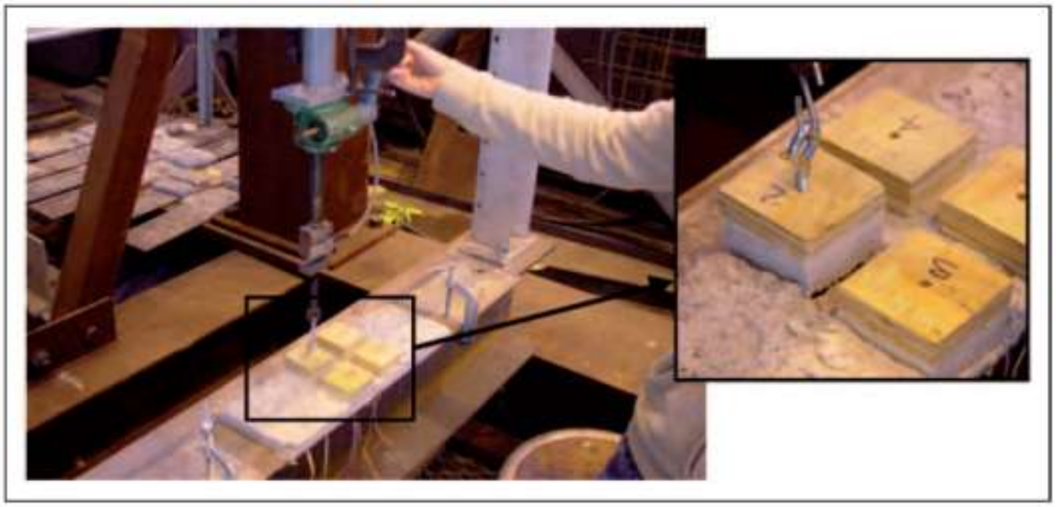

a) Test setup and specimens

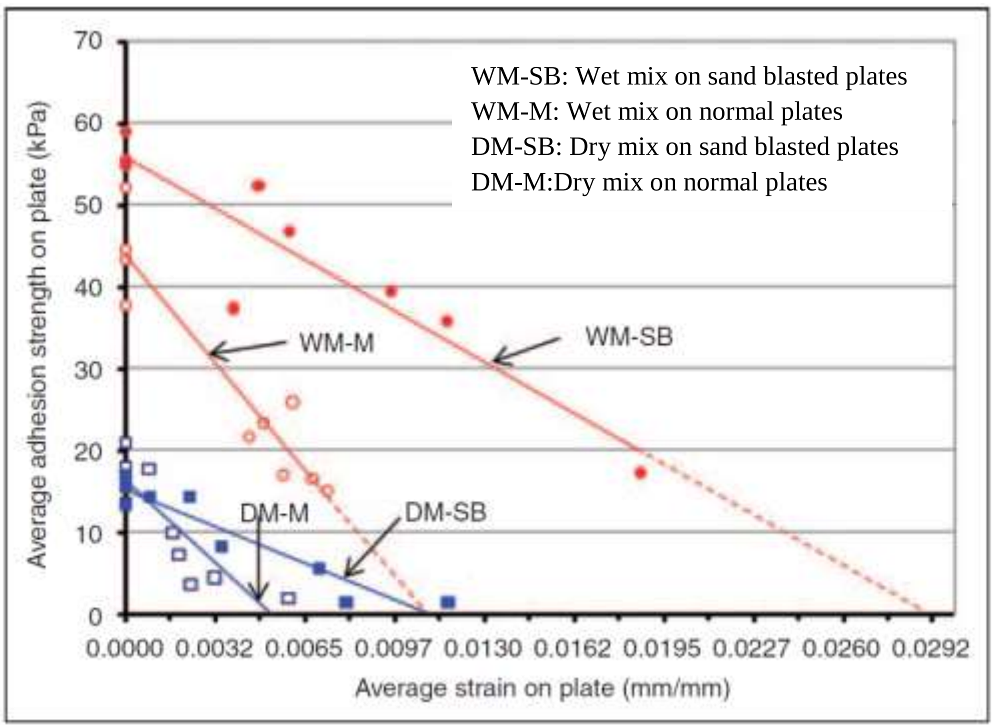

b) Bond strength vas strain level in steel substrate

Figure 2.2 Normal bond experiments performed by Braxtan and Pessiki (2011a)

The above discussed tests reported in the literature are strength-based and thus they do not address the effect of interfacial cracks on bond performance. Tan et al. (2011) proposed a new test method for measuring adhesion of SFRM on steel to overcome some of the current limitations in ASTM E736 (2006) for characterizing the SFRM-steel bond performance. This test method is based on linear elastic fracture mechanics (LEFM) approach and assumes pre-existing flaws at SFRM-steel interface. Figure 2.3 illustrates the schematics of single-arm cantilever test specimen utilized by Tan et al. (2011) in their fracture experiments. In the tests, field conditions were simulated for the application of SFRM on steel. While holding the SFRM in-place, the end of steel coupon was peeled-off with a constant displacement rate of 0.1 mm/s and the corresponding applied load was measured. Series of loading and unloading cycles were simulated to study the relation among fracture energy and initial crack length. The recorded load-displacement curves for different initial crack sizes are shown in Figure 2.4.

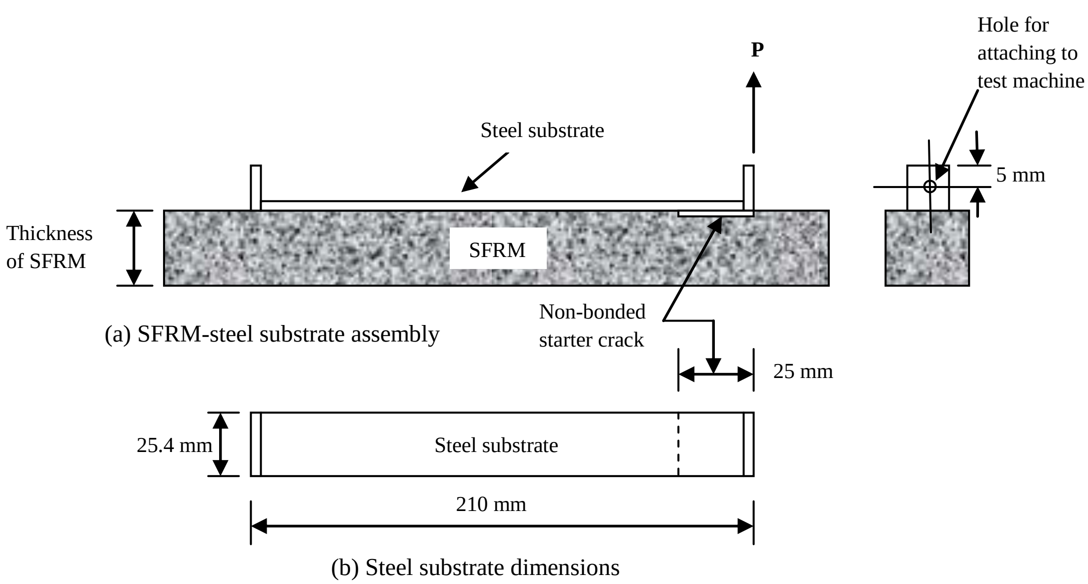

Figure 2.3 Experimental setup designed by NIST to measure fracture energy at steel-SFRM interface (Tan et al. (2011))

Tan et al. (2011) adopted two different approaches to deduce the fracture energy; an analytical solution based on theory of beam on elastic foundation and an experimental compliance calibration method. Results from these two approaches were in good agreement. The measured critical fracture energy for gypsum-based SFRM was in the range of 2 J/m^2 to 6 J/m^2, while this was between 6 J/m^2 to 12 J/m^2 for compositely reinforced fibrous SFRM. It should not be overlooked that this test method only takes into consideration the critical fracture energy in normal fracture mode for evaluation of delamination at interface and does not take into account the frictional mode in evaluating delamination. Further, as will be outlined later, the application of linear elastic fracture mechanics for cementitious materials, which develop a large fracture process zone at crack tip, is not accurate.

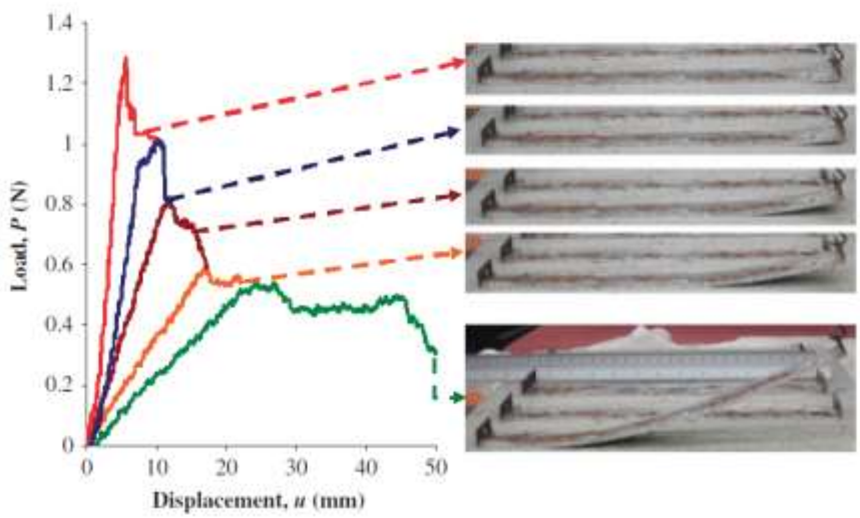

Figure 2.4 Load-displacement curves for different initial crack size measured by Tan et al. (2011) in their fracture tests

Zhang and Li (2014) introduced a fire-resistive engineered cementitious composite (FR-ECC) to address the current issue of lack of durability (adhesion and cohesion) of SFRM on steel structures. In particular, they studied the effectiveness of employing acrylic polymer latex as admixtures and interfacial adhesive to enhance interfacial fracture properties of FR-ECC at its interface with steel substrate. The interfacial fracture resistance was evaluated by utilizing a fracture test proposed by Tan et al. (2011). Based on the measured critical fracture energy between latex modified FR-ECC matrix and steel, they reported that using latex as admixture and interfacial adhesive can efficiently improve the interfacial critical fracture energy at the interface of FR-ECC and steel by 54% and 147%, respectively. Further, they attributed the enhanced adhesive properties to the change in composition and microstructure of interfacial transition zone (ITZ) between latex modified FR-ECC matrix and steel.

2.2.2 Structural Level Tests

At structural level, Braxtan and Pessiki (2011b) studied damage pattern in SFRM applied on a beam-column assembly subjected to quasi-static cyclic loading through large-scale experiments, where the cyclic loading represented a strong seismic event. Substantial damage of SFRM in bottom and top flanges and partial damage of SFRM in web of beam were observed. Figure 2.5 illustrates the overall geometry and member sizes for the beam-column assembly connection. In moment resistant steel frames subjected to lateral forces, inflection points form at the mid-height of the columns and at the mid-span of the beams. An exterior beam-column assembly was tested by Braxtan and Pessiki (2011b) and inflection points were simulated through attaching the column to a reaction wall by pin supports. A vertical load was applied at the beam tip. Lateral torsional buckling in beam was prevented by providing enough lateral supports. This beam-column assembly was subjected to the cyclic displacement-controlled loading protocol as per ATC procedure (FEMA 461, 2007).

Based on their cyclic monotonic tests, Braxtan and Pessiki (2011b) reported that at story drift of 3% and 4%, SFRM damage is localized in the beam flanges where large inelastic deformation and local instabilities occur. According to their observation for beam-column assembly insulated with SFRM type Blaze Shield-II, the SFRM on the beam web remained intact throughout the duration of the test. However, it was found during the post-testing inspection that the SFRM was delaminated over most of the beam web. In case of SFRM type Cafco300, the extent of delamination over the flanges is less as compared to SFRM type Blaze Shield-II. Figure 2.6 shows the delamination of SFRM type Blaze Shield-II from bottom flange of the beam.

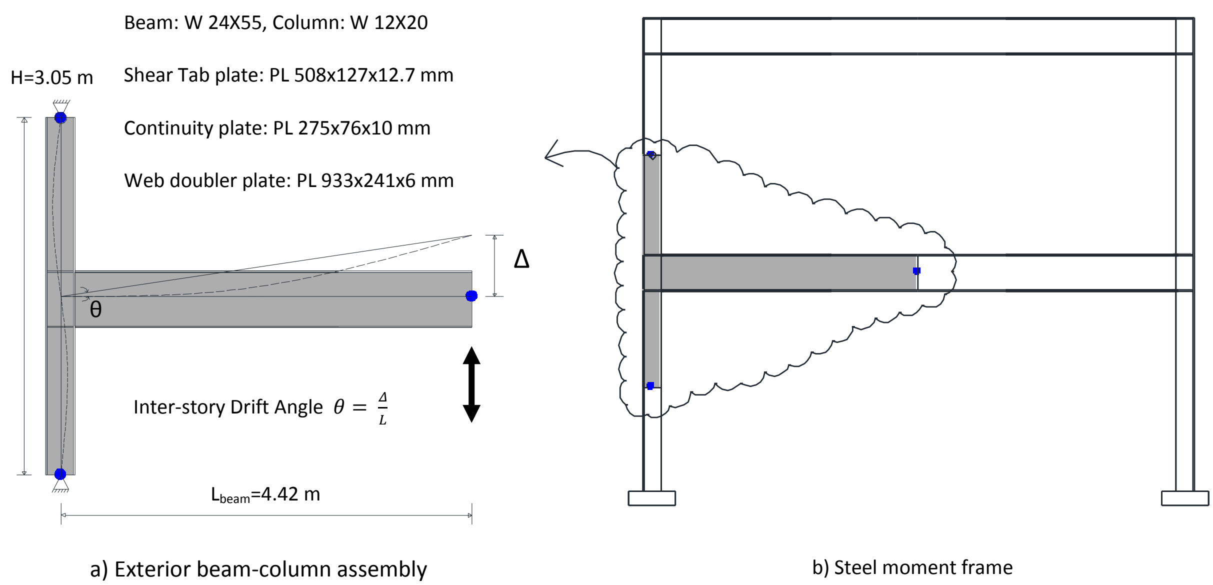

Figure 2.5 Test setup of an exterior beam-column assembly to measure delamination of SFRM (Braxtan and Pessiki (2011b)

Wang et al. (2013) conducted experiments to investigate failure pattern of SFRM type YC3 applied on steel cantilever columns under large quasi-static cyclic moments, induced at the bottom of the steel column. Figure 2.7 depicts the experimental set-up designed and used by Wang et al. (2013). They concluded that adhesion of SFRM to steel remains weak so that noticeable delamination occurs under large moments. In addition, they also inferred that cyclic loading intensifies the extent of damage owing to damage accumulation effects. However, the effect of damage accumulation has not yet been quantified. The observed damage and delamination of fire insulation in their tests is shown in Figure 2.8.

Figure 2.6 Delamination of SFRM type Blaze Shield-II from bottom flange of the beam-column assembly tested by Braxtan and Pessiki (2011b)

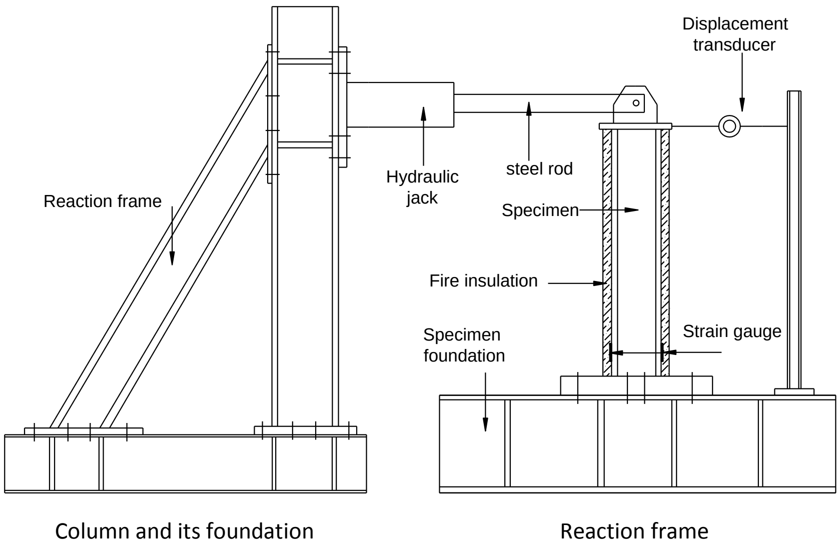

Figure 2.7 Test set-up for fire insulated column test (Wang et al. (2013))

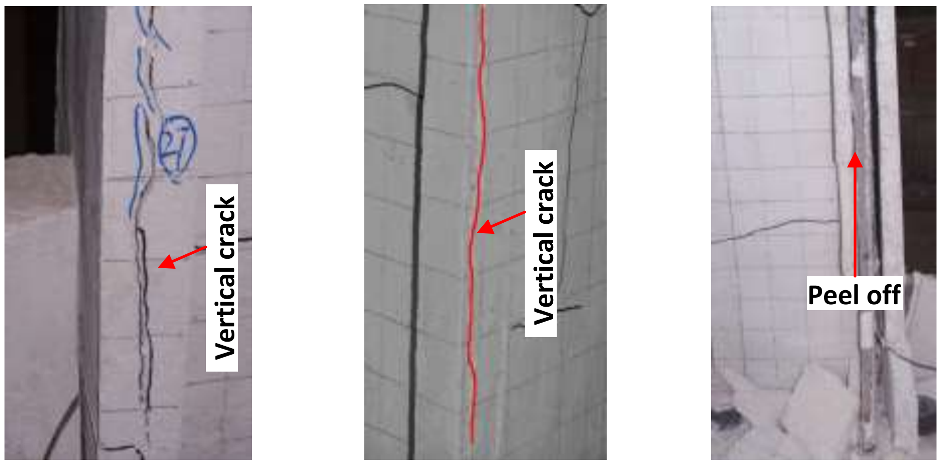

Figure 2.8 Debonding and fracture of SFRM from steel column at high levels of quasi-static load (Wang et al. (2013))

2.3 Numerical Studies

Most of the previous numerical studies focused on studying the effect of partial loss of fire insulation on the fire resistance of steel structural members. In these studies, damage mechanism in SFRM and causes of interfacial delamination of fire insulation from steel surface were not taken into consideration. However, the consequences of arbitrary insulation loss were quantified.

Tomecek and Milke (1993) studied the effect of partial loss of fire insulation from flange and web of steel columns on the fire resistance of the columns using computer program FIRES-T3. The authors carried out 2D thermal analysis to compute the temperature evolution over the cross section of the column. No structural analysis was performed; instead, the average steel temperature over the cross section was used to determine the time to failure of the columns based on the criteria outlined in ASTM E119 (2014). Based on their analysis, Tomecek and Milke (1993) found that fire resistance of steel column can appreciably decrease in case of insulation loss and the level of reduction depends on the extent of insulation loss, the size of column and the position of protection loss. The fire resistance degradation of columns depends on the initial fire-rating of the columns such that columns with higher fire-rating undergo higher fire resistance reduction. For instance, 2% insulation loss on a one-hour-rating and three-hour-rated column (W10X49) leads to 10% and 28% decrease in fire resistance of the column, respectively. Further, columns with heavy sections experience less reduction in fire resistance compared to columns with small sections. Figure 2.9 depicts the finite element model along with the fire resistance reduction curves for W10X49 column.

Ryder et al. (2002) also investigated the reduction in the fire resistance of steel columns due to the loss of SFRM directly on the column using FIRES-T3 computer program. They performed 3D thermal analysis to predict temperature distribution within the column over the time. The computed thermal field is used in conjunction with thermal endpoint criteria specified in ASTM E119 to estimate the fire resistance of the column. Their results showed that insulation loss, though to a very small extent, can significantly influence the fire resistance of a steel column. Further, they concluded that the reduction in fire resistance is mainly affected by the extent of insulation loss rather than the size of the column. The schematics of missing SFRM from flange and web of the column, along with the temperature time-history at exposed flange and web, is shown in Figure 2.10.

Kwon et al. (2006) investigated the effect of SFRM removal from both web and flange of a steel column. They utilized Abaqus software to conduct thermal and structural analysis. Based on their numerical results, they concluded that the loss of even small amount of SFRM caused a reduction in strength of the column and the consequences of SFRM removal from the flange was found to be more severe than the removing the SFRM from the web.

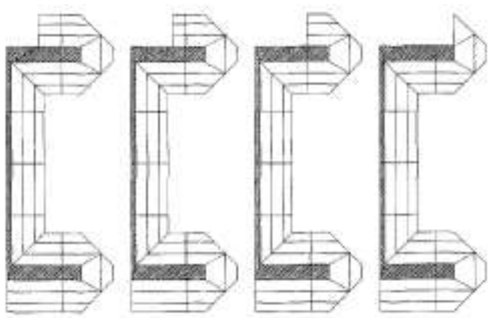

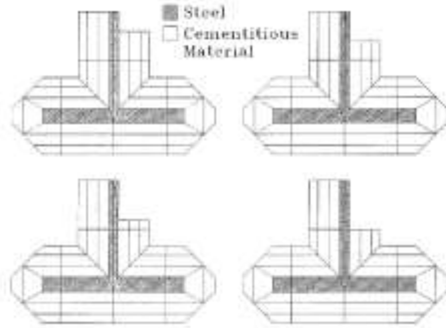

a) Fire insulation loss from flange

b) Fire insulation loss from web

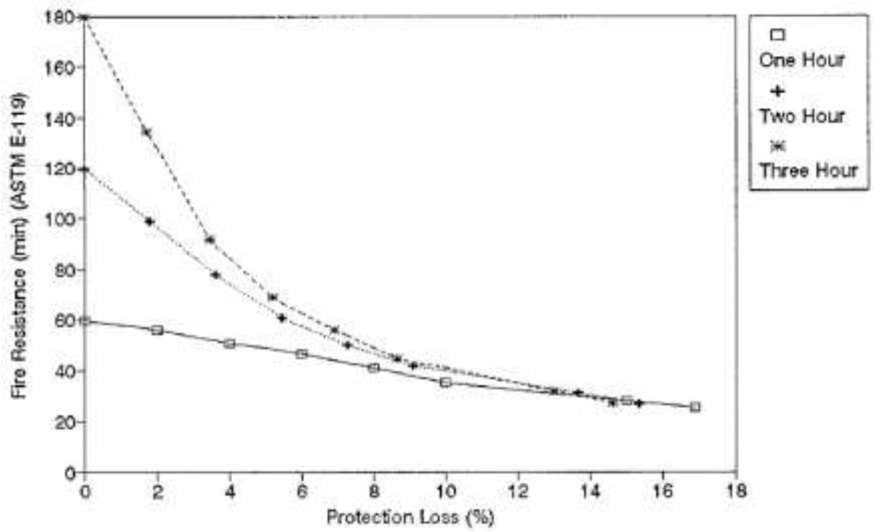

c) Fire resistance of W 10X49 versus percentage loss of fire insulation from flange

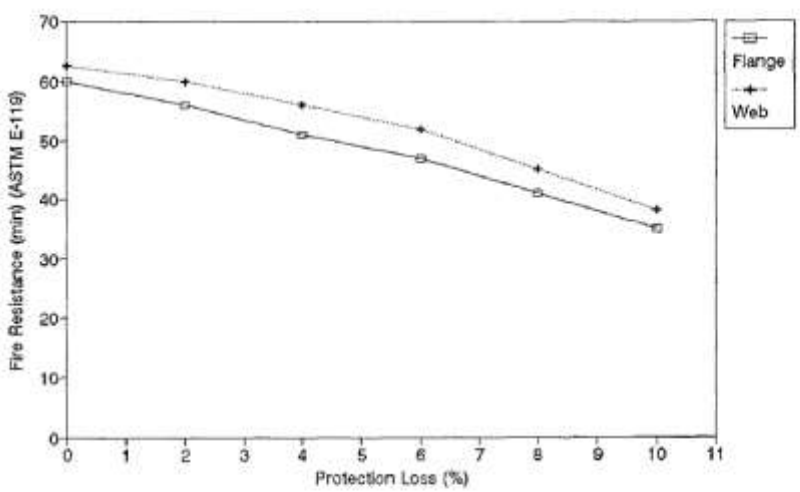

d) Fire resistance of W 10X49 versus percentage loss of fire insulation from flange and web

Figure 2.9 Effect of partial loss of fire insulation on fire resistance of steel columns (Tomecek and Milke (1993))

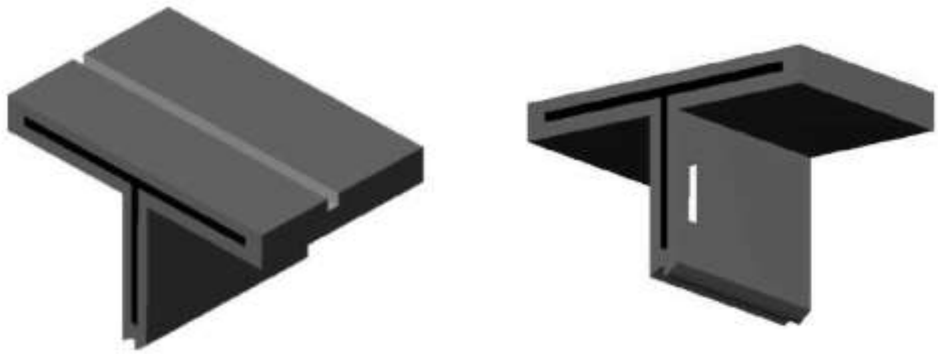

a) Missing SFRM in flange b) Missing SFRM in web

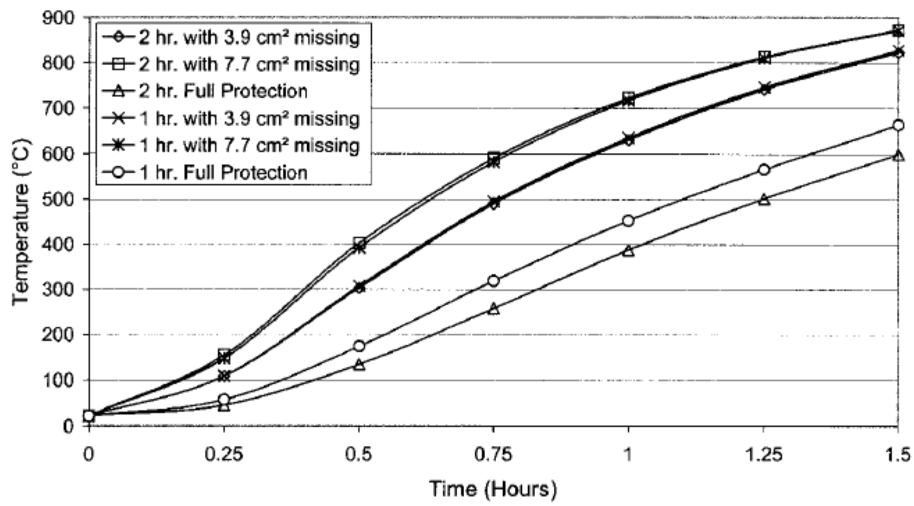

c) Temperature at exposed flange surface of W 6X16 column

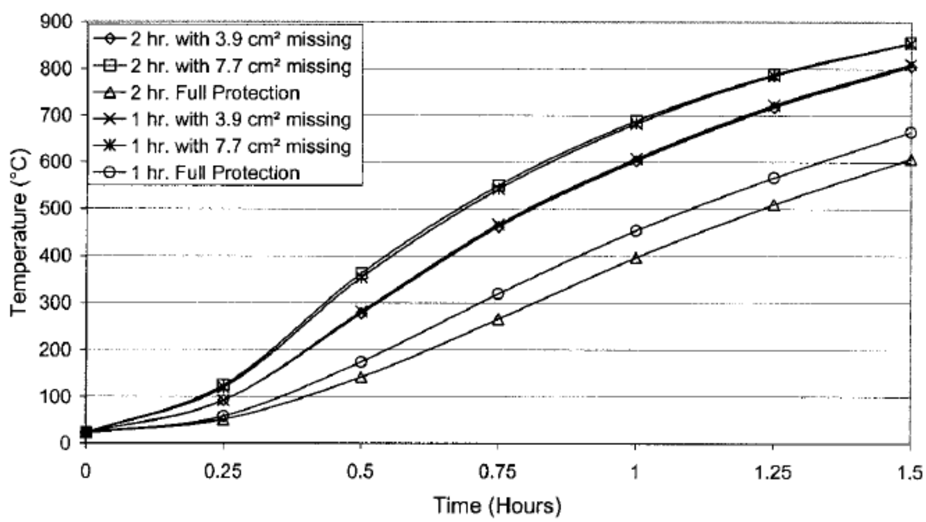

d) Temperature at exposed web surface of a W 6X16 column

Figure 2.10 Effect of partial loss of fire insulation on fire resistance of steel columns (Ryder et al. (2002))

The finite element model of the W14X109 column analyzed in Kwon et al. (2006)'s study is depicted in Figure 2.11 along with the temperature evolution over the time in different locations of the cross section. The reduction in structural capacity of the column as a function of fire duration, for different fire insulation missing scenarios is shown in Figure 2.12

Gu and Kodur (2011) carried out parametric studies on six-story steel-framed building to illustrate the effect of insulation damage on fire response of a steel structure. In their analysis, realistic fire scenarios, loading, and failure criteria were taken into consideration. Figure 2.13 shows the steel frame considered in the analysis along with the insulation damage pattern, deformation of frame for 10% insulation damage and the fire resistance reduction of the frame as a function of insulation damage percentage. Based on their analysis results, they concluded that the fire resistance of a steel-framed structure is significantly influenced by the extent of insulation loss, type of fire scenario, and level of lateral load. Gu and Kodur (2011) also highlighted that the insulation damage can result in faster deterioration in the structural response of framed buildings under the combined effect of fire and lateral loading.

Dwaikat and Kodur (2012) developed a simplified approach for predicting temperature rise in steel sections with locally damaged fire insulation and validated their approach against numerical simulations of ANSYS finite element software. Based on the fire resistance analysis on a W14x145 steel column, they showed dramatic reduction in plastic capacity of column due to 5% loss of 25 mm applied SFRM insulation, as shown in Figure 2.14. The fire resistance of this column decreased from 180 minutes to 90 minutes due to 5% loss in fire insulation.

Keller and Pessiki (2012) conducted an analytical case study to evaluate the effect of SFRM delamination patterns observed in experiments carried out by Braxtan and Pessiki (2011b) on thermo-mechanical response of steel moment beam-column assembly during post-earthquake compartment fire exposure. Figure 2.15 illustrated their finite element model developed in Abaqus software and the moment-rotation response of the beam-column connection after being exposed to fire scenarios with different duration. As is clear in Figure 2.15, significant temperature-induced softening occurs in moment-rotation response of beam-column connection, and as a consequence, flexibility of the structural system for sideway motion is increased resulting in intensified drift demands under the action of residual post-earthquake destabilizing forces.

Dwaikat and Kodur (2011) performed 2D finite element analysis adopting a cohesive zone approach to model spontaneous initiation and propagation of delamination at SFRM-steel interface under static and impact loads. They studied delamination under three loading cases, including pure tension, pure bending moment and drop mass at the tip of a cantilever beam. Figure 2.16 depicts schematics of the models analyzed in ANSYS software and the delamination percentage under tensile loading condition. They concluded that interfacial tensile stresses at SFRM-steel interface are lower in case of thin layers of insulation and also thickness of SFRM can be optimized with respect to impact energy.

a) Finite element model of the column (W14X109) and the missing insulation form flange (l_p)

b) Temperature time-history for $l_p=b_f/16$ (b_f=flange width)

c) Temperature time-history for $l_p=b_f$ (b_f=flange width)

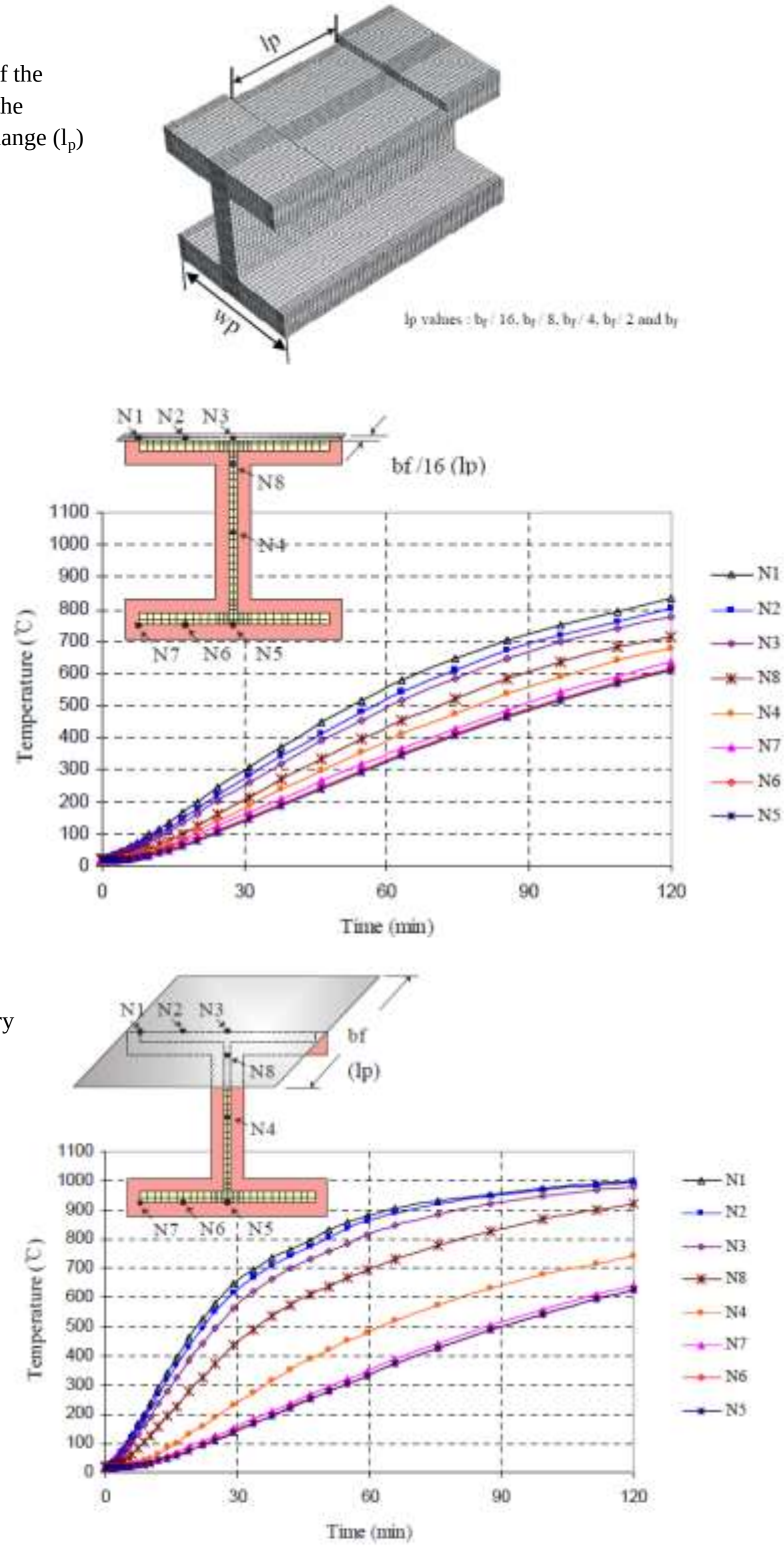

Figure 2.11 Temperature distribution over the cross section of steel column as a consequence of missing fire insulation from flange (Kwon et al. (2006))

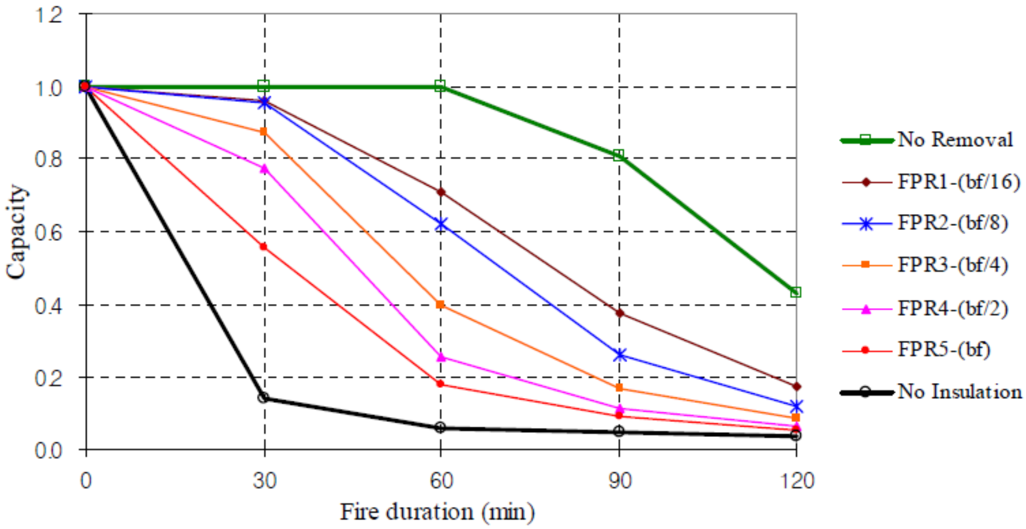

a) Capacity reduction for different fire insulation missing scenarios

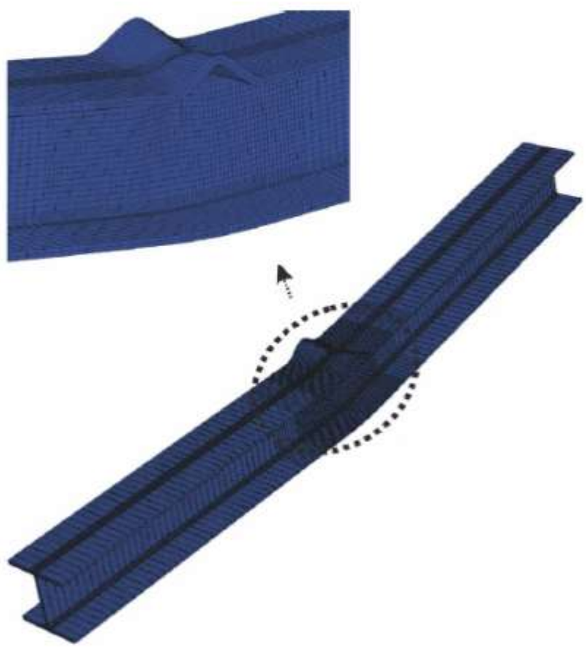

b) Column deformation for l_p=b_f and fire duration of 90 min

Figure 2.12 Capacity reduction of the column versus fire duration (Kwon et al. (2006))

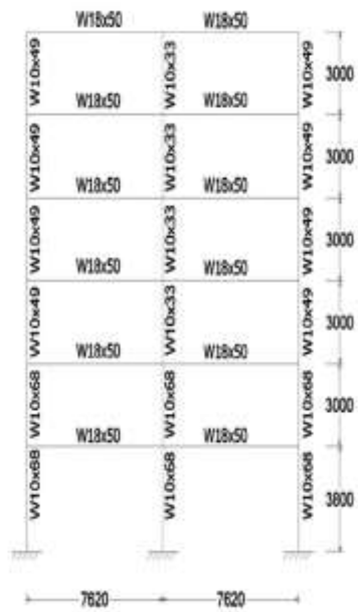

a) Steel frame analyzed

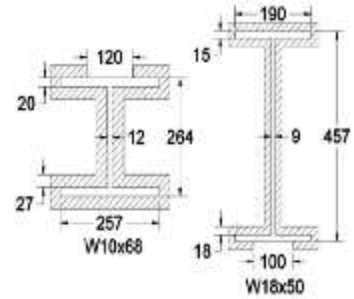

b) Assumed insulation damage

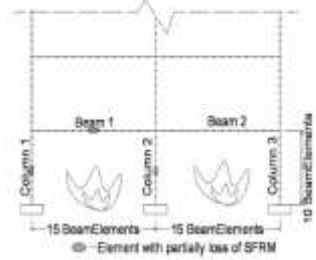

c) Ground floor of the frame exposed to fire

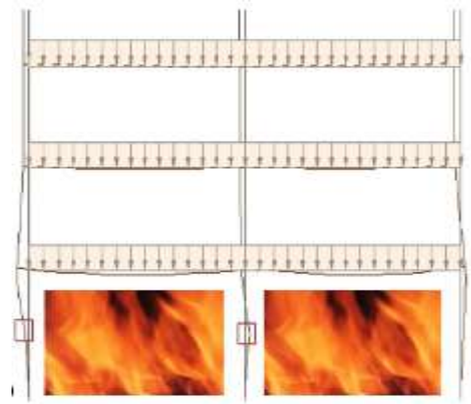

d) Deformation of steel frame under 10% insulation damage

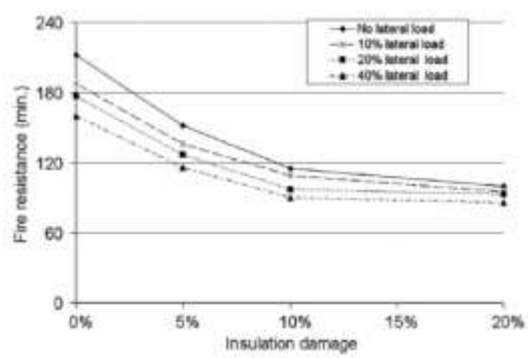

e) Fire resistance reduction

Figure 2.13 Effect of fire insulation damage on fire resistance of a moment resisting frame (Gu and Kodur, (2011))

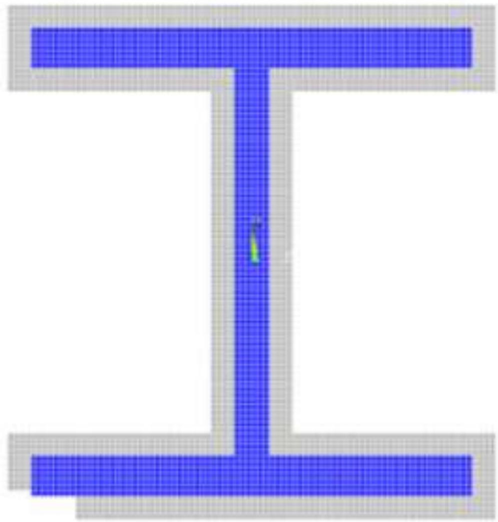

a) Fire insulated steel column and missing insulation

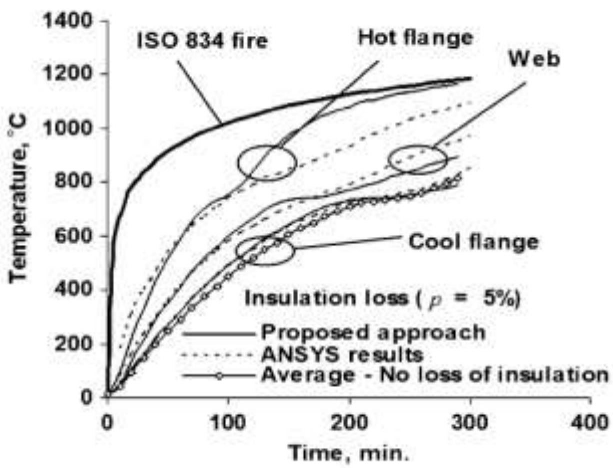

b) Temperature rise in steel

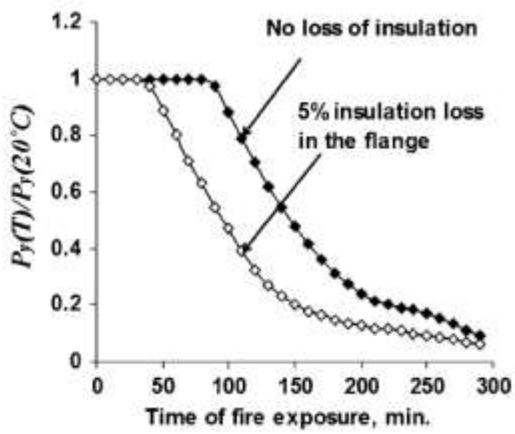

c) Reduction in plastic capacity of steel column

Figure 2.14 Effect of fire insulation damage on fire resistance of a steel column (Dwaikat and Kodur, (2012))

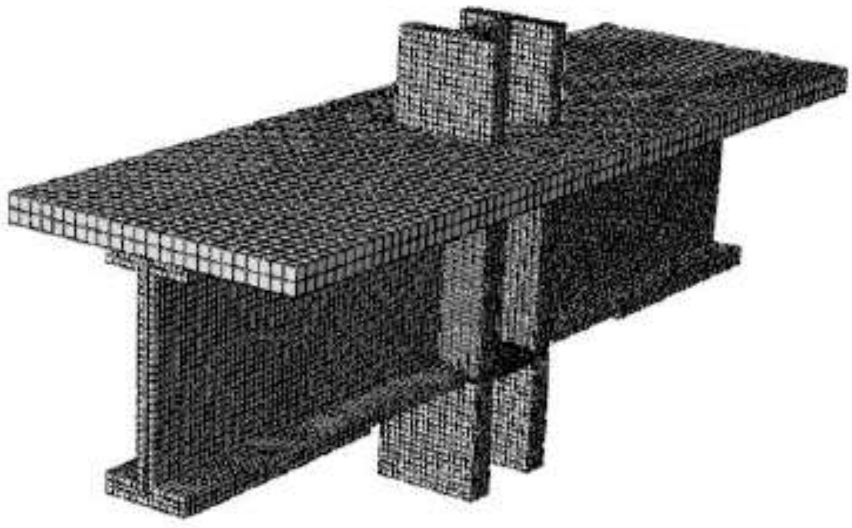

a) Finite element model of beam-column connection

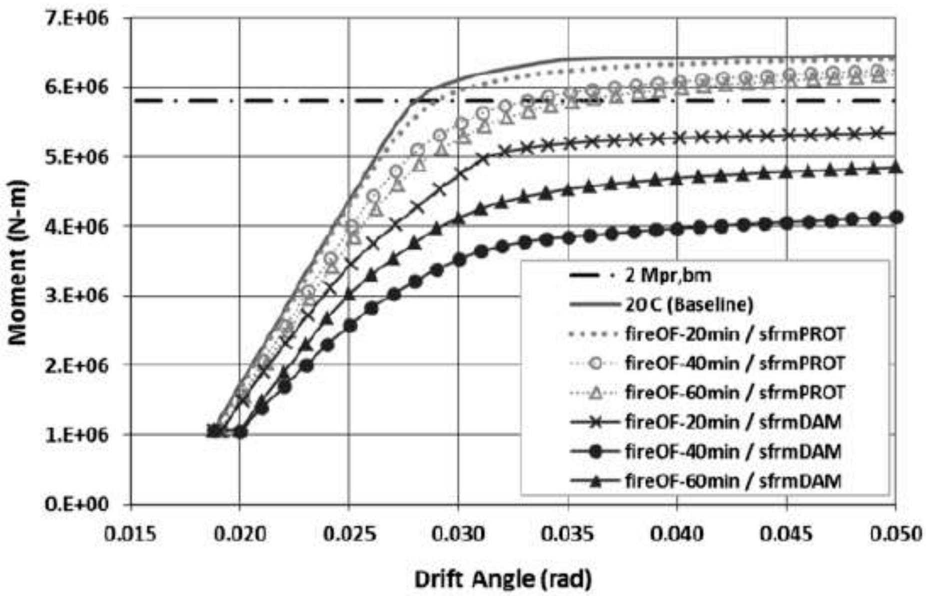

b) Moment-rotation response of beam-column connection after being exposed to different fire scenarios

Figure 2.15 Effect of fire insulation damage on moment-rotation response of beam-column connection (Dwaikat and Kodur, (2012a))

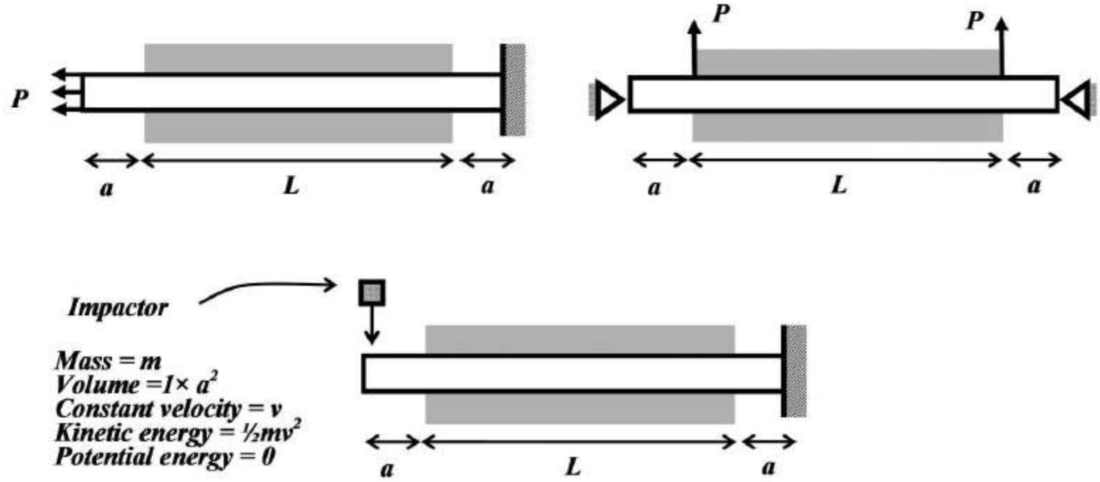

a) Different loading cases

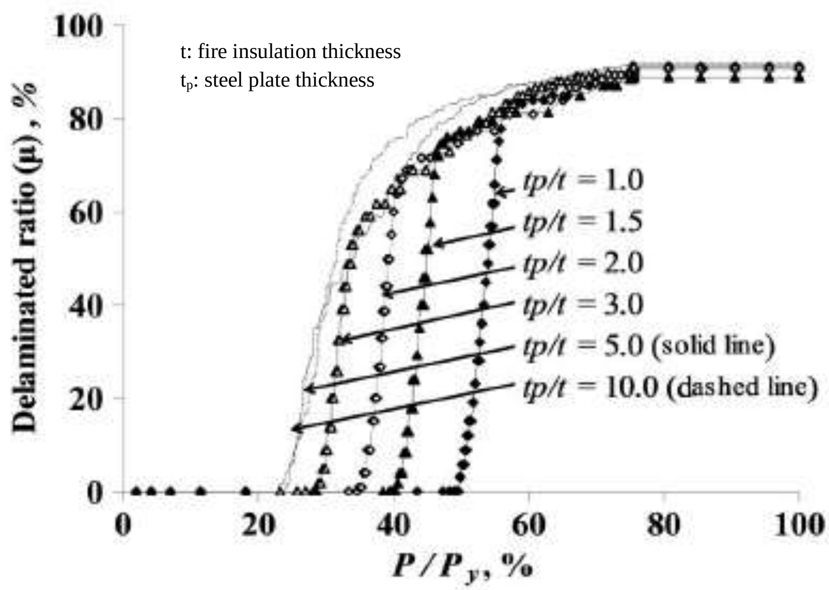

b) Delamination percentage as a function of loading

Figure 2.16 Numerical modeling of fire insulation delamination from steel surface (Dwaikat and Kodur, (2011)) The above literature review shows that previous experimental and numerical studies, though provided valuable understanding on fire insulation delamination, have two major disadvantages. First, most of the previous researchers performed strength-based studies and hence did not adopt a fracture mechanics approach towards describing the cracking and delamination of fire insulation. Second, most of the experiments, both at material and structural levels, have been carried out under static and cyclic monotonic loadings. There has been no research on establishing dynamic and rate-dependent fracture properties of SFRM. Further, there have been no experimental and numerical studies on dynamic delamination of SFRM from steel structures subjected to high strain rate loading.

2.4 Codes of Practice

The durability requirements for insulation materials are specified in codes and standards for buildings. Also, there are some recent reports, which highlight the role of critical properties of insulation materials in achieving satisfactory fire performance of steel structures.

A number of ASTM tests are currently used to gauge the durability and integrity of SFRM under normal life of structure; during construction process; and under extreme conditions (such as earthquake and severe fires). A major drawback of most of these tests is that they are not fundamentally linked to materials science (Bentz et al., 2009) and they do not measure many of critical engineering parameters that are necessary for understanding the mechanics of SFRM under severe loading conditions, such as fracture energy and the debonding stresses.

For instance, the current method for testing the cohesive/adhesive properties of SFRM, ASTM E736 (2011), consists of a disk with a hook for hanging a weight, and that disk is attached to the SFRM through a quick setting adhesive. The SFRM material must withstand a minimum weight before it is dislodged. The weakness of this method is that it provides only one value of failure load without any distinction whether the failure is due to poor adhesion, or poor cohesion. Figure 2.17 illustrated the test method prescribed in ASTM E736 for measuring bond strength between fire insulation and steel substrate.

ASTM E760 (2011) is another standard, which specifies a test method for evaluating the SFRM performance under impact loads. This standard requires that no visible cracks or spalling of the SFRM should be observed when it is subjected to the following prescribed impact test. The impact test is performed using an impactor of leather bag with mass of 27.7 kg dropped from a height of 1.2 m on the middle of a 3.6 m free span insulated cellular steel deck with concrete topping, as shown in Figure 2.18. As obvious, the impact simulated in this test is comparable to impacts that can occur in normal “service” cases which would result from dropping heavy objects on floors, and thus, the prescribed test does not represent severe impacts that would result from blast or earthquake loading.

The performance of SFRM under service deflection is assessed by the ASTM E759 (2011) standard. A steel deck-concrete slab assembly, similar to that used in ASTM E760 standard mentioned above, is also used in this standard. A point load is applied at the center of the slab assembly with the insulation applied at the bottom surface (tension side) of the steel deck. The SFRM is deemed to satisfy the test if cracks or dislodging due to the induced deflection is not observed until a deflection limit of $L/120$ is reached, as illustrated in Figure 2.19.

Figure 2.17 Normal bonding test between steel and fire insulation based on ASTM E736 (2011)

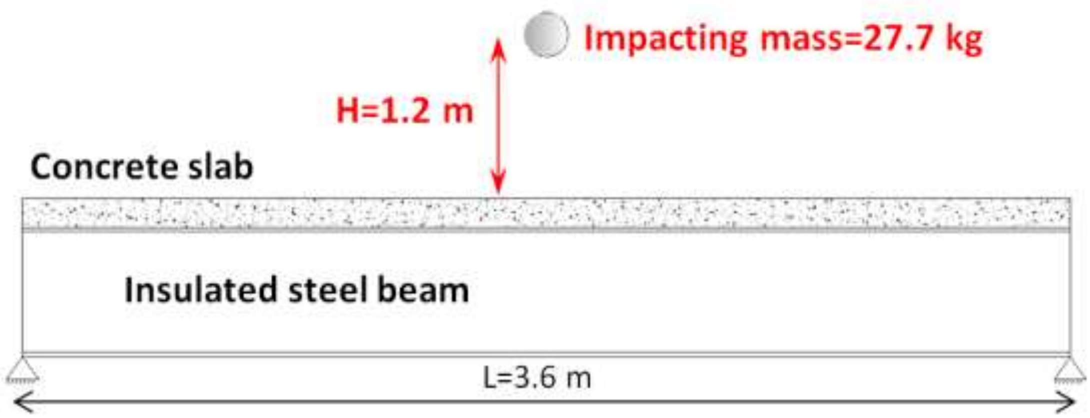

Figure 2.18 Drop mass test for measuring durability of fire insulation under accidental impact loading based on ASTM E760 (2011)

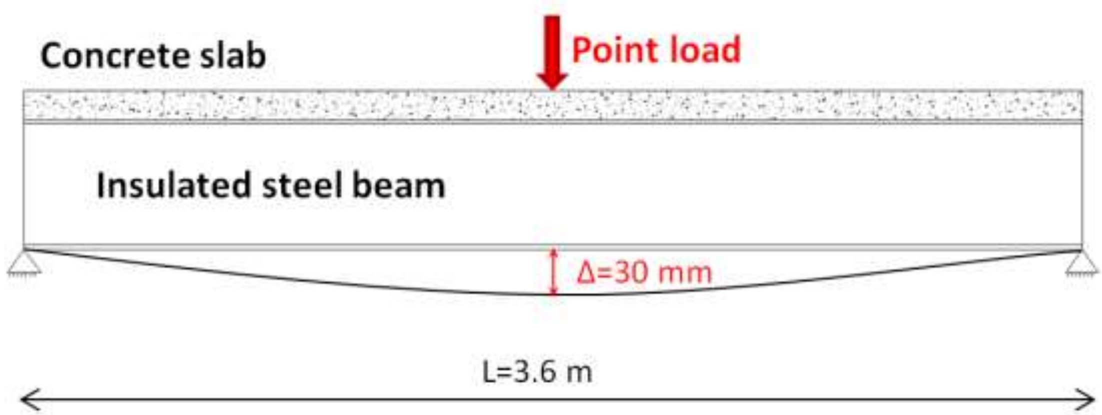

Figure 2.19 Point load test for measuring durability of fire insulation under service loading conditions based on ASTM E759 (2011)

Eurocode 3 (2010) does not give any specific requirements for the durability characteristics of fire insulation. It only states that "supplementary requirements concerning the use of approved insulation and coating materials, including their maintenance are not given in Eurocode 3, because they are subject to specification by the competent authority."

International Building Code (IBC 2012) section 714.4 states "where the fire protective covering of a structural member is subjected to impact damage from moving vehicles, the handling of merchandise or other activity, the fire protective covering shall be protected by corner guards or by a substantial jacket of metal or other noncombustible material to a height adequate to provide full protection." This indicates that fire insulation in structures that are susceptible to extreme loading events, should be protected to avoid any damage.

Recent reports by NIST (2005) and Federal Emergency Management Agency (FEMA 2002) on the collapse of WTC buildings highlighted the need for satisfactory fire insulation performance under extreme loading scenarios. NIST report concludes that in WTC buildings "damage to fire insulation occurred not only in locations where direct debris impact happened, but also in perimeter columns (not directly impacted by debris) due to structural vibration". Therefore, NIST recommends the development of appropriate criteria, test methods and standards: i) for the in-service performance of SFRM used to insulate steel structural components; and ii) to ensure that these materials, as installed, confirm to conditions in tests used to establish the fire resistance rating of components, assemblies, and systems. In addition, FEMA report on WTC building performance study concludes that the performance of spray-applied fire protection material played a crucial role in the collapse of twin towers (WTC). It also concludes that, adhesion and cohesion characteristics of SFRM are not well understood, and that there is an urgent need for developing performance based requirements for SFRM.

Based on recent recommendations of NIST (2005), U.S. General Services Administration (GSA, 2010) has introduced updated provisions for the use of robust fireproofing materials in steel framed buildings. The proposed provisions require fireproofing materials to have bond strength of 20.6 kPa for buildings below a height of 128 m, and 47.9 kPa for buildings above a height of 128 m. Also, based on these recommendations by NIST, amendments were made in the IBC (2012) code to increase the bond strength for fireproofing by nearly three times greater than currently required for buildings 75-420 feet in height and seven times greater for buildings more than 420 feet in height.

2.5 Knowledge Gaps

Based on the above review, it is clear that there is limited data on mechanical properties of SFRM, especially fracture properties. Also, there is lack of understanding on the initiation and propagation of damage and delamination in fire insulation applied on steel structures during cyclic and impulsive loading as encountered during earthquake, impact and explosion, respectively. Further, there is lack of numerical models to predict the delamination phenomenon at SFRM-steel interface in steel structures subjected to seismic, impact and blast loading. Hence, further research is needed in following key areas:

- Fracture properties need to be determined in mode-I fracture and mode-II fracture for different types of SFRM commonly applied on steel structures. These experiments can not only deliver bond strength but also provides fracture toughness and fracture ductility over the fracture process zone. This data will provide core input to the numerical models dealing with delamination of SFRM from steel structures in practical scale.
- A numerical approach for modeling delamination of fire insulation from steel structures subjected to seismic, impact or blast loading conditions on practical scale is not reported

in literature. Such a numerical model, once validated against experiments at material and structural level, can be used to carry out extensive parametric studies to identify critical factors governing delamination of fire insulation from steel structures subjected to seismic, impact or blast loading.

- Delamination of fire insulation from steel structures subjected to blast loading is not studied literature. In order to investigate this issue, experimental study needs to be carried out either by directly exposing the insulated steel elements to blast overpressure or conducting impact tests (drop mass tests) to generate a high stain rate field similar to the one expected during explosion events.
- In current practice, normal bonding strength, along with density, are the only mechanical properties which are reported in material specifications and there are standard test methods to measure these properties. However, there are other factors, namely tangential bond strength, normal critical fracture energy, tangential critical fracture energy, elastic modulus and SFRM thickness that can influence initiation and propagation of cracks at the interface of fire insulation and steel surface. A more rigorous parameter is needed to account for all critical factors governing delamination phenomenon by maintaining interdependency among different factors.
- In previous numerical studies, the effect of fire insulation damage has been accounted for by arbitrarily choosing the location and amount of missing insulation. However, a more realistic evaluation of fire performance of steel structures during fire following earthquake, or impact or explosion is to be carried out in which the delamination extent is adopted from the results of fracture mechanics-based numerical model. Hence, the fracture mechanics-based numerical model should be combined with a thermal-structural

model to simulate the effect of extreme loading and subsequent fire, sequentially. This type of analysis has not been performed thus far.

- The above stated knowledge gaps are to be overcome to enhance the understanding on fire insulation delamination from steel structures and also to develop a fracture mechanics-based approach to study the effect of critical parameters on initiation and progression of delamination of fire insulation from steel structures subjected to static and dynamic loading conditions. This dissertation is designed to undertake required studies for overcoming the above knowledge gaps.

CHAPTER 3

3 EXPERIMENTAL STUDY

3.1 General

The previous experimental and numerical studies, though provided valuable understanding on delamination of fire insulation, have two major disadvantages. First, most of the previous researchers adopted strength-based test approaches and hence did not adopt a fracture mechanics approach for evaluating cracking and delamination of fire insulation. Second, most of the experiments, both at material and structural levels, have been carried out under static or cyclic monotonic loading. There has been no research on establishing dynamic and rate-dependent fracture properties of SFRM. Further, there have been no experimental and numerical studies on dynamic delamination of SFRM from steel structures subjected to high strain rate loading.

The experimental program undertaken in this study is divided into two parts. In the first part, the constitutive relations of SFRM over the fracture process zone, namely cohesive laws is determined using a series of static fracture tests. The fracture tests are conducted on three types of SFRM commonly utilized in current buildings. In the second part, drop mass impact tests are carried out to investigate the dynamic delamination of SFRM from steel beams, insulated with the very three types of SFRM, under impulsive loading conditions. In this chapter, first the test procedures adopted to determine fracture process zone properties along with the obtained results are presented. Subsequently, test procedures, designed and applied for performing a drop mass impact test on SFRM-insulated beams, with corresponding results, are described.

3.2 Determination of Fracture Process Zone Properties for SFRM

As outlined in Chapter 1, to predict the crack propagation at SFRM and steel interface it is indispensable to establish the cohesive stress-displacement relationship over the fracture process zone (FPZ) at steel-SFRM interface, namely cohesive laws. In this section, test procedures adopted to determine these cohesive laws are presented.

3.2.1 Test Procedures to Evaluate Cohesive Laws over FPZ

There are, in general, two approaches for obtaining stress-displacement relationship in FPZ of cementitious materials; direct approach and indirect approach. In direct approach, stress-displacement response is measured by means of a tension test for Mode I fracture (Peterson, 1985; Reinhardt, 1987; Guo and Zhang, 1987). In this method, although pre-existing flaws start to grow at discrete locations during initial stages of loading, localization of deformation occurs in the FPZ once the maximum load has been attained (Cotterell and Mai, 1996). Specimen dimensions must be large enough to accommodate full development of the FPZ across the area undergoing the tensile loading. Stress-displacement relationship obtained from a tension test can directly generate all three parameters of cohesive law namely, cohesive stiffness, cohesive strength and fracture energy. No further numerical work is therefore required for extracting cohesive laws over FPZ. However, the fracture evolution across the tensile area must be uniform;

otherwise local instabilities such as “bumps” are observed in stress-displacement curve (Hordijk et al., 1987).

There are various indirect methods proposed in the literature for deriving stress-displacement relationship in FPZ of cementitious materials. For instance, Li’s approach (1987) involves measurement of *J*-integral and crack tip opening displacement (CTOD) to obtain the stress-displacement curve. In this method, two specimens have to be used which makes interpretation of results difficult due to inhomogeneous behavior of cementitious materials. Indirect approach has also extensively been used for composite materials and interface of two materials (Sorensen and Jacobsen, 2003; Gordnian et al., 2008; Lee et al. 2010; Valoroso et al. 2013). In recent years, Double Cantilever Beam (DCB) specimens (ASTM D5528, 2013) and End Notched Flexure (ENF) (ASTM WK22949, 2009) specimens are widely utilized to extract the fracture energy in pure modes I and II, respectively. However, fracture energy is the only outcome from these tests. Two other parameters of cohesive laws, namely cohesive stiffness and cohesive strength, are therefore to be determined through numerical modeling. To extract theses parameters, an ideal stress-displacement curve is assumed and numerical simulation is carried out. The predicted overall load-displacement relationship is compared to the experimental behavior and this iterative process is repeated until the best agreement is obtained between experimental and simulation results. However, due to mesh sensitivity of cohesive solutions, the above explained computational effort can be quite significant and the predicted cohesive zone properties may not be accurate. In fact, sensitivity analyses with respect to cohesive parameters may not be successful for some sample geometries (Alfano et al., 2011).

With respect to fire insulation, DCB and ENF tests cannot be used because SFRM does not contribute to structural capacity (strength) of SFRM-steel assembly. That is, delamination at

SFRM-steel interface will not cause any softening in the overall load-displacement relationship. Single Cantilever Beam (SLB) specimens proposed by Tan et al. (2011) to measure fracture energy of SFRM in pure Mode I entails using a very thin steel substrate (0.35 mm) which may affect the interfacial fracture phenomenon. Tan et al.'s (2011) test is based on LEFM theory and therefore does not account for the strain-softening in FPZ. Further, no testing procedure has so far been proposed for measurement of fracture energy in pure Mode-II at SFRM-steel interface. Therefore, direct approach is adopted in this study to establish cohesive laws for mode-I and mode-II delamination at steel-SFRM interface.

3.2.2 Materials and Specimen Geometry

For evaluating fracture-based cohesive properties, three types of commercially available SFRM that are commonly used in building applications, have been selected. The generic type of these three SFRMs is summarized in Table 3.1. Figure 3.1 illustrates the overall plate geometry and the specimens after saw cutting. All specimens were prepared at the SFRM manufacture's laboratory. After 6-weeks of curing, the specimens were carefully shipped to Michigan State University's Civil and Infrastructure Laboratory for fracture tests. The specimens were carefully cut to the desired dimensions. The clear space left between specimens is large enough to fit the clamps in between for constraining the specimen plate into the testing machine. Tensile test specimens measured 76.2 x 76.2 x 25.4 mm and shear test specimens measured 101.6 x 25.4 x 25.4 mm. With respect to size of specimens, it was attempted to adopt as large specimens as possible to reduce the size effects and hence generate as realistic data as possible which can be applicable in practice. The issue of size effect has been studied by Bazant (1984), Bazant and Kazemi (1990) and Bazant and Kazemi (1991) for concrete and rock.

Table 3.1 Three type of SFRM utilized in experiments

Name	Type of SFRM
A	Medium density gypsum-based
B	Medium density Portland cement-based
C	Mineral-fiber-based

3.2.3 Experimental Setup for Fracture Mode-I

A special test setup was designed for undertaking fracture tests on SFRM insulated steel plates to measure normal cohesive stress-displacement response. Details of the test specimens and the testing procedure designed for measuring fracture mode-I properties at steel-SFRM interface is depicted in Figure 3.2a and Figure 3.3a. A plywood block with thickness of 15 mm is carefully drilled at the center to which an eyebolt is screwed in. The wooden block is glued on top of tensile specimen using wood glue. After gluing wooden block to SFRM, wood surface is leveled and clamped to the steel plate to make a perfectly flat surface. After 24-hours, the specimens are unclamped and prepared for testing. The test is carried out on an electromechanical material testing system (MTS) shown in Figure 3.3a. The steel plate is clamped to an I-beam, which is connected to bottom actuator, to prevent deformation of plate during the test. The eyebolt is connected to the upper rigid block using a shackle-eye nuts-threaded rod assembly. Special care is taken to ensure that no eccentricity exist between MTS loading direction and specimen center. Displacement-controlled load is applied on the specimens and load-displacement relationship is recorded while the loading rate is kept constant at 1μm/sec. Test is terminated once the full fracture of SFRM occurs and specimen can no longer withstand any further load.

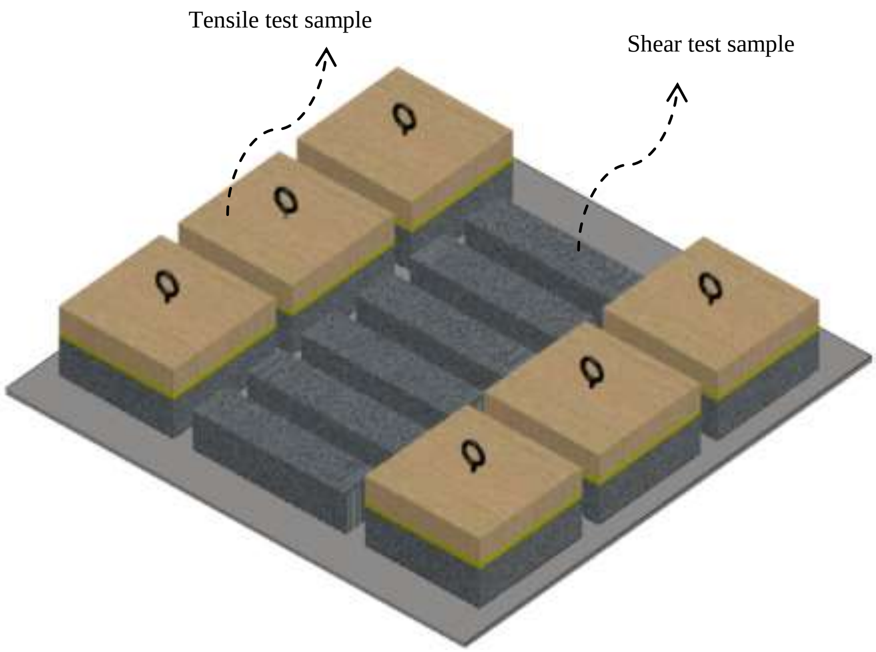

a) 3D view of SFRM samples

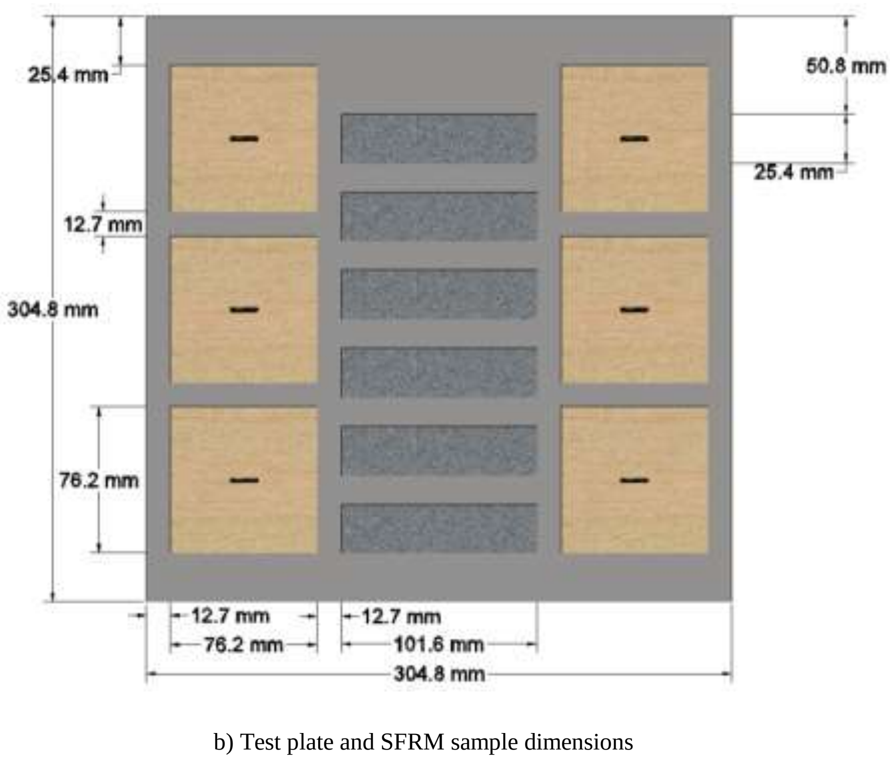

b) Test plate and SFRM sample dimensions

Figure 3.1 Test plate geometry for measuring fracture parameters

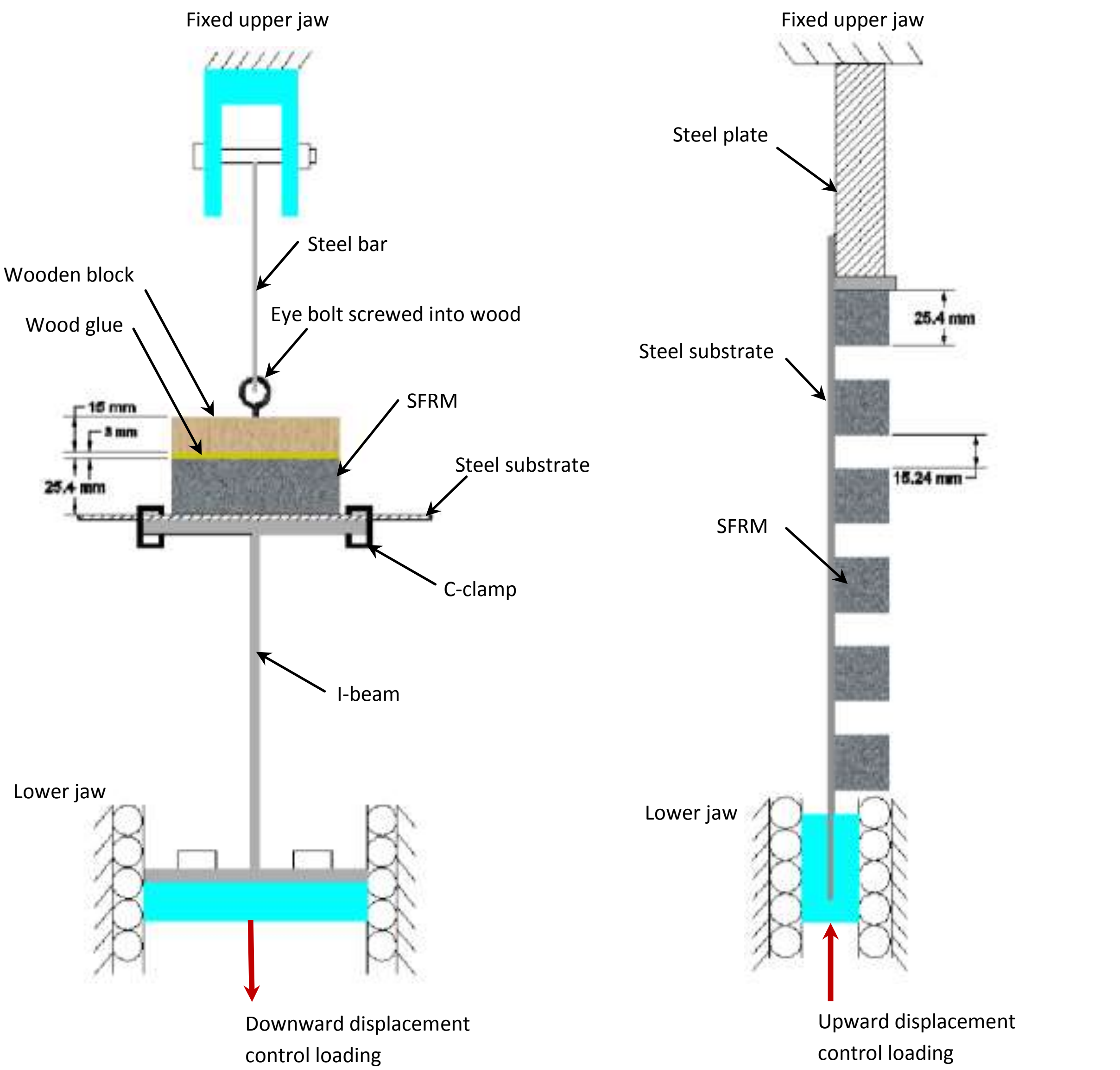

a) Test schematic for model-I delamination

b) Test schematic for model-II delamination

Figure 3.2 Schematic of test assembly for determination of CZM parameters

3.2.4 Experimental Setup for Fracture Mode-II

Direct shear test is conducted to measure the stress-displacement response in fracture mode-II at the interface of SFRM and steel plate. The specimen details and testing method is illustrated in Figure 3.2b and Figure 3.3b. The SFRM block is pushed against the steel plate thereby inducing direct shear stresses at the interface of steel and SFRM.

a) Test set up for model-I delamination

b) Test set up for model-II delamination

Figure 3.3 Test set up designed for measuring CZM parameters at steel-SFRM

The width of the test specimen along loading direction was chosen to be small enough to preclude cohesive failure within the SFRM. A small gap was introduced between the loading plate and test specimen plate so that friction between two plates is eliminated. The test is carried out through a displacement control loading technique with a constant displacement rate of 1μm/sec. The stress-displacement recording is continued until the SFRM block is fully delaminated from steel surface and the total applied load returns to zero value.

3.2.5 Elastic Modulus Tests

The elastic modulus for three types of SFRM was determined by conducting compression tests on SFRM blocks of 50.8 mm x50.8 mm x50.8 mm size. Displacement controlled loading was applied with a constant displacement rate of 1μm/sec. The measured elastic modulus on three types of SFRM is listed in Table 3.2.

Table 3.2 Cohesive zone model parameters obtained in experiment for three types of SFRM

SFRM type	σ_c (kPa)	τ_c(kPa)	$\frac{\tau_c}{\sigma_c}$	G_{cn} (J/m^2)	G_{ct} (J/m^2)	G_{ct}/G_{cn}	K_n (kPa/mm)	K_t (kPa/mm)	μ_n	μ_t	E (MPa)	Manufacture σ_c range (kPa)
A	22.9	49.6	2.2	7.9	32.8	4.2	57.3	107.9	1.73	2.98	11.5	7.2-20.5
B	52.8	107.3	2.0	33.7	74.4	2.2	57.4	162.6	1.40	2.11	38.4	20.8-409.6
C	13	24.6	1.9	4.3	22.5	5.2	39.3	61.4	2.03	4.63	2.6	7.2-17.9

3.3 Results from Fracture Tests

The force-displacement relationships recorded from tensile tests are shown in Figure 3.4 for three types of SFRM insulated specimens. It is apparent that the response of Portland cement-based SFRM is relatively brittle as compared to the gypsum-based and mineral fiber-based SFRM. For gypsum-based and mineral fiber-based SFRM types, interfacial force rises almost linearly to critical cohesive strength, and subsequently, decreases with increasing normal displacement. The softening behavior observed in the force-displacement curves, confirms that the size of fully developed FPZ is noticeable for gypsum-based and mineral fiber-based SFRM. Even in the case of Portland cement-based SFRM, there is no rapid load drop as would be the case for elastic-brittle materials. For this SFRM type, force-displacement curve is nonlinear up to the peak load which is followed by a sharp drop to 20 percent of peak load as can be seen from force-displacement response in Figure 3.4. Then the load response slowly diminishes to zero with further interfacial deformation. Ultimate fracture displacement in this case is higher than those obtained for gypsum-based and mineral fiber-based SFRM.

In all specimens, prior to reaching cohesive strength (peak load) there was no sign of crack development throughout the specimen. However, once damage is localized and FPZ formation starts, cracks started appearing in decay phase of force-displacement curve and get fully developed and visible upon reaching to the failure displacement. Delayed development of FPZ can be attributed to the fact that in plain tensile specimens no initial crack or notch is introduced. Consequently, this is no focus point for the formation of FPZ and thus dispersion of initial microcracking occurs. Since SFRM is substantially softer than steel (E_{SFRM}=30 MPa<<E_{steel}=200GPa) and also the applied loading on the specimen is very low (maximum 0.4 kN), deformation of steel accessories used in the tensile test has a negligible influence on the recorded displacement. In addition, the elastic contribution from FPZ can be neglected because FPZ is narrow as compared to the thickness of specimen. However, the contribution of bulk SFRM to elastic deformation before reaching to cohesive strength should be accounted for. As will be shown shortly, the compliance of bulk SFRM affects the initial elastic response and thus the associated energy and displacement are removed from stress-displacement curves while establishing cohesive laws.

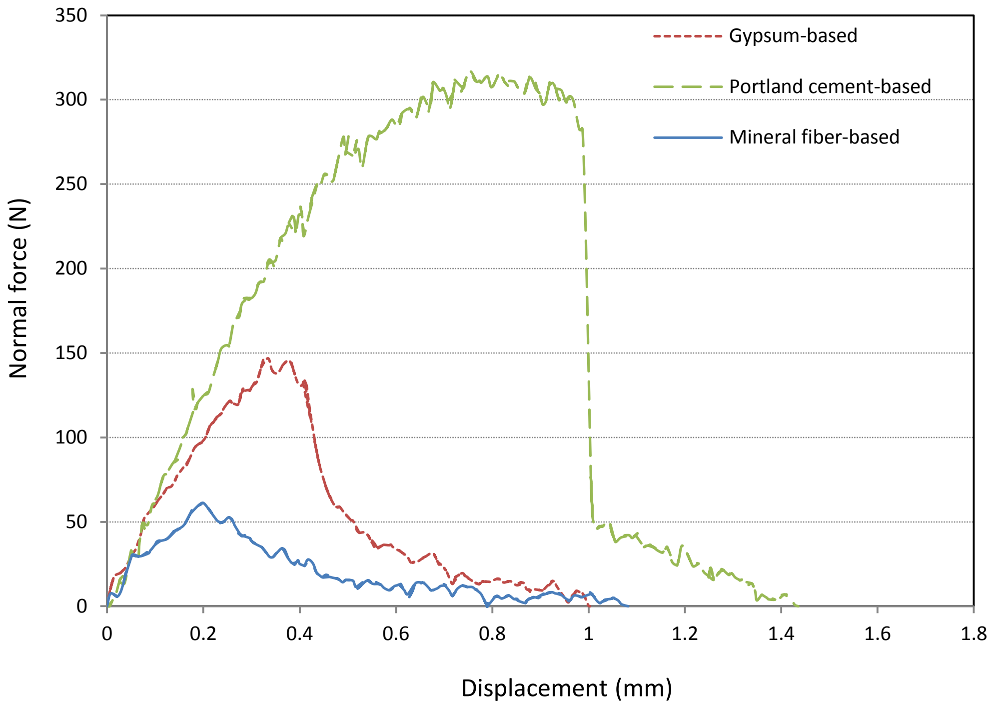

Figure 3.4 Normal force-displacement relationship (fracture mode-I)

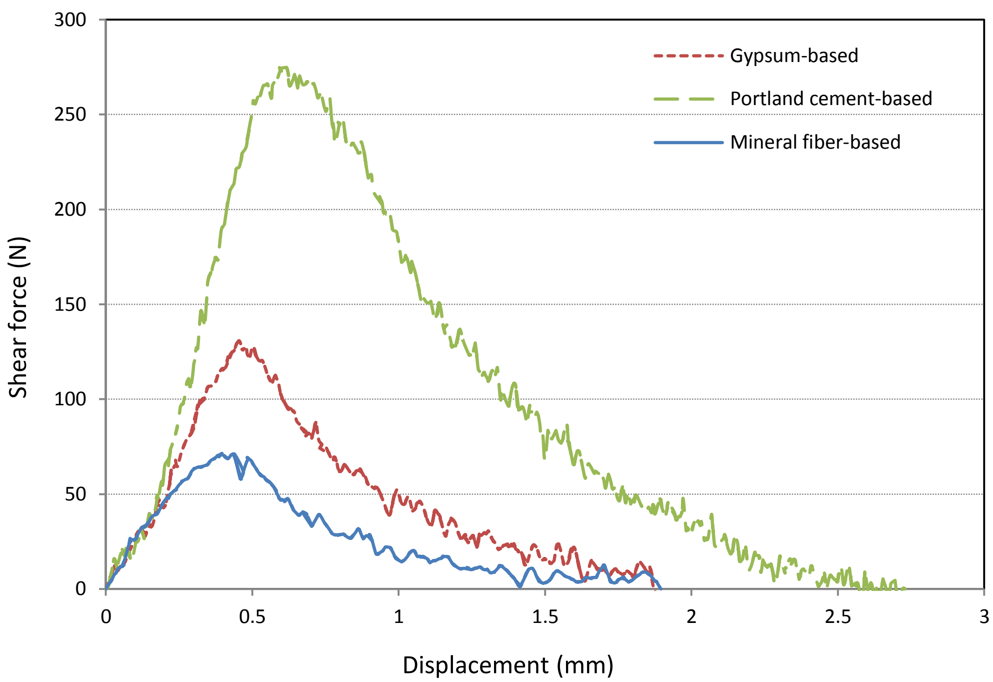

Figure 3.5 Shear force-displacement relationship (fracture mode-II)

From cohesive strength viewpoint, Portland cement-based SFRM possesses the highest strength, while gypsum-based SFRM possesses moderate strength and mineral fiber-based SFRM exhibits the least cohesive strength as can be seen in Figure 3.4. Cohesive stiffness also decreases from Portland cement-based SFRM to gypsum-based SFRM and from gypsum-based SFRM to mineral fiber-based SFRM, as was the case for cohesive strength. Further, as is apparent from the area under each curve, Portland cement-based SFRM offers the highest level of fracture energy, while gypsum-based SFRM and mineral fiber-based SFRM exhibit moderate and low level of fracture energy, respectively. It should be noted that, there is substantial difference in fracture energy between Portland cement-based and gypsum-based SFRM, whereas this is not the case with gypsum-based and mineral fiber-based SFRM. Further, it can be seen in Fig. 3.4 that there is a nonlinear behavior in the case of Portland cement-based SFRM before reaching to cohesive strength. In this case, a different microcracking mechanism both at steel-SFRM interface and bulk SFRM can be responsible for the observed nonlinearity.

In Mode-II fracture, as is depicted in Figure 3.5, all three materials show similar force-displacement trend though with different level of cohesive zone parameters. Shear force at steel-SFRM interface surges to the maximum cohesive strength and subsequently reduces smoothly as the microcracking activity is completed in FPZ and failure crack tip displacement is attained. Hence, in shear mode of delamination, ductile behavior is dominant in all three types of SFRM, which once more endorses the fact that the size of FPZ is considerable for SFRM. Portland cement-based SFRM provides the superior performance both in terms of cohesive strength and fracture energy. Gypsum-based SFRM performs better than mineral fiber-based SFRM; however, the level of enhancement from mineral fiber-based SFRM to gypsum-based SFRM is not comparable to the one from gypsum-based SFRM to Portland cement-based SFRM.

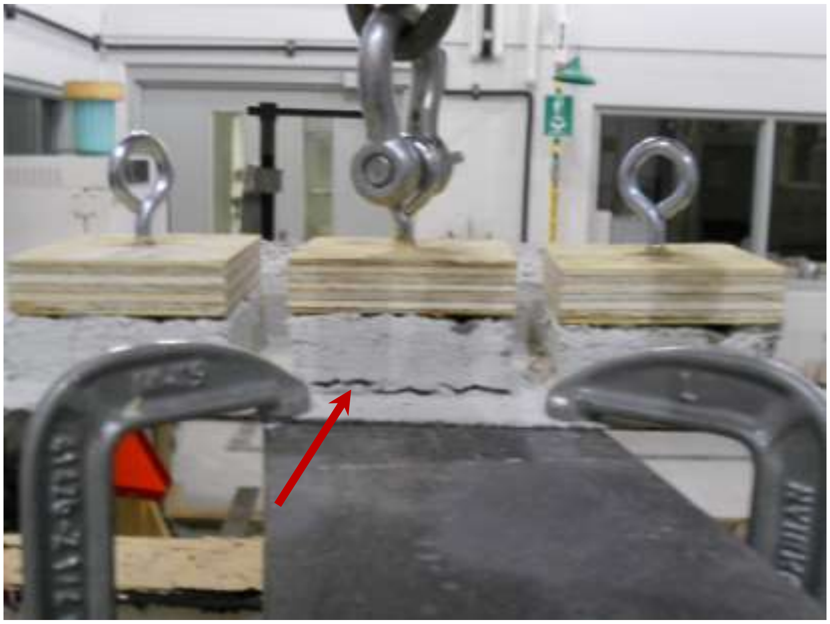

a) Fracture in typical tensile test specimen

b) Fracture in typical shear test specimen

Figure 3.6 Fracture at steel-SFRM interface observed in the experiments

Further, interfacial stiffness is proportional to the level of cohesive strength as was the case with mode-I fracture. Overall, force and displacement peak values shown in Figure 3.4 and Figure 3.5 suggests that cohesive resistance in mode-II is higher than that in mode-I. Note that, crack progression phenomenon in shear tests was similar to the one observed in tensile tests, as discussed above.

Displacement ductility over the FPZ is an additional parameter of interest for characterizing cohesive laws. This parameter determines the extent of the stain-softening portion of cohesive stress-displacement curve. Displacement ductility over the FPZ is defined here as the ratio of fracture displacement to displacement corresponding to cohesive strength. It is clear from Figure 3.4 and Figure 3.5 that mineral fiber-based SFRM possesses the highest displacement ductility over cohesive zone, while gypsum-based SFRM possesses moderate ductility, and Portland cement-based SFRM offers the least ductility. It can be inferred that, the softer the SFRM is, the higher the displacement ductility over the FPZ will be.

It was indicated in previous section that results of direct test method are acceptable provided the failure surface progresses uniformly through tensile or shear zones. Figure 3.6 illustrates the uniform evolution of damage at steel-SFRM interface in tensile and shear tests. In tensile tests, one of the specimens from Portland cement-based SFRM, did not show this behavior and the result from this specimen was discarded. In shear tests, all specimens developed a uniform shear failure at the steel-SFRM interface. Also, it was discussed that force-displacement curves for fracture mode-I show ductile behavior in all cases except in the case of Portland cement-based SFRM under tensile loading. Even in this case, it was concluded that the material does not behave purely brittle. In addition, all three types of SFRM demonstrated ductile performance in fracture mode-II. Therefore, from fracture mechanics perspective, SFRM may be considered as a "quasi-brittle" material, rather than "brittle" material.

Average cohesive strength obtained from tensile and shear tests are plotted in Figure 3.7. The cohesive strength is calculated by dividing the recorded force to cross sectional area under tension and shear (σ=P/A). As is represented by error bars, the scatter in the data is relatively small which proves the reliability of results. The mean values of cohesive strength are tabulated in Table 3.2. The shear cohesive strength is almost twice as high as normal cohesive strength for all three types of SFRM. In both normal and shear modes of fracture, Portland cement-based SFRM exhibits the highest cohesive strength, gypsum-based SFRM exhibits average strength and mineral fiber-based SFRM exhibits the least strength. Manufacturer of these SFRMs has only provided the normal cohesive strength (bonding strength) which is included in Table 3.2. The normal bonding test (adhesion test) is performed by manufactures according to ASTM E736 (2006). The normal cohesive strength from tests for gypsum-based and mineral fiber-based SFRM are very close to value given by the manufacturer; however, for Portland cement-based SFRM, manufacturer reports a very high upper bond value for normal cohesive strength which was not observed in the tests carried out in this study.

Figure 3.8 shows the critical fracture energy measured in fracture mode-I and mode-II tests. The error bars in this case are also fairly small validating reproducibility of fracture energies extracted from the experiments carried out in this study. The order of performance in terms of fracture energy is identical to the one mentioned above for cohesive strength. However, the ratio of shear fracture energy to normal fracture energy is 4 and 5 for gypsum-based and mineral fiber-based SFRM, respectively, while this ratio is close to 2 for Portland cement-based SFRM. Further, irrespective of all differences among the quantities and performances of SFRMs, one fact is very obvious that the amount of critical fracture energy is low as compared to other cementitious material such as mortar and concrete. This characteristic of SFRM raises concern regarding the delamination at SFRM-steel interface when the steel substrate undergoes large strains under the action of extreme loading events on steel structures.

To obtain bilinear stress-displacement curves over the FPZ, which are to be utilized in numerical modeling, the concept of equal energy can be adopted as displayed in Figure 3.9. The displacement corresponding to cohesive strength can be extracted by equalizing the area under the curve up to experimental culmination displacement with the corresponding area of a triangle in bilinear model. The elastic energy absorbed by bulk SFRM is removed from the total elastic energy. The elastic deformation of bulk SFRM is calculated using Hook's law by knowing the elastic modulus and maximum stress experienced by SFRM during test. The displacement corresponding to cohesive strength is also reduced by elastic deformation of bulk SFRM. Likewise, the failure displacement at cohesive zone can be obtained by associating the total areas under experimental curve (reduced due to compliance of bulk SFRM) and bilinear model. The result of this equalization process is plotted in Figure 3.10 and Figure 3.11 where cohesive laws pertaining to fracture mode-I and fracture mode-II for three types of SFRM are shown, respectively. Table 3.2 presents the cohesive law parameters along with elastic modulus for three type of SFRM. These CZMs can be utilized for simulation of progressive delamination at steel-SFRM interface in different structural assemblies insulated with SFRM.

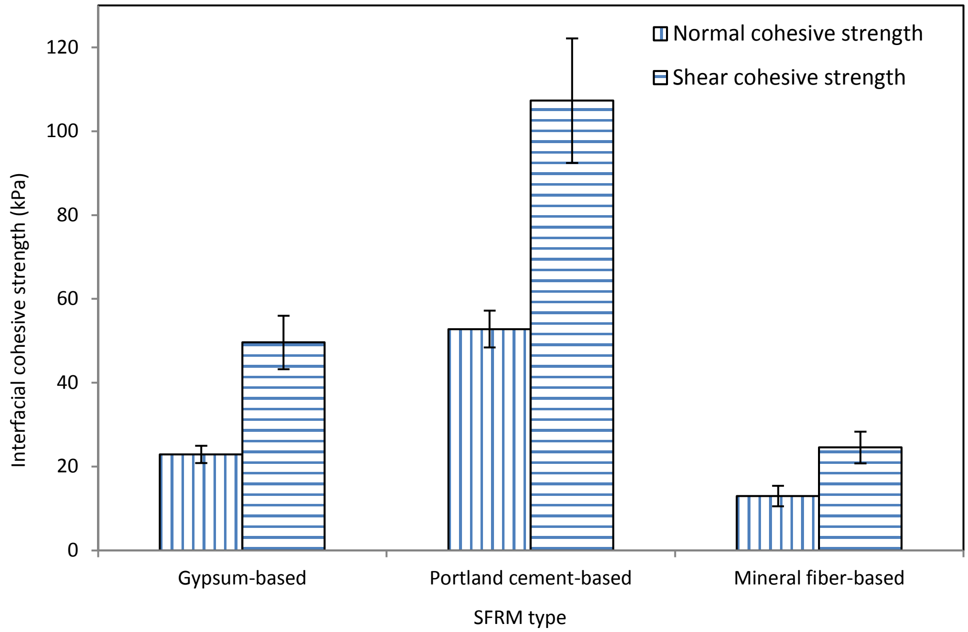

Figure 3.7 Interfacial cohesive strength for three types of SFRM

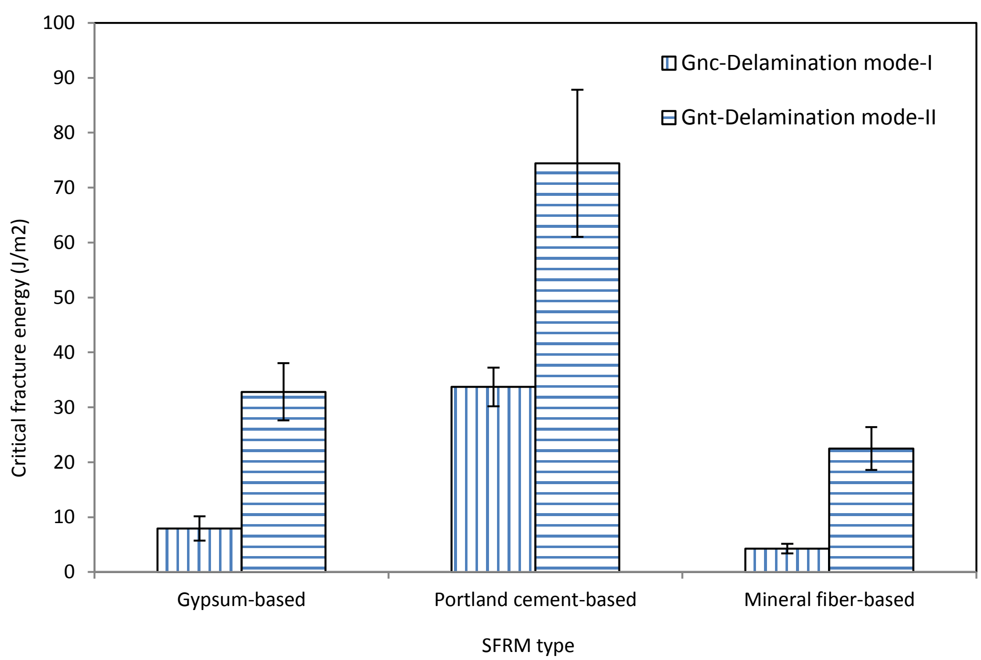

Figure 3.8 Interfacial critical fracture energy for three types of SFRM

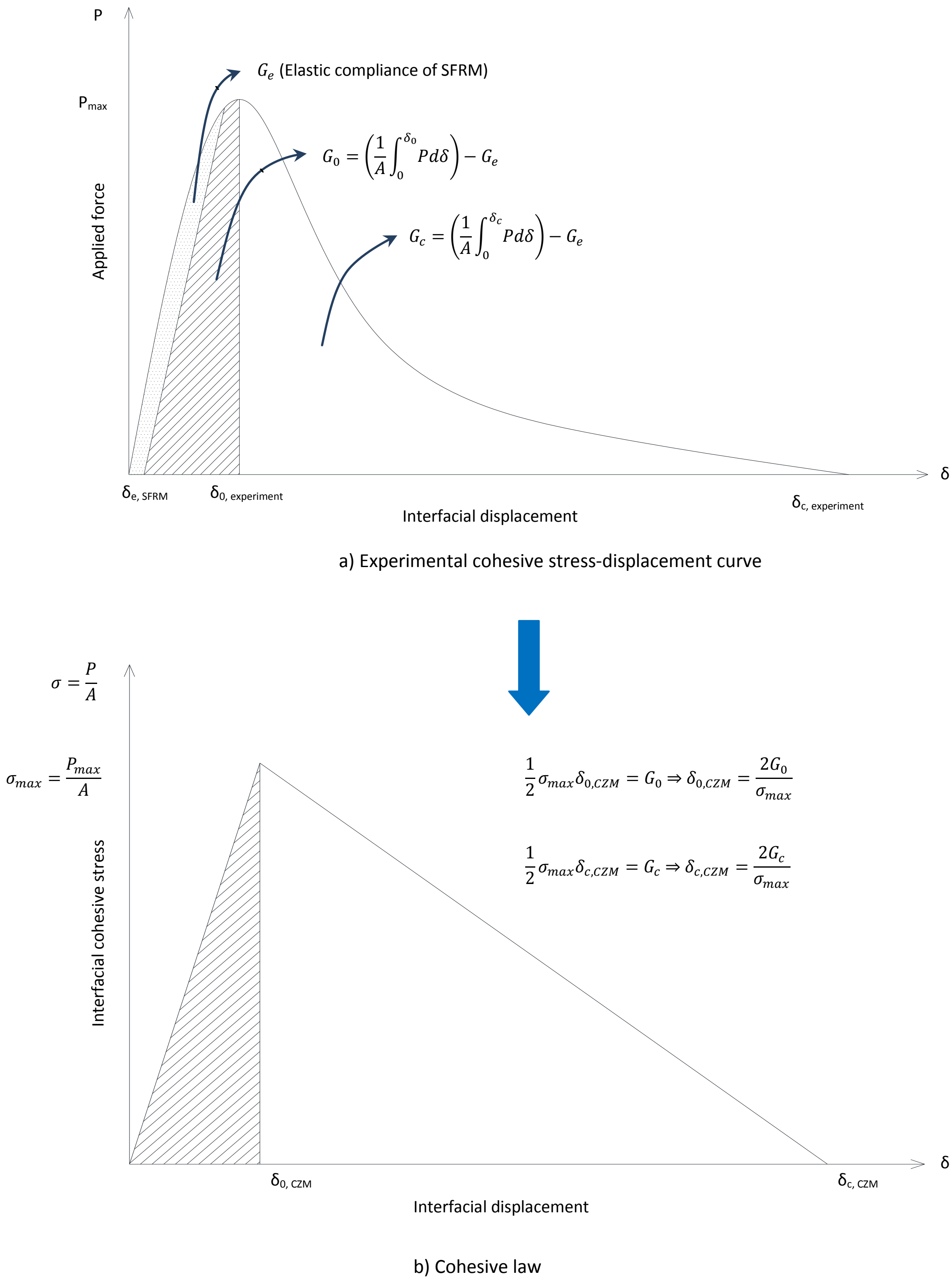

Figure 3.9 Determination of bilinear cohesive law based on experimental results

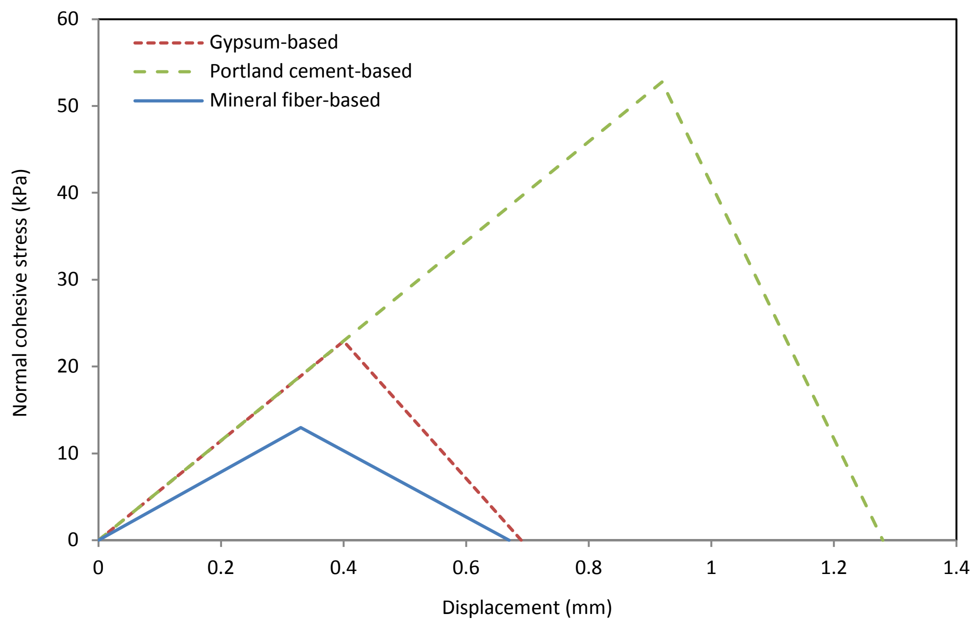

Figure 3.10 Bilinear cohesive law for fracture mode-I determined from experiments

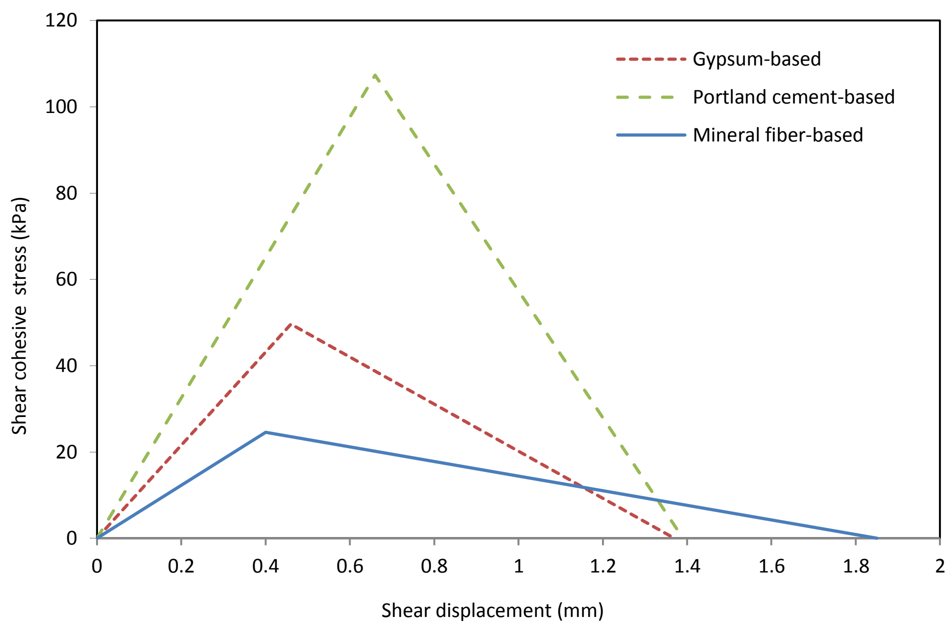

Figure 3.11 Bilinear cohesive law for fracture mode-II determined from experiments

3.4 Drop Mass Impact Test

In the second part of experimental studies, impact tests are carried out on insulated steel beams to simulate high strain rate conditions experienced during impact or blast scenarios. In the drop mass impact test, with the height and mass known, impact energy and impact velocity can be predicted using principles of conservation of energy.

3.4.1 Selection of Experimental Approach

Under dynamic loading conditions, there is neither a test standard nor a generally accepted procedure for measuring fracture energy at the interface of two materials. The direct dynamic tests are not possible to carry out due to limitations in loading machines with respect to applying very high strain rates. Indirect test methods are therefore utilized. Split Hopkinson pressure bar (SHPB) is an indirect test method which is used to study the mechanical behavior of materials at high strain rates (Hopkinson, 1914). There are limited research (Schular et al., 2006; Brara and Klepaczko, 2007; Chen et al., 2013) on application of SHPB test method for measuring fracture energy of cementitious material. When this test method is applied for concrete-like materials that undergo extensive cracking during dynamic impulsive loading, the results should be interpreted with caution such that the inertia effects at micro-cracking are not mixed with the effect of strain rate dependency (Ožbolt et al., 2014). Drop mass impact test has also been used to study dynamic fracture of structures during impulsive loading (Zeinoddini et al., 2008; Liew et al., 2009; Fujikake et al., 2009; Deng et al., 2012; Wang et al., 2013; Remennikov et al., 2013; Bambach et al., 2008; Zhang et al., 2009).

The application of SHPB test for measuring interfacial fracture energy at the interface of steel and fire insulation did not seem feasible due to size limitations in SHPB test and also because of above explained issues regarding interpretation of results. Therefore, in this study, drop mass impact test is selected to indirectly assess the dynamic fracture and delamination of fire insulation form steel structures. Numerical modeling is also employed to supplement this indirect test method to quantify the strain rate-dependency of fracture at the steel and fire insulation interface. The numerical modeling will be detailed in next chapter.

3.4.2 Impact Test Set-up

A special impact test machine is designed and fabricated to undertake the experiments planned in this study. A schematic view of drop mass impact test is shown in Figure 3.12. Two columns of 3.66 m height, installed on a base plate, form the backbone of the impact test machine. The columns are linked through two link beams sitting atop of the columns. A striking hammer, with the mass of 120 Kg, is designed so as to attach to an electric magnet installed on the link beam, as shown in Figure 3.12. The hammer is designed in such a way that its mass is adjustable by adding or removing plates. An indenter is also attached to the drop hammer, which forms the striking head of the hammer. Two track wheels, installed on the columns, provide the lateral support for hammer as well as the rail for free fall of the hammer. The base plate is anchored to the strong floor (reinforced concrete foundation) by using four pre-stressed anchor rods, as illustrated in Figure 3.12. The insulated beam (test specimen) is rested on the base plates, while being clamped by two plates at the supports location. A round half-bar is welded to the support plates so as to simulate free rotation of the beam at supports location. The post-tensioned bar, shown in Figure 3.12, is extended upward through the support plates, and once the beam is located in its position, the support plates and the base plate is anchored to the foundation, simultaneously.

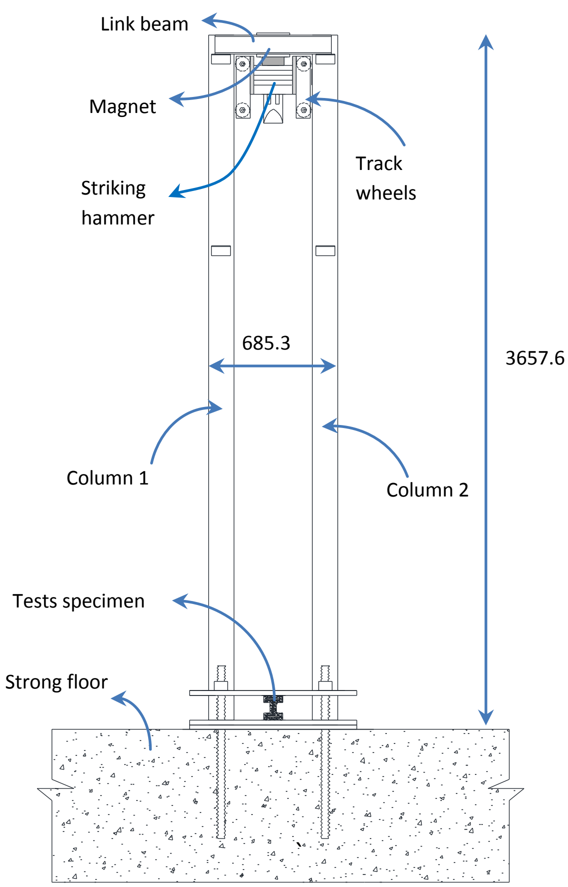

a) Components of test machine and dimension (mm)

b) General view of test set-up

c) Close view of hammer attached to the magnet

d) Close view of the base plate and specimen support plates

Figure 3.12 Schematic view of drop weight impact test set-up

The striking head of drop hammer is instrumented with four strain gauges to measure the impacting force. The deflection at mid-span and at one end of beam is measured by attaching a linear variable differential transformer (LVDT). A high speed data acquisition system (supplied by National Instruments Corporation) is used to capture time history of strain and displacement for the entire period of the impact incident. A high speed video camera with capability of capturing 400 frames per second is used to monitor the impact events, in particular the progressive delamination of fire insulation from beam. The recorded data in each test include applied load, beam deformation, strain at different locations on beam and the extent of SFRM delamination from steel surface.

3.4.3 Test Specimens

A total of 6 steel beams were subjected to impact loading at the mid-span by a 120 Kg hammer as depicted in Figure 3.13. The beams are of S4X7.7 steel sections and are made of ASTM A992- Gr.50 steel. The clear span of test beams is 609.6 mm and the total length of the beam is 762 mm. The cross section and the span of the beam have carefully been designed such that global lateral torsional buckling will not occur. The beams were insulated with three types of SFRM, namely Portland cement-based, gypsum-based, and mineral fiber-based, which are commonly utilized in providing fire protection to steel structures. The fire insulation on the impact zone at the top flange of the beam is removed such that the hammer strikes the top flange directly. This also simplifies the numerical simulation of impact area. A distance of 101.6 mm at both ends of the beams are not insulated, thus the beam can easily be positioned between support plates, as shown in Figure 3.13.

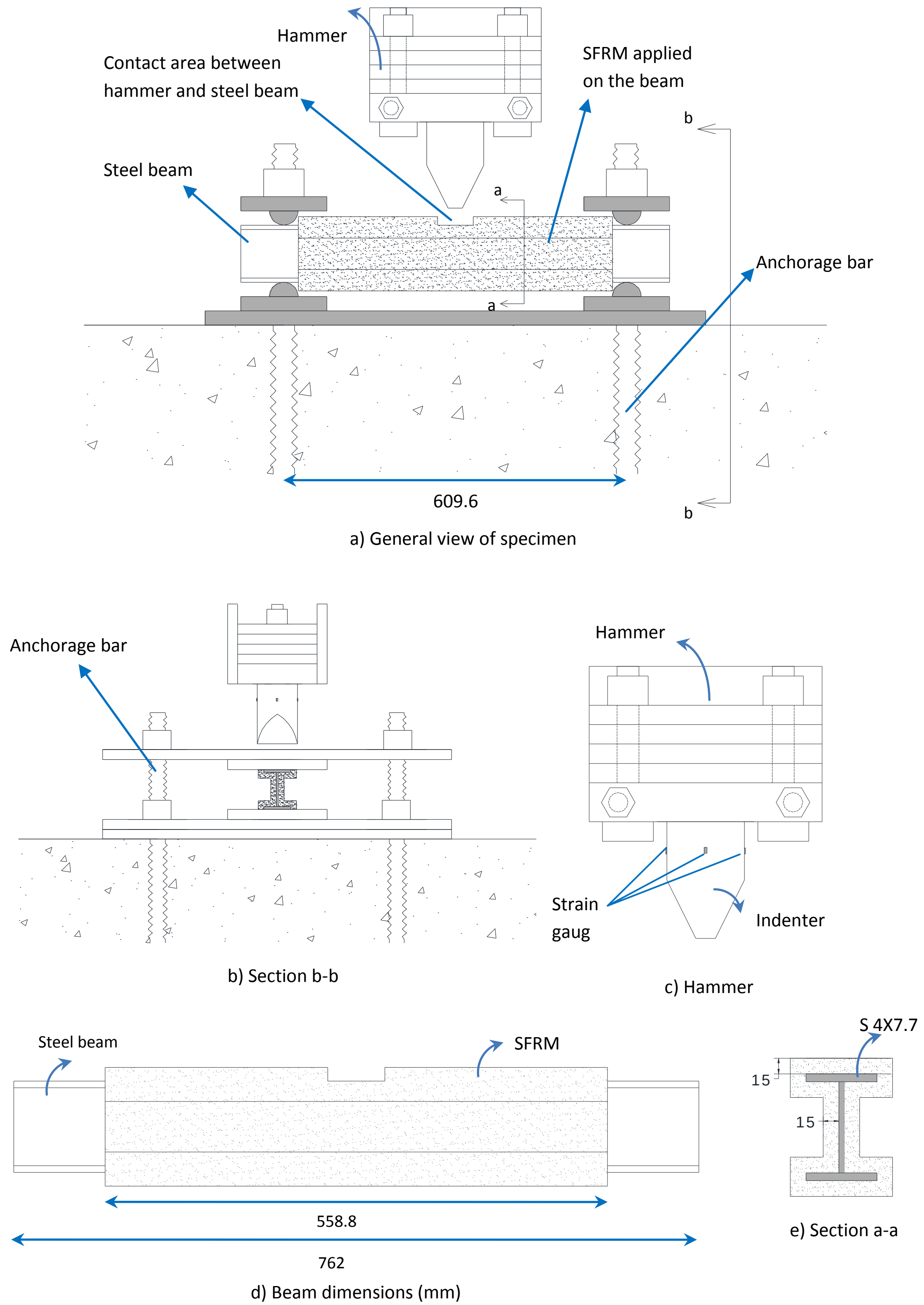

Figure 3.13 Schematic view of specimen

All test specimens are sprayed with insulation at the SFRM manufacture's facility. Before applying fire insulation, four strain gauges are mounted at the top and bottom flange of beam (at mid span) to trace the yielding of material during impact loading. After 6-weeks of curing, the specimens were carefully shipped to Michigan State University's Civil and Infrastructure Laboratory for impact tests. The target thickness of SFRM applied on beams was 15 mm, however, thickness measurements before conducting tests showed a small variation from 15 mm which is shown in Table 3.3. The insulated beams are stricken at two levels of velocities, namely 6.66 m/ and s 8.05 m/s, by changing the drop height. Preliminary numerical simulations demonstrated that this level of velocities can induce considerable strain rate on the beam in the range of 5-20 s^{-1}. Numerous non-insulated dummy beams were also tested before testing the insulated beams to ensure the integrity of testing equipment. The test variables are summarized in Table 3.3.

Table 3.3 Fire insulated steel specimens and test variables

Test #	Steel section	SFRM type	SFRM thickness (mm)	Impact velocity (m/sec)
B1	S 4X7.7	Portland cement-based	16.7	8.05
B2	S 4X7.7	Portland cement-based	16.7	8.05
B3	S 4X7.7	Gypsum-based	15.6	8.05
B4	S 4X7.7	Gypsum-based	15.6	6.66
B5	S 4X7.7	Mineral fiber-based	14.2	8.05
B6	S 4X7.7	Mineral fiber-based	14.2	6.66

3.5 Results from Impact Tests

The experimental observations and data acquired during the impact test are analyzed with respect to applied impact force, deformation of beam and cracking and delamination of fire insulation under the applied impact loading.

3.5.1 Impact Force

The impact force applied on the beams is obtained by averaging the readings from the four strain gauges systematically mounted on the rigid indenter, as shown in Figure 3.13c. The impact force-time history is plotted in Figure 3.14 for beams insulated with three types of SFRM and subjected to two levels of impact energy. Note that, the test on beams insulated with Portland cement-based SFRM was repeated with velocity of 8.05 m/s, since no insulation dislodgement was observed during the first test, therefore the impact energy was not reduced. In general, the impact force developed at the contact interface of two bodies depends on the structural configuration of the colliding bodies namely, geometry, mass and stiffness. The recorded impact force-time histories exhibit three distinct regions, and each region can be explained using fundamental physics laws.

Upon the first impact, the hammer tends to accelerate the beam (test specimen) by changing the beam velocity from zero at rest position to the hammer velocity. Consequently, significant force is rapidly developed at the contact area between the hammer and the beam within the first 0.5 ms (millisecond) of the impact duration, which can be attributed to the effect of beam inertia and should not be mistaken as plastic flexural response of the beam. Hence, the peak initial inertia force increases by increasing the impact momentum, while the duration of this impulse is regardless of impact velocity, as is clear in Figure 3.14. In the present study, the time duration of peak impact force was very short because of the hard steel-to-steel contact between the indenter tip and top flange of the beam. The local deformation in the impact zone (top flange of the beam) mainly occurs during this period. This type of response of structures to impacting mass has been reported by many other researchers (Liew et al., 2009; Fujikake et al., 2009; Deng et al., 2012; Wang et al., 2013; Remennikov et al., 2013; Bambach et al., 2008).

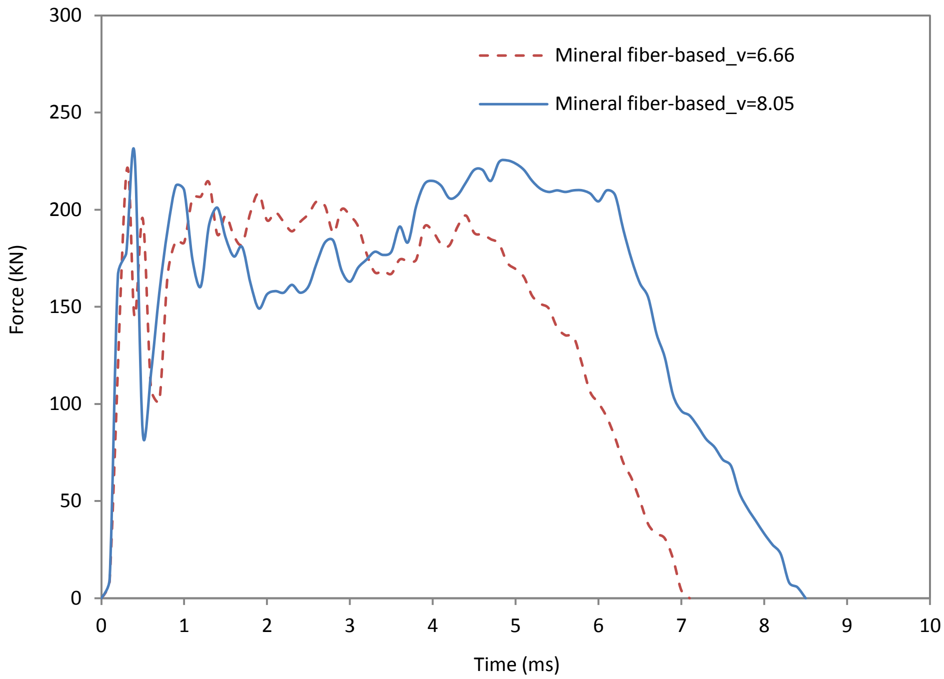

a) Mineral fiber-based SFRM

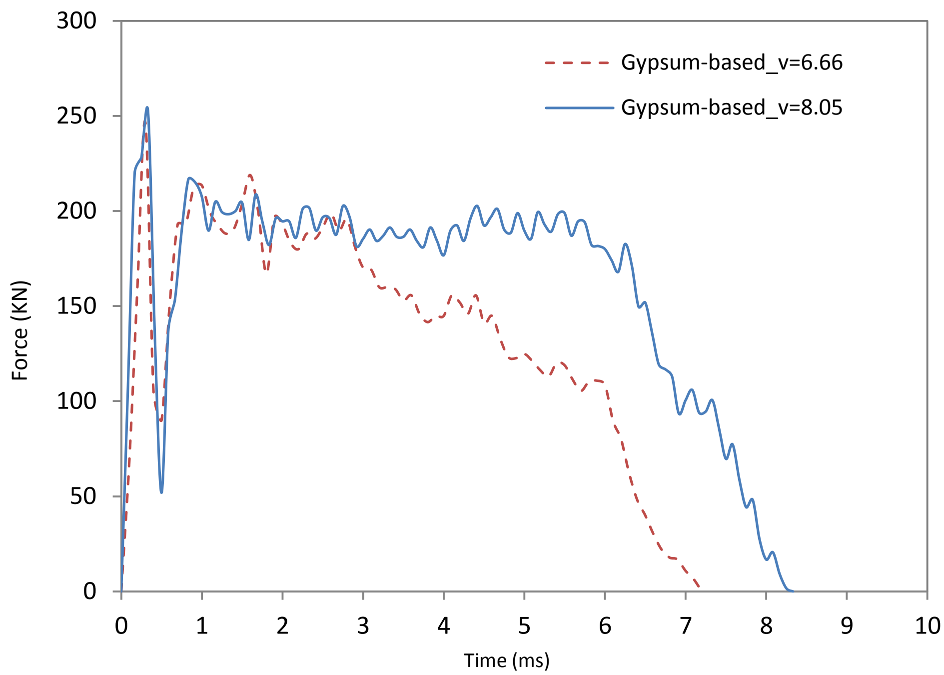

b) Gypsum-based SFRM

Figure 3.14 Force-time history recorded during impact tests on the beams insulated with different types of SFRM

Figure 3.14 (cont'd)

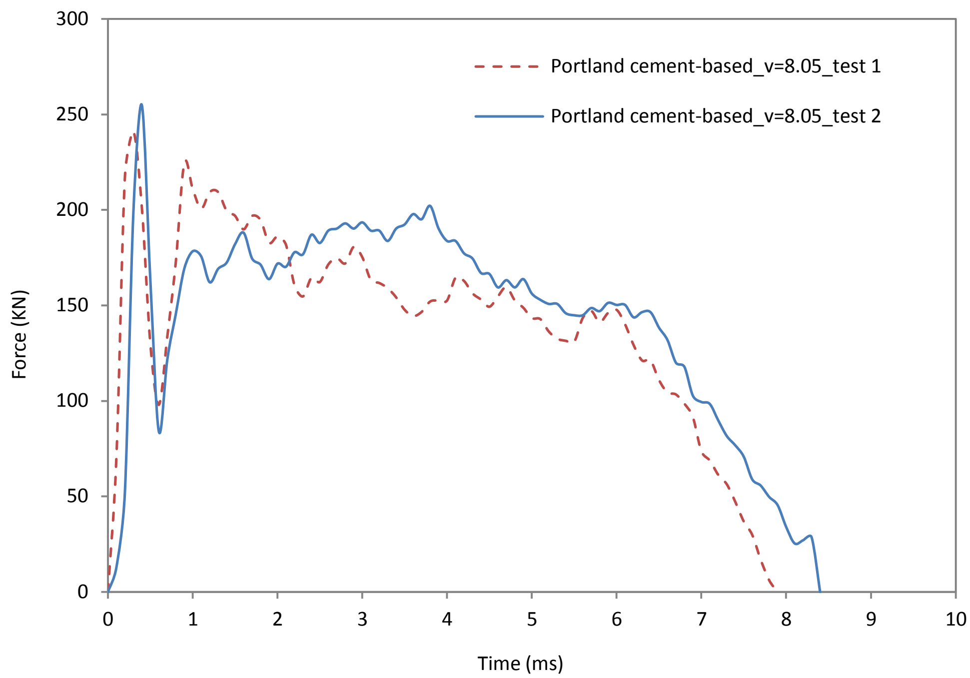

c) Portland cement-based SFRM

As shown in Figure 3.14, once the first pulse is passed through, the applied force dramatically reduces because a plastic hinge forms at the mid span under the impact momentum and the beam starts deflecting downward. In other words, since the kinetic energy of the hammer is higher than the elastic energy capacity of the beam, the beam undergoes plastic flow to absorb the imposed external energy. At the same time, the beam starts bending and the end supports start experiencing the applied load. As a result, over this plateau region of force-time history, the beam and hammer move downward with the same velocity until the maximum deflection of the beam is reached, which occurs around 6 ms.

In the second region, the recorded force represents both inertial and flexural response of the beam. Subsequently, the beam starts to rebound resulting in decrease in impact force until complete separation occurs between the hammer and the beam. The hammer moves upward and then aims to strike the beam for the second time, and this process continues until the hammer comes to rest on the beam. However, the secondary and subsequent impacts have negligible effect on the dynamic behavior of beam since the hammer travels with considerably low velocity. The digital measurements as well as video records from high speed camera, confirm this behavior. Note that, as can be seen in Figure 3.14, the total duration of impact increases by increasing the impact velocity.

3.5.2 Displacement

The displacement time-history of the beams is recorded using displacement transducer (LVTD), attached to the beam end. The displacement transducer is not attached to the mid-span of the beams insulated with SFRM mainly because the attachment process would induce an initial crack within the SFRM applied on the bottom flange, which indeed is the most critical region where the crack initiates and propagates from there. Therefore, the displacement transducer is attached to the beam end, assuming that the mid-span deflection can directly be associated to the end displacement. However, in the non-insulated beam, the displacement transducer is attached to the mid-span and the recorded data is utilized to validate the numerical model, as will be outlined in Chapter 4. The recorded displacement time histories at the end of the beams insulated with different types of SFRM are depicted in Figure 3.15 for two levels of hammer velocity. The peak displacement occurs approximately at 6 ms after hammer strikes the beam and subsequently the deformation of beam is recovered to some extent and finally the deformation gets steady which is indicative of permanent plastic deformation of the beam.

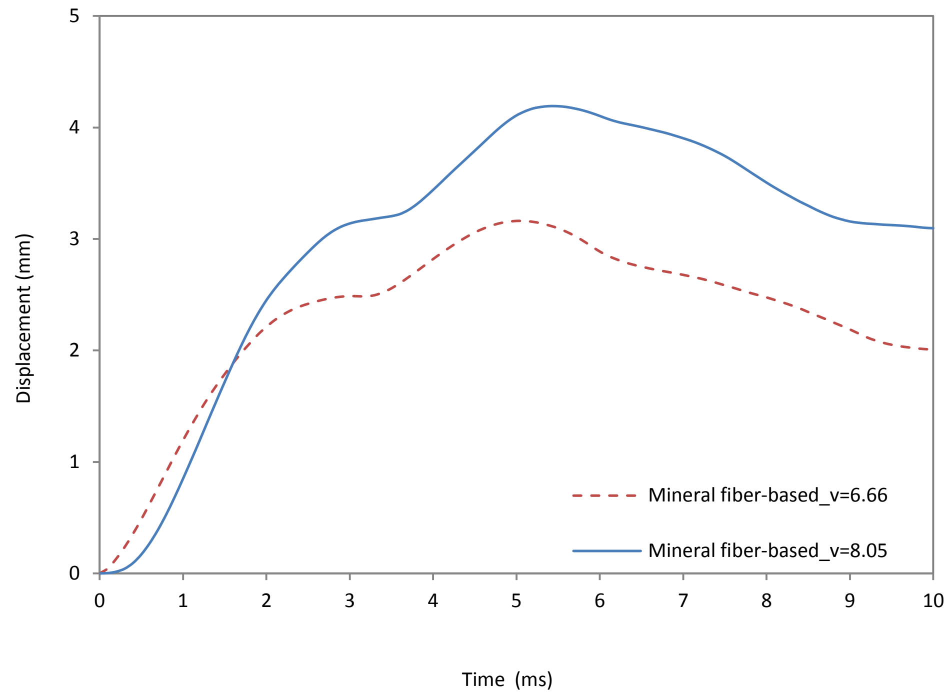

a) Mineral fiber-based SFRM

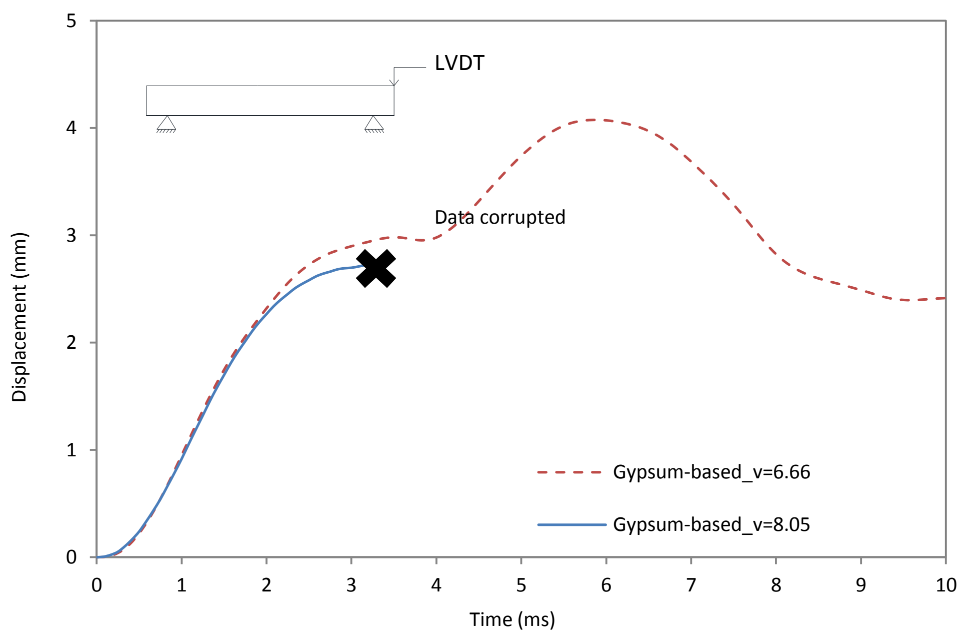

b) Gypsum-based SFRM

Figure 3.15 Vertical displacement time history recorded during impact tests at the end of the beams insulated with different types of SFRM

Figure 3.15 (cont'd)

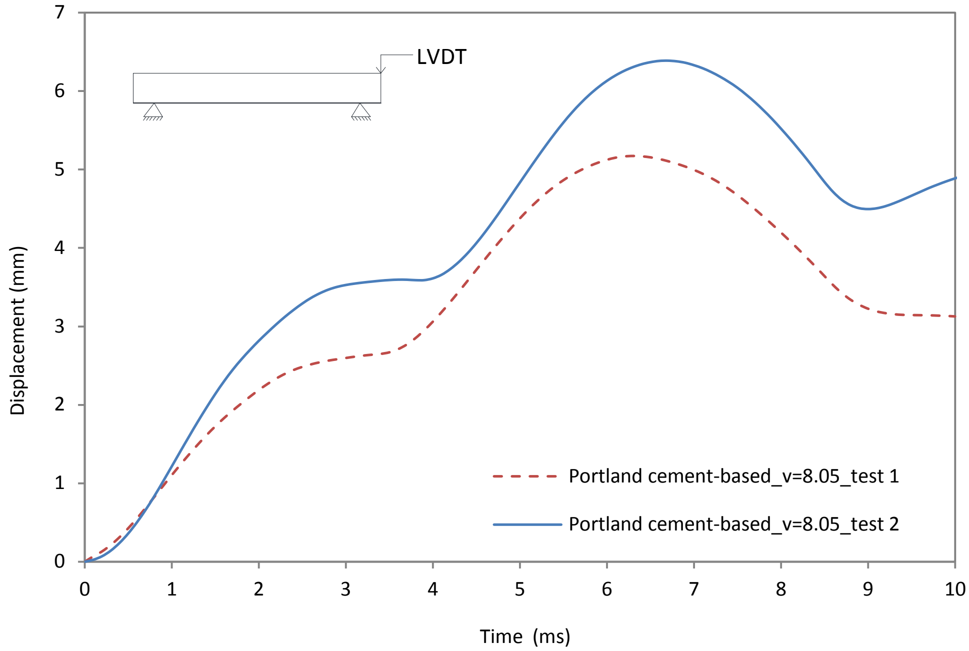

c) Portland cement-based SFRM

3.5.3 Extent of Delamination of Fire Insulation

One of the very important response parameters monitored in the present experimental program is the extent of fire insulation delamination over the steel beam. The results from tests indicate that delamination mostly occurs at the bottom flange of the beams (or non-impacted side of the beam) where SFRM is highly susceptible for spalling under the transmitted stress waves. No delamination of insulation on web of the beam was observed. Only one vertical crack in the insulation on web at the mid-span was observed which can be attributed to local instability in the web. Figure 3.16 shows the bottom flange of the beams where the most cracking and delamination has occurred. Figure 3.17 illustrates a series of photos captured by high speed camera at various time steps. The best possible view was chosen from camera recordings, given the geometrical restrictions of the test machine, as illustrated in Figure 3.17a. The observed behavior of tested beam can be explained by closely analyzing both Figure 3.16 and Figure 3.17, as following.

Results of first impact test on the beam insulated with Portland cement-based SFRM showed no delamination of insulation at impact velocity of 8.05 m/s. Therefore, the velocity was not reduced during the second (repeated) test to ensure that the obtained result for this type of SFRM is accurate and reliable. Both tests exhibited development of a wide crack at the mid-span and on the bottom flange extending to the web to some extent. Although no visible delamination of fire insulation occurred (no insulation fell-off), high speed camera record demonstrates that once the middle crack at the bottom flange is initiated, the crack propagates up to 40 mm towards both ends of the beam. The extent of cracking is completely visible at time 7.5 ms as portrayed in Figure 3.17d. However, the whole integrity of insulation was maintained due to the fact that the cohesive resistance provided by surrounding material, prevented complete insulation delamination. This type of response of Portland cement-based SFRM can be attributed to its higher cohesive strength and critical fracture energy as compared to other insulation types used in this study.

The gypsum-based SFRM applied on the beams underwent delamination on the bottom flange as shown in Figure 3.16. It is obvious in this figure that increasing impact velocity has expanded the delamination area. The percentage delamination area on the bottom flange increased from 25.1 % to 41% by increasing the impact velocity from 6.66 m/s to 8.05 m/s. As is clear, while the impact energy is increased by 46 %, the delamination area is spread by 63 %. Further, Figure 3.17c shows complete detachment of fire insulation from bottom flange of the beam at a time of 5 ms. In these tests, the whole insulation in the delaminated area is suddenly detached (spalling) at the same time.

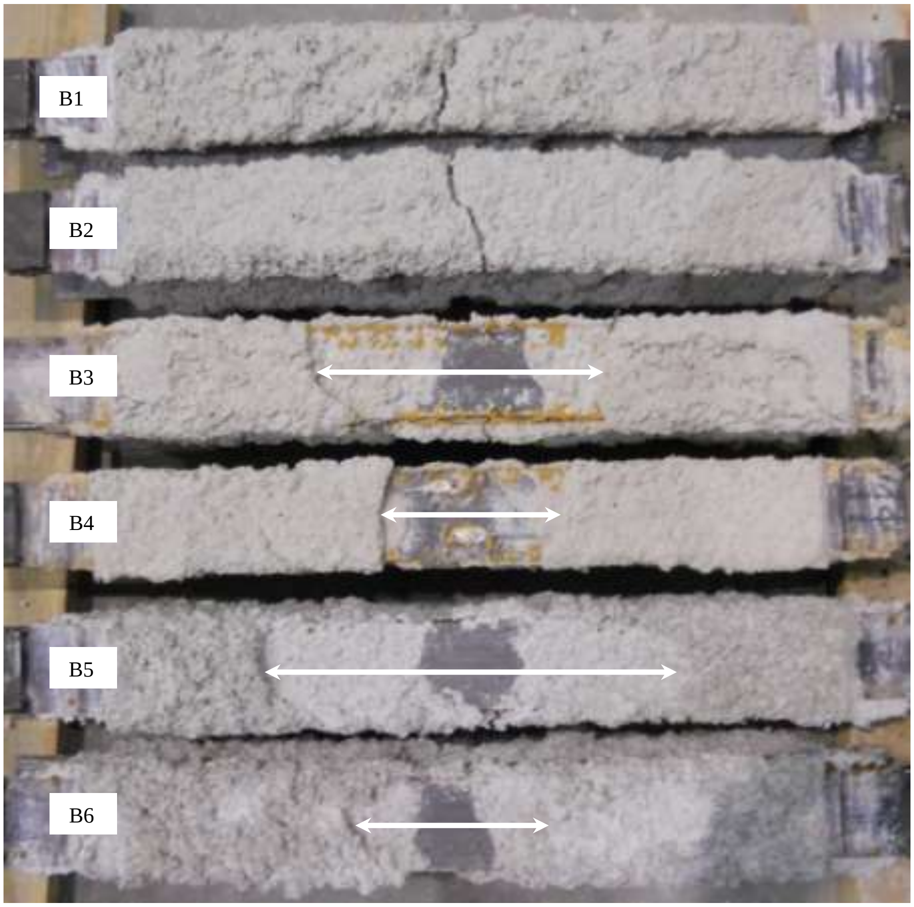

Figure 3.16 Extent of delamination of different types of SFRM from bottom flange of the I-beams subjected to impact loading

a) Camera view

Figure 3.17 Illustration of high speed camera snapshots during impact on steel beams insulated with different types of SFRM (v=8.05 m/sec)

Figure 3-17 (cont'd)

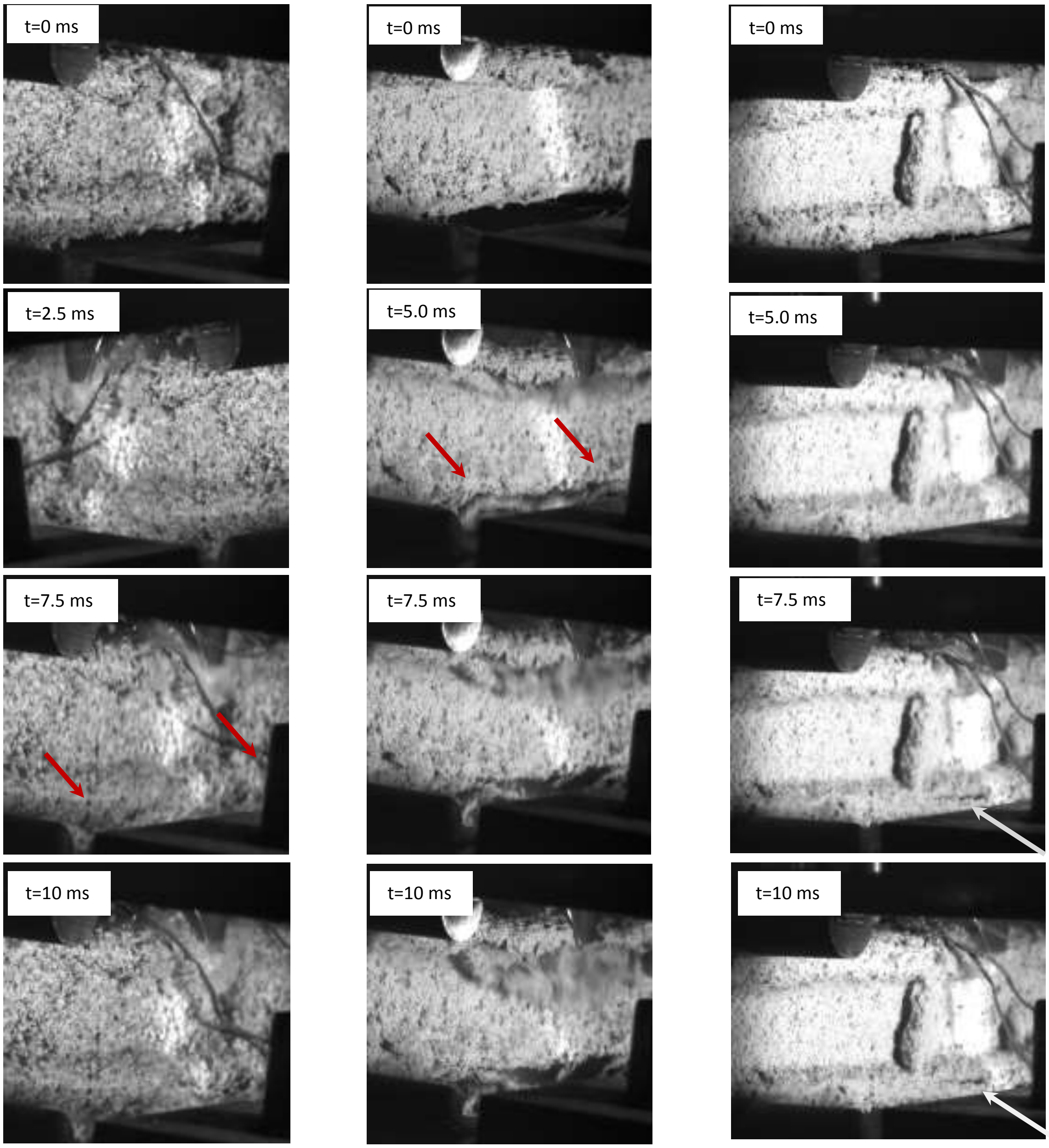

b) Mineral fiber-based SFRM

c) Gypsum-based

d) Portland cement-based

The beams insulated with mineral fiber-based insulation experienced the maximum delamination area on the bottom flange. This can be attributed to lower fracture properties of this type of insulation as compared to the gypsum-based and Portland cement-based SFRM. The percentage delamination area on the bottom flange increased from 26.8 % to 56.8% by increasing the impact velocity from 6.66 m/s to 8.05 m/s. That means 46 % increase in impact kinetic energy led to 112 % increase in the extent of delamination on the bottom flange. Due to very low stiffness of mineral fiber-based SFRM and its fibrous nature, the delaminated insulation is seen as powder splashing in the air as illustrated in Figure 3.17b.

3.6 Summary

In this chapter, the experimental program designed to study static and dynamic delamination of SFRM from steel structures is outlined and the obtained results are described. First, cohesive laws at the interface of steel and SFRM for three types of SFRM widely used in current buildings, namely Portland cement-based, gypsum-based and mineral fiber-based SFRM, were determined using direct fracture tests. The cohesive laws over the fracture process zone were obtained for two modes of fracture namely mode-I (normal model) and mode-II (shear mode). It was concluded that Portland cement-based SFRM possesses highest fracture energy and cohesive strength as compared to two other types of SFRM namely gypsum-based and mineral fiber-based SFRM.

Subsequently, details of an impact machine, designed for conducting drop mass impact tests on insulated beams, is presented. The results recorded during impact tests on beams insulated with three types of SFRM are discussed. Results showed that mineral fiber-based SFRM has the least resiliency against delamination from steel structures subjected to impact load, while Portland cement-based SFRM shows the superior performance in withstanding fracture and delamination.

CHAPTER 4

4 NUMERICAL MODELING

4.1 General

A large scale experimental program for evaluating delamination of fire insulation from steel structures under the action of extreme loading conditions would be substantially expensive and difficult to carry out. In additions, interpretation of acquired experimental results may not yield the influence of all critical parameters. Alternatively, numerical modeling can be a quite powerful and economical substitute to large scale experiments. The numerical models, once validated against experiments, can be utilized to perform comprehensive parametric studies exploring influence of critical factors governing the problem at hand. Further, such numerical models can be quite useful in assessing the shortcomings of current fire insulation material in use, as well as design of new generation of fire insulation material to be utilized in construction of steel structures.

The numerical modeling in this study comprises of two distinct parts. In the first part, to develop an understanding on the damage mechanisms of fire insulation in steel structures, a fracture mechanics-based numerical model is developed to analyze the fire insulation damage problem under the action of earthquake, impact and blast loading. In the second part, a thermal-structural model is developed to evaluate the post-earthquake and post-blast fire performance of steel structures based on the extent of delamination predicted in the first part of the numerical modeling. Different features of developed numerical models, its validation and application is presented in this chapter.

4.2 Fracture Mechanics-Based Numerical Model

A numerical approach that can simulate onset of delamination and propagation at fire insulation-steel interface is an essential tool in evaluating response of structures subjected to chain events and yet it is missing from literature. Without such numerical model, a rational investigation on survivability of steel structures subjected to fire in the aftermath of an earthquake, impact, and explosion events will not be practical.

4.2.1 Characterizing SFRM Delamination using Fracture Mechanics

As was outlined in Chapter 3, microcracking and debonding between the cement/gypsum matrix and the vermiculite/mineral wool fibers occurs over the vicinity of crack tip, namely fracture process zone (FPZ). The crack propagation at the interface of steel and SFRM can be characterized through adopting two approaches within the fracture mechanics framework depending on the size of FPZ. Application of classic linear elastic fracture mechanics (LEFM) approach for evaluating damage, which is based on single parameter, namely stress intensity factor (or equivalently energy release rate), is limited to problems for which the size of FPZ is very small, no strain-softening occurs over the FPZ and the material behaves linearly elastic outside the FPZ. However, in cementitious materials, strain-softening behavior is observed in the vicinity of crack over a large fully developed FPZ (Cotterell and Mai, 1996). For instance, the FPZ length in mortar is around 30 mm (Hu and Wittmann, 1989).

In contrast to LEFM, cohesive zone model (CZM) approach can tackle the effect of FPZ size, as well as strain-softening over the FPZ (cohesive zone), in fracture process of materials (Dugdale, 1960 and Barenblatt, 1962). In fact, it was first proposed by Dugdale (1960) to lump the plastic zone at crack tip into a narrow band along which the crack faces are subjected to constant stress (steel yield stress). This idealization was later generalized to many other fracture processes where the debonding can be localized in a strip-shaped process zone which is called cohesive zone. This zone is characterized by cohesive stresses binding the crack faces which are dependent on separation between crack faces. Cohesive law, which is material-specific, expresses the relation between traction and separation over the cohesive zone. The cohesive laws for both fracture modes (mode I and II) were developed for steel-SFRM interface in chapter 3. Cohesive zone approach has successfully been applied for characterizing fracture in ductile metals, fiber reinforced materials, ceramics, concretes and interfacial delamination between materials (Camanho etl., 2003; Scheider and Brocks, 2006; Turon et al., 2006; Park et al., 2008; Alfano et al., 2009).

4.2.2 Implementation of Fracture Mechanics in Finite Element Model

The fracture mechanics approaches explained in the previous section can be implemented in a finite element framework by adopting different approaches. Virtual crack closure technique (VCCT) is mostly adopted when LEFM can be used (Rybicki and Kanninen, 1977). In VCCT, it is assumed that when a crack propagates by a small amount, the energy released in the process is equal to the work required to close the crack to its original length. The energy release components are then computed from nodal forces and displacements obtained from the solution of a finite element model and compared to the fracture energy release rates. However, application of VCCT entails pre-knowledge regarding location of initial crack and crack propagation path. Further, difficulties arise when more than one crack propagating in different directions. In particular, application of this method in 3D problems may require complex moving mesh techniques to model crack propagation.

Cohesive zone model approach, however, overcomes the difficulties surrounding VCCT. In CZM, strength-based approach is used for identifying damage initiation and fracture mechanics is used for simulating damage propagation. The main advantage of using CZM over VCCT is the capability to predict both onset and propagation of delamination with no need for preceding crack location and propagation direction. Cohesive zone model is usually implemented in finite element method in conjunction with either interfacial elements or contact interaction elements. In either case, the surface of adjacent steel and SFRM elements are initially bonded. As the steel-SFRM assembly starts to deform, the interface behavior is characterized by tracing stress-displacement relationships (cohesive laws) established as a material constitutive model at steel-SFRM interface. Two approaches, namely extrinsic and intrinsic, are basically adopted for embedding cohesive/contact elements at the border of bulk finite elements. In intrinsic approach (Xu and Needleman, 1994), the cohesive/contact elements exist at the interface of volumetric finite elements from the beginning of the analysis, whereas in extrinsic approach (Zhang and Paulino, 2005) bulk finite elements are bordered by cohesive/contact elements in an adaptive manner.

There are numerous CZMs proposed in literature to cope with different material types and practical situations. The models developed by Hillerborg et al. (1976), Mi et al. (1998) and

Alfano and Crisfield (2001) are a bilinear type. Xu and Needleman (1994) proposed an exponential form of traction-separation relation. Trapezoidal cohesive law was proposed by Tvergaard and Hutchinson (1996) to deal with fracture in adhesive joints. Among other models, bilinear cohesive zone model has successfully been utilized by many researchers for modeling delamination of interfaces (Alfano and Crisfiled, 2001; Camanho et al., 2003; Alfano et al., 2009; Atas et al., 2012; Ye and Chen, 2011; Lee et al., 2010). Bilinear model obviously assumes a linear softening rule; however, the other alternatives for softening part of the cohesive zone model are tri-linear, exponential and higher polynomials. These types of softening laws, established for concrete, have been evaluated by Hofstetter and Meschke (2011).

Alfano (2006) evaluated the influence of the shape of the interface law on the application of cohesive zone models and concluded that the degree of influence that shape of the cohesive law can impose depends on the ratio between the interface toughness and the stiffness of the bulk material. For a typical double-cantilever beam test, the solution was found to be practically independent from the shape of the cohesive law. While the difference among predictions of linear and exponential softening laws was negligible, the linear softening law always demonstrated the superior efficiency in terms of CPU time. In this study, CZM is utilized to model cohesive failure over the FPZ and the cohesive laws are assumed to be bilinear.

4.2.3 Modeling Delamination of SFRM during Seismic Loading

To develop a fracture mechanics-based implicit finite element model for predicting delamination of fire insulation from steel structure subjected to seismic loading, ANSYS software has been chosen due to its unique capabilities in tackling nonlinear problems. ANSYS provides a comprehensive library of material constitutive models, contact interaction algorithms and state-of-the-art solution techniques for nonlinear problems. ANSYS solves the equations of motion implicitly, therefore it can simulate low strain rate problems such as static, quasi-static and dynamic loading encountered during earthquake.

4.2.3.1 Finite Element Discretization

To obtain the response of structure under seismic loading, equations of motion are solved using finite element technique. First, derivation of structural matrixes is outlined and subsequently the type of elements utilized for modeling steel and SFRM is explained.

The principle of virtual work states that a virtual (very small) change of the internal strain energy of an element must be offset by an identical change in external work due to the applied loading on the element. This is expressed by following equation:

$$\delta U_{in} = \delta U_{ex} \tag{4.1}$$

where, U_{in} is strain energy, U_{ex} is the external work and δ is a virtual operator.

The virtual strain energy is given as:

$$\delta U_{in} = \int_V \{\delta\epsilon\}\{\sigma\}dV \tag{4.2}$$

where, $\{\epsilon\}$ is strain vector, $\{\sigma\}$ is stress vector and V is the volume of element.

Material constitutive relation is expressed as:

$$\{\sigma\}=[D]\{\epsilon\} \tag{4.3}$$

where, $[D]$ is stress-strain matrix, which relates strain to stress based on material behavior.

The strains may be related to the nodal displacements by:

$$\{\epsilon\} = [B]\{u\} \tag{4.4}$$

where, $[B]$ is strain-displacement matrix based on the element shape functions and $\{u\}$ is the nodal displacement vector.

Combining Equations (4.2), (4.3) and (4.4) leads to following expression for internal energy of the element:

$$\delta U_{in} = \{\delta u\}^T \int_V [B]^T [D][B]\{u\}\, dV \tag{4.5}$$

The external virtual work comprises of inertial effects, nodal force and pressure applied to the element. The inertial effects can be given as:

$$\delta U_{ex,1} = -\int_V \{\delta w\}^T \frac{\{F^a\}}{V} dV \tag{4.6}$$

where, $\{w\}$ is vector of displacement of a general point and $\{F^a\}$ is inertial force vector. According to Newton's second law:

$$\frac{\{F^a\}}{V} = \rho \frac{\partial^2}{\partial t^2}\{w\} \tag{4.7}$$

where, ρ is density, V is element volume and t is time.

The displacements within the element are related to the nodal displacements by:

$$\{w\} = [N]\{u\} \tag{4.8}$$

where, $[N]$ is matrix of shape functions.

Combining Equations (4.6), (4.7) and (4.8), and assuming that ρ is constant over the volume of element, leads to:

$$\delta U_{ex,1} = -\{\delta u\}^T \rho \int_V [N]^T [N] \frac{\partial^2}{\partial t^2} \{u\} dV \tag{4.9}$$

The pressure force vector formulation starts with:

$$\delta U_{ex,2} = \int_{A_p} \{\delta w\}^T \{P\} dA_p \tag{4.10}$$

where, $\{P\}$ is the applied pressure vector (normally contains only one nonzero component) and A_p is area over which pressure acts.

Combing Equation (4.10) and (4.8) gives the following expression for external energy imposed by pressure loading:

$$\delta U_{ex,2} = \{\delta u\}^T \int_{A_p} [N] \{P\} dA_p \tag{4.11}$$

External energy imposed by nodal forces applied to the element can be accounted for by following:

$$\delta U_{ex,3} = \{\delta u\}^T \{F_e^{nd}\} \tag{4.12}$$

where, $\{F_e^{nd}\}$ is the nodal force applied to the element.

Finally, combination of Equations (4.5), (4.9), (4.11) and (4.12) and equating work done from internal actions and external energy results in:

$$\{\delta u\}^T \int_V [B]^T [D][B]\{u\}\, dV = \{\delta u\}^T \rho \int_V [N]^T [N] \frac{\partial^2}{\partial t^2} \{u\} dV$$

$$+ \{\delta u\}^T \int_{A_p} [N]\{P\} dA_p + \{\delta u\}^T \{\mathrm{F_e^{nd}}\} \tag{4.13}$$

Noting that the $\{\delta u\}^T$ vector is a set of arbitrary virtual displacements, which is common in all of the above terms, the condition required to satisfy above equation reduces to:

$$[K]\{u\} = [M]\{\ddot{u}\} + \{F_e^{pr}\} + \{F_e^{nd}\} \tag{4.14}$$

in which, $[K] = \int_V [B]^T [D][B] dV$ is element stiffness matrix, $[M] = \rho \int_V [N]^T [N] \, dV$ is element mass matrix and $\{F_e^{pr}\}$ is element pressure vector.

Effect of geometrical nonlinearities is accounted for using an updated Lagrangian formulation in which the stress stiffness (or geometric stiffness) contribution is included when developing the element tangent stiffness matrix. The element stiffness matrix,$[\bar{K}]$, is extended to:

$$[\bar{K}] = [K] + [S] \tag{4.15}$$

where, $[K]$ is the original stiffness matrix and $[S]$ is the element geometric stiffness matrix which is given as:

$$[\mathrm{S}] = \int_{\mathrm{V}} [\mathrm{G}]^{\mathrm{T}} [\mathrm{T}][\mathrm{G}] \, \mathrm{dV} \tag{4.16}$$

where,[G] is a matrix of shape function derivatives and [T] is a matrix of the current Cauchy (true) stresses.

The above explained approach is used to construct the element stiffness and mass matrixes for all individual finite elements in the model. Subsequently, the individual matrixes for elements are assembled forming a global stiffness and mass matrixes. After imposing boundary conditions, the global system of equation is solved using implicit time integration method. In implicit solution, such as Newmark's method the unknown variables at current time step (displacement and velocity) are related to known variable at preceding time step as well as unknown variable at current time step (acceleration). Therefore, the system of equations is coupled and special solution techniques should be adopted to solve the matrix equations (i.e. spars solver).

Steel elements including beam, column and truss chord are discretized using 4-noded shell elements (SHELL181) that have three translational and three rotational degrees of freedom at each node. This element is well-suited for linear, large rotation and large strain nonlinear applications and hence it can capture local and global buckling. The formulation of this element is based on logarithmic strain and true stress measures. SHELL181element supports full integration with incompatible modes. Since bilinear elements are too stiff in in-plane bending when fully integrated, SHELL181element uses the method of incompatible modes to enhance the accuracy in bending-dominated problems. This element does not have any spurious energy mechanisms such as hourglass. This specific form of SHELL181element is highly accurate, even with coarse meshes. Further, SHELL181element accounts for linear effects of transverse shear deformations. This capability of element is important when shear failure dominates the response of steel beams. An assumed shear strain formulation of Bathe-Dvorkin is used to alleviate shear locking (ANSYS, 2014).

SFRM insulation on steel assembly is discretized using 8-noded solid element (SOLID185) that has three translational degrees of freedom at each node. This element has the capability for handling large deformations, geometric and material nonlinearities. Enhanced strain formulation is adopted to prevent shear locking in bending dominated problems and volumetric locking in nearly incompressible cases.

4.2.3.2 Contact Interaction

At the steel-SFRM interface, surface-to-surface contact is employed such that steel and SFRM surfaces are discretized using 4-noded target (TARG170) and contact (CONTA173) elements, respectively. The node ordering of contact elements is consistent with the node ordering of the underlying solid and shell elements. The positive normal is given by the right-hand rule going around the nodes of the element and is identical to the external normal direction of the underlying shell or solid element surface. Contact elements are nonlinear and require a full Newton-Raphson iterative solution, regardless of whether large or small deflections are specified. Contact elements with Multi Point Constraint (MPC) algorithm is also utilized to model hinge boundary condition at both ends of column since regular boundary conditions will not simulate the true behavior. This is because constraining axial deformation will constrain the cross section against rotation as well.

The contact algorithm used in this study is an iterative series of penalty methods which is called augmented lagrangian method (ANSYS, 2014). This method is less sensitive to contact stiffness compared to pure penalty method, though it may require additional iterations in case of noticeable mesh distortions. The amount of penetration is controlled by contact penalty stiffness, the parameter that needs to be high enough to preclude penetration and concurrently low enough to not cause ill-conditioning of global stiffness matrix leading to convergence issues. However, resolving penetration problem is generally less cumbersome than dealing with convergence difficulties. Thus, analysis is initially carried out with low penalty stiffness, and subsequently the amount of penetration and the number of equilibrium iterations is monitored in each sub-step.

Provided that excessive penetration is recognized to be responsible for global convergence issue, the stiffness has been underestimated. In contrast, if numerous equilibrium iterations are required to diminish the out of balance force, the stiffness can be overestimated. In either case, required adjustment is made and the analysis is rerun. Note that, during the analysis course, the penalty stiffness is updated according to stiffness changes in interacting bodies arising from nonlinear behavior.

4.2.3.3 Material Constitutive Model

Material constitutive laws is split in two parts; stress-strain laws and failure surfaces for bulk material (steel and SFRM) and cohesive laws for interface of steel and SFRM. Multi-linear kinematic hardening material model is adopted for modeling steel. This model employs a Von Mises yield criteria as yield surface, and an associated plastic flow rule is adopted. Kinematic hardening assumes that the yield surface remains constant in size and the surface translates in stress space with progressive yielding.

Drucker-Prager constitutive model (Drucker and Prager, 1952), which is commonly used for modeling dry soil and rock, is used here to model the SFRM behavior outside the FPZ. This model, albeit not perfect, is feasible since it captures cohesive failure and has a tension cut-off limit. The yield surface does not change with progressive yielding, hence there is no hardening rule and the material is elastic-perfectly plastic. This is a modification of the Von Mises yield criterion that accounts for the influence of the hydrostatic stress component. The Drucker-Prager yield criterion takes the form of:

$$f = \sqrt{J_2} + \alpha I_1 - k = 0 \tag{4.17}$$

where I_1 and J_2 are first the invariant of stress tensor and the second invariant of stress deviator tensor, respectively, while α and k are positive material constants related to cohesion (c) and internal friction angle of material (φ):

$$\alpha = \frac{2\,\sin\varphi}{\sqrt{3}\,(3-\sin\varphi)} \qquad k = \frac{6c\,\cos\varphi}{\sqrt{3}\,(3-\sin\varphi)} \tag{4.18}$$

Cohesive zone model is adopted as material constitutive model for contact elements inserted at the interface of steel and SFRM. Figure 4.1 shows CZM constitutive relations for both normal (mode-I) and tangential (mode-II) directions utilized in this study. The model has a linear elastic part followed by a linear softening part. Delamination is initiated when the cohesive stress reaches cohesive strength (σ_c or τ_c) and subsequently progresses until the cohesive stress reaches zero value, the point at which delamination is completed. Once completely delaminated, further separation occurs without any cohesive stress. The delaminated surfaces may interact again, however, the contact behavior will be a standard one (i.e. frictional contact). If unloading takes place at any point on softening part, traction-separation follows a linear trend back to zero stress. Subsequent reloading does not follow the original stiffness, instead takes the previous unloading path with reduced stiffness. This way, effect of partial delamination and damage accumulation is taken into consideration.

The analytical expression for mixed mode delamination (combination of constitutive relations depicted in Figure 4.1) can be represented as:

$$\begin{Bmatrix} \sigma \\ \tau \end{Bmatrix} = \begin{Bmatrix} K_n \delta_n (1-d) \\ K_t \delta_t (1-d) \end{Bmatrix} \tag{4.19}$$

where, K_n and K_t are normal and tangential contact stiffness, δ_n, δ_t are normal separation and tangential slip distance and d is damage parameter which is expressed as:

$$d = \left(\frac{\Delta-1}{\Delta}\right)\chi \quad 0 \leq d \leq 1 \tag{4.20}$$

where, $$\Delta = \sqrt{\left(\frac{\delta_n}{\delta_{n,o}}\right)^2 + \left(\frac{\delta_t}{\delta_{t,o}}\right)^2} \tag{4.21}$$

in which $\delta_{n,o}$ and $\delta_{t,o}$ are separation distances corresponding to normal (σ_c) and shear cohesive strength (τ_c), respectively and the parameter χ is given as:

$$\chi = \frac{\delta_{n,c}}{\delta_{n,c}-\delta_{n,o}} = \frac{\delta_{t,c}}{\delta_{t,c}-\delta_{t,o}} \tag{4.22}$$

in which $\delta_{n,c}$ and $\delta_{t,c}$ are normal and tangential separation at the end of cracking, respectively.

For $\Delta \leq 1$, the damage parameter is zero ($\mathrm{d} = 0$), and for $\Delta > 1$, d-value falls between zero and 1($0 < d \leq 1$). Note that, in 3D models isotropic behavior is assumed in terms of tangential slip distance:

$$\delta_t = \sqrt{\delta_{t,1}^2 + \delta_{t,2}^2} \tag{4.23}$$

where, $\delta_{t,1}$ and $\delta_{t,2}$ are tangential slip distance components. Fracture energies (G_n and G_t) released at any displacement level is calculated as:

$$G_n = \int \sigma \, d\delta_n \tag{4.24}$$

$$G_t = \int \tau \, d\delta_t \tag{4.25}$$

The normal (G_{nc}) and tangential (G_{tc}) critical fracture energies are computed as:

$$G_{nc} = \frac{1}{2}\sigma_c \delta_{n,c} \tag{4.26}$$

$$G_{tc} = \frac{1}{2}\tau_c \delta_{t,c} \tag{4.27}$$

For decoupled fracture mode delamination, occurs once the current energy level reaches critical value, whereas for mixed mode delamination an interaction curve needs to be defined since both normal and tangential energies contribute to total fracture energy. In this study, a power law criterion established to predict delamination propagation under mixed mode loading is used which is prevalent in fracture mechanics (Alfano and Crisfield 2001):

$$\left(\frac{G_n}{G_{nc}}\right) + \left(\frac{G_t}{G_{tc}}\right) = 1 \tag{4.28}$$

where G_n and G_{nc} are normal current and critical fracture energy; and G_t and G_{tc} are tangential current and critical fracture energy.

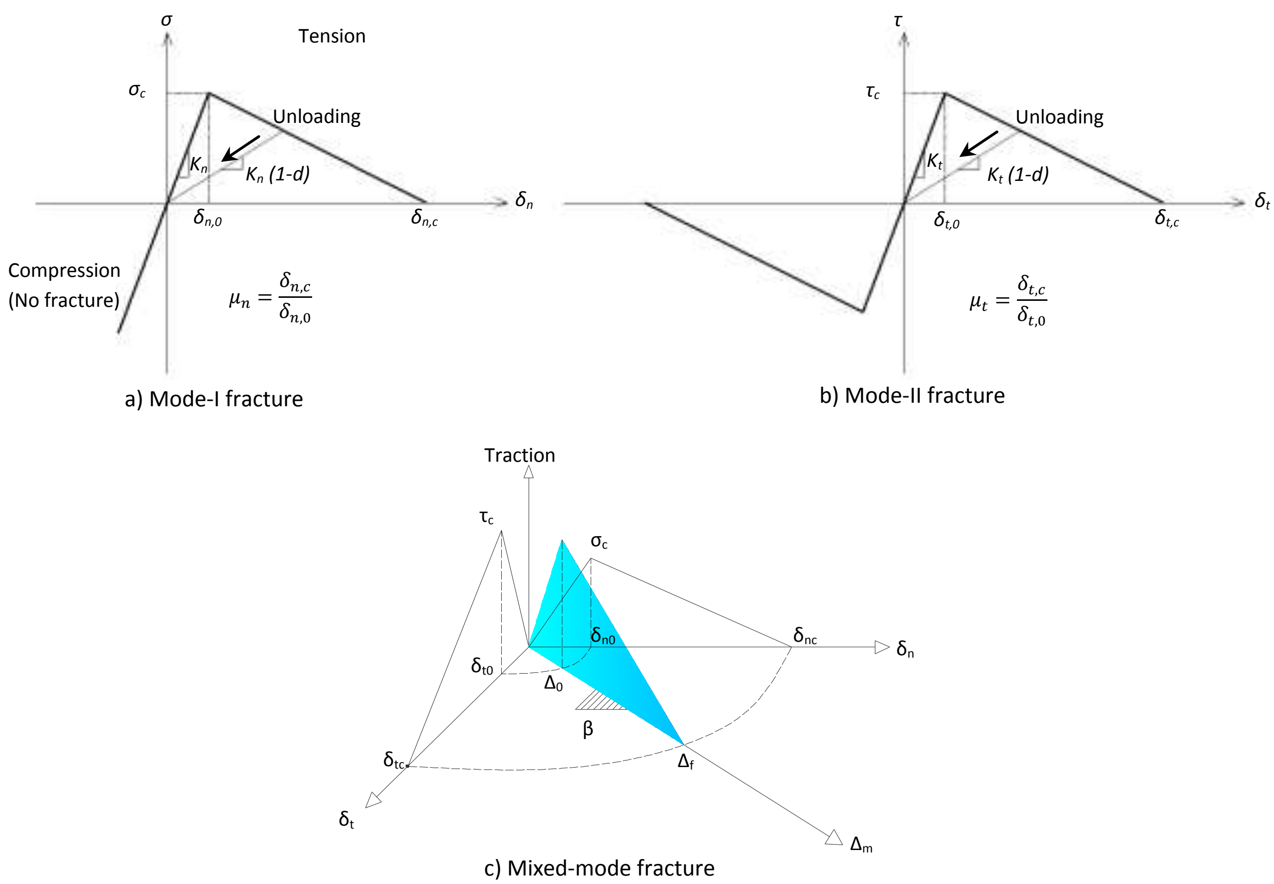

Figure 4.1 Cohesive zone constitutive model for SFRM

4.2.3.4 Material Properties

In numerical simulations under seismic loading, SFRM properties derived from fracture experiments are utilized, as summarized in Table 3.2 (as presented in Chapter 3). The cohesive laws depicted in Figure 3.10 and Figure 3.11 (as presented in Chapter 3) is used to trace the SFRM-steel interface behavior. The steel material of beam-column assembly and truss member is assumed to be of A992 (σ_y=355 MPa, E=200 GPa and υ=0.3).

4.2.3.5 Mesh Size

In numerical solutions involving implicit finite element scheme, serious convergence issues can occur when applied to problems that contain material softening. Due to the fact that CZM carries a significant level of nonlinearity in terms of cohesive laws, determination of element size requires due consideration. In fact, enough number of elements should span the cohesive zone to ensure as correct dissipation of energy as possible. The final size of the finite element mesh is certainly controlled by the cohesive zone behavior. The size of the cohesive zone (or in other words, FPZ) is therefore to be predicted prior to identifying the element size. Turton et al. (2007) have summarized some of the expressions with respect to computation of cohesive zone length. In this study the cohesive zone length is estimated using an expression given by Hillerborg et al. (1976) for concrete as a cementitious material:

$$l_{cz} = \frac{EG_c}{(\sigma_c)^2} \tag{4.29}$$

in which, E, G_c and σ_c are elastic modulus, critical fracture energy and cohesive strength for fracture mode-I, respectively. The minimum number of elements spanning over the cohesive zone has not been well-established (Turton et al., 2007). The values between 2 to 10 have been used by researchers (Falk et al., 2001; Dávila et al., 2001; Moës and Belytschko, 2002).

The cohesive zone length computed by Equation (4.29) for SFRM types A, B and C are 187 mm, 481 mm and 79 mm, respectively. It should be noted that, the Equation (4.29), which is also termed as characteristic length in fracture mechanics literature (Cotterell and Mai, 1996), can only provide an approximate extension of fully developed FPZ at steel-SFRM interface. This equation is utilized in this study to only approximate the size of FPZ (cohesive zone) in order to have an estimation of initial mesh size over the cohesive zone. Nonetheless, mesh sensitivity analyses is performed to ensure that sufficient number of cohesive elements is embedded in cohesive zone to correctly capture the nonlinearity in this zone. Consequently, in current numerical modeling, at least 10 elements were inserted in cohesive zone to ensure accuracy of the solution.

4.2.3.6 Nonlinear Solution Predicaments

Numerical solution in the case of contact interaction analysis is highly nonlinear making computational efforts cumbersome even though material properties remain elastic. Indeed, once material and geometrical nonlinearities are taken into account, the level of complexity in the analysis further increases. In the above discussed numerical model various nonlinearities are present; therefore, special nonlinear solution strategies are employed to achieve an accurate solution.

In addition, convergence problems arise when the response reaches softening zone of CZM. Crisfield et al. (1994) inferred that Newton-Raphson method is not efficient enough due to convergence issues while using either load-controlled (with arc length) or displacement-controlled loading. To rectify the problem, Crisfield et al. (1994) proposed line search procedure. In this study, displacement-controlled loading, in conjunction with line search method, is used thereby enhancing the capabilities of Newton-Raphson method to achieve convergence faster.

Nonetheless, convergence issues may arise at some load steps which is treated by adopting nonlinear stabilization method provided in ANSYS. Nonlinear stabilization in ANSYS can be understood as adding an artificial damper or dashpot element at each node of an element. The damper element coefficient is then optimized such that the stabilization process will not influence the accuracy of solution.

4.2.4 Modeling Delamination of SFRM during Impact and Blast Loading

Application of implicit solution method for analysis in which structure undergoes very large strains, or when duration of loading is very short, is either not successful or not efficient due to very small time steps required to satisfy convergence criteria or capture the loading scenario. Hence, to develop a fracture mechanics-based finite element model to cope with delamination of fire insulation from steel structures subjected to blast and impact loading, an explicit solution needs to be adopted. For this reason, LS-DYNA software, known to be perfectly capable of carrying out explicit solutions, has been selected. LS-DYNA offers wide variety of contact algorithms and material constitutive models enabling users to tackle very complex problems encountered in research and practical scales.

4.2.4.1 Finite Element Discretization

The finite element formulation is similar to the one outlined in section 4.2.3.1. However, Equation (4.14) is solved explicitly. In explicit solution, velocity and accelerant in dynamic equation of motion is approximated using a finite difference method (i.e. central difference). In other words, the unknowns variables at current step are related to known variables at preceding time step, and therefore, the system of equations are decoupled. However, the time step should be selected very small to maintain the stability of solution.

Steel structure and SFRM are discretized using 8-noded solid element with linear displacement interpolation functions and reduced integration (one point). These explicit elements are best suited for nonlinear applications with large defamation as usually encountered during blast and impact loading. The plate stack in the hammer (as used in the experiments presented in Chapter 3) is also modeled using 8-noded solid elements. However, the indenter is discretized using 10-noded tetrahedron elements which use a quadratic displacement interpolation function with five integration points. These elements are well suited for modeling irregular meshes such as those encountered in hammer indenter (LS-DYNA, 2014).

4.2.4.2 Contact Interaction

To simulate dynamic interaction between striking hammer and the flange of the steel beam, contact type "Automatic_One_Way_Surface_To_Surface" is used (LS-DYNA, 2014). This contact formulation is based on standard penalty method in which each "slave node" is checked for penetration through the "master surface". If penetration occurs, an interfacial force, with a magnitude that is proportional to the amount of penetration, is applied between the slave node and its contact point. The contact force developed between indenter tip and the flange of the beam is considered as impact force.

Lower stiffness of SFRM as compared to steel (E_{SFRM}=0.01GPa<<E_{steel}=200 GPa), can seriously reduce the contact stiffness when standard penalty method is utilized. The diminished contact stiffness can cause excessive penetration among slave and mater surfaces. LS-DYNA adopts two approaches to tackle this problem. On method is to artificially enhance the contact stiffness. Increasing contact stiffness may result in solution instability, in particular, when the soft material has a low density the stable time step should be reduced. An alternative for standard penalty method is soft constraint penalty formulation in which an additional stiffness is calculated, which is based on the stability of a local system comprised of two masses connected by a spring. The stability contact stiffness (k_{cs}) is calculated by:

$$k_{cs} = 0.5\ \alpha\ m^* \frac{1}{\Delta t_c(t)} \tag{4.30}$$

where, α is a scale factor for soft constraint penalty formulation, m^* is a function of the mass of the slave nodes and master nodes and $\Delta t_c(t)$ is the solution time step as the analysis proceeds. Contact type "Automatic_One_Way_Surface_To_Surface_Tiebreak" with soft constraint penalty formulation (SOFT=1) is utilized to model delamination between fire insulation and steel surface. Upon failure, the contact type is changed to "Surface_To_Surface".

4.2.4.3 Material Constitutive Model

Steel behavior is modeled using "Piecewise_Linear_Plasticity" material model (LS-DYNA, 2014). This constitutive model accounts for strain rate dependency utilizing Cowper-Symonds model (Cowper and Symonds, 1957) and also can model failure based on effective plastic strain criteria. In Cowper-Symonds model, the yield stress is scaled by a strain rate dependent dynamic increase factor (DIF):

$$\sigma_{equ} = DIF\ (\sigma_0 + E_p \varepsilon_{eff}^p) \tag{4.31}$$

where, σ_{equ} and σ_0 denote the equivalent dynamic yield stress and equivalent static yield stress, respectively; E_p and ε_{eff}^p represent plastic hardening module and effective plastic strain, respectively. Dynamic increase factor (DIF) is computed as:

$$DIF = 1 + \left(\frac{\dot{\varepsilon}_{equ}}{D}\right)^{\frac{1}{q}} \tag{4.32}$$

where, $\dot{\varepsilon}_{\text{equ}}$ represents equivalent strain rate and D and q are strain rate parameters.

The true stress-strain should be adopted since the finite element formulation is based on the true stress and true strain definition (LS-DYNA, 2014)

Drucker-Prager constitutive model (Drucker and Prager, 1952) is used to model cohesive failure of bulk SFRM. The characteristics of this constitutive model were provided in section 4.2.3.3.

The crack initiation and propagation at the interface of fire insulation and the steel beam is modeled using a fracture mechanics and cohesive zone approach which is the extension of Dycoss discrete crack model (Lemmen and Meijer, 2001) that accounts for mixed-mode fracture using a power law damage criterion. This model is very similar to the one developed by Alfano and Crisfiled (2001) model (explained in section 4.2.3.3). However, the approach by which the crack initiation criterion is derived is somewhat different. Figure 4.1 illustrates the mixed-mode cohesive zone model concept utilized in Dycoss discrete crack model. The traction-separation laws over the cohesive zone (FPZ) at both modes of fracture, i.e. mode-I and mode-II, have a linear shape up to cohesive strength followed by a linear softening law.

In this cohesive zone model, the total mixed-mode relative displacement Δ_m is defined as:

$$\Delta_m = \sqrt{{\delta_n}^2 + {\delta_t}^2} \tag{4.33}$$

where δ_n, δ_t are separation in normal and tangential directions. The mixed-mode crack initiation criterion (onset of damage and softening at interface) is given as:

$$\Delta_0 = \delta_{n0}\delta_{t0}\sqrt{\frac{1+\beta^2}{(\delta_{t0})^2+(\beta\delta_{n0})^2}} \tag{4.34}$$

where, $\delta_{n0}= \sigma_c/K_n$, $\delta_{t0}= \tau_c /K_t$and $\beta=\delta_t / \delta_n$ (mode mixity parameter). The K_n and K_t are initial slope of the stress-displacement relationships in the normal and tangential fracture modes, respectively. The failure criterion is given as:

$$\Delta_f = \frac{2(1+\beta^2)}{\Delta_0}\left[\left(\frac{K_n}{G_{nc}}\right)^{\alpha} + \left(\frac{K_t.\beta^2}{G_{tc}}\right)^{\alpha}\right]^{-\frac{1}{\alpha}} \tag{4.35}$$

in which α (the mixed-mode exponent) is in the range of 1.0 to 2.0.

With respect to material damping, due to a very short duration of impact and blast events, which is much shorter than the natural period of beam and hammer assembly, the material viscous effects do not considerably contribute to the dynamic response of the structure (Jones, 2012; Stronge and Yu, 1993). Hence, the stabilization effect of material damping is not taken into account in the numerical modeling.

4.2.4.4 Material Properties

The entire true stress-true strain relationship of ASTM A992-Gr.50 steel is plotted in Figure 4.2. This stress-strain curve has been derived using an experimental-numerical approach adopted by (Arasaratnam, et al., 2011). The yield stress and elastic modulus of ASTM A992 steel are 444 MPa and 200 GPa, respectively. The Cowper-Symonds coefficients are D=40.4 and q=5 (Jones, 2012) and the true failure plastic strain is ε_f =0.99.In numerical simulations under impact and blast loading, SFRM properties derived from fracture experiments are utilized, as summarized in Table 3.2. The cohesive laws, depicted in Figure 3.10 and Figure 3.11 (as presented in Chapter 3), is used to trace the SFRM-steel interface behavior.

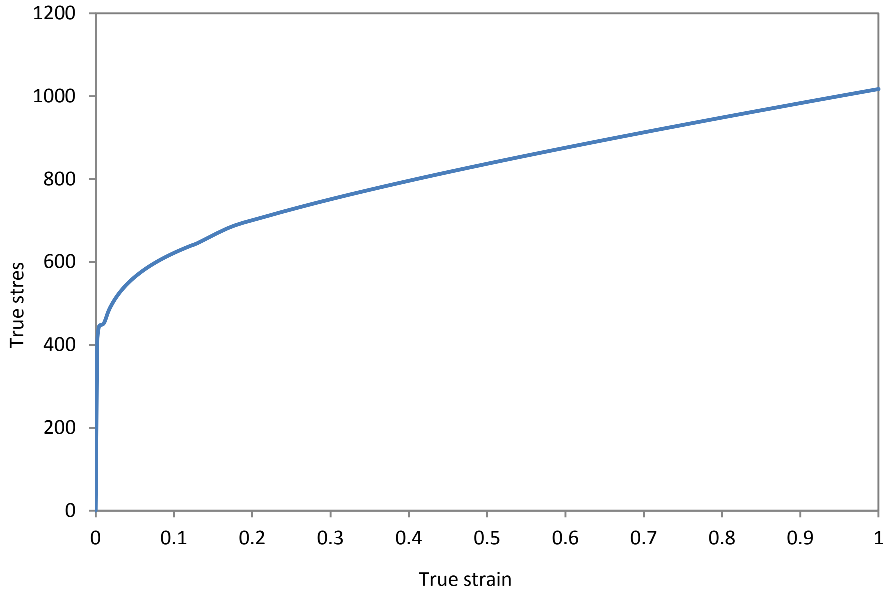

Figure 4.2 True stress-true strain relationship for A992-Gr. 50 steel

4.2.4.5 Mesh Size

The issue of mesh size over cohesive zone is tackled in a similar way as it is coped with in implicit analysis, as outlined in section 4.2.3.5. However, reduced integration elements suffer from hourglassing problem, which is another factor to be accounted for in determining the finite element mesh. However, mesh sensitivity analysis shows that the minimum mesh size is controlled by the cohesive zone behavior.

4.2.4.6 Pitfalls in Explicit Solution

Reduced integration elements (one-point integration), commonly utilized in explicit solution, have a major drawback which is the need to control the zero-energy modes, namely hourglass modes. These undesirable oscillatory modes tend to have periods that are typically much shorter than the periods of the structural response. One method to tackle this issue is to incorporate small viscous damping or small elastic stiffness to prevent formation of such zero-energy deformation modes. This method, though has a negligible effect on the global deformation modes, it stabilizes the solution. Without including some level of artificial damping, the entire solution can be compromised and the results can become unreliable. Since hourglass modes are orthogonal to the strain calculations, work done by the hourglass resistance is neglected in the energy equation. The amount of energy required to resist the formation of hourglass modes should be monitored during the course of analysis. The amount of this energy should not exceed 5% of the total energy (LS-DYNA, 2014). Kosloff and Frazier (1974) developed the pioneering three-dimensional algorithms for controlling the hourglass modes.

4.3 Thermal-Structural Numerical Model

The above explained fracture mechanics-based numerical model can estimate the extent of delamination over the steel structural elements. However, it does not address the post-earthquake or post-impact and post blast fire response of the steel structures. To predict the consequences of delamination of fire insulation during fire following earthquake and blast loading, a thermal-structural numerical model is developed in ANSYS software. The thermal-structural analysis can be carried out using two approaches; fully coupled analysis or decoupled analysis. Since the amount of heat generated as a result of structural deformation is not comparable to the amount of heat imposed on the structure during fire, the complexity of coupled analysis is avoided and decoupled analysis is performed.

In decoupled thermal-structural analysis, the thermal analysis is conduced first and thereby the evolution of temperature time-history within the structure is computed. The extent of delamination of fire insulation is accounted for in this step. Subsequently, structural analysis is carried out and temperature time history, calculated from previous thermal analysis, is applied on the structural model as temperature loading. The finite element derivation of structural analysis matrices, explained in section 4.2.3.1, is expanded by taking into account the thermal strain effects. The finite element discretization and derivation of matrices pertaining to heat transfer analysis is detailed in followings.

4.3.1 Structural Analysis

The finite element formulation presented in section 4.2.3.1was developed based on the fact that the total strain of a finite element has only one component, namely mechanical strain. However, when thermal effects have to be simulated, an additional strain component, namely thermal strain should be incorporated into the finite element formulation. Therefore, total strain is defined as:

$$\varepsilon_{\mathrm{t}} = \varepsilon_{\mathrm{m}} + \varepsilon_{\mathrm{th}} \rightarrow \quad \varepsilon_{\mathrm{m}} = \varepsilon_{\mathrm{t}} - \varepsilon_{\mathrm{th}} \tag{4.36}$$

where, ε_{t} is total strain, ε_{m} is mechanical strain and $\varepsilon_{\mathrm{th}}$ represents thermal strain. Note that creep effects are not accounted for in current numerical model.

Thermal strain is expressed as:

$$\varepsilon_{\mathrm{th}} = \alpha \Delta \mathrm{T} \tag{4.37}$$

where, α and $\Delta\mathrm{T}$ are thermal expansion coefficient and temperature increment. Noted that, thermal strain (expansion) is temperature-dependent and can be measured for each material.

Replacing the term ε with $(\varepsilon_{\mathrm{t}} - \varepsilon_{\mathrm{th}})$ in Equation (4.2) and following the same procedure adopted in subsequent equations, eventually leads to addition of thermal load vector to right hand side of Equation (4.14) as is expressed in following:

$$[K]\{u\} = [M]\{\ddot{u}\} + \left\{F_e^{pr}\right\} + \{F_e^{nd}\} + \{F_e^{th}\} \tag{4.38}$$

where, $F_e^{th} = \int_V [B]^T [D]\{\varepsilon_{th}\} \, dV$ represents element thermal load vector.

4.3.2 Thermal Analysis

According to first law of thermodynamics, thermal energy is conserved therefore the governing equation for heat transfer analysis can be written as:

$$\rho c \frac{\partial T}{\partial t} + \nabla q = Q \tag{4.39}$$

where, ρ is density, c is heat capacity, T is temperature, t is time, q is heat flux and Q represents heat source defined as the amount of heat produced for a unit volume of the material. In fire conditions the amount of internal heat generation is zero (Q=0). However, the term heat flux (q) should be evaluated within the finite element volume as well as over the surfaces of the finite element.

Fourier's law can be used to relate the heat flux vector to the thermal gradients within the finite element which is known as transfer of heat through conduction:

$$q = -[k]\nabla T \tag{4.40}$$

where, $[k]$ represents thermal conductivity matrix.

The heat flux over the surface of a finite element, or in other words the heat flow into or out of the element, has two main sources, namely convective heat flux or radiative heat flux. The heat flux through the convection (q_c) over the surface of a finite element can be expressed as following based on Newton's law of cooling:

$$q_c = h_f(T - T_B) \tag{4.41}$$

where, h_f is film coefficient, T is temperature at the surface of the finite element and T_B is bulk temperature of adjacent fluid (air). For surfaces exposed to fire, T_B is taken as the fire temperature ($T_B = T_f$), whereas for unexposed surfaces T_B is taken as ambient temperature (room temperature).

The radiative heat flux (q_r) over the surface of a finite element is computed using Stefan-Boltzmann Law:

$$q_r = \varphi\sigma\varepsilon\left(T^4 - {T_f}^4\right) \tag{4.42}$$

where, σ is Stefan-Boltzman constant = 5.67×10-8 (W/m^2.°K^4), φ is radiation view factor and εrepresents emissivity factor and it is related to the visibility of the surface exposed to the fire. As it is clear from Equation (4.42), the radiation term is highly nonlinear with respect to temperature. To be consistent with the convective boundary condition, Equation (4.42) is re-written as:

$$q_r = \varphi\sigma\varepsilon\left(T^2 + {T_f}^2\right)\left(T + T_f\right)\left(T - T_f\right) = h_r\left(T - T_f\right) \tag{4.43}$$

Pre-multiplying Equation (4.39) by a virtual change in temperature (δT), integrating over the volume of the element (V) and surface of the element (S), and combining with Equation (4.40), Equation (4.41) and Equation (4.43) with some manipulation yields to:

$$\int_V \left(\rho c\delta T\frac{\partial T}{\partial t} + \nabla(\delta T k \nabla \mathrm{T})\right) dV = \int_S \left(\delta T h_f(T_B - T) + \delta T h_r\left(T_f - T\right)\right) dS \tag{4.44}$$

The temperature within the element is related to the nodal temperatures by:

$$\{T\} = [N]\{T_e\} \tag{4.45}$$

where, T=T(x,y,z,t) is temperature, $[N]$ is element shape functions and $\{T_e\}$ is nodal temperature vector of element.

Therefore, virtual change in temperature can be given as:

$$\{\delta T\} = [N]\{\delta T_e\} \tag{4.46}$$

The time derivatives of Equation (4.45) can be written as:

$$\dot{T} = [N]\{\dot{T}_e\} \tag{4.47}$$

Also, space derivatives of temperature can be written as:

$$\nabla\{T\} = \nabla[N]\{T_e\} = [B]\{T_e\} \tag{4.48}$$

The variational statement of Equation (4.44) can be combined with Equation (4.45) to Equation (4.48) that yields to following equation:

$$\int_V \rho c\{\delta T_e\}[N][N]^T\{\dot{T}_e\}dV + \int_V \{\delta T_e\}[B]^T[k][B]\{T_e\}dV =$$

$$\int_S \{\delta T_e\}[N]h_f(T_B - [N]\{T_e\})dS + \int_S \{\delta T_e\}[N]\, h_r\left(T_f - [N]\{T_e\}\right) dS \tag{4.49}$$

Equation (4.49) is rearranged by dropping $\{\delta T_e\}$ from all terms:

$$\rho \int_V c[N][N]^T dV\{\dot{T}_e\} +$$

$$\int_V [B]^T[k][B]dV\{T_e\} + \int_S [N]^T[N]\, h_f\{T_e\}dS + \int_S [N]^T[N]\, h_r\{T_e\}dS =$$

$$\int_S [N]h_f T_B dS + \int_S [N]h_r T_f dS \tag{4.50}$$

Equation (4.50) can be rewritten in matrix form:

$$[C_e^t]\{\dot{T}_e\} + ([K_e^d] + [K_e^c] + [K_e^r]) = \{F_e^c\} + \{F_e^r\} \tag{4.51}$$

where, $[C_e^t] = \rho \int_V c[N][N]^T dV$ is element specific heat (thermal damping) matrix, $[K_e^d] = \int_V [B]^T[k][B]dV$ is element conductivity matrix, $[K_e^c] = \int_S [N]^T[N]\, h_f dS$ is element surface convection matrix, $[K_e^r] = \int_S [N]^T[N]\, h_r dS$ is element surface radiation matrix, $\{F_e^c\} = \int_S [N]h_f T_B dS$ is element convective load vector and $\{F_e^r\} = \int_S [N]h_r T_f dS$is element radiative load vector.

Equation (4.51) is solved using implicit time integration and nonlinear solution scheme namely Newton-Raphson method is exploited. Solution of Equation (4.51) provides spatial distribution (3D model) as well as time history of temperature during fire exposure time.

In thermal analysis, 8-noded solid element (SOLID70), that has temperature degree of freedom at each node, is adopted to model steel and fire insulation. Convective boundary condition on fire-exposed surfaces is easily modeled using surface loading option available in ANSYS. However, simulation of radiation loading in ANSYS requires some extra consideration. Surface element (SURF152) is overlaid on surface exposed finite elements to simulate radiation effects. This element is associated with an extra node to which the fire temperature is assigned. The radiation constants are defined as a part of material properties.

4.3.3 Material Constitutive Model

Multi-linear kinematic hardening plasticity model based on Mises yield surface is used to characterize the constitutive relation for steel material. Fire insulation is modeled in thermal analysis; however it is removed from the finite element mesh in the structural analysis since it does not contribute to the structural response due to very small strength and stiffness of the material.

4.3.4 Temperature-Dependent Material Properties

Two sets of material properties are required to model effect of post-earthquake and post-blast fire in a structure; thermal properties and mechanical properties. Both thermal and mechanical properties vary with temperature. In this study, these material properties are adopted from Eurocode 3 (2010). Figure 4.3 illustrates the time-dependent engineering stress-strain curves prescribed in Eurocode 3 (2010) for evaluation of fire performance of steel structures made of steel type S350. Since the finite element formulation is based on true logarithmic strain, the engineering stress-strain curves should be converted to true stress-strain curve using following equations:

$$\varepsilon_T = \mathrm{Ln}(1 + \varepsilon_E) \tag{4.52}$$

$$\sigma_T = \sigma_E(1 + \varepsilon_E) \tag{4.53}$$

where, ε_E and σ_E are engineering strain and engineering stress, respectively. Also, ε_T and σ_T are true strain and true stress, respectively. It should be emphasized here that the above Equations are valid before necking occurs in steel. In fact, the above equations cannot be utilized to find the true failure conditions. The only method to estimate the true failure strain and corresponding true failure stress is through applying an experimental-numerical approach as adopted by Zhang and Li (1994), Ling (1996), Khoo (2000) and Arasaratham et al., (2011). However, in this study the level of strains during fire does not exceed the strain corresponding to necking (ultimate strain), hence the application of above equations is deemed valid. Note that, despite available data on temperature-dependent engineering stress-strain curves for structural steel, the true stress-strain relationship for structural steel at elevated temperature has not yet been established. This is partly due to complexities added while differentiating among plastic strain and creep strain. Figure 4.4 also depicts degradation of elastic modulus by temperature for structural steel based on curve prescribed in Eurocode 3 (2010).

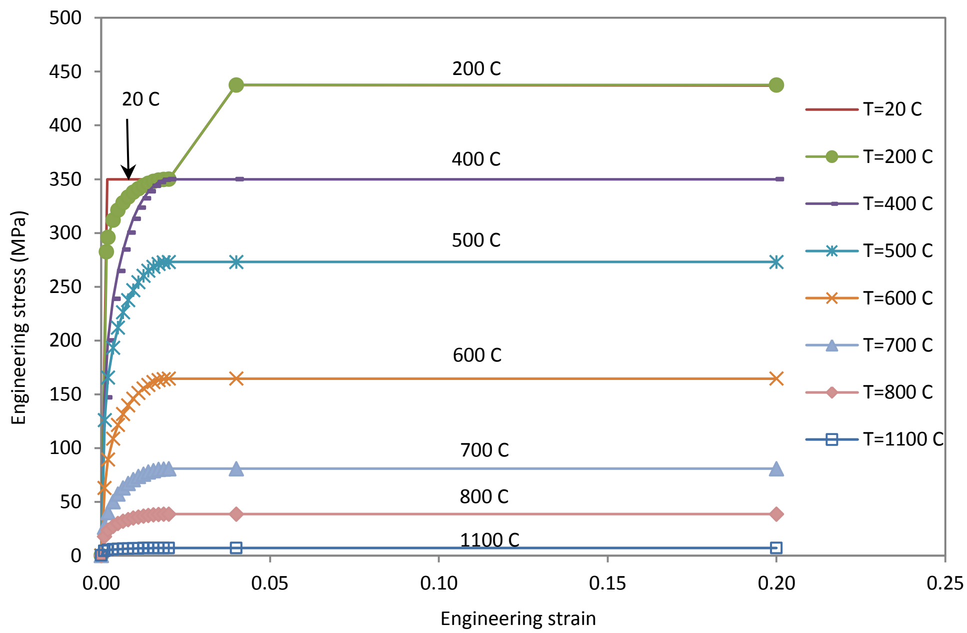

Figure 4.3 Time-dependent engineering stress-strain relationship for S350 steel (EC3, 2005)

Three main thermal properties of steel and fire insulation for evaluating temperature evolution and structural response are thermal strain (elongation), thermal conductivity and specific heat. The thermal strain is used in structural analysis while two other parameters are utilized in thermal analysis. Figure 4.5 plots thermal strain of structural steel as a function of temperature. Note that, thermal strain of SFRM is not required because the fire insulation is not included in the structural model. Variation of thermal conductivity and specific heat of structural steel (carbon steel) is illustrated in Figure 4.6 and Figure 4.7, respectively.

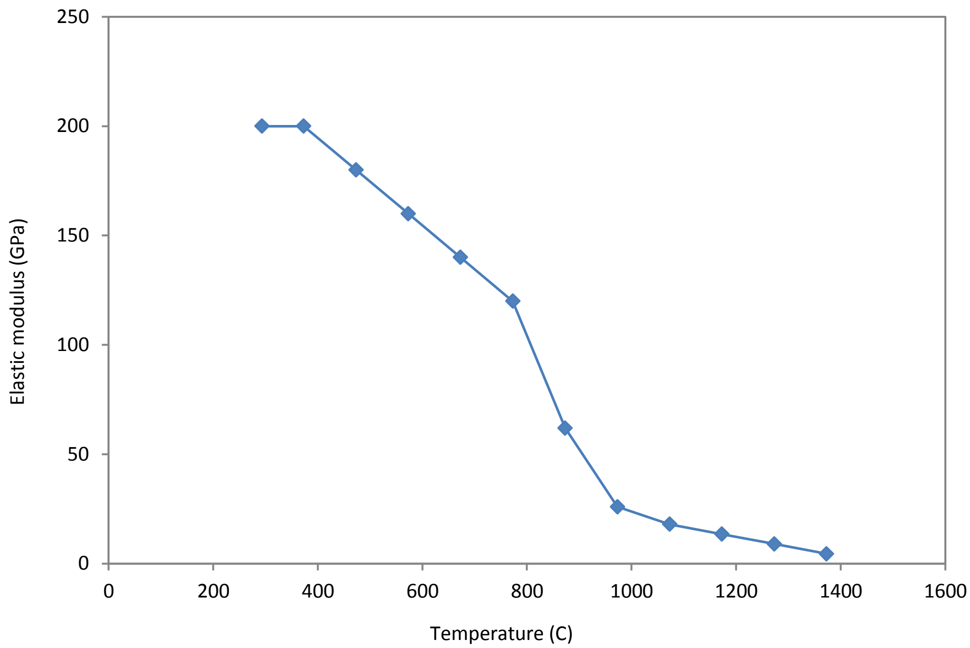

Figure 4.4 Time-dependent modulus of elasticity for structural steel (EC3, 2005)

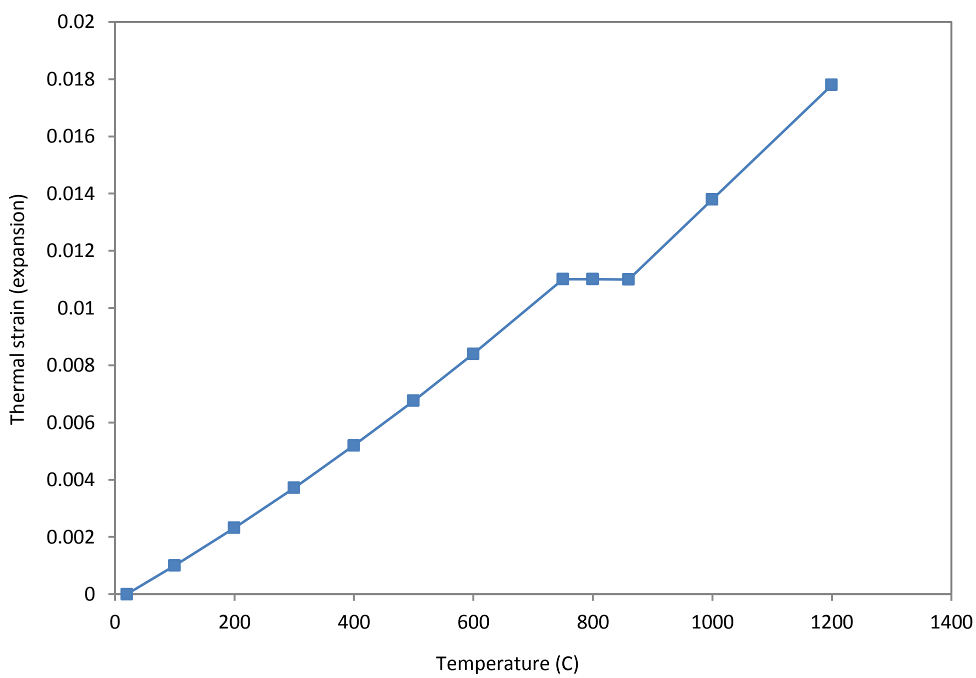

Figure 4.5 Time-dependent thermal strain for structural steel (carbon steel) (EC3, 2005)

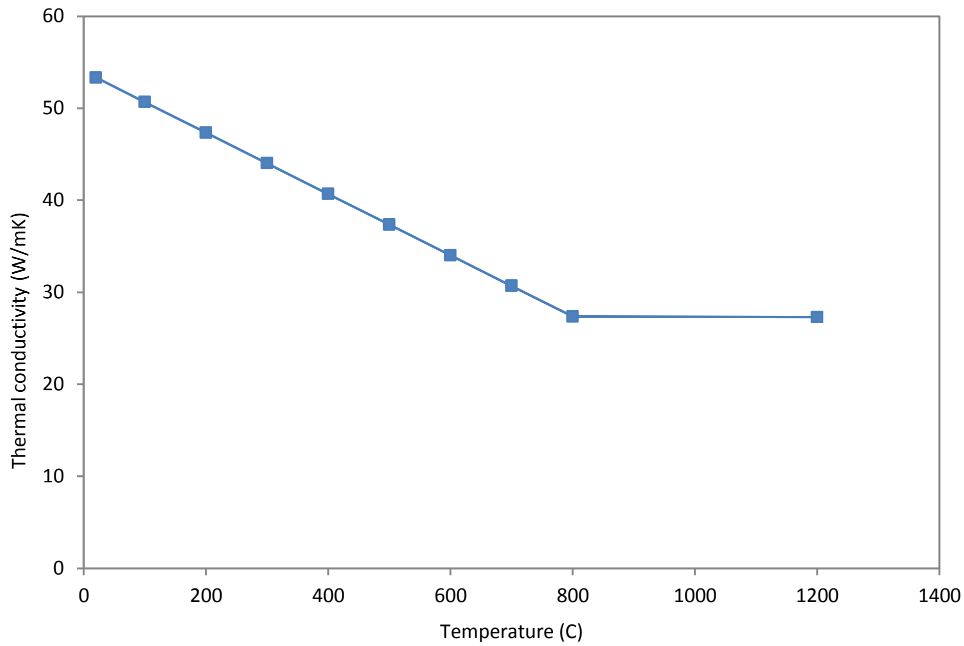

Figure 4.6 Variation of thermal conductivity with temperature for structural steel (carbon steel) (EC3, 2005)

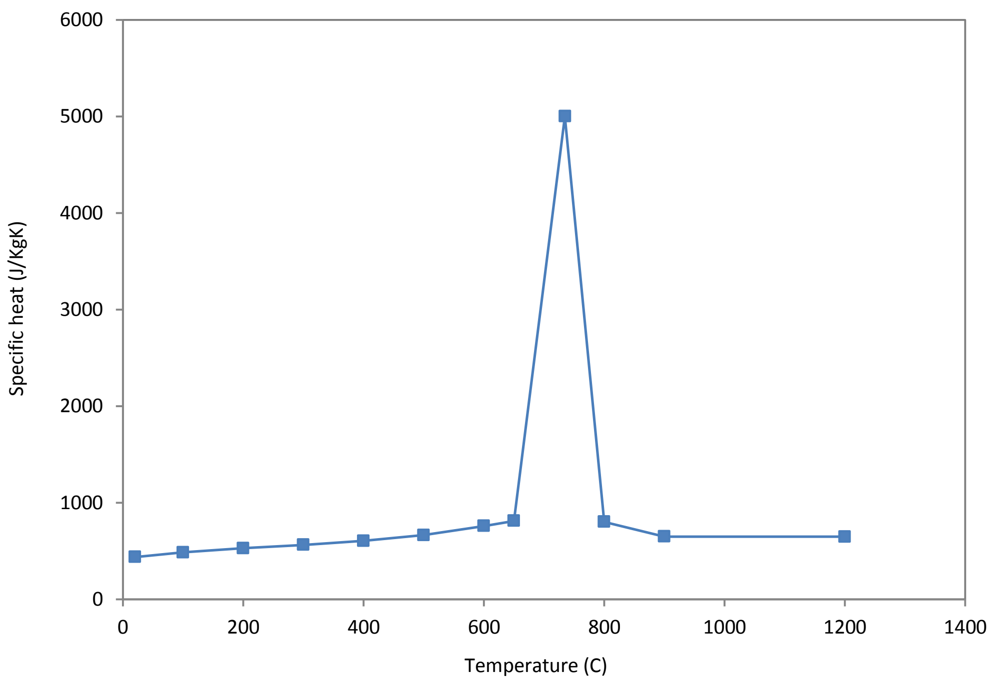

Figure 4.7 Variation of Specific heat with temperature for structural steel (carbon steel) (EC3, 2005)

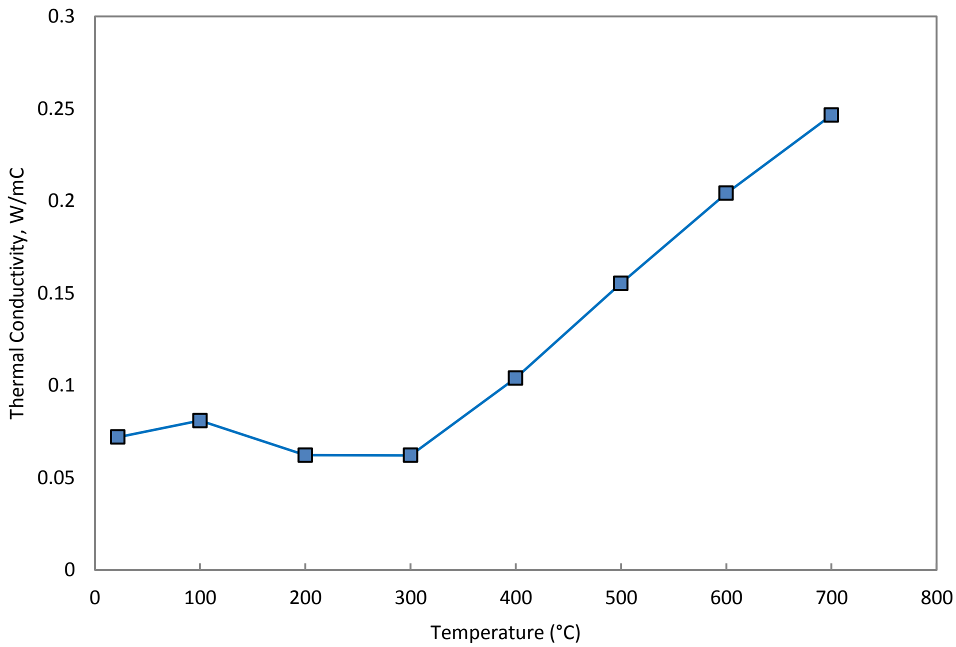

Figure 4.8 Variation of thermal conductivity with temperature for gypsum-based SFRM (Kodur and Shakya, 2013

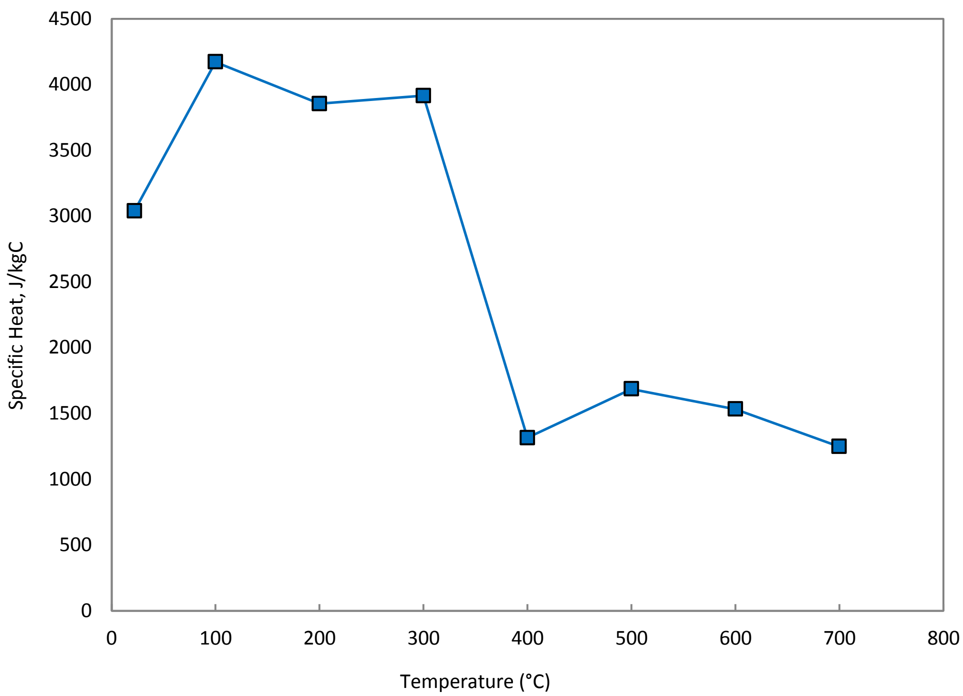

Figure 4.9 Variation of specific heat with temperature for gypsum-based SFRM (Kodur and Shakya, 2013)

As was noted before, three types of SFRM namely, gypsum-based, Portland cement-based and mineral fiber-based SFRM have been studied in this research. The thermal properties of gypsum-based SFRM have been tested by Kodur and Shakya (2013); however, there is no available data on temperature-dependent thermal properties of other types of SFRM. Hence, in this study, post-earthquake and post-blast fire performance of steel structures insulated with gypsum-based SFRM is evaluated using above developed thermal-structural modeling approach. Figure 4.8 and 4.9 show variation of thermal conductivity and specific heat with respect to temperature increase for gypsum-based SFRM, respectively.

4.3.5 Fire Scenario

For evaluating fire response of steel structures during fire following earthquake or blast, the steel structure, be beam-column assembly of beam-column is subjected to temperature evolution prescribed in ASTM E119 (which is similar to ISO 834 standard fire). The following equation expresses the time variation of the fire temperature:

$$T_f = 750\left[1 - e^{-3.79553\sqrt{t_h}}\right] + 170.41\sqrt{t_h} + T_0 \tag{4.54}$$

where, T_0 is room temperature (in ^{o}C) and t_h is time (hours). The above temperature time history is assigned to the additional node associated with element SURF152 as temperature loading in order to model radiation effects, as explained in section 4.3.2.

4.4 Validation of Numerical Model

The above developed numerical models need to be validated before being utilized in extensive parametric studies. Both fracture mechanics-based numerical model and thermal-structural numerical model are validated against series of experiments conducted in this study as well as other studies reported in the literature. This validation process will provide reasonable confidence on further expanding this study to investigate critical factors governing delamination of fire insulation from steel structures and its consequences during fire exposure.

4.4.1 Validation of Fracture Mechanics-Based Numerical Model

The fracture mechanics-based numerical model is validated against material level tests and structural level tests. The selected material tests comprise of direct fracture tests carried out in this study and indirect fracture tests conducted at NIST (Tan et al., 2011). The experiments at structural level, chosen for validation of numerical model, compose of quasi-static tests and dynamic tests. The quasi-static tests include a fire insulated steel plate under tension (Braxtan and Pessiki, 2011a), a fire insulated cantilever column subject to quasi-static loading (Wang et al, 2013) and a beam-column assembly subjected to cyclic monotonic loading representing seismic loading (Braxtan and Pessiki, 2011b). The dynamic experiments consist of drop mass impact tests on insulated beams conducted in this study and blast tests carried out on beam-column by Nassr et al. (2013).

4.4.1.1 Direct Fracture Tests

In the first set of simulations, the fracture tests carried out in this study on three types of SFRM are simulated through above developed fracture mechanics-based finite element model. Steel substrate and SFRM are discretized using 8-noded solid elements available in ANSYS. At the interface of steel and SFRM, surface-to-surface contact is employed such that steel and SFRM surfaces are discretized using 4-noded target and contact elements, respectively. The proposed cohesive laws developed using experimental data (shown in Figure 3.10 and Figure 3.11) are utilized here as steel-SFRM interface constitutive model. The test conditions are represented in the numerical model with as much details and accuracy as possible in terms of boundary conditions and geometrical aspects.

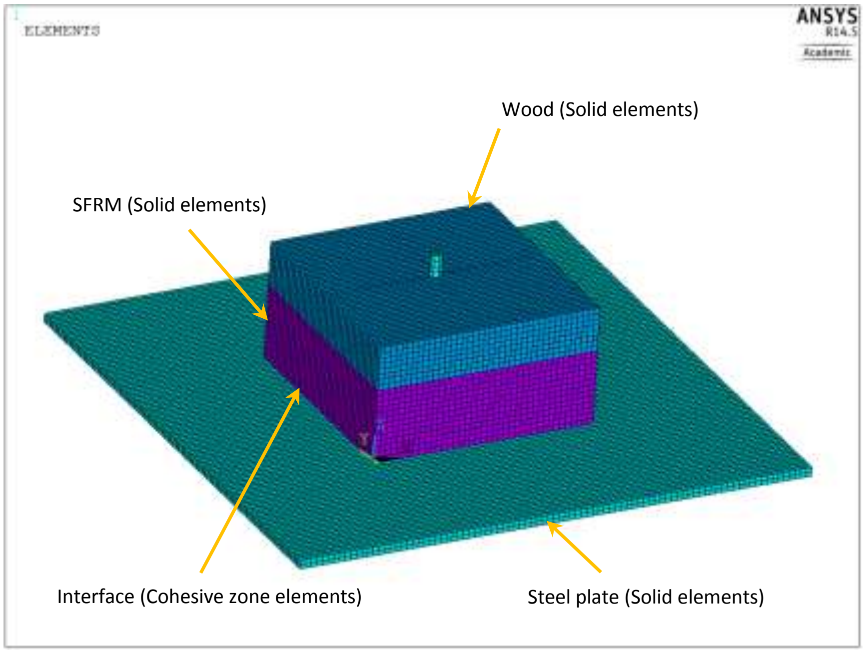

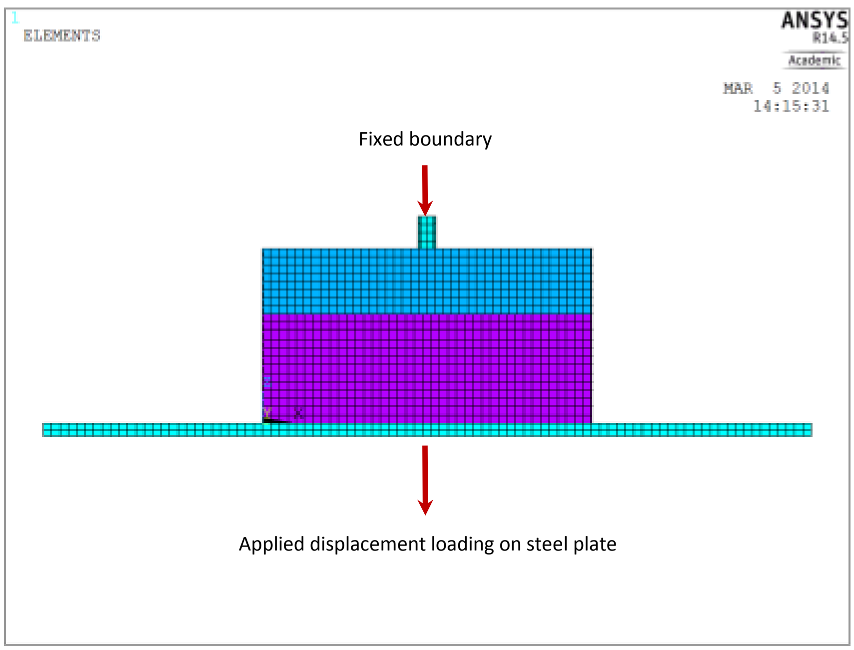

Figure 4.10 Finite element model of SFRM-steel assembly in mode-I fracture experiments

Boundary conditions and loading methods encountered in experiments, which is illustrated in Figure 3.2, are adopted in the numerical modeling. Figure 4.10 and Figure 4.11 depict the finite element model generated to predict fracture modes I and II, respectively, observed in the experiments. The model comprises of the steel plate, SFRM, wooden block and eyebolt. The elastic modulus of SFRM, obtained through compression tests is utilized. The steel plate is assumed to be of Grade A36 (σ_y=245 MPa, E=200 GPa and υ=0.3).

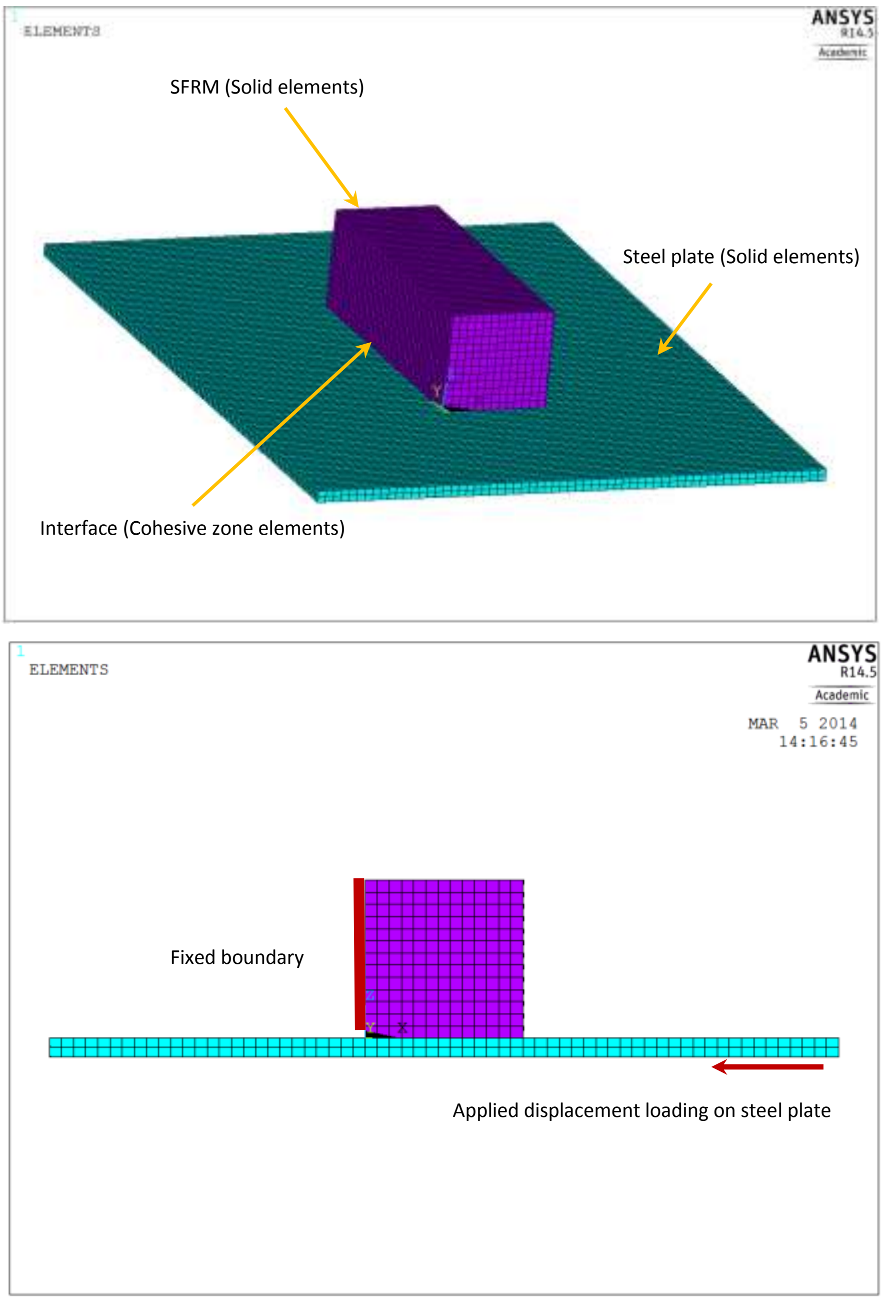

Figure 4.11 Finite element model of SFRM-steel assembly in mode-II fracture experiments

The numerical and experimental results are superimposed in Figure 4.12, Figure 4.13 and Figure 4.14. A quite reasonable agreement can be seen in these figures between numerically predicted force-displacement relationship and the observed experimental behavior. Both cohesive strength and fracture energy are satisfactorily predicted in both modes of fracture. In normal mode, as shown in Figure 4.12a, Figure 4.13a and Figure 4.14a, the predicted initial slope is linear up to cohesive strength and is in close agreement with the experimental curve, while there is discrepancy in softening part of the numerical and experimental curves. This is due to the fact that the input CZM is bilinear and hence the response is expected to be bilinear, whereas, in experiments the response is close to an exponential function.

In shear mode, as shown in Figure 4.12b, Figure 4.13b and Figure 4.14b, the initial response is linear until reaching to cohesive strength where the curve slightly becomes nonlinear. The softening portion of the response is nonlinear as well, and correlates reasonably with the results obtained in the experiments. Despite normal mode, in the shear mode the softening part is not linear even though the input CZM is linear. This is probably due to interaction between normal and tangential modes as a result of a small eccentricity between the applied force and the steel-SFRM interface, which can create some tensile stresses at the steel-SFRM interface. This effect is captured in the numerical simulation as both normal and shear CZM are defined while analyzing the specimen behavior.

Above explained simulation demonstrate that the developed numerical procedure is practically capable of predicting observed fracture mechanisms for both modes of fracture.

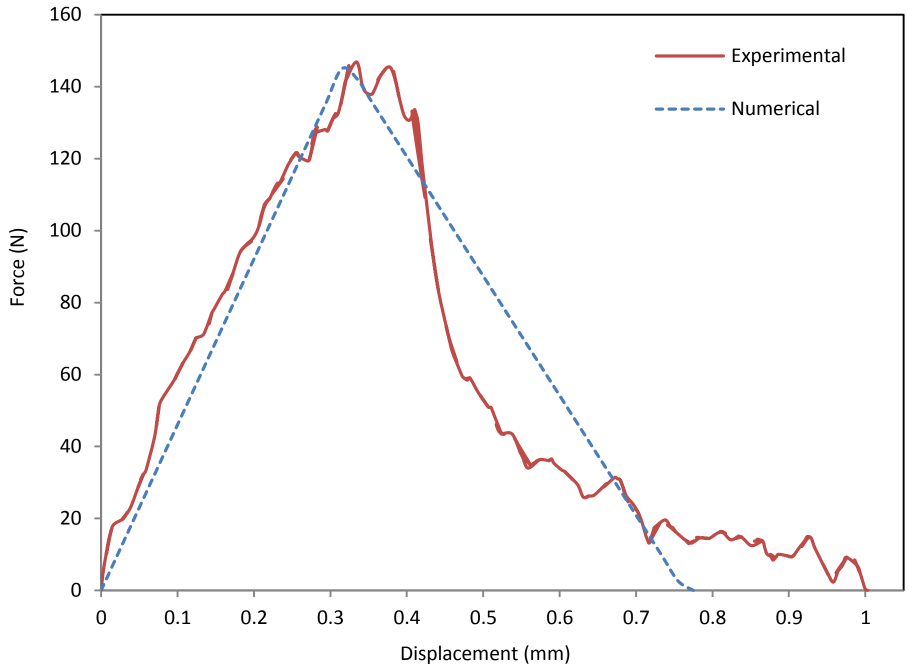

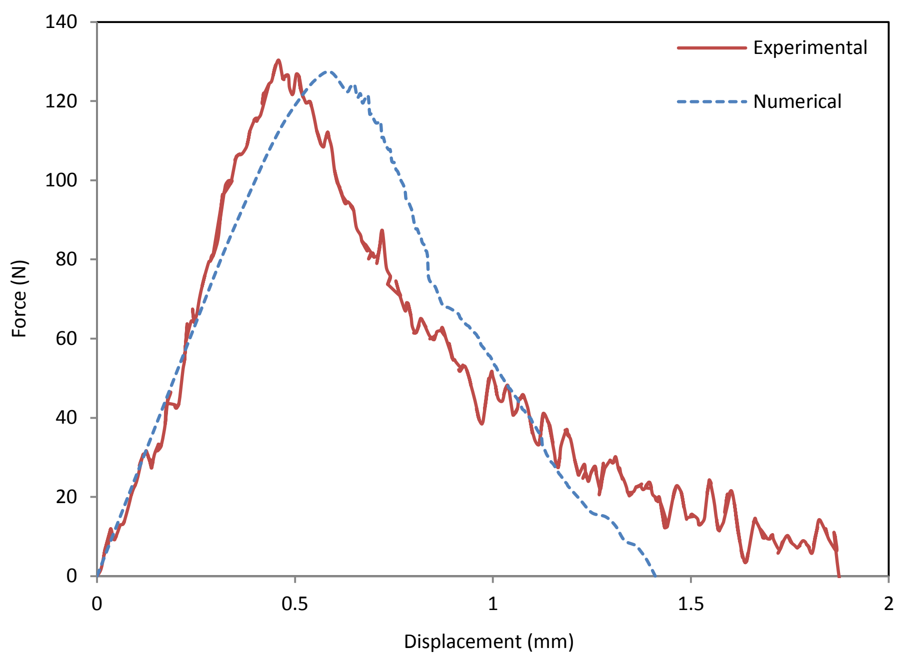

b) Mode-II fracture

Figure 4.12 Comparison of force-displacement relationship predicted from numerical model with measured values from experiments for gypsum-based SFRM

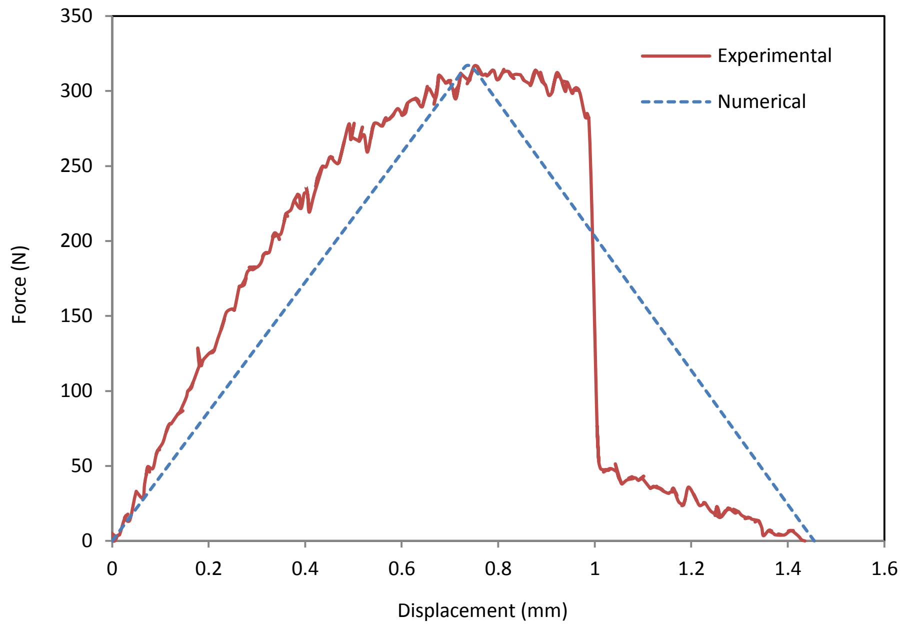

a) Mode-I fracture

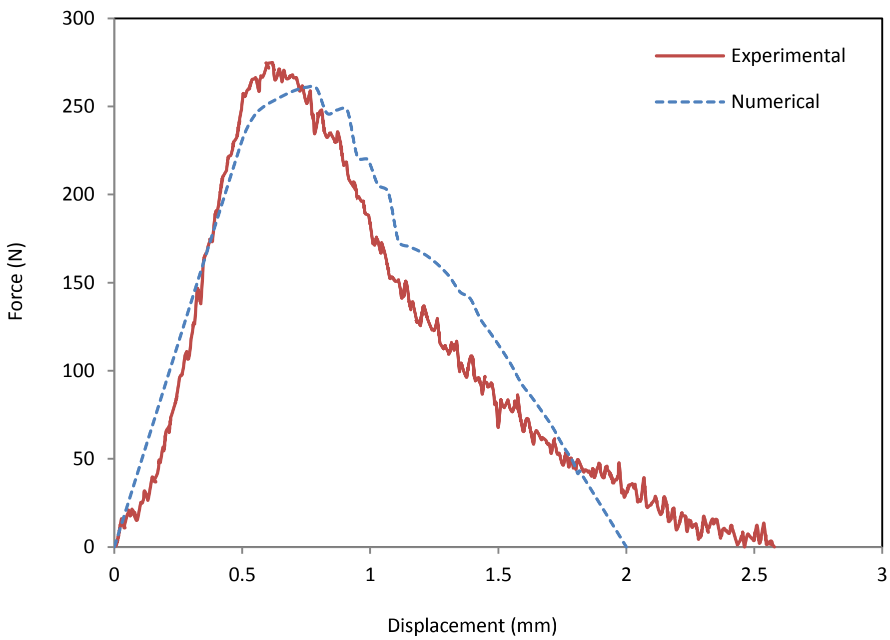

b) Mode-II fracture

Figure 4.13 Comparison of force-displacement relationship predicted from numerical model with measured values from experiments for Portland cement-based SFRM

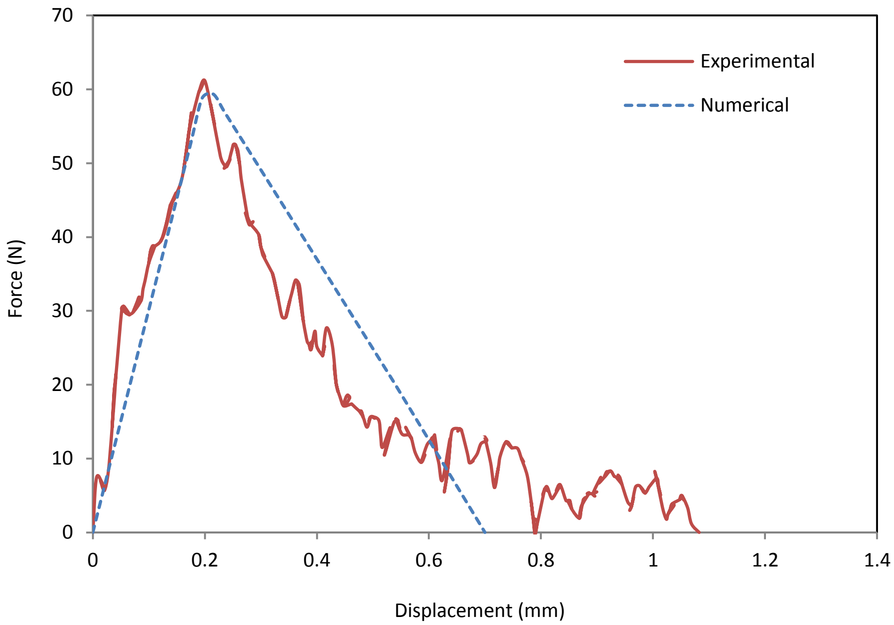

a) Mode-I fracture

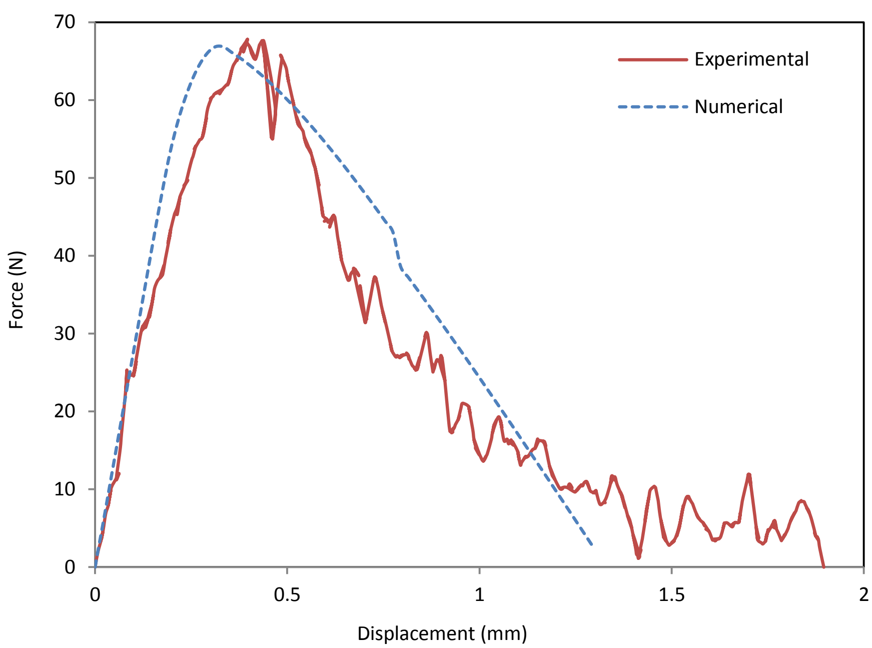

b) Mode-II fracture

Figure 4.14 Comparison of force-displacement relationship predicted from numerical model with measured values from experiments for mineral fiber-based SFRM

4.4.1.2 Indirect Fracture Tests

National Institute of Standards and Technology (NIST) conducted a set of experiments on thin steel plates insulated with thick SFRM. The test set-up used in the experiments is shown in Figure 4.15. In the tests, field conditions were simulated for the application of SFRM on steel. While holding the SFRM in-place, the end of steel coupon was peeled-off with a constant displacement rate of 0.1 mm/s and the corresponding applied load was measured. Series of loading and unloading cycles were simulated to study the relation among fracture energy and initial crack length.

Finite element model of the test set-up is created in ANSYS as shown in Figure 4.16. The steel substrate and SFRM are discretized using 4-noded shell elements and 8-noded solid elements, respectively. The contact elements with cohesive zone behavior are inserted at the interface of steel and SFRM. Results from the analyses are compared against test data in Figure 4.17 where predicted and measured load-displacement curves are plotted. Results presented in Figure 4.17 were obtained for critical fracture energy (G_c) of 6 J/m^{2}and cohesive strength of 20kPa. As is shown in this figure, the loading phase up to maximum load is predicted satisfactorily. Complexities in real crack propagation pattern in SFRM are very hard to be captured with numerical model. Hence, the discrepancy in softening phase can be attributed to approximations used in the analyses. Nonetheless, proposed numerical approach is capable of predicting the maximum load as well as the subsequent stable crack growth behavior, which was confirmed by optical observations in experiments (Tan et al. 2011), in a fairly acceptable manner.

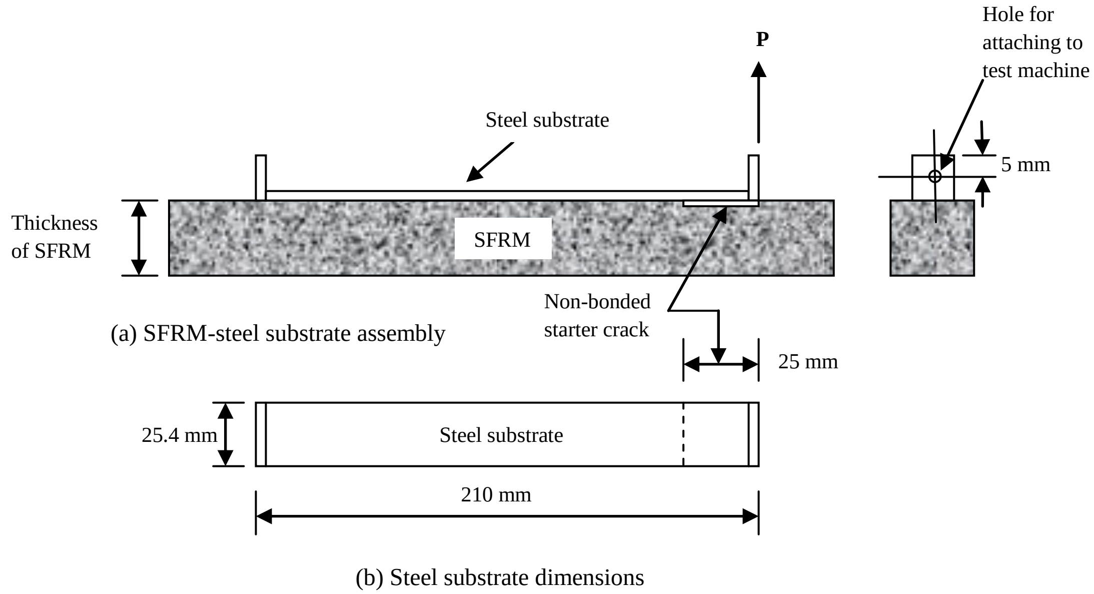

Figure 4.15 Experimental setup for fracture tests carried out by NIST to measure fracture energy of SFRM

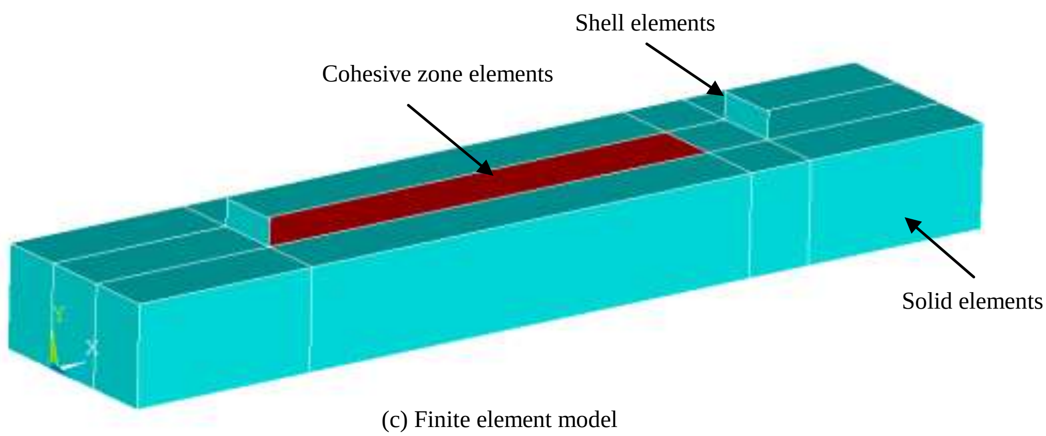

Figure 4.16 Finite element model for fracture test conducted by NIST

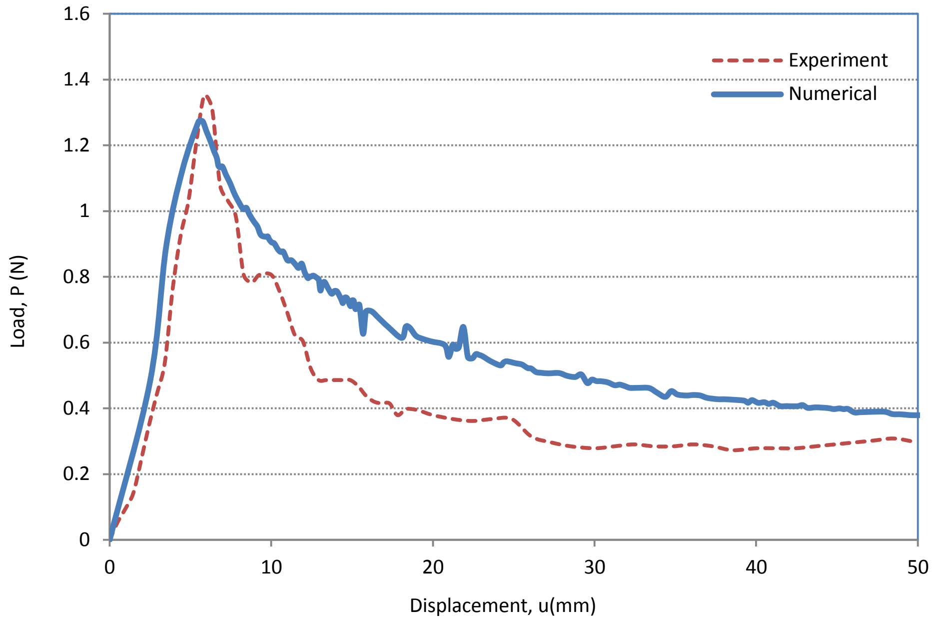

(a) Force-displacement relation

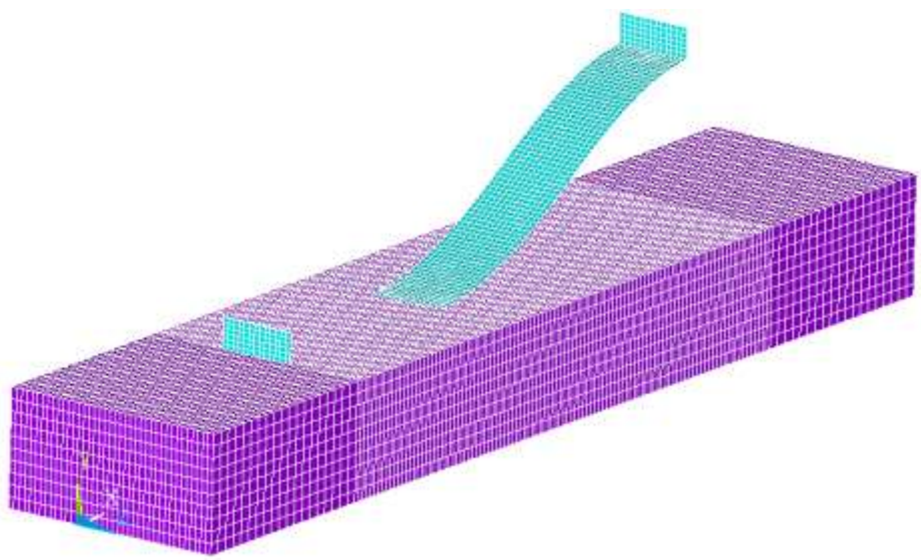

(b) Predicted deformation of steel-SFRM

Figure 4.17 Measured and predicted force-displacement response at the steel-insulation interface for material level tests conducted at NIST

4.4.1.3 Steel plate-SFRM Assembly under Tension

In the second set of simulations, a delamination test reported by Braxtan and Pessiki (2011a) on an insulated steel plate is modeled. Figure 4.18 depicts the test plate setup and the associated geometry. The test plate measured 1100 mm long × 152 mm wide × 6 mm thick and was covered with mineral fiber-based SFRM at the central 457 mm of one face of plates. A distance of 305 mm was then left bare on each end enabling specimen to fit in universal testing machine's upper and lower jaws. Strain gauges were attached to steel plate to measure the strain level during tensile tests. The plate was loaded through displacement control at a loading rate of 1.27 mm/min.

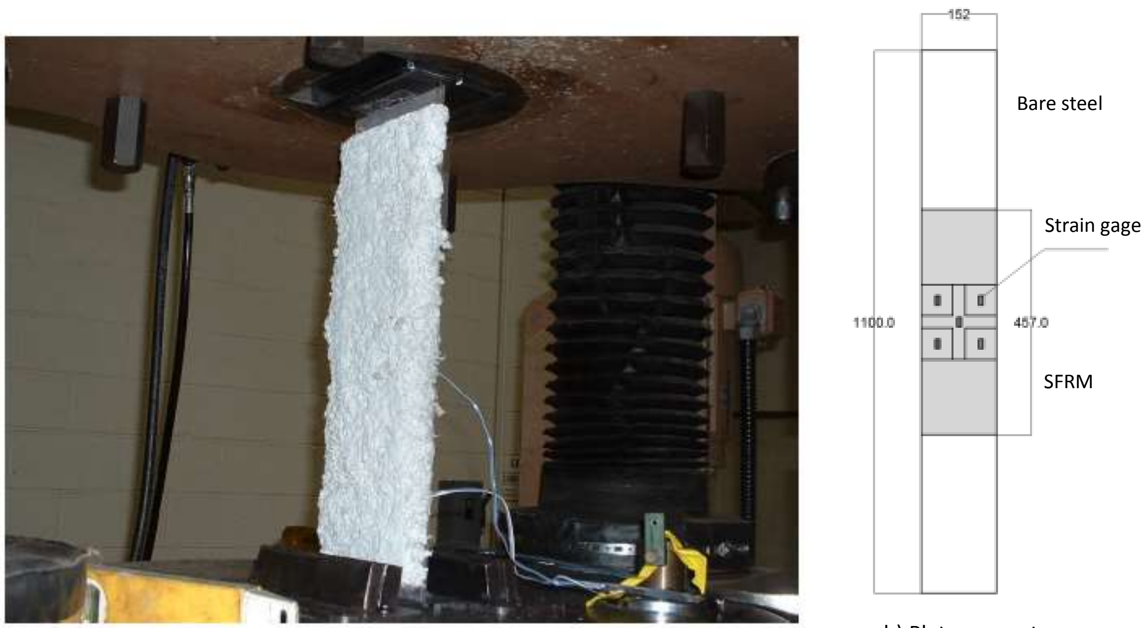

a) Plate test setup

b) Plate geometry
(dimensions are in mm)

Figure 4.18 Experimental setup for plate covered with mineral fiber-based SFRM (Braxtan and Pessiki, 2011a)

The finite element model of plate-SFRM assembly is illustrated in Figure 4.19. The steel plate is discretized using 4-noded shell elements and SFRM is discretized using 8-noded solid elements. SFRM-interface behavior is simulated through contact interaction elements by implementing the CZM as material constitutive model. Mesh sensitivity analysis was carried out to find the optimum mesh size. While incrementally reducing the mesh size from 20mm to 10mm, it was found that, there is negligible improvement from mesh size of 12 mm to 10 mm. The average cohesive properties of mineral fiber-based SFRM derived in this study were used to model bulk SFRM and SFRM-steel interface behavior. The grade of steel used in this plate is A36 (σ_y=325 MPa, E=200 GPa and υ=0.3).

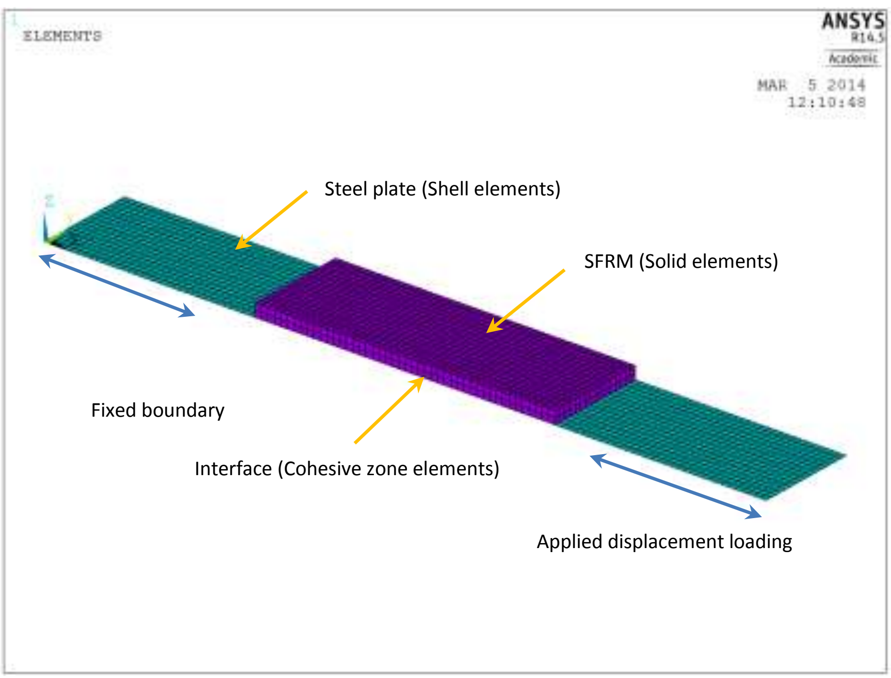

Figure 4.19 Finite element model for plate covered with mineral fiber-based SFRM

The predicted delamination progression on steel plate covered with mineral fiber-based SFRM is shown in Figure 4.20 and compared to the one obtained from experiment. The delamination length at the end of steel plate is predicted to be 134 mm at strain level of $11.8\varepsilon_y$, while the measured fracture extent is 127 mm in experiments at strain level of $10.4\varepsilon_y$. Given the fact that average values of fracture properties were used for SFRM in numerical model, which may not be exactly identical to the SFRM properties in the experiment, the correlation between predicted and measured extent of fracture is fairly satisfactory. This clearly shows the applicability of cohesive zone models proposed in this study for modeling progressive delamination of SFRM from steel structure where mixed-mode delamination governs failure.

a) Test results (Braxtan and Pessiki, 2011a)

Figure 4.20 Delamination length predicted and measured on a plate covered with mineral fiber-based SFRM

Figure 4.20 (cont'd)

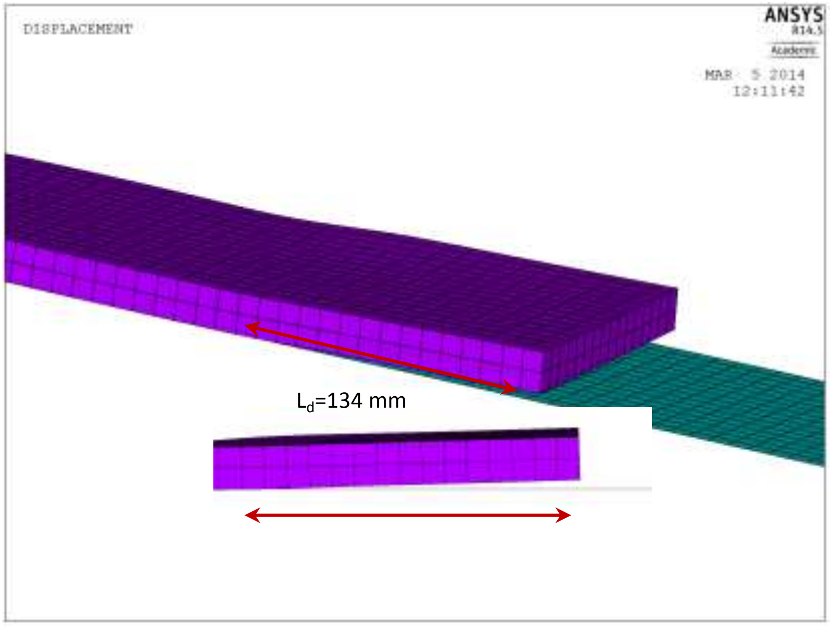

b) Simulation results

4.4.1.4 Cantilever Column Subjected Quasi-Static Loading

The second validation at the structural level consisted of comparing predicted and measured force-displacement response on an insulated column tested by Wang et al. (2013). The selected insulated column is 2 m in length and is made of H cross section of 300X300X10X15 (mm). The column was provided with fire insulation of type YC-3 with thickness of 25 mm. This type of SFRM is comprised of vermiculite, granite and cohesive material. Material properties provided in Wang et al. (2013) were used in numerical model. Figure 4.21 shows the test setup and column dimensions. For the finite element analysis, this tested column was discretized as illustrated in Figure 4.22. In the test, it was reported by Wang et al. (2013) that, horizontal shrinkage cracks developed at approximately 400 mm intervals along the column before loading started. Therefore, while distributing contact element locations within SFRM, it was ensured that contact condition is placed at these locations because of high susceptibility of insulation to fracture.

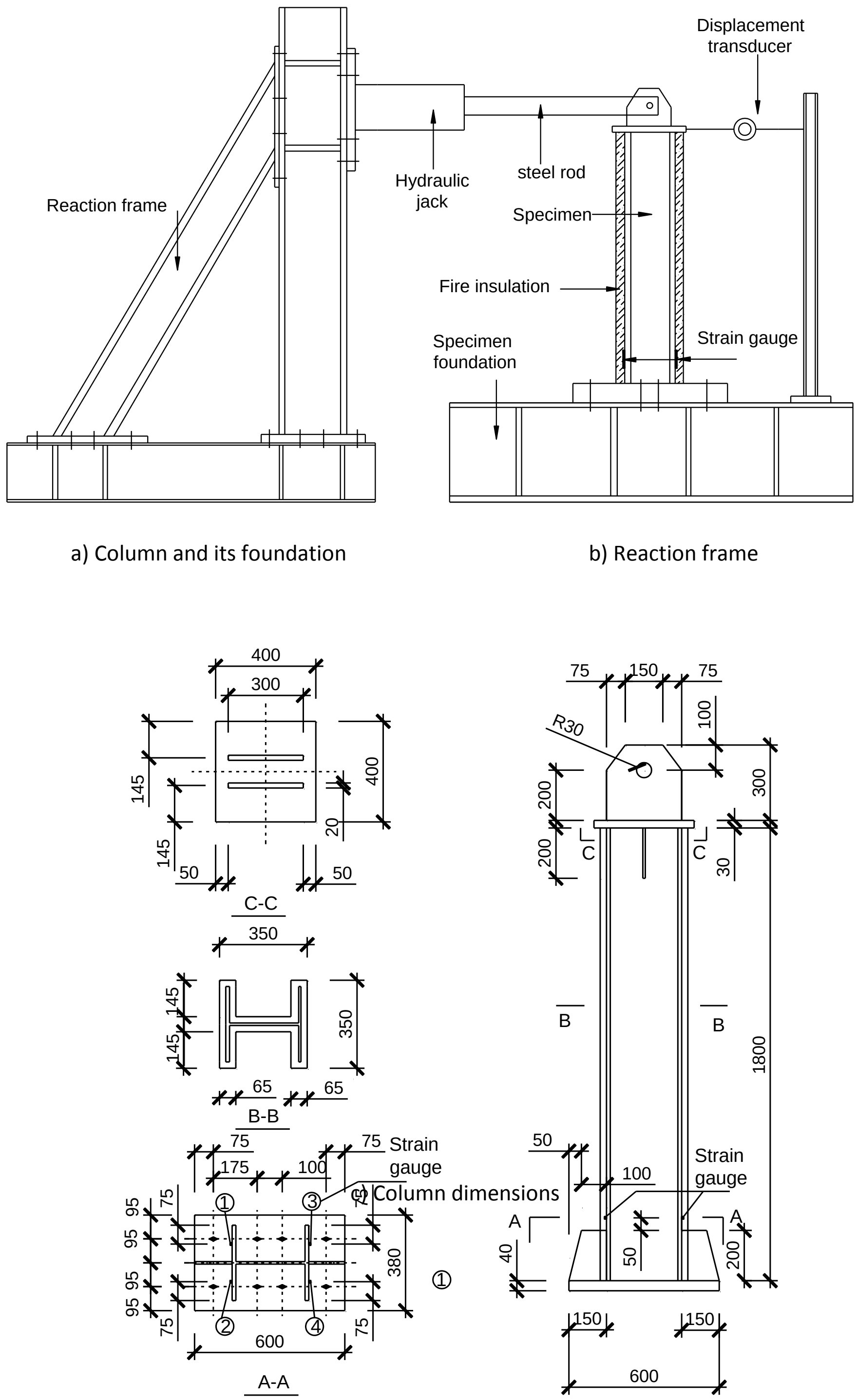

Figure 4.21 Experimental set-up for quasi-static loading of a cantilever column insulated with SFRM (Wang et al., 2013)

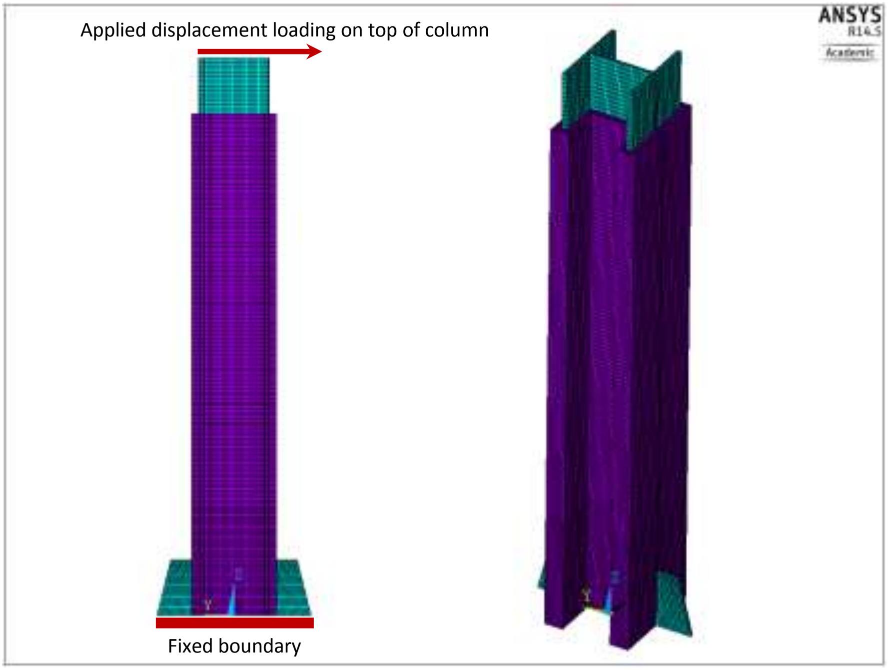

a) Finite element model and boundary conditions

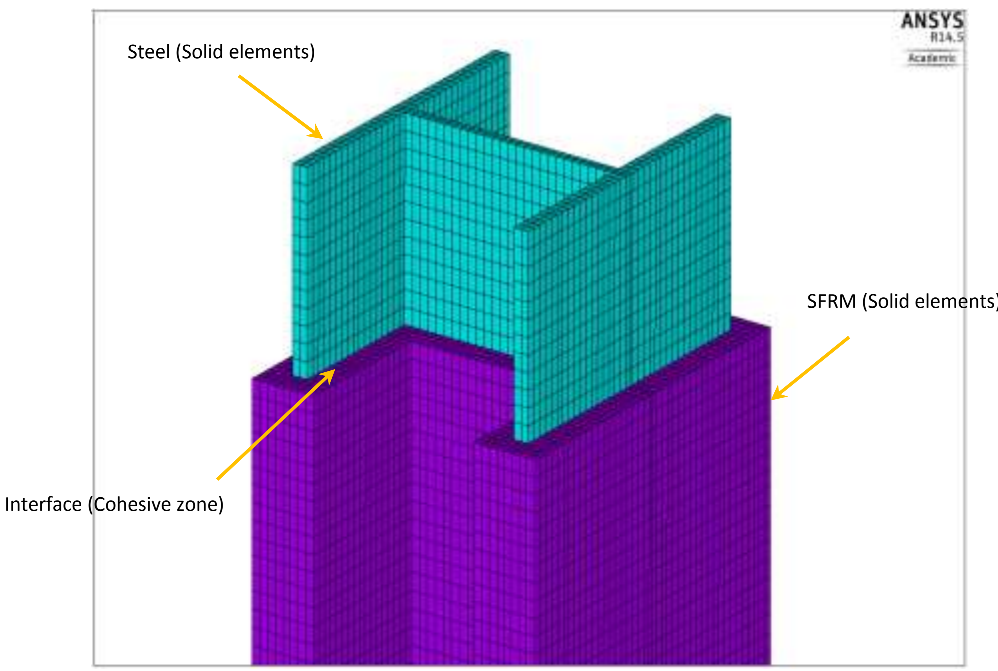

b) Closed view of finite element model

Figure 4.22 Finite element model for quasi-static loading of a cantilever column insulated with SFRM

The predicted load-displacement response of fire insulated column is compared with measured data in Figure 4.23. The displacement was measured at the top of the column. Though, the actual stress-strain curve is not reported by Wang et al. (2013), measured load-displacement curve entails hyperbolic shape for hardening portion of stress-strain curve. Hence, hyperbolic shape of hardening was assumed after yield point up to ultimate strength. As can be seen in this figure, the predicted and measured displacements are well-correlated.

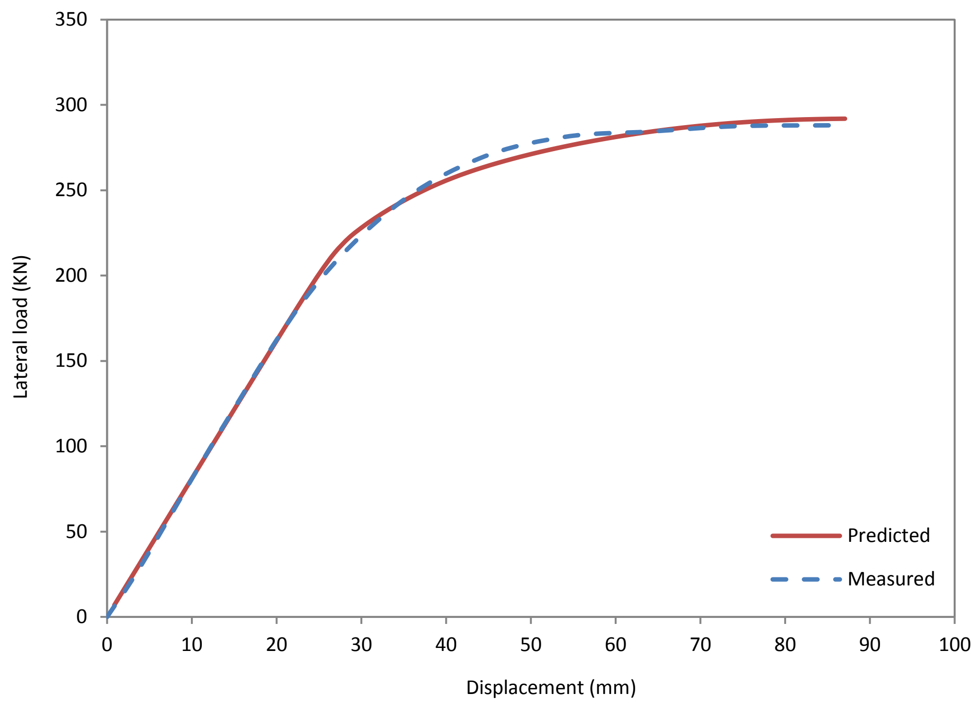

Figure 4.23 Load-displacement response of the insulated steel column tested by Wang et al. (2013)

The progression of fracture and delamination of SFRM from steel column surface is illustrated in Figure 4.24, where internal fracture can be seen at the flange tip, as well as delamination at SFRM-steel interface. The predicted delamination in the analysis, albeit not perfect, is analogous to the observations recorded in experiments. The shrinkage cracks at the tensile flange gets widened with increasing load level whereas the cracks get closed at compressive flange where two interacting surfaces penetrate into each other. Therefore, internal fracture starts from initial shrinkage cracks, and simultaneously, delamination initiates at the bottom of column and propagates upward. The longitudinal fracture of insulation at the flange tip is more noticeable in compressive flange; on the contrary, the flange tip insulation is completely debonded in tensile flange. This is because the compressive flange endures local buckling resulting in different strain levels at two sides of the flange. This debonded insulation is susceptible to fall-off under gravity loading or owing to any vibrations experienced by the column. In spite of substantial fracture and delamination of insulation in flanges, no damage of insulation occurs in the web. This phenomenon was also observed by Wang et al. (2013) in the experiments.

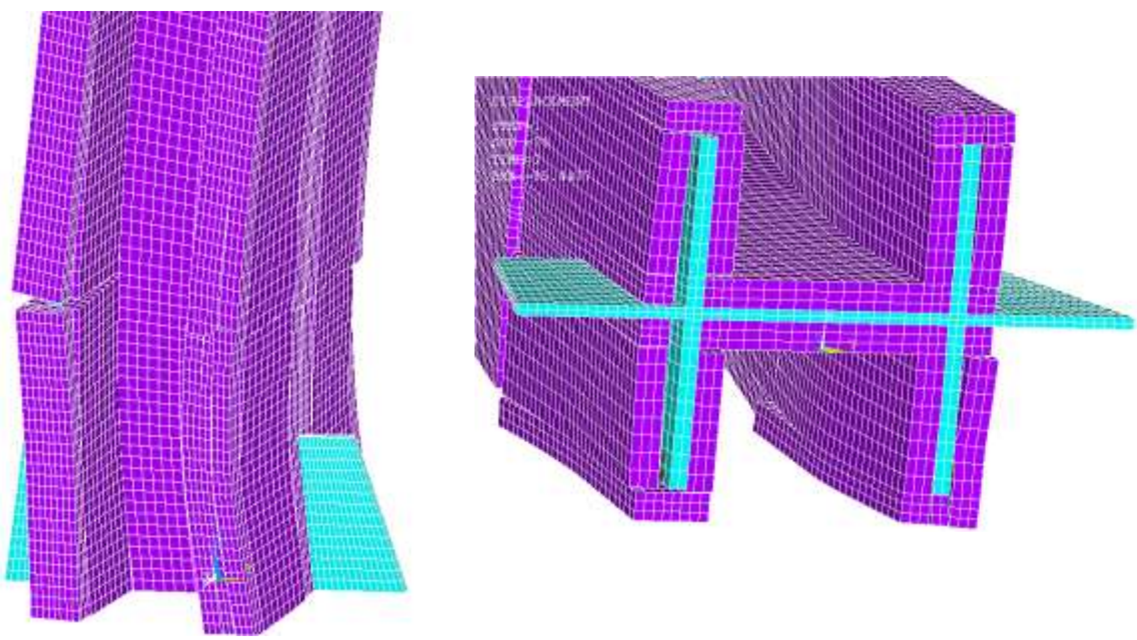

a) Predicted delamination in finite element analysis

Figure 4.24 Delamination and fracture of SFRM from steel column at high levels of static load

Figure 4.24 (cont'd)

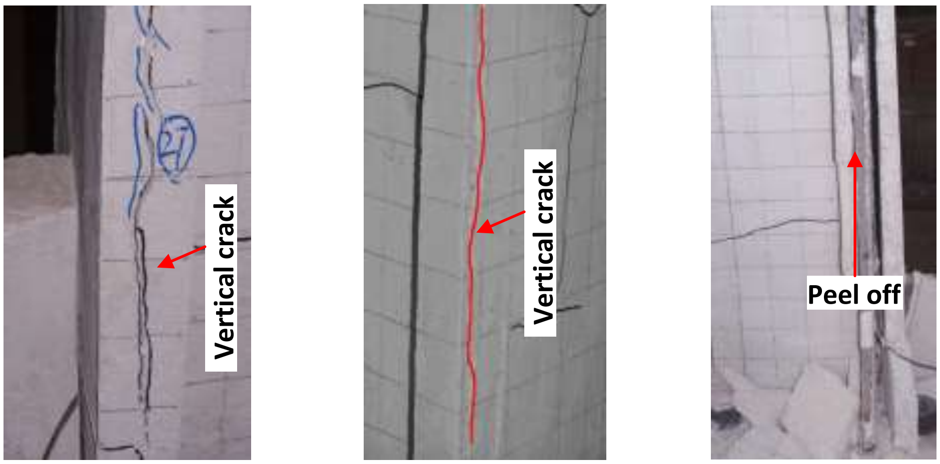

b) Observed delamination and cracks in experiments

4.4.1.5 Beam-Column Assembly Subjected to Seismic Loading

The third validation at the structural level consists of comparing predicted and measured force-displacement response, as well as extent of SFRM delamination over an insulated beam-column assembly, tested by Braxtan and Pessiki (2011b). Figure 4.25 illustrates the overall geometry and member sizes for the beam-column assembly connection. In moment resistant steel frames subjected to lateral forces, inflection points form at the mid-height of the columns and at the mid-span of the beams, as depicted in Figure 4.25a. An exterior beam-column assembly was tested by Braxtan and Pessiki (2011b) and inflection points were simulated through attaching the column to a reaction wall by pin supports. The column was a W12 x 120 section and the beam was a W24 x 55 section. Both sections were made of A992 Grade 50 steel. A vertical load was applied at the beam tip. Lateral torsional buckling in beam was prevented by providing enough lateral supports. This beam-column assembly was subjected to the cyclic displacement-controlled loading protocol as per FEMA 461 procedure (2007).

Performance of gypsum-based SFRM and mineral fiber-based SFRM were evaluated in these tests. The SFRM was applied in the connection region. The SFRM was applied on the beam up to approximately 1 m from the face of the column. The SFRM was applied on the column approximately 0.6 m above and below the top and bottom flange of the beam, respectively. For analyses, the material properties of SFRM are chosen based the adhesion testes carried out by Braxtan and Pessiki (2011a). Table 3.2 (as presented in Chapter 3) lists the material properties used in the numerical model for structural level verification.

Finite element model for tested assembly is illustrated in Figure 4.26 where the element types, the boundary conditions and loading condition are shown in the figure. The SFRM applied on the column is omitted in numerical model since column is intended to remain elastic due to strong column-weak beam response of the assembly during the course of loading. Further, results of experiments reported no delamination in SFRM applied on the column. Therefore, tremendous amount of computation time is saved by excluding SFRM on the column. Lateral supports are provided at the beam tip and mid-span through applying fixities on lateral directions. Cyclic displacement load, shown in Figure 4.27, is applied on the beam tip and reaction forces at the pin connections are extracted to plot the load versus drift response of the assembly.

The predicted load-drift response of the beam-column assembly is compared with measured data for assembly insulated with gypsum-based SFRM in Figure 4.28. An examination of stress distribution at the beam-column assembly shows that plastic hinge forms in the beam close to the column face. Reduction in load level, both at drift level of $\pm 3.91\%$, can be attributed to destabilizing effects resulting from local buckling in flanges and web. Numerical results, albeit not perfect, correlates with the observations recorded in experiments reasonably well.

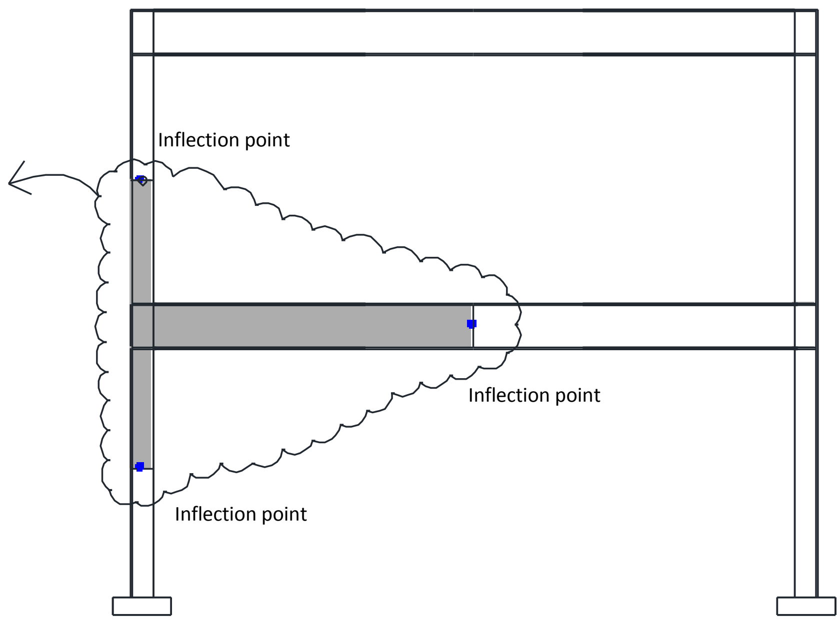

a) Steel moment frame

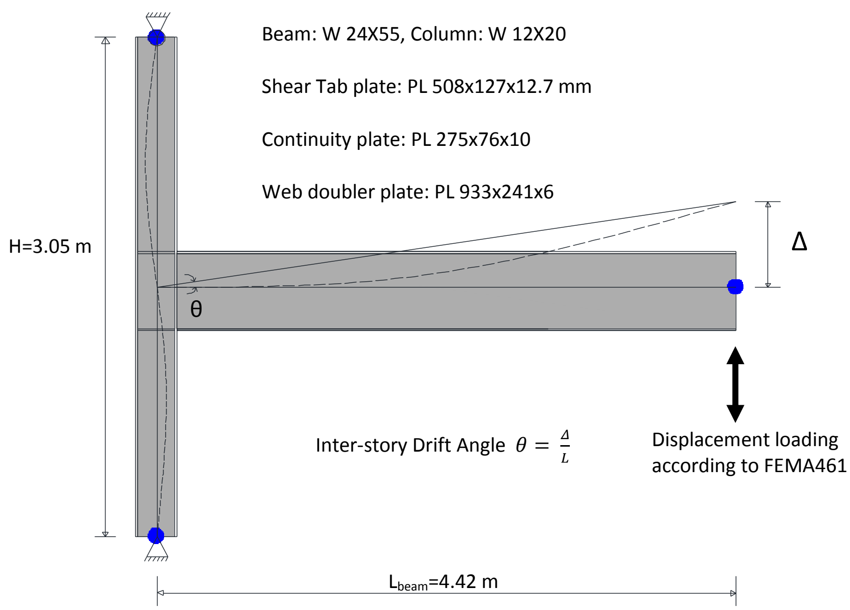

b) Exterior beam-column assembly

Figure 4.25 Test setup of an exterior moment frame assembly to measure delamination of SFRM (Braxtan and Pessiki (2011b)

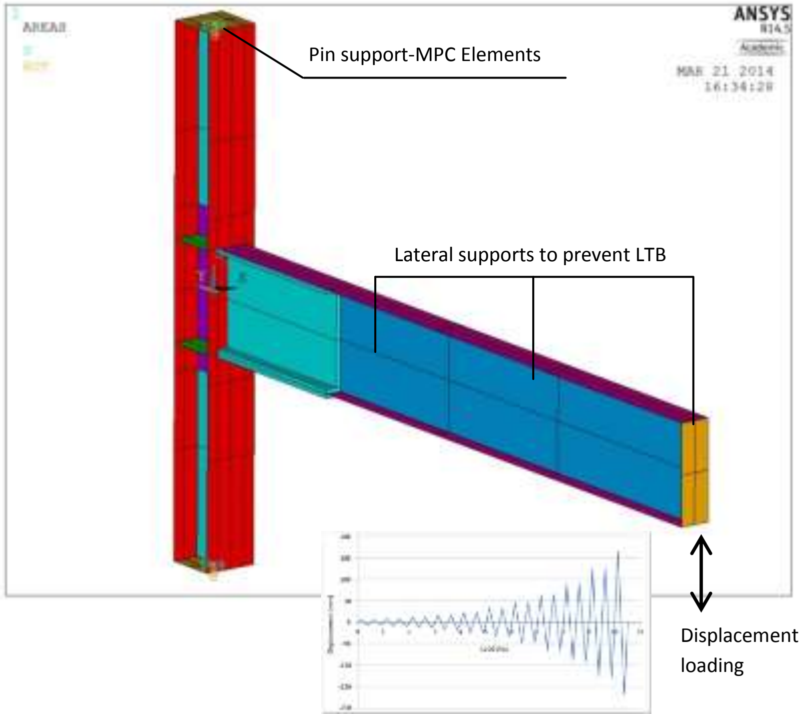

a) Loading and boundary condition

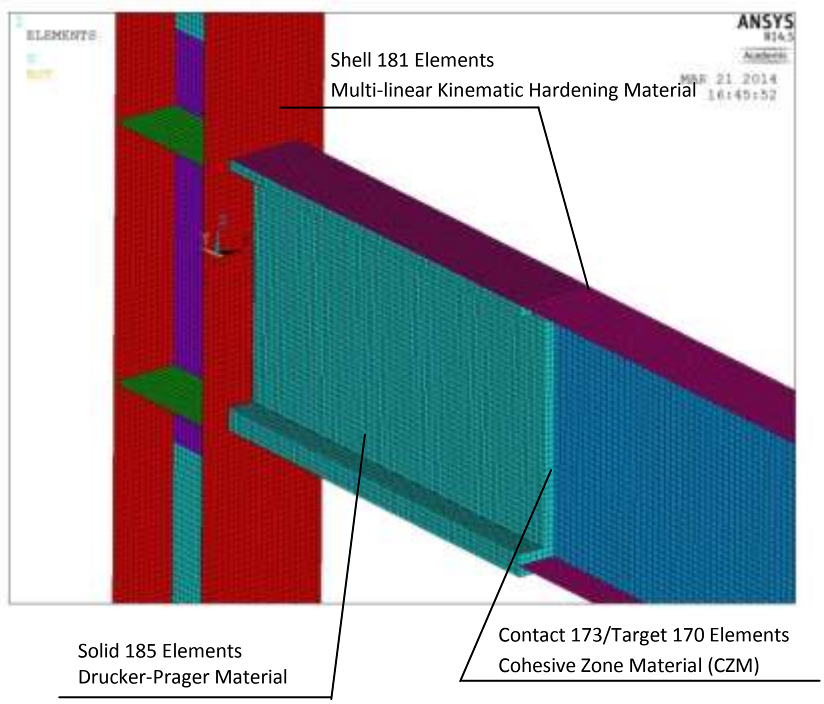

b) Element types and material

Figure 4.26 Finite element model of beam-column assembly tested by Braxtan and Pessiki (2011b)

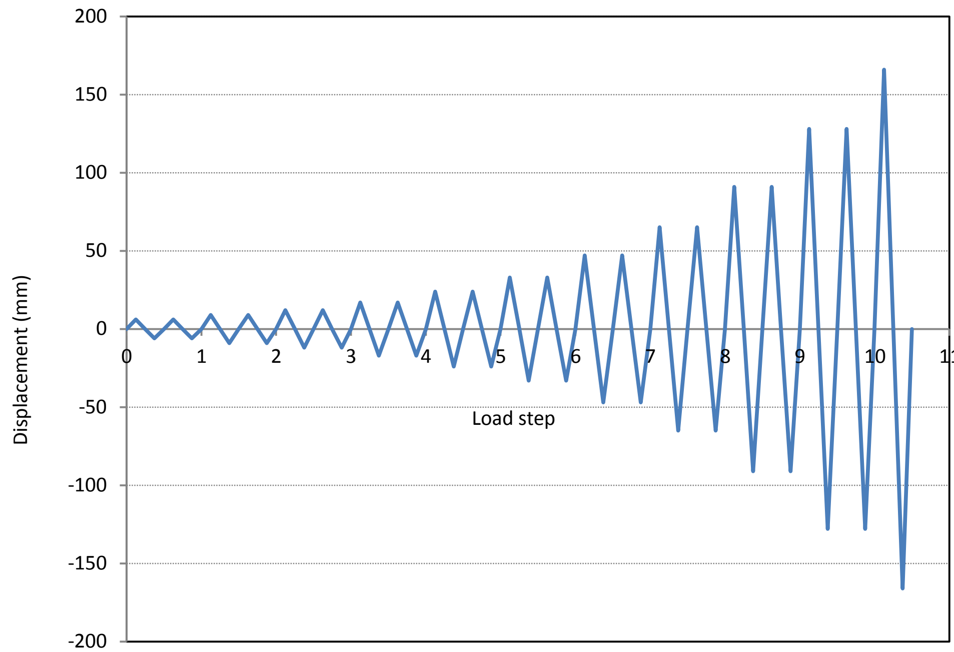

Figure 4.27 Cyclic displacements applied at beam tip for validation of SFRM delamination

The progression of fracture and delamination of SFRM from bottom flange surface in beam-column assembly insulated with gypsum-based SFRM and mineral fiber-based SFRM is illustrated in Figure 4.29 and Figure 4.30, respectively. Note that, assembly insulated with mineral fiber-based SFRM is loaded up to two cycles at $\pm$3.0% story drift, while assembly insulated with gypsum-based SFRM is loaded up to one cycle at 3.91% story drift. According to numerical results, in the case of assembly insulated with gypsum-based SFRM, delamination progresses up to 483 mm from the face of column compared to 381 mm observed in experiment. In the case of assembly insulated with mineral fiber-based SFRM, delamination extends up to 576 mm from the face of column, while in experiments delamination length is 457 mm. However, in this case, 102 mm of SFRM was left in place in experiments. This may be because of cohesive resistance of the SFRM at the intersection of beam and column which keeps a small portion of beam SFRM in place. Further, SFRM staying in place does not guarantee that bonding has not been deteriorated. This part might have delaminated, however is held in place by the column SFRM. The predicted delamination in the analysis, even though not ideal, is analogous to the observations recorded in the experiments.

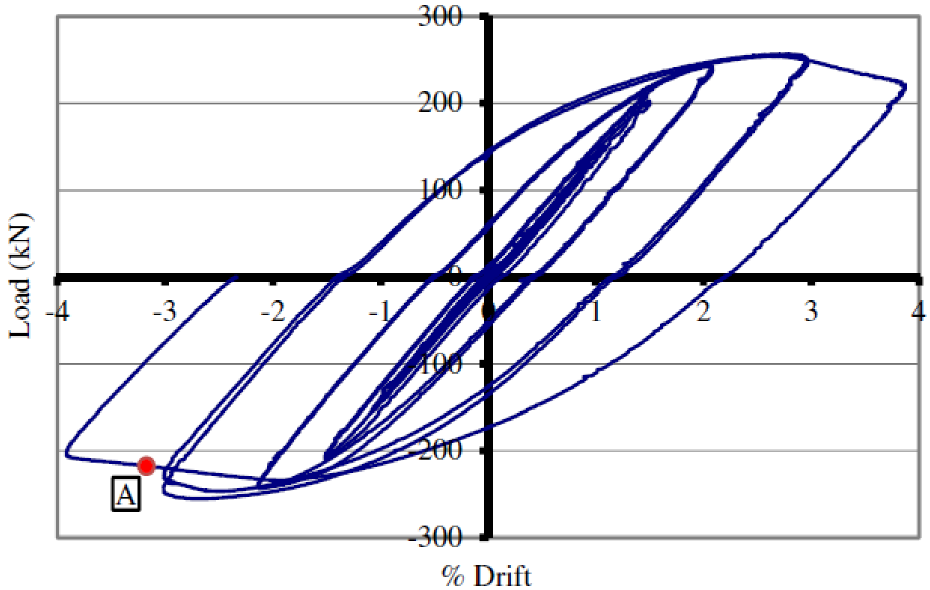

a) Measured

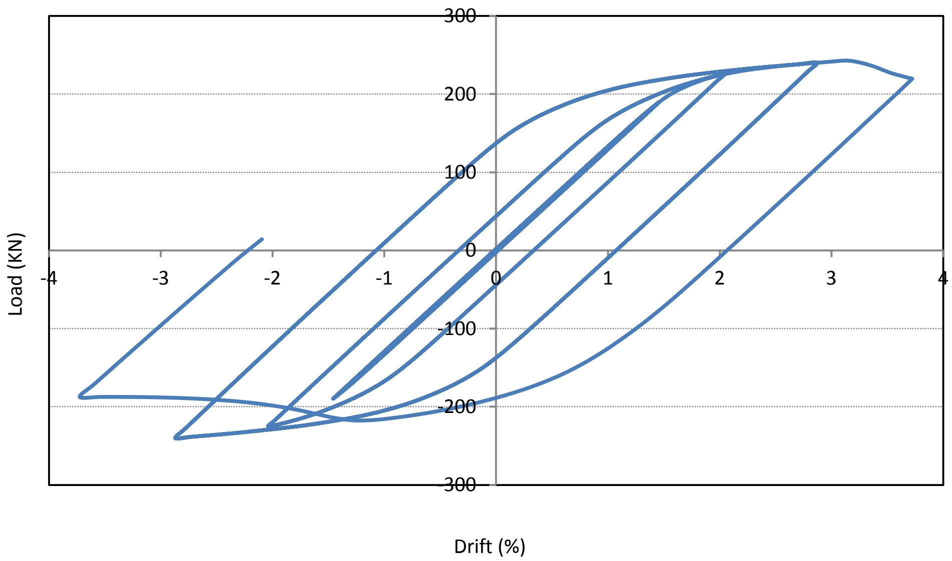

b) Predicted

Figure 4.28 Comparison of predicted and measured load versus percent drift in insulated beam-column assembly

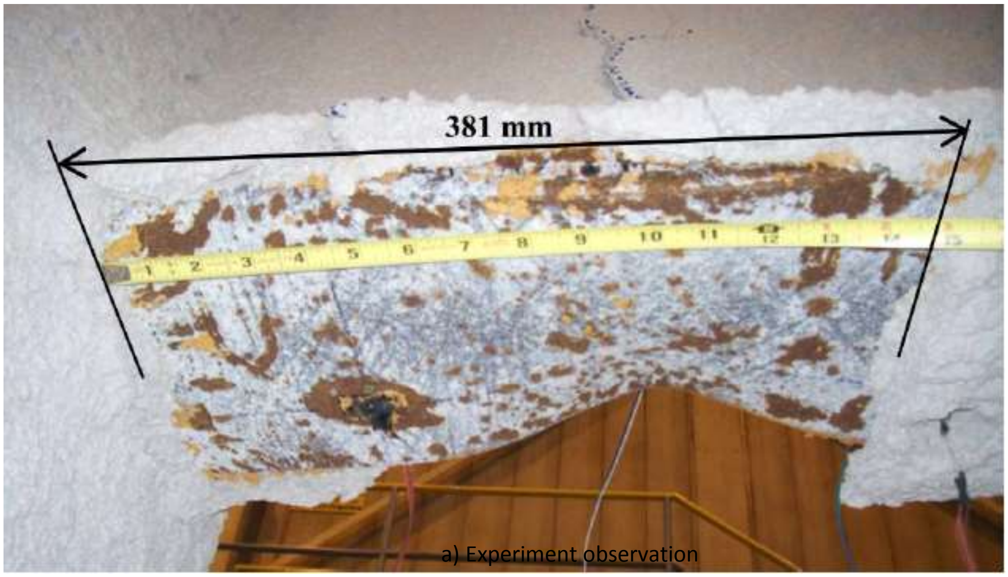

a) Experiment observation

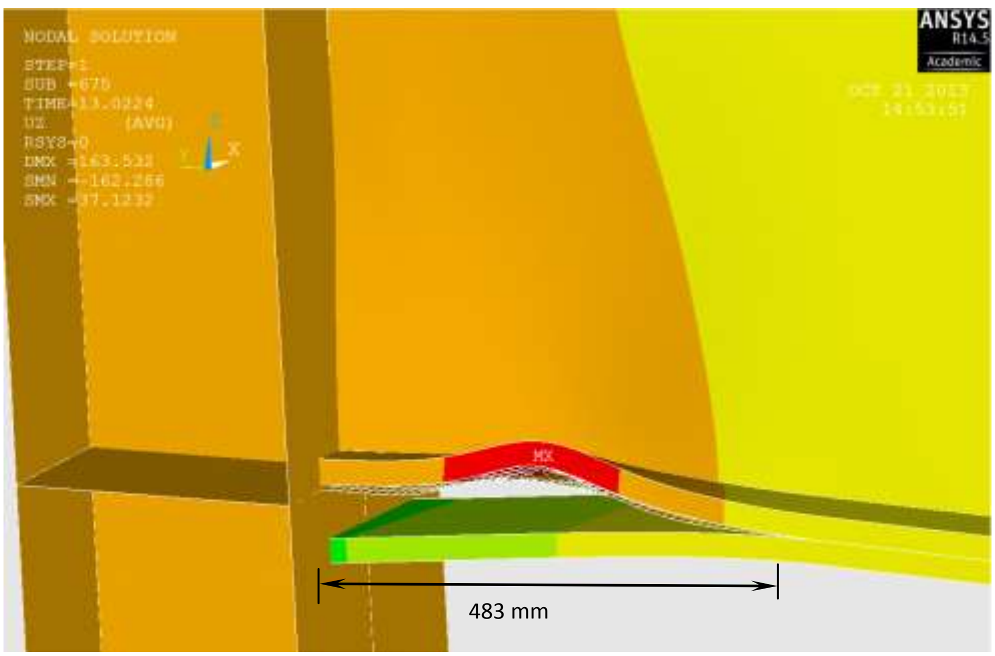

b) Numerical simulation

Figure 4.29 Comparison of predicted and measured extent of delamination in beam-column assembly insulated with gypsum-based SFRM

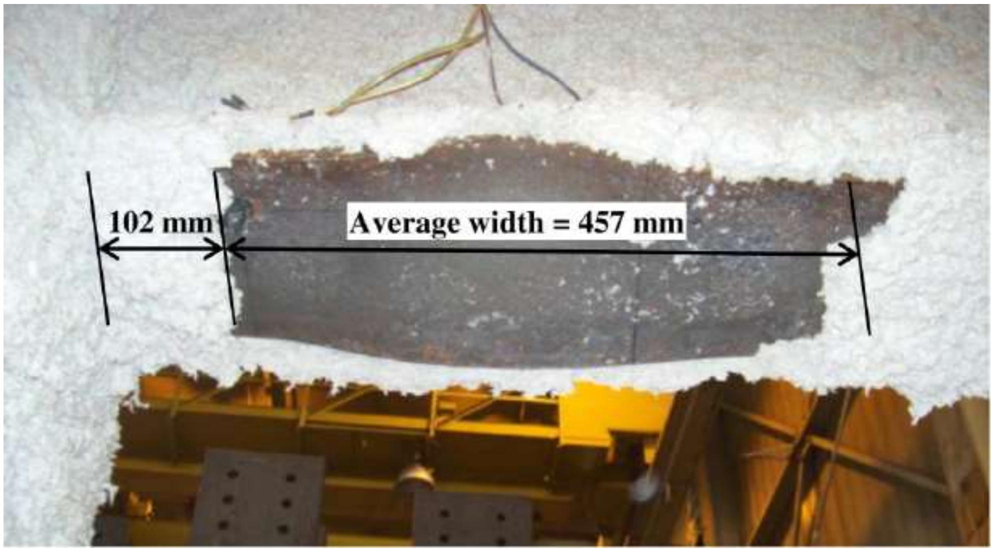

a) Experiment observation

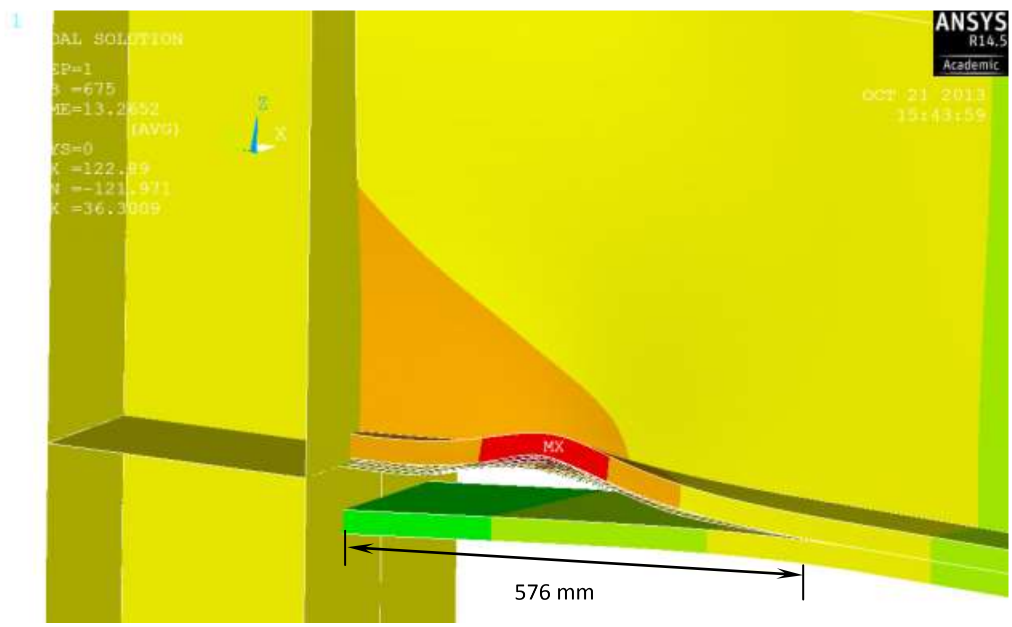

b) Numerical simulation

Figure 4.30 Comparison of predicted and measured extent of delamination in beam-column assembly insulated with mineral fiber-based SFRM

4.4.1.6 Beam Subjected to Impact Loading

As mentioned before the fracture mechanics-based numerical model need to be verified against dynamic tests. The drop mass impact tests, carried out as a part of experimental program in this study and presented in Chapter 3, are selected as the first set of dynamic tests against which the numerical model is validated. In the validation process, behavior of the non-insulated and insulated beams and the effect of boundary conditions are evaluated. The results from numerical simulations are compared to those obtained by experiments with respect to impact force and beam deflection.

4.4.1.6.1 Insulated Beam Behavior

The impact tests are modeled using LS-DYNA explicit finite element program. Figure 4.41 illustrates the finite element model created for a steel beam insulated with SFRM. The steel beam and SFRM are discretized using 8-noded solid elements with linear displacement interpolation functions and reduced integration. The plate stack in the hammer is also modeled using 8-noded solid elements. However, the indenter is discretized using 10-noded tetrahedron elements which use a quadratic displacement interpolation function with five point of integration.

The hammer is positioned at a distance of 2 mm above the flange of the beam, and an initial velocity calculated by energy conservation approach, is assigned to the hammer nodes. To simulate dynamic interaction between striking hammer and the flange of the steel beam, contact type “Automatic_One_Way_Surface_To_Surface” is used (LS-DYAN, 2014). The contact force developed between indenter tip and the flange of the beam is considered as impact force. Contact type “Automatic_One_Way_Surface_To_Surface_Tiebreak” with option=9 and soft contact algorithm (SOFT=1) is utilized to model delamination between fire insulation and steel.

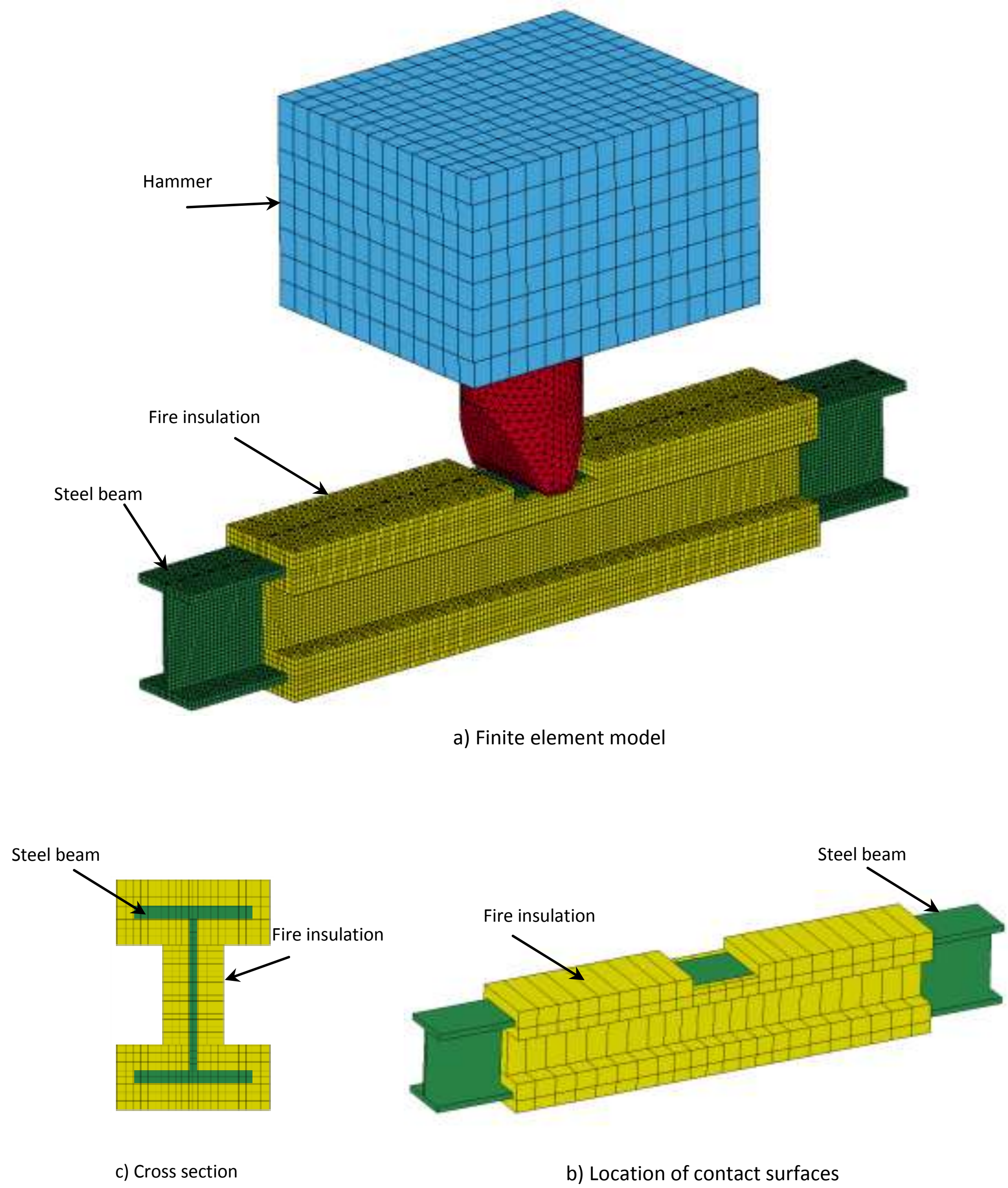

Figure 4.31 Numerical model of experimental setup for fire insulated beams in drop mass impact test

The predicted impact forces on beams insulated with three types of SFRM are plotted in Figure 4.42, Figure 4.33 and Figure 4.34 where results for two impact velocities are presented. It can be seen that there is quite a fair agreement between numerical predictions and experimental data over the initial stages of impact (inertial response), however these are some levels of discrepancies during the flexural response phase particularly for beams stricken by hammer with velocity of 8.05 m/s. This level of discrepancy is frequently encountered while modeling impact tests, and was observed by other researchers (Fujikake et al., 2009; Wang et al., 2013; Remennikov et al., 2013). The differences between numerical and experimental results can be attributed to the fact that the real material behavior under high strain rate loading is not captured in the numerical model. Further, finite element approximations in modeling contact behavior between the impacting object and the structure increases the level of error in the simulations. The computed impact duration however correlates fairly well with the one recorded in the experiments.

Figure 4.35, Figure 4.36 and Figure 4.37 compare the numerically and experimentally obtained time history of deflection at beam end for beams insulated with three types of SFRM and subjected to two levels of impact velocities. The numerically predicted response curves, though not perfect, can follow the experimental curves to some acceptable level. The experimental curve tends to have a peak, followed by a steady state, while the numerical curve has a smooth apex, followed by a smooth softening. The observed behavior in the experiments may be attributed to the fact that the LVDT at the end of the beam is installed on a short plate attached to the beam, thus the cantilever-like behavior of this plate may be responsible for the sharp peak on the experimental curve. Despite discrepancy in predicting peak response, the residual displacement is reasonably predicted.

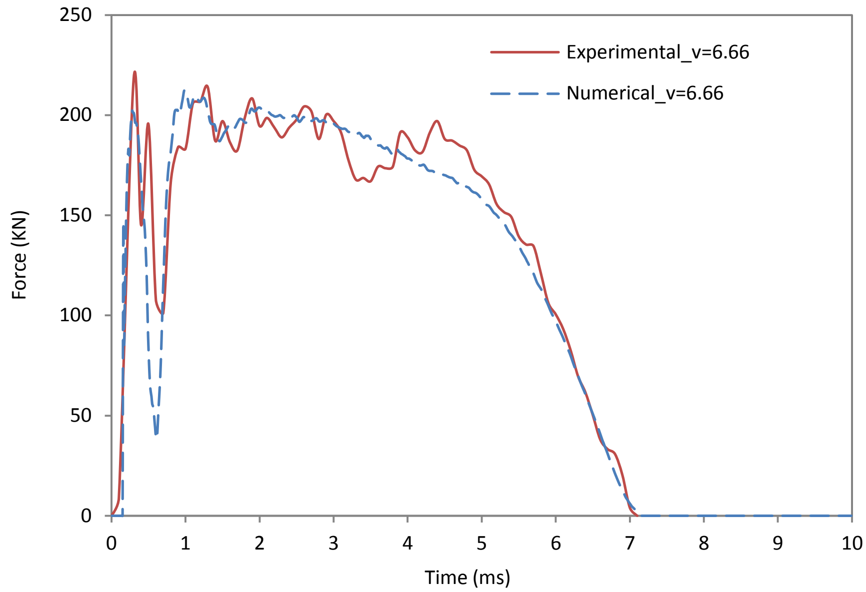

a) Impact velocity = 6.66 m/s

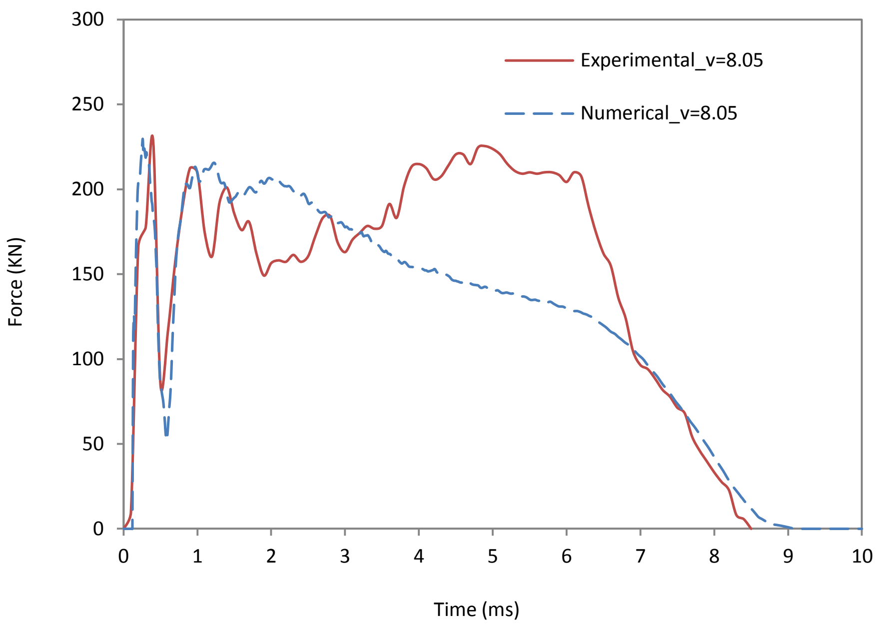

b) Impact velocity = 8.05 m/s

Figure 4.32 Comparison of experimental and predicted impact force for beams insulated with mineral fiber-based SFRM subjected to two different impact velocities

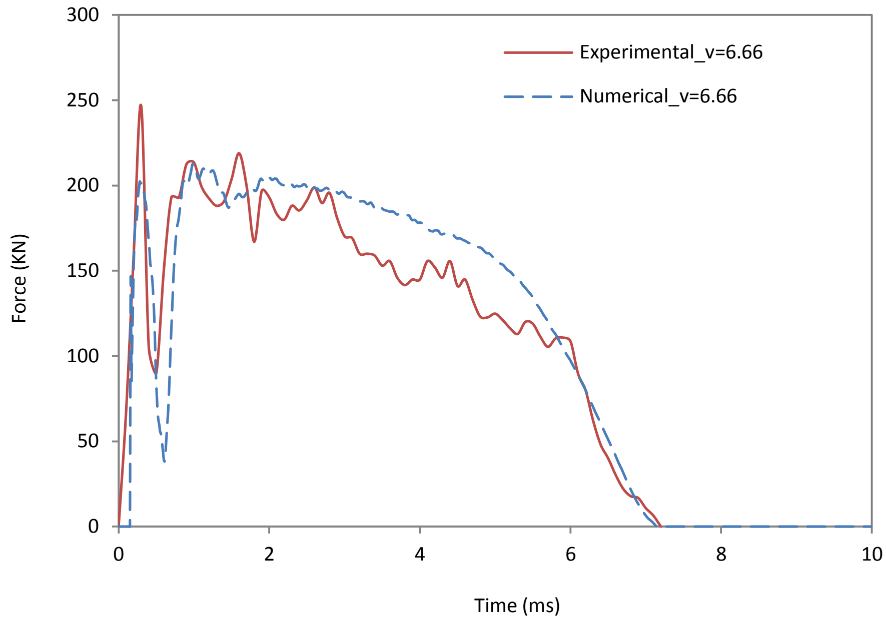

a) Impact velocity = 6.66 m/s

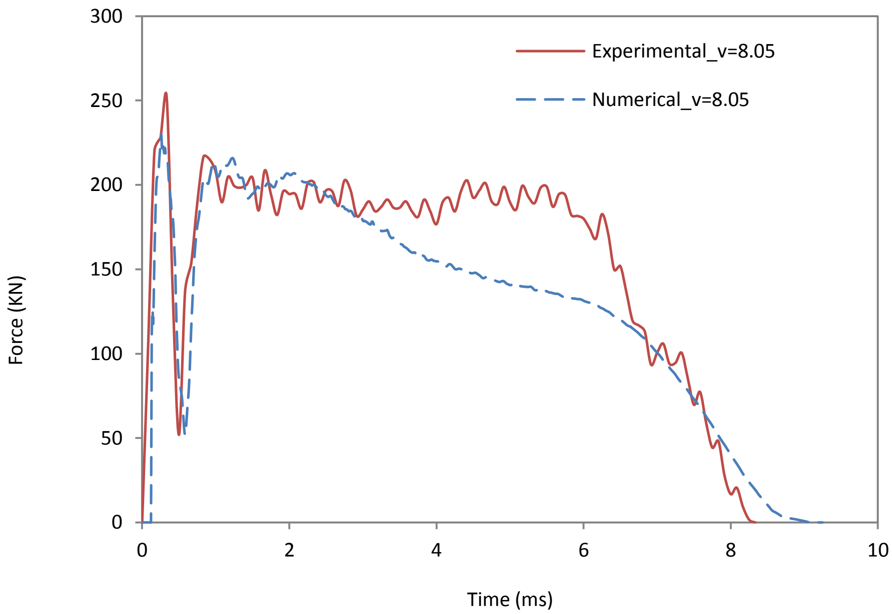

b) Impact velocity = 8.05 m/s

Figure 4.33 Comparison of experimental and predicted impact force for beams insulated with gypsum-based SFRM subject to two different impact velocities

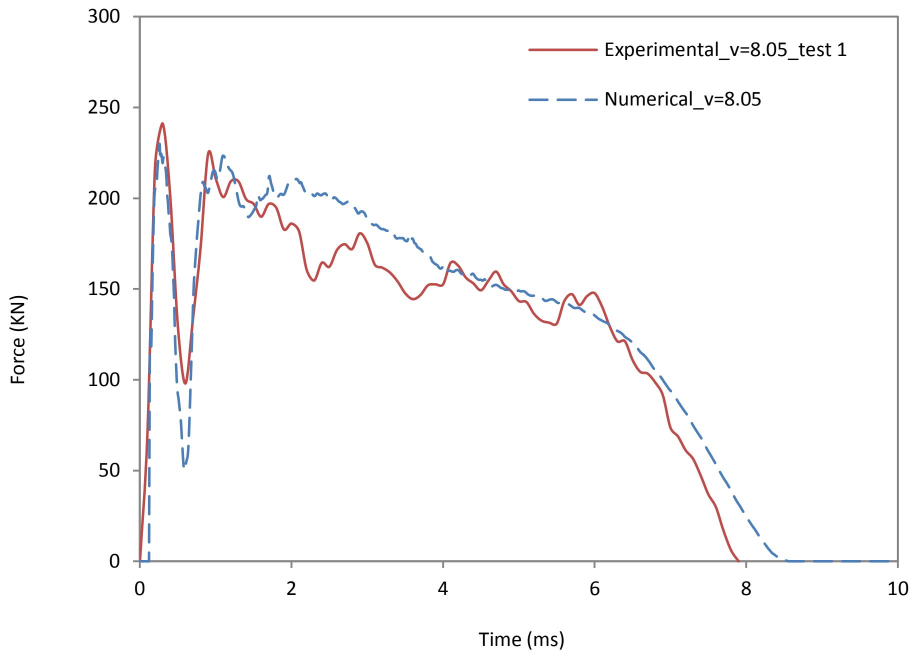

a) Impact velocity = 6.66 m/s

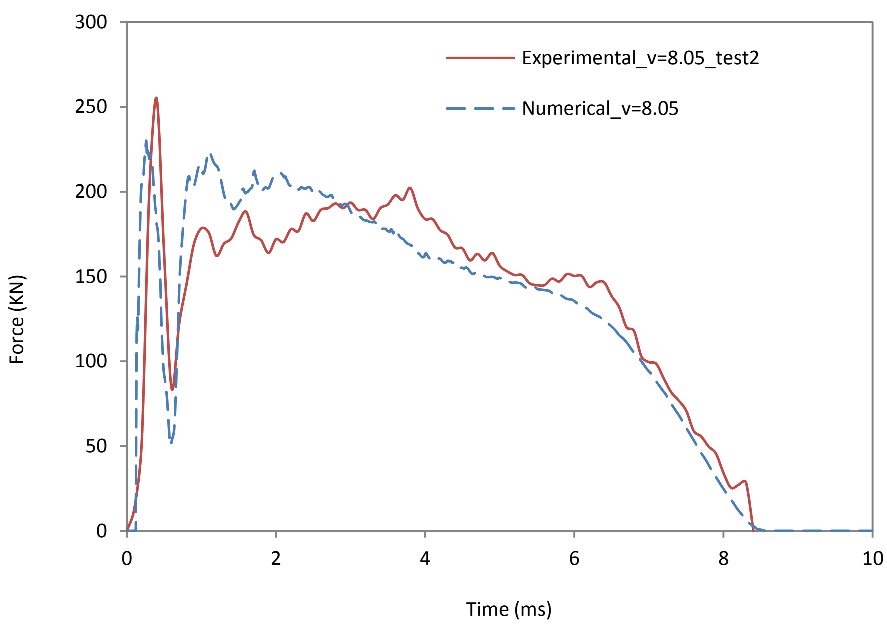

b) Impact velocity = 8.05 m/s

Figure 4.34 Comparison of experimental and predicted impact force for beams insulated with Portland cement-based SFRM subject to two different impact velocities

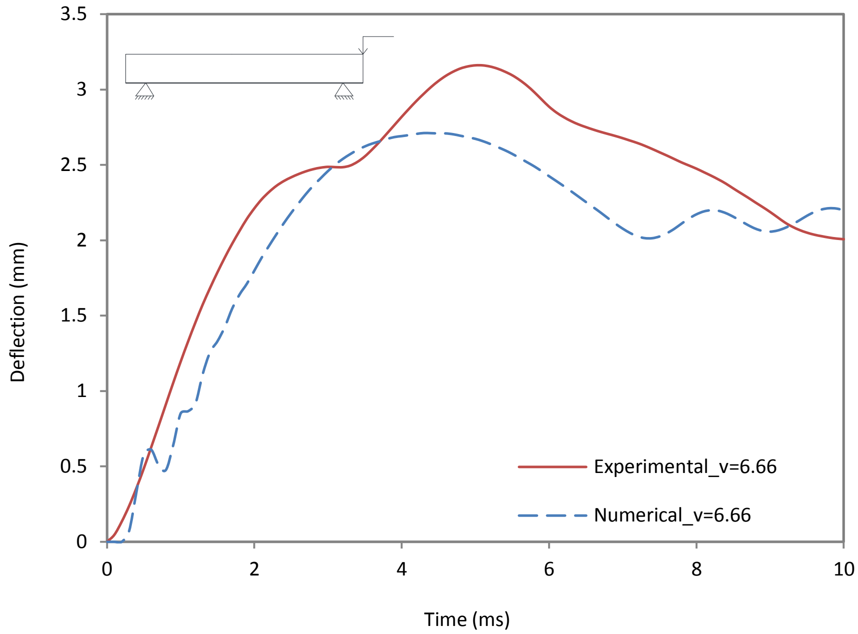

a) Impact velocity = 6.66 m/s

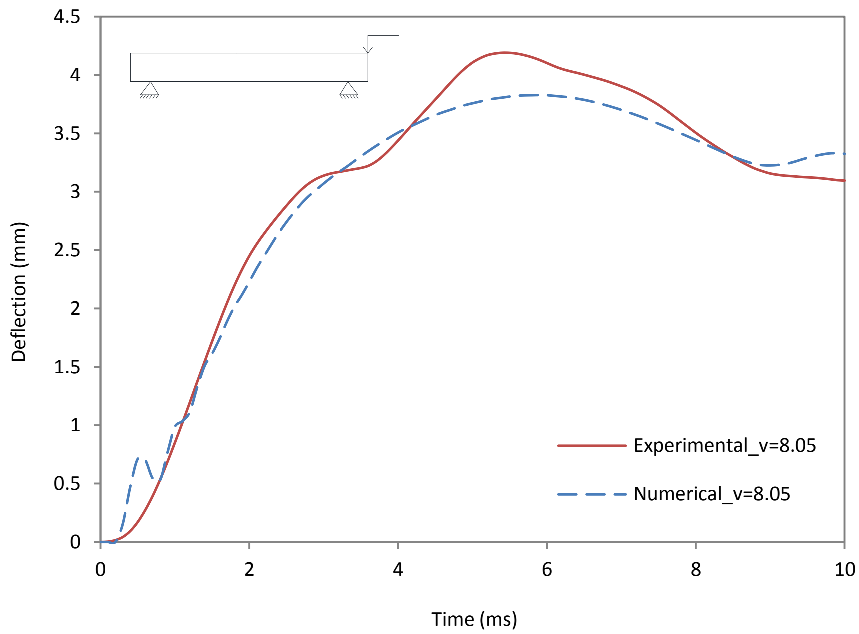

b) Impact velocity = 8.05 m/s

Figure 4.35 Comparison of experimental and predicted vertical deflection at one end of beams insulated with mineral fiber-based SFRM and subjected to two different impact velocities

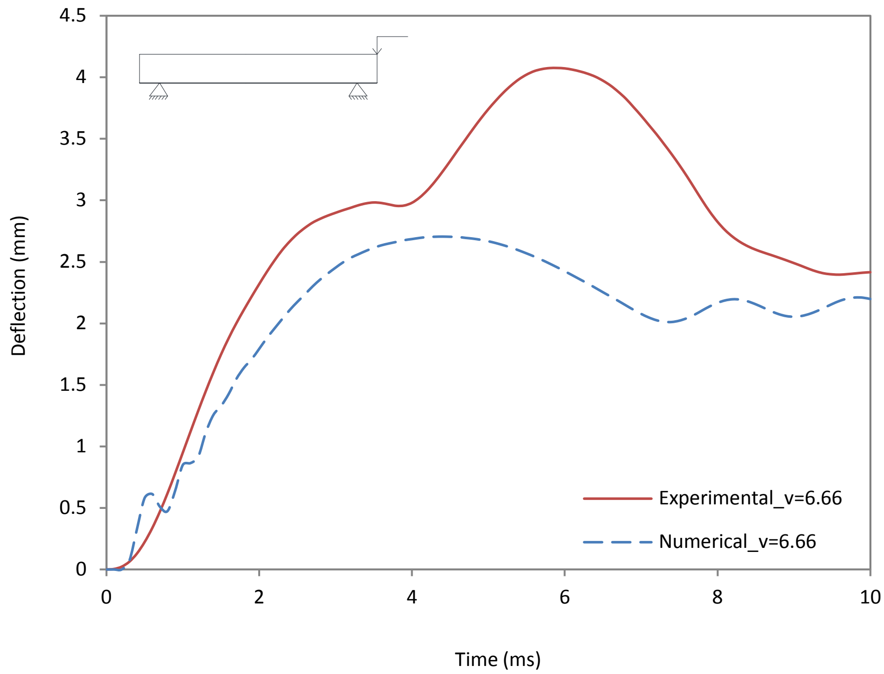

a) Impact velocity = 6.66 m/s

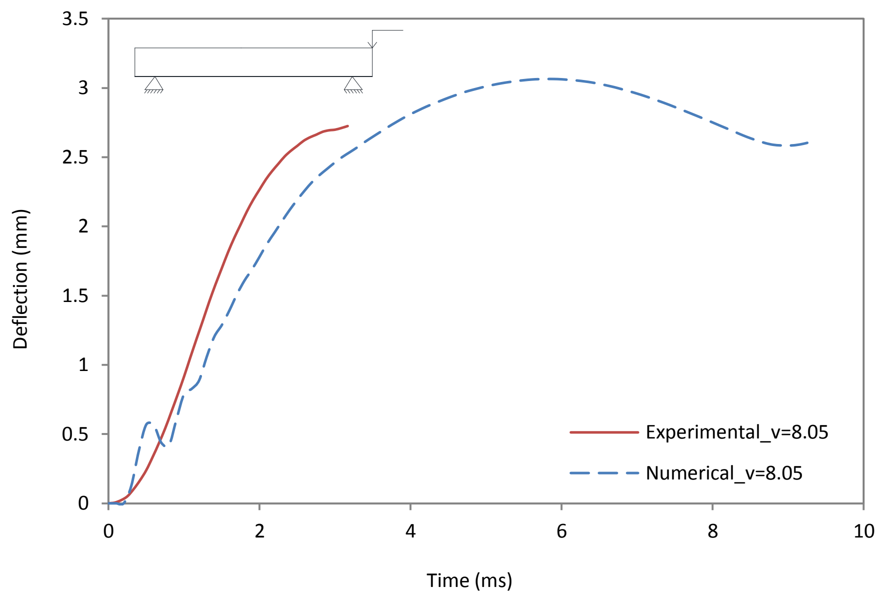

b) Impact velocity = 8.05 m/s

Figure 4.36 Comparison of experimental and predicted vertical deflection at one end of beams insulated with gypsum-based SFRM and subjected to two different impact velocities

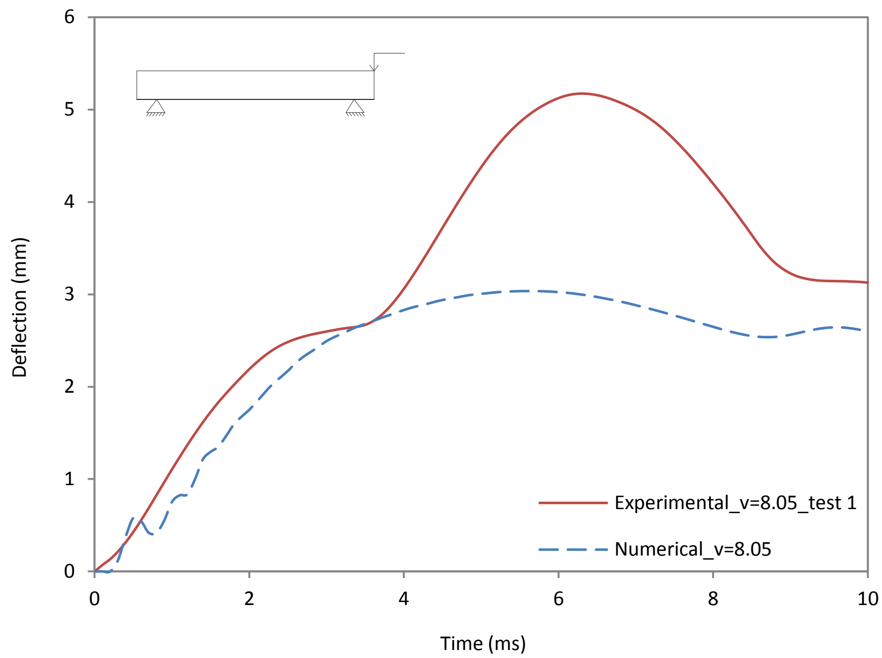

a) Impact velocity = 6.66 m/s

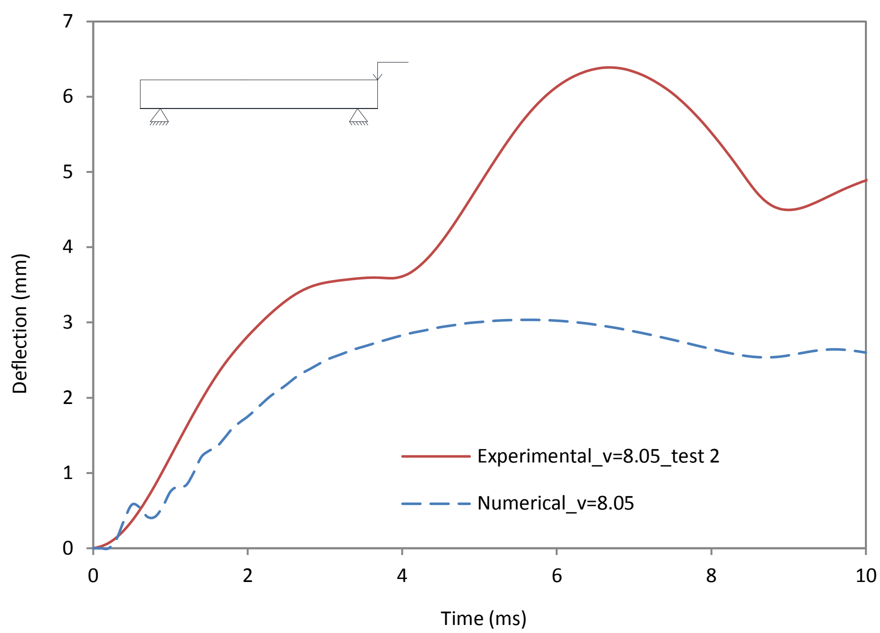

b) Impact velocity = 8.05 m/s

Figure 4.37 Comparison of experimental and predicted vertical deflection at one end of beams insulated with Portland cement-based SFRM and subjected to two different impact velocities

4.4.1.6.2 Non-insulated Beam Behavior

As explained in chapter 3, in impact tests the attachment of LVDT at the mid-span of the insulated beams was not possible due to interruption it would cause in crack initiation at the most critical section of the beam. Consequently, the displacement time history at the end of the beam is the only measured response parameter that can be used to verify the numerical prediction of beam deformation. To validate the reliability of displacement predictions at the end of the beam on insulated specimens, it is also required to somehow compare the numerical predictions and experimental records at the mid span. To accomplish this, an impact test with hammer velocity of 8.05 m/s is carried out on a non-insulated steel beam for which there is no limitation on installation of LVDT at the mid-span as well as one end of the beam.

The results of numerical simulation on this beam are compared to the experimental records in Figure 4.38. As can be seen in this figure, the recorded impact force, displacements at mid-span and end of the beam correlate with numerical simulation results quite satisfactorily. The maximum impact load and subsequent reduction due to response of the beam is captured very well. Also, the decay phase of the load time-history is predicted reasonably well while the predicted load is slightly less than recorded one. In the displacement response the peak displacement as well as residual displacement is in close agreement with the recorded results. The predicted vertical displacement at one end of the beam is slightly smaller than the obtained results in the experiment.

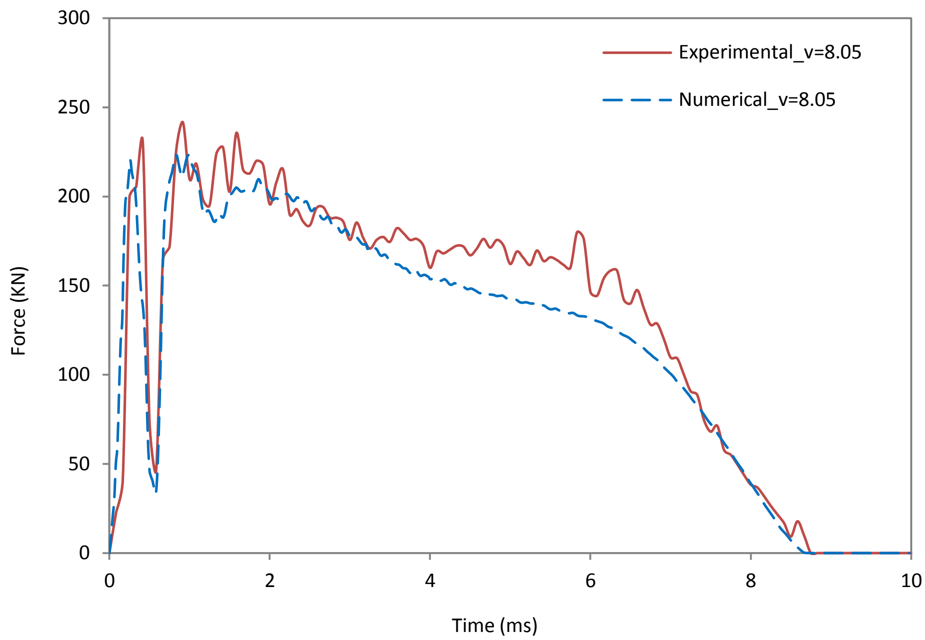

a) Impact load

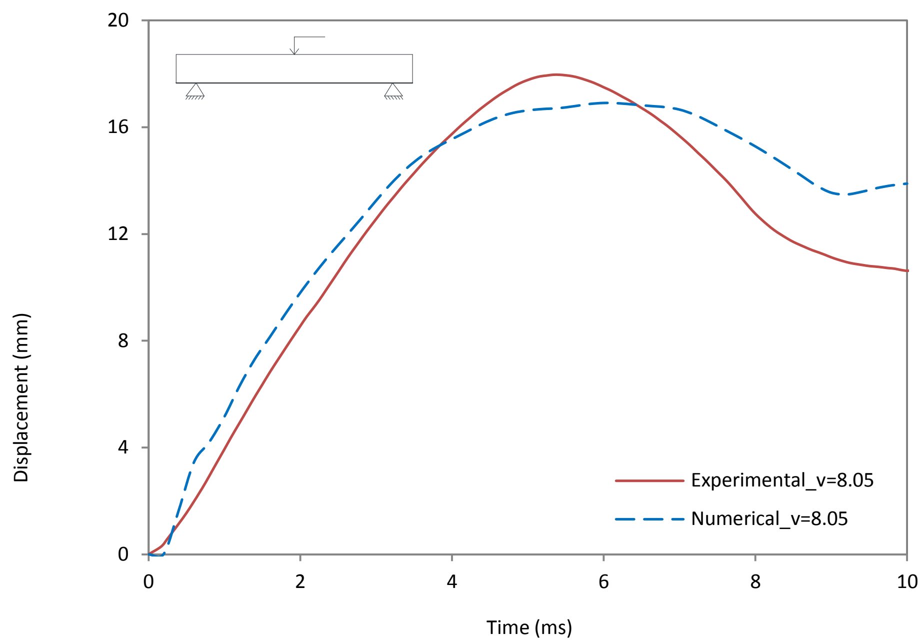

b) Vertical displacement at mid span

Figure 4.38 Comparison of experimental and predicted responses for a steel beam without insulation

Figure 4.38 (cont'd)

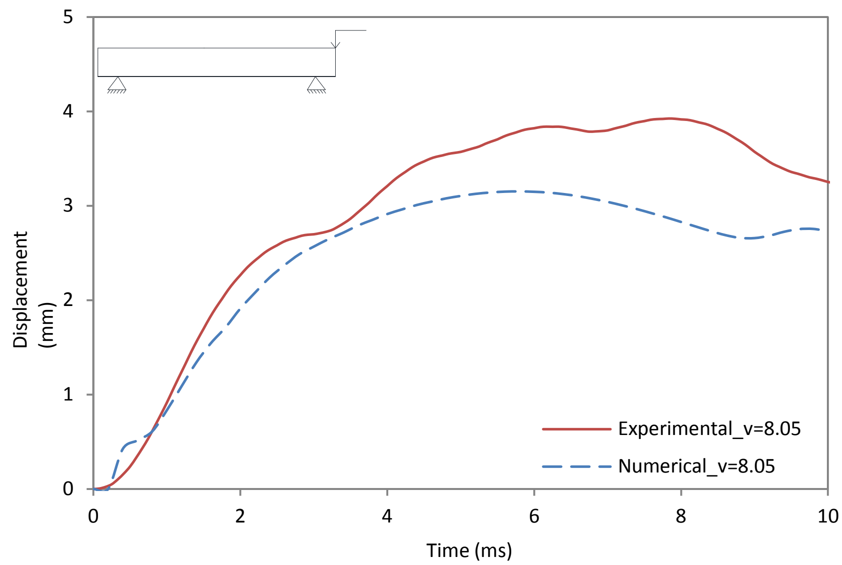

c) Vertical displacement at one end

4.4.1.6.3 Effect of Boundary Conditions

In numerical simulation, including all the details in the model can noticeably increase the cost of the analysis. However, tremendous amount of time and computational effort can be saved by simplifying the modeling details while negligibly affecting the obtained results. The influence of boundary conditions on the results of numerical modeling is always a concern. In this study, to ensure that simplifications made in the numerical modeling of support conditions do not substantially affect the accuracy of the numerical results, the support configuration used in the experiment is included in the numerical model as shown in Figure 4.39. However, fire insulation is not modeled since it does not have any effect on the structural response of the beam. Also, only half of the experimental set-up is modeled and symmetrical boundary condition is imposed. In Figure 4.40, the results of numerical predictions from a model containing the support details are compared to the one obtained through simplified model. As is clear, the discrepancy between the results of two models is not noticeable for both mid-span deflection and applied impact force.

Based on this comparison, the interaction among supports and the beam is not included in the model to be utilized in parametric studies. Instead, the nodes at the support locations are vertically and laterally restrained while they can move freely in longitudinal direction.

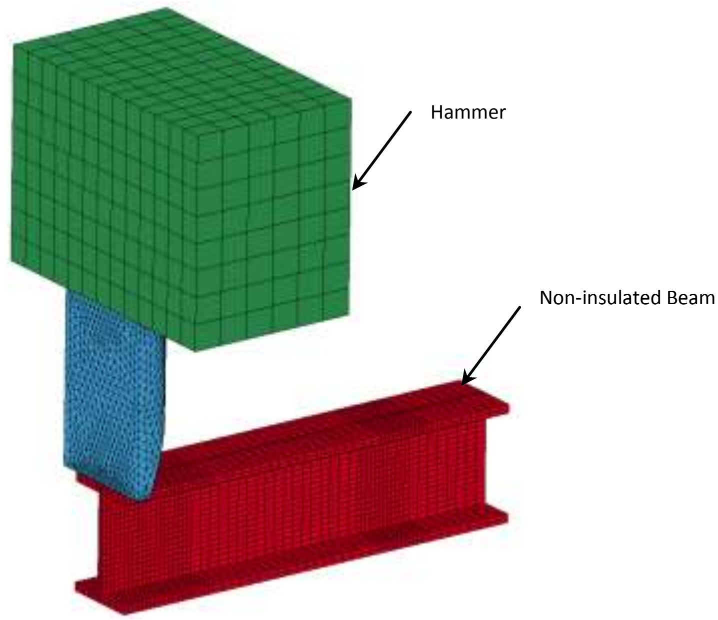

a) Half finite element model without including supports

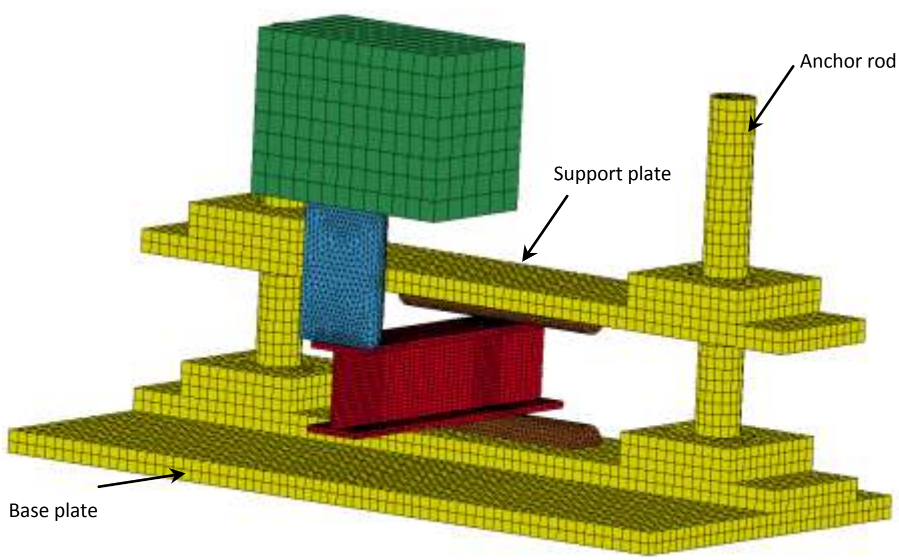

b) Half finite element model including supports

Figure 4.39 Numerical models created for evaluating the effect of supports on beam behavior in drop

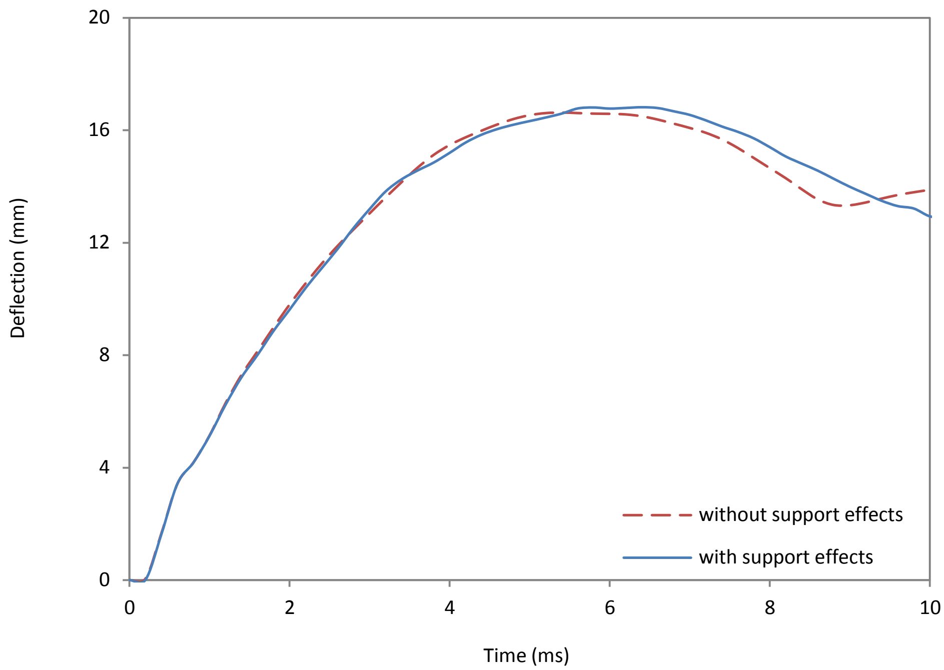

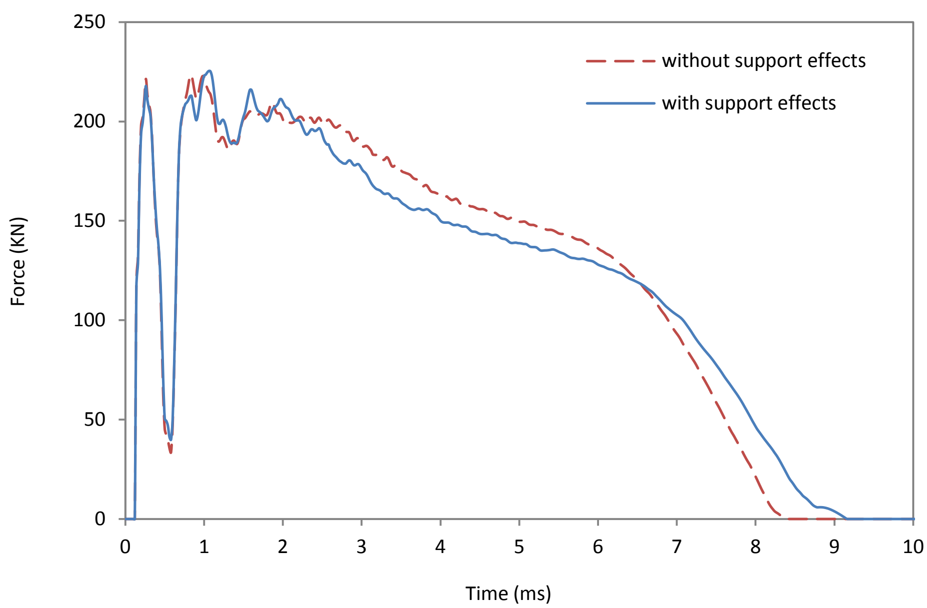

b) Impact load

Figure 4.40 Effect of including support details in numerical predictions

4.4.1.7 Beam-Column Subjected to Blast Loading

The predictions from the above developed numerical model are validated against blast experiments. The experiment selected for validation is a blast test carried out on a full scale steel beam-column by Nassr et al. (2013). The experimental set-up for the blast test is illustrated in Figure 4.41. The explosive charge contained 150 Kg of ammonium nitrate and fuel oil (ANFO) and the stand-off distance was 9 m. The beam-column had a section size of W150 X 24 and height of 2413 mm, and it is loaded about the major axis. The static axial load on the beam-column was applied using pre-stressing wires which were simultaneously stressed up to 25 % of the static axial capacity of member ($P=0.25P_{cr}=270kN$). The boundary conditions of the beam-column are hinge and roller at the top and bottom of the member, respectively, as shown in Figure 4.42.

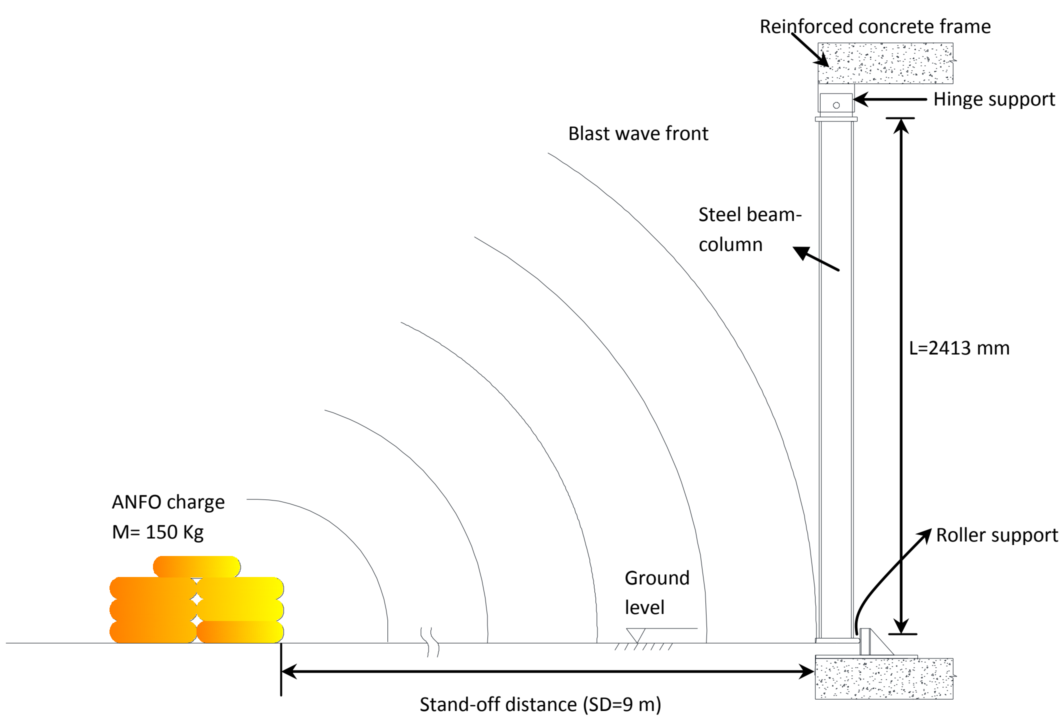

Figure 4.41 Schematic view of blast tests on steel beam-column conducted by Nassr et al. (2011)

The finite element model of the tested beam-column is depicted in Figure 4.42 where boundary conditions and blast load are shown on the figure. The beam-column is discretized using 8-noded solid elements with reduced integration. The end boundary conditions are simulated by including two rigid end plates at both ends of the member. On the pin end, all displacement degrees of freedom of the rigid plate are constrained except for the rotational degree of freedom about which the beam-column can rotate. The boundary condition on the roller end is similar to the pin end, expect translational degree of freedom is released in the axial direction of the beam-column to accommodate applying static axial load.

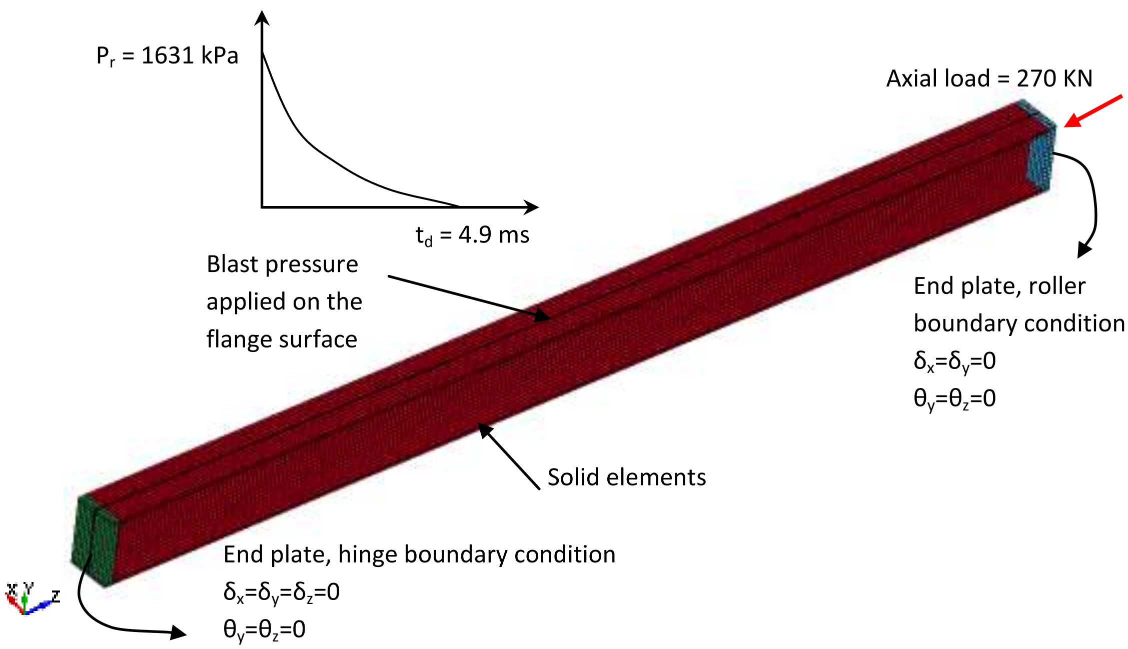

Figure 4.42 Finite element model of beam-column tested by Nassr et al. (2011)

The blast overpressure time history is determined using modified Friedlander equation (Baker et al., 1983):

$$P(t) = P_{max}\left(1-\frac{t}{t_d}\right)\exp\left(-\gamma\frac{t}{t_d}\right) \tag{4.55}$$

where, P_{max} is peak pressure; γ is a shape parameter; t_d is positive load duration and t is time. The P_{max} and t_d recorded during blast experiment were reported as 1631 kPa and 4.9 ms, respectively (Nassr et al., 2013).

Results obtained from numerical simulation (in LS_DYNA) are shown in Figure 4.43 where deflection contour in the direction of blast pressure and displacement time-history at mid height of the beam-column is plotted. As can be noticed in this figure, the numerical model can predict the displacement of the beam-column quite satisfactorily. The level of delamination over a structural member during blast has a direct relationship with the magnitude of deformation induced by blast overpressure. Therefore, the successful prediction of beam-column deflection under blast loading validates efficiency of the numerical model to be employed in predicting the extent of fire insulation delamination over a beam-column subjected to blast loading.

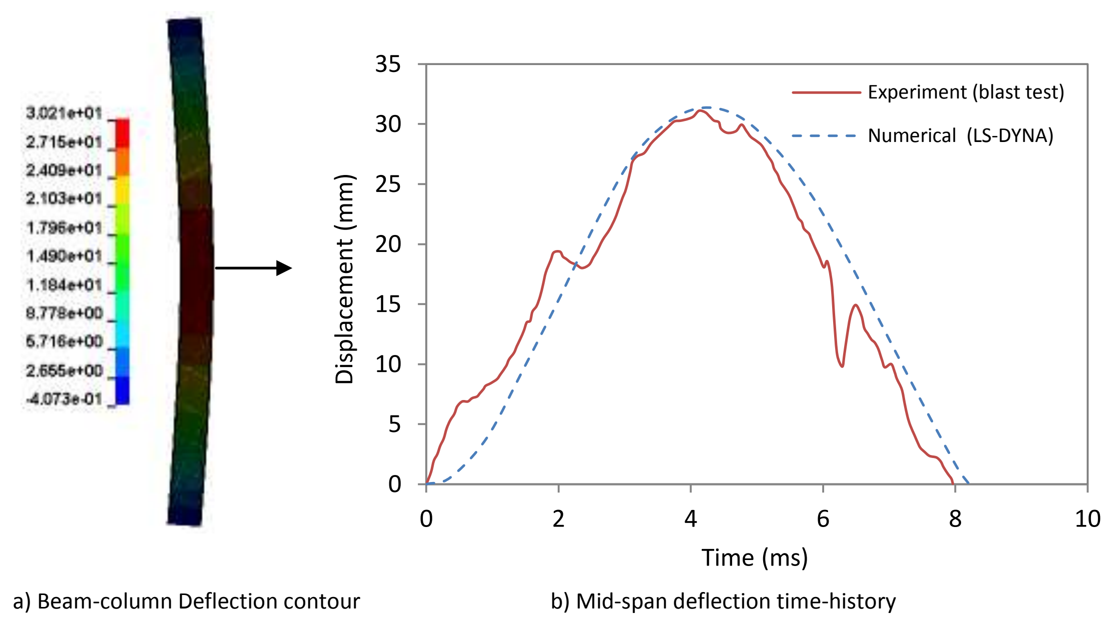

Figure 4.43 Comparison between numerical prediction and experimentally measured deflection at mid-span of the beam-column under blast loading

4.4.2 Validation of Thermal-Structural Numerical Model

The developed thermal-structural numerical model is verified by simulating structural performance of concrete filled steel tubes during fire conditions. Canadian national research council (CNRC) first conducted an extensive research program in order to evaluate the fire performance of concrete filled hollow steel columns. Both circular and square columns were investigated and columns were filled with plain concrete (Lie and Chabot, 1992), steel fiber reinforced concrete (Kodur and Lie, 1996) and bar reinforced concrete (Lie and Kodur, 1996). The column SQ24 tested in CNRC project (Lie and Chabot, 1992) was selected to be analyzed. The test parameters are summarized in Table 4.1. Figure 4.44 shows the location of thermocouples and displacement transducers. The column has been exposed to ASTME119 fire. Results from the experiments were utilized to propose an equation that incorporates critical factors influencing fire resistance of a concrete filled HSS column (Kodur and Lie, 1996) and estimates fire rating of the column. The concrete-filled steel column is selected for validation since detailed information was available for this test. The primary purpose of this validation is to verify the thermal analysis procedure.

The thermos-structural response of the column is simulated using the approach outlined in section 4.3. In thermal analysis, 8-noded solid element (SOLID70), that has temperature degree of freedom at each node, is adopted to model heat transfer through steel and concrete materials. The surface element (SURF152) is utilized to model radiation and convection effects. In structural analysis, steel tube is discretized using 8-noded solid element (SOLID185). The concrete core is modeled using 8-noded solid element (SOLID65) capable of modeling concrete cracking and crushing. At steel-concrete interface, surface-to-surface contact is used and steel and SFRM surfaces are discretized using 4-nodedtarget (TARG170) and contact (CONTA173) elements, respectively. Figure 4.45 shows the finite element discretization of the concrete filled HSS column.

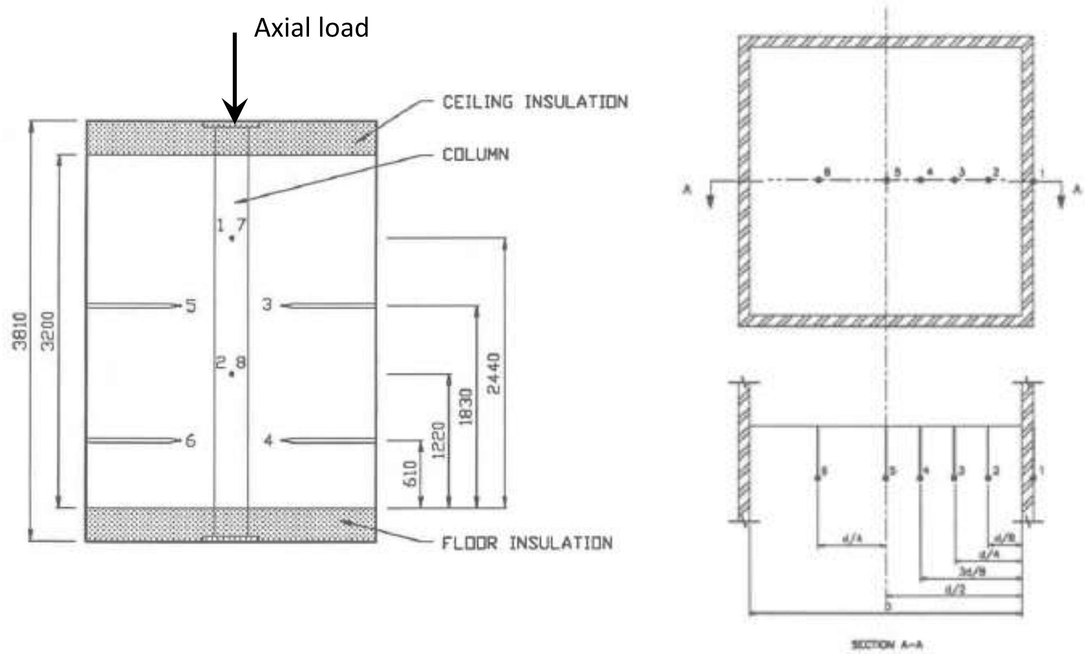

Figure 4.44 Location of thermocouples in cross section of the concrete filled column SQ24

Table 4.1 Material properties used for verification of thermal-structural model

Parameter	Description
Column No.	SQ24
Width (mm)	304.8
Wall thickness (mm)	6.35
Yield Strength (MPa)	350
Concrete Strength (MPa)	58.8
Aggregate	siliceous
End Condition	Pin-Pin
Factored resistance (KN)	4247
Test Load (KN)	1130
Fire resistance (min)	131

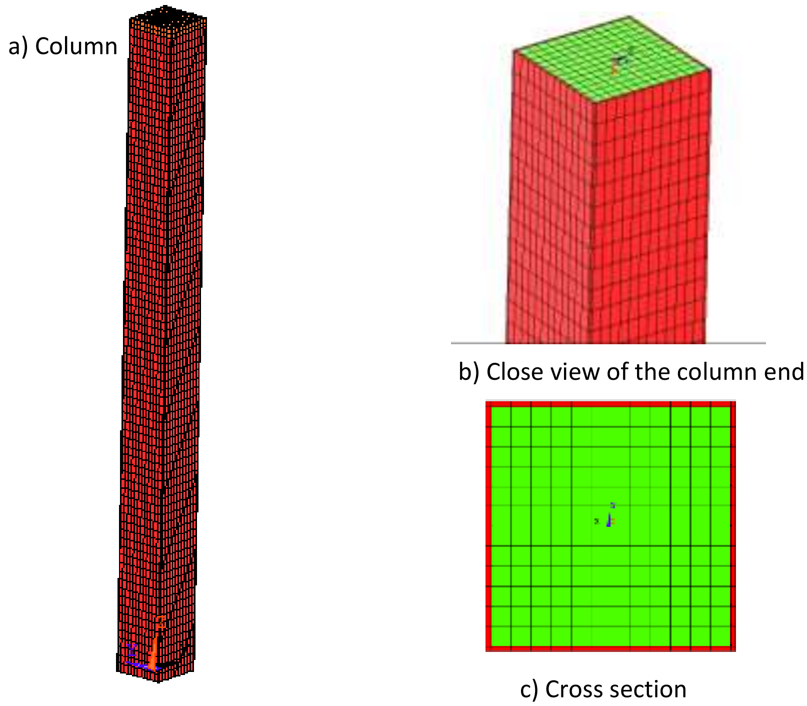

Figure 4.45 Finite element Model for concrete filled steel column

To simulate the column behaviour at elevated temperatures thermal-structural analysis is carried out in a sequential manner by incremental time steps till failure of concrete filled HSS column under fire conditions. First, a fraction of capacity at ambient condition is applied on column under ambient conditions. Subsequently, thermo-structural analysis commences while the axial load is kept constant. At any time step under a given fire scenario, the fire temperatures are established at cross section by solving the transient heat transfer equation with associated radiation and convection boundary conditions. In the next step, structural analysis is performed while the material properties are updated due to effect of temperature. Figure 4.46 depicts the temperature time history at three different locations in cross section. As is shown, the numerical method fairly predicts the temperature distribution in cross section. Figure 4.47 also shows the temperature distribution in cross section at 120 min after the column is exposed to ASTM E119 (ASTAM E119, 2014) fire.

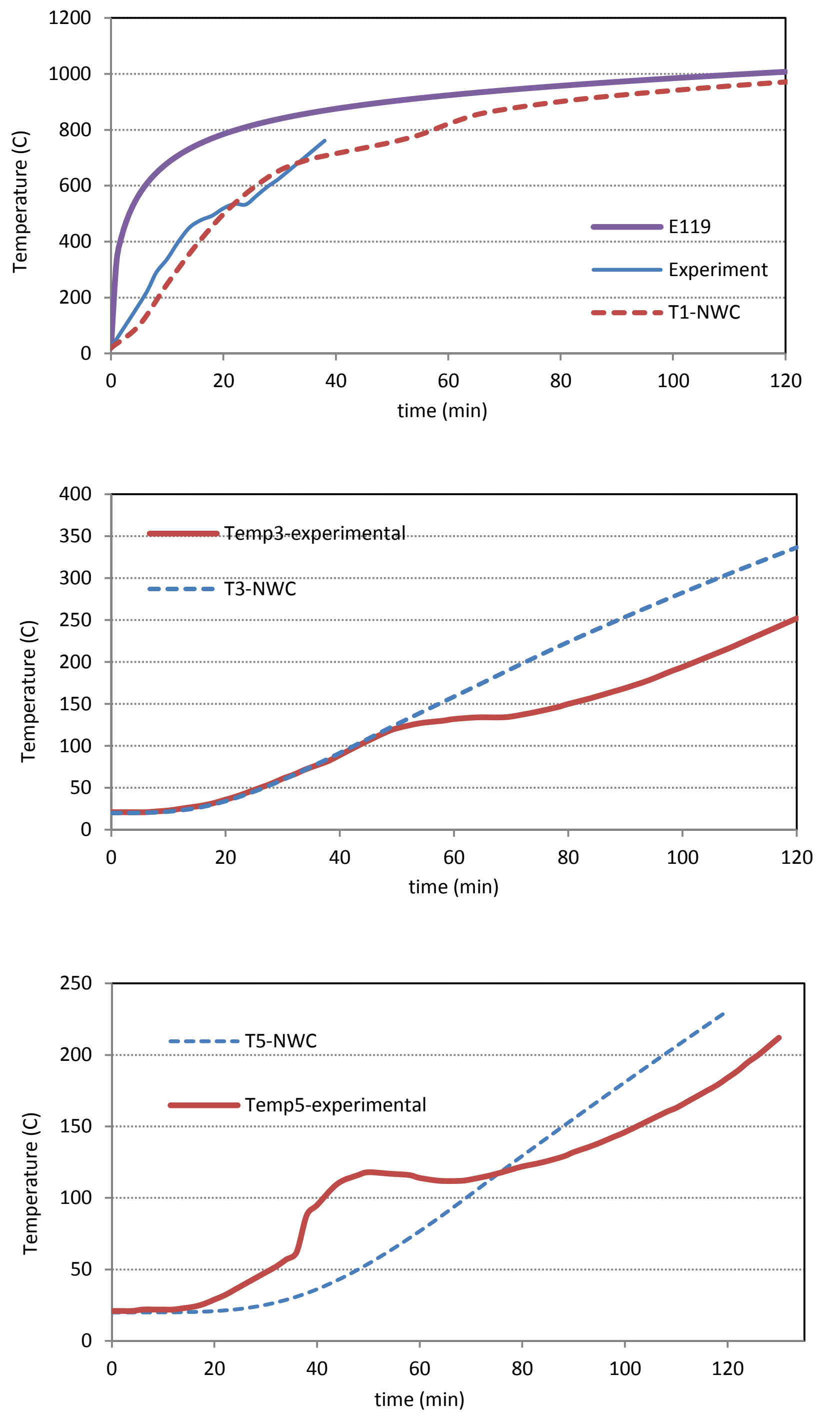

Figure 4.46 Temperature prediction

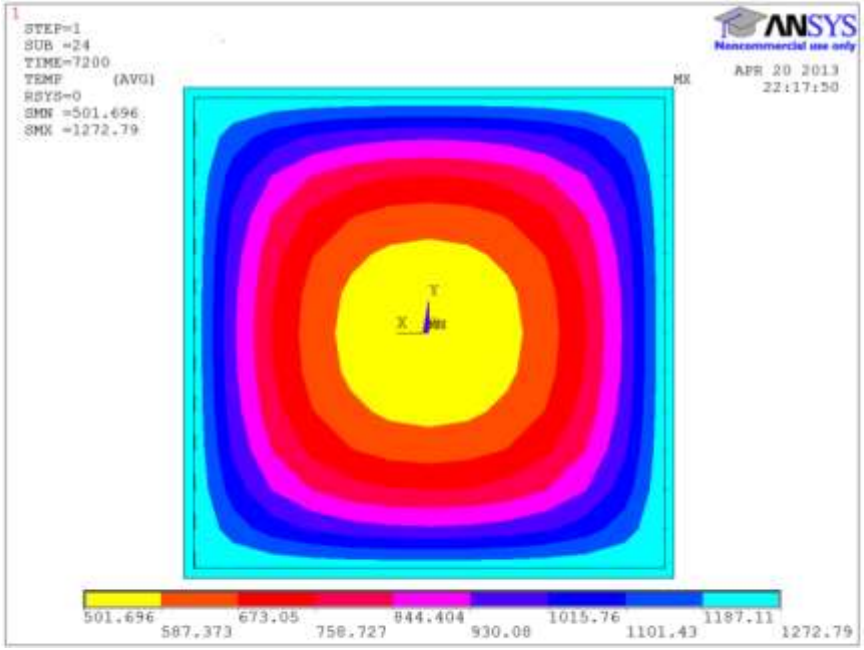

Figure 4.47 Temperature (°K) distribution at cross section

The predicted axial deformation of column is illustrated in Figure 4.48 where result of analyses for steel tube filled with concrete is compared against experimental observations. Upon subjecting the unprotected steel column to elevated temperature, steel tube experiences dramatic increase in temperature that results in considerable rise in thermal strain. Due to difference in thermal strains developed in steel and concrete, the steel-concrete surface bond is lost and steel expands upward carrying the entire vertical load. Once mechanical properties of steel are degraded due to temperature rise (usually this occurs around 20 minutes), steel loses its capacity in carrying the vertical load and shrinks down. Once the steel can no longer withstand the vertical load, the concrete core carries the vertical load up to the failure point where the concrete material properties are degraded and the exciting vertical load breaches the buckling capacity of the concrete core as a column. The computed fire resistance for concrete filled HSS column is 119 min, while the observed fire resistance is 130 minutes. The discrepancy between the results of numerical model and experimental observations can be attributed to the uncertainties in thermal and mechanical properties of concrete and steel materials at elevated temperature, as well as variations in furnace temperature.

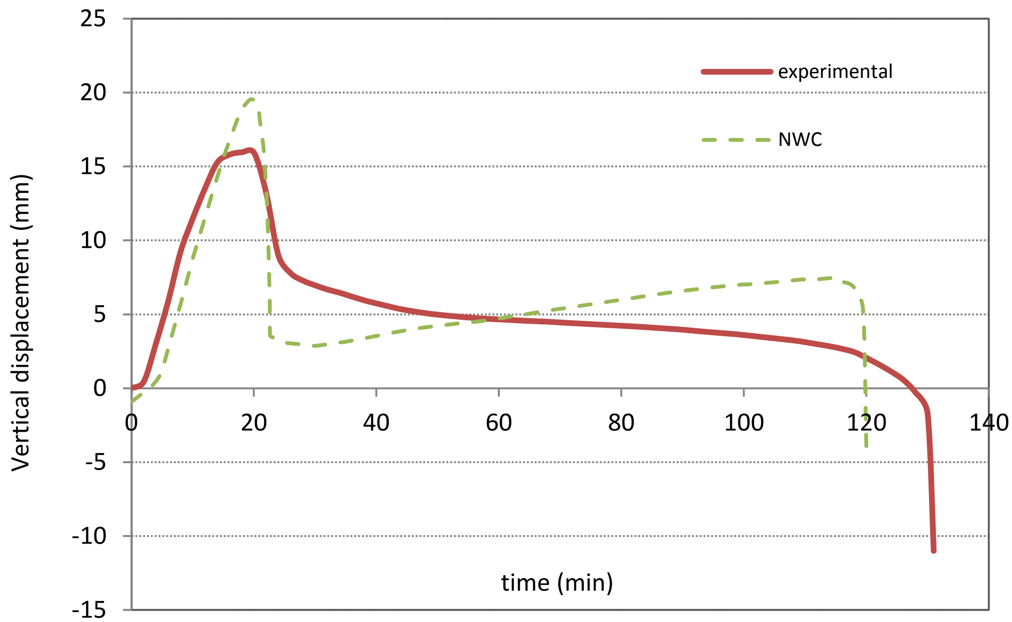

Figure 4.48 Axial deformation of the column

4.5 Summary

In this chapter two types of numerical models were developed. The first model is a fracture mechanics-based numerical approach in which principles of fracture mechanics are combined with finite element formulation to simulate crack initiation and propagation at the interface of fire insulation material and steel structures. In this numerical model, depending on the problem, two different solution approaches are adopted. For the structures subjected to quasi-static and seismic loading, implicit solution is utilized and ANSYS software is employed. However, to simulate behavior of structure under the action of impact and blast loading, explicit solution is used and LS-DYNA software is employed. The second numerical model is a thermal-structural model that can simulate effects of elevated temperatures as encountered by structure during fire. This numerical model is developed in ANSYS software and is capable of incorporating temperature dependent material properties.

Both numerical models were validated by comparing response predictions from the model with experimental data. The fracture mechanics-based model is validated against both static and dynamic experiments conducted in this study, as well as test results reported by other researches. The thermal-structural model is verified by comparing the model predictions with results of fire tests reported in the literature. It should be noted that, the developed numerical models can predict the overall response of the structural system very well. However, there are some discrepancies between experiments and predictions that can be attributed to uncertainties in the material properties and behavior, as well as approximations inherent in numerical solutions. The validation process reinforced the required assurance to further expand the developed the numerical models to carry out parametric studies. The validated fracture mechanism-based model will be utilized to explore critical factors influencing the delamination of fire insulation from steel structures subjected to seismic and blast loading, in Chapter 5. Further, the validated thermal analysis will be applied to predict the ramifications of fire insulation delamination from steel structures during fire following earthquake and explosion, in Chapter 6.

CHAPTER 5

5 PARAMETRIC STUDY

5.1 General

A validated numerical model is a powerful tool to study the effect of various parameters that influence fracture and delamination of fire insulation from steel structures and thereby save tremendous amount of time and cost which otherwise would have to be spent on experimental studies. In this study, the numerical approach which outlined and validated in Chapter 4, is applied to carry out a series of parametric studies to quantify effect of critical factors governing fracture and delamination of fire insulation from steel structures. First, the governing factors are identified and rationales for selecting them are explained. Subsequently, the parametric studies are systematically designed to span wide range of material properties applicable to SFRM commonly used in practice to quantify effect of each parameter. Further, various types of loading conditions are also considered in the analyses.

The parametric studies are carried out on a slender steel truss subjected to quasi static deformation, a beam-column assembly subjected to cyclic monotonic loading representing seismic loading, an insulated beam subjected to impact loading and a beam-column subjected to blast loading. Response of three types of SFRM namely gypsum-based, Portland-cement-based and mineral fiber-based is evaluated in the parametric studies. Results from parametric studies are utilized to define two delamination characteristic parameters to establish interdependency among governing factors. The first delamination parameter is defined for quasi static and seismic loading and the second parameter is defined for blast loading. Further, parametric study under impact loading is used to estimate effect of loading rate on fracture energy at the interface of SFRM and steel. Subsequently, the extent of delamination over the structural members is related to the delamination characteristic parameter.

5.2 Factors Governing Delamination of SFRM from Steel Structures

The fracture energy at steel-SFRM interface, thickness of SFRM and elastic modulus of SFRM are three critical material properties that can influence the delamination of SFRM from steel surface. The normal cohesive strength is the only mechanical parameter that is tested and reported in the literature relating to material specification of SFRM. However, based on the fracture mechanics principles developed for cementitious materials (Cotterell and Mai, 1996), fracture energy is the most effective factor that can describe crack formation and progression within the material. The fracture energy incorporates both cohesive strength and formation of fracture process zone at the interface of SFRM and steel. Tan et al. (2011) also highlighted the crucial role of fracture energy in delamination phenomenon at the interface of fire insulation and steel. The crucial role of fracture energy is quantified in this parametric study.

The elastic modulus is not reported in current material specifications of SFRM due to the fact that it is not considered an effective design parameter. Consequently, the important role of elastic modulus is overlooked since in fracture mechanics the dependency of cohesive zone length on elastic modulus has been proposed by many researches (Hillerborg et al., 1976; Irwin, 1960; Dugdale, 1960). Therefore, the extent of delamination of SFRM from steel structures under blast load is expected to be influenced by the elastic modulus of SFRM.

In current fire design provisions, fire resistance requirements prescribe the required SFRM thickness neglecting the delamination issue associated with this material. Thicker SFRM fulfills its fire protection responsibility more effectively; however, the thicker SFRM might not survive a seismic, impact or explosion event leaving the structural member fully or partially exposed to following fire. Delamination concerns therefore have not been taken into consideration while assessing post-earthquake, post-impact or post-blast fire performance of steel structures. Thickness of SFRM can influence the extent of delamination due to its effect on amount of energy absorbed by the insulation. In horizontal members such as beams, the thicker SFRM can easily detached from the steel surface due to gravity loading and leave the structural members unprotected.

5.3 Delamination of Fire Insulation from Slender Steel Truss

To quantify extent of delamination of fire insulation from slender steel truss members subjected to extreme loading, and further to investigate effect of crucial parameters on delamination phenomenon a parametric study is carried out with respect to influential parameters. Results of this parametric study are detailed in the followings subsections.

5.3.1 Analysis Details

Figure 5.1 illustrates an 18.29 m long truss with geometry similar to the one used in collapsed world trade center (WTC) tower 1 and 2. In current numerical modeling, the bottom chord of WTC truss is selected for quantification of the extent of SFRM delamination from truss member under extreme tensile deformations. This truss is composed of top chord, bottom chord and diagonal members made of double angle sections. The bottom chord of truss, which is 1016 mm long and is covered with SFRM with thickness of 20 mm, is discretized as depicted in Figure 5.2. Under displacement-control static loading, truss member get stretched and the extent of delamination of SFRM is monitored as a function of strain level developed at the steel substrate.

Steel truss is discretized using 4-noded shell elements (SHELL181) that have three translational and three rotational degrees of freedom at each node. This element is well-suited for linear, large rotation, and large strain nonlinear applications. The formulation of this element is based on logarithmic strain and true stress measures. SFRM is discretized using 8-noded solid element (SOLID185) that has three translational degrees of freedom at each node. This element has the capability for handling large deformations, geometric and material nonlinearities.

At the interface, surface-to-surface contact is employed such that steel and SFRM surfaces are discretized using 4-noded target (TARG170) and contact (CONTA173) elements, respectively. The node ordering of contact elements is consistent with the node ordering of the underlying solid and shell elements. The positive normal is given by the right-hand rule going around the nodes of the element and is identical to the external normal direction of the underlying shell or solid element surface. Initially, two surfaces are assumed to be bonded and subsequently, under applied loading conditions, separation or slip distance is simulated in accordance with corresponding cohesive laws. Contact elements are nonlinear and require a full Newton iterative solution, regardless of whether large or small deflections are specified.

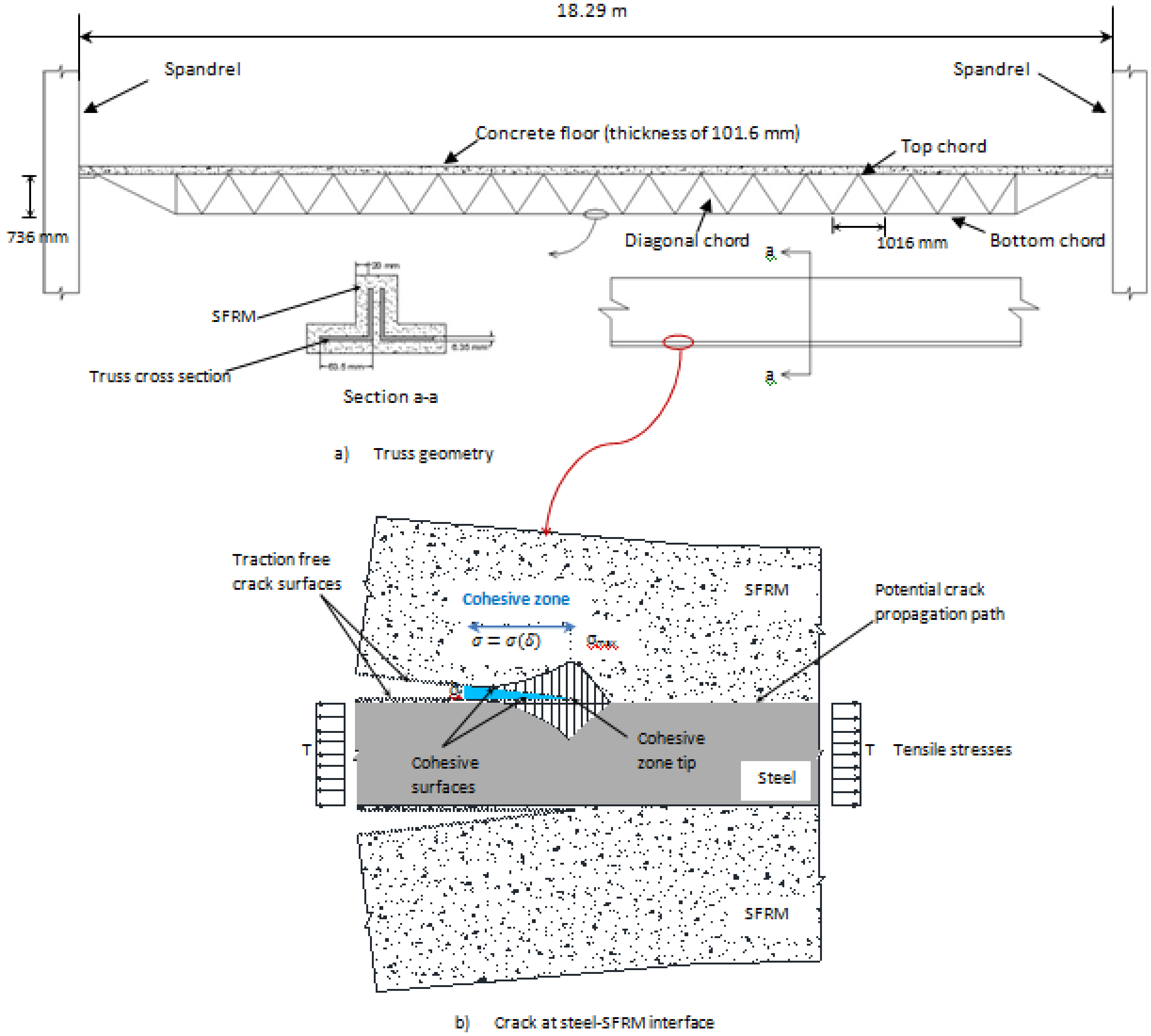

Figure 5.1 Progression of crack at the interface of steel and SFRM (based on cohesive zone model concept)

5.3.2 Effect of Type of SFRM on Delamination

Experimentally obtained cohesive laws for three types of SFRMs are utilized in the numerical model to quantify the steel strain at which delamination initiates and propagates throughout the member. Results from these analyses provide a quantitative evaluation of onset of delamination and its progression as a function of strain ductility demand of steel during extreme loading conditions. Figure 5.3 plots the percentage of delamination in outer faces of truss chord versus strain ductility demand ($\mu_s = \varepsilon_s / \varepsilon_y$) in steel. It is obvious that until ductility demand in steel has not reached a value of $\mu_s = 4.5$, there is no sign of delamination in either of SFRM types.

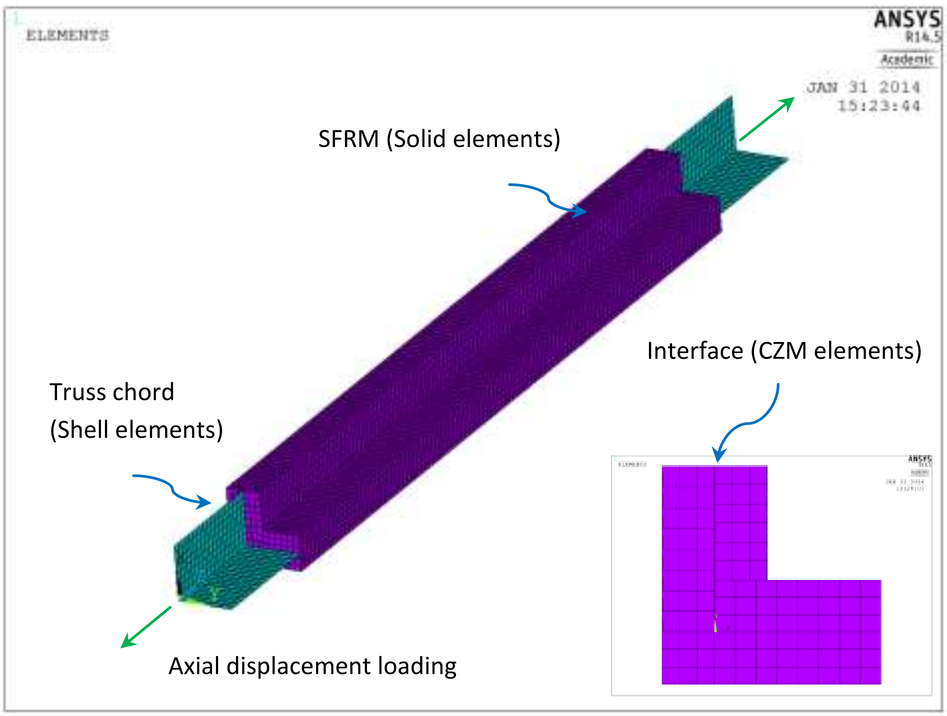

Figure 5.2 Finite element model of bottom chord of truss encapsulated with SFRM

It is interesting to note that Portland cement-based SFRM, which retains the highest fracture energy and cohesive strength, takes the lead in terms of onset of delamination at strain ductility level of 4.65, whereas, gypsum-based and mineral fiber-based SFRM show initiation of delamination at strain ductility level of 5.62 and 11.03, respectively. This is however believed to be due to the effect of SFRM elastic modulus, as well as cohesive displacement ductility which will be addressed shortly.

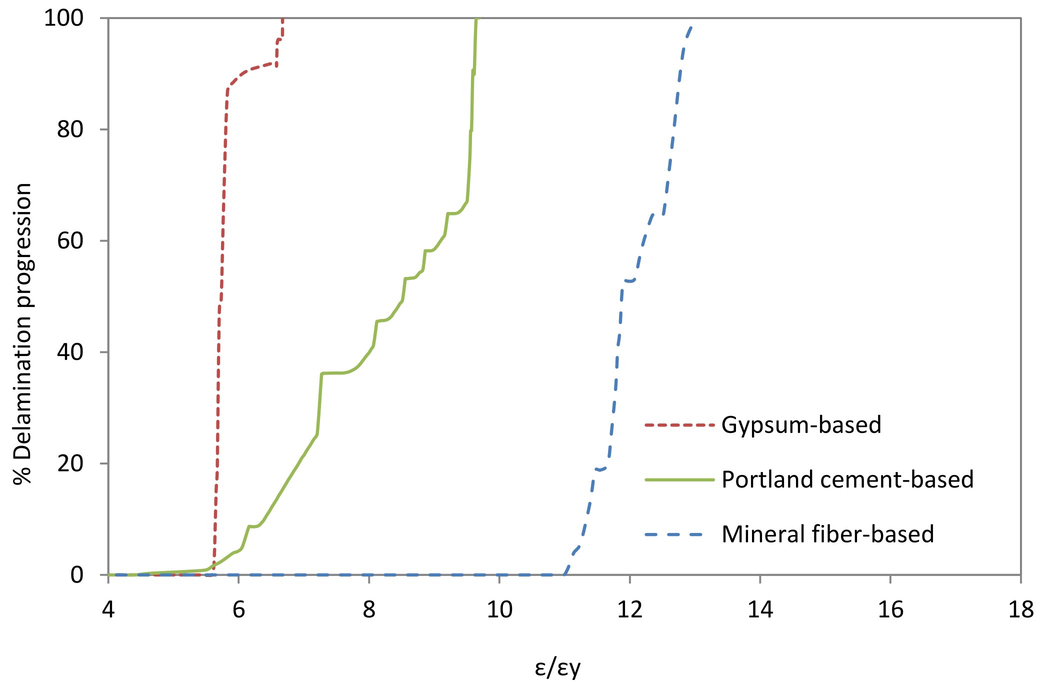

Figure 5.3 Percentage of delamination progression on outer sides of truss chord with respect to average axial strain developed in truss member

Further, the pace of delamination propagation is quite substantial, such that for gypsum-based SFRM, steel strain ductility demand at delamination initiation and completion are 5.62 and 6.67, respectively. That is, after delamination starts, it only takes additional strain equivalent to ε_y , for full delamination to occur over the member length. The delamination progression however occurs slower in the case of Portland cement-based SFRM due to higher level of fracture toughness and cohesive strength as compared to that in gypsum-based and mineral fiber-based SFRM.

As depicted in Figure 5.4, interfacial fracture initially takes place at both ends of the truss member and subsequently propagates towards the center of member. The fracture energy released separately at each fracture modes (mode-I and mode-II) is illustrated in Figure 5.5. It is apparent that, mixed-mode delamination is the case at both ends and also over a large area extending toward the center of member, whereas at vicinity of the mid-span, mode-I predominantly governs the fracture.

Table 5.1 shows that mineral fiber-based SFRM possesses the least cohesive strength, fracture energy and elastic modulus, while it carries the highest cohesive displacement ductility level. However, it is a point of interest that, despite the first expectation, mineral fiber-based SFRM demonstrates the superior performance compared to the other two SFRM types. This behavior can be attributed to the interdependency among the critical factors influencing the delamination process which is neglected in the current design provisions. In this case, though mineral fiber-based SFRM has the least cohesive strength and fracture energy, it seems that the higher displacement ductility of cohesive zone and lower elastic modulus has enhanced the delamination resistance of mineral fiber-based SFRM as compared to the other two SFRM types.

Table 5.1 Cohesive zone model parameters obtained in experiments for three types of SFRM

SFRM type	σ_{max} (kPa)	τ_{max} (kPa)	G_{nc} (J/m^2)	G_{tc} (J/m^2)	K_n (N/mm^3)	K_t (N/mm^3)	μ_n	μ_t	E (MPa)
Gypsum-based	22.9	49.6	7.9	32.8	0.057	0.108	1.73	2.98	11.5
Portland cement-based	52.8	107.3	33.7	74.4	0.057	0.163	1.40	2.11	38.4
Mineral fiber-based	13	24.6	4.3	22.5	0.039	0.061	2.03	4.63	2.6

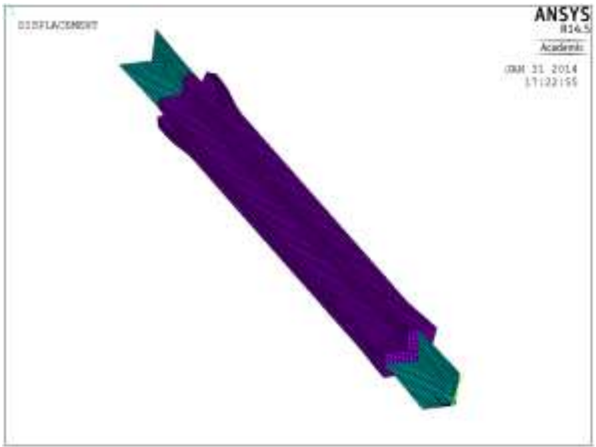

ε/ε_y=5.621

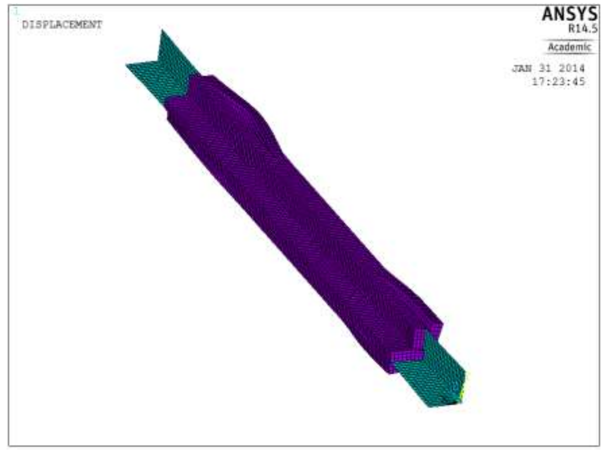

ε/ε_y=5.654

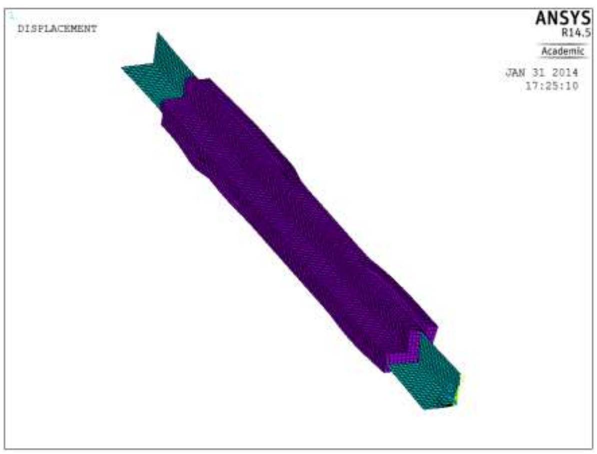

ε/ε_y=5.671

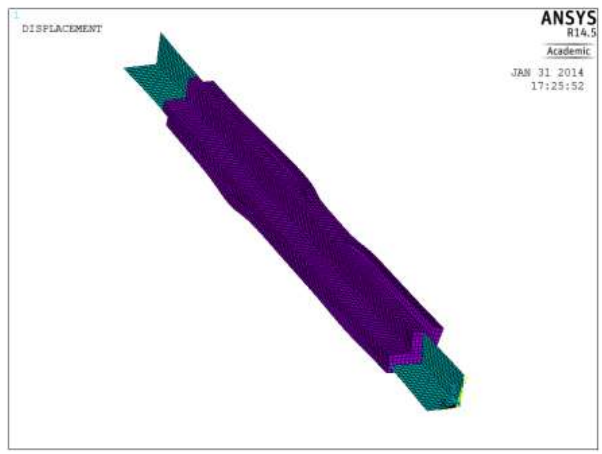

ε/ε_y=5.688

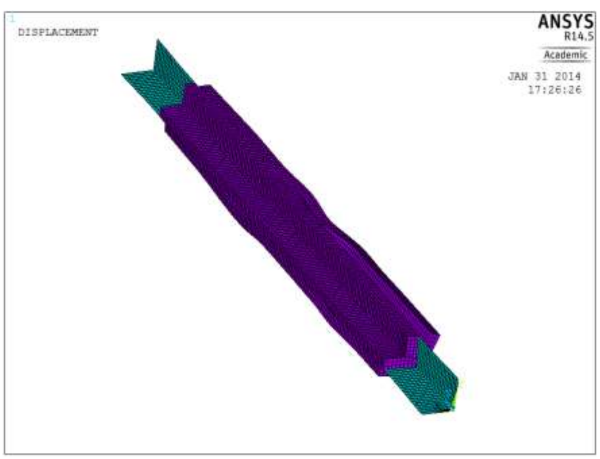

ε/ε_y=6.046

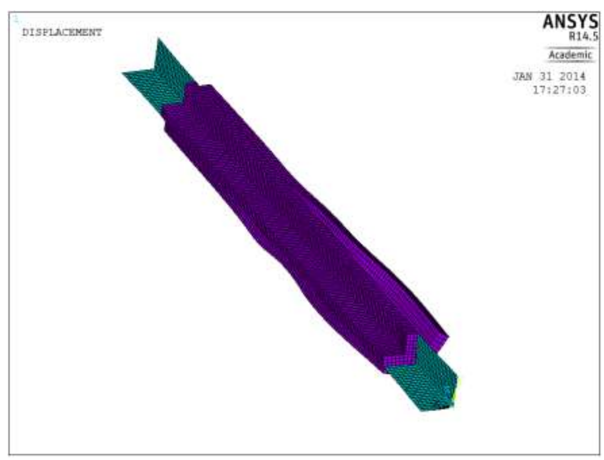

ε/ε_y=6.673

Figure 5.4 Crack propagation pattern at the interface of steel and gypsum-based SFRM at different strain levels

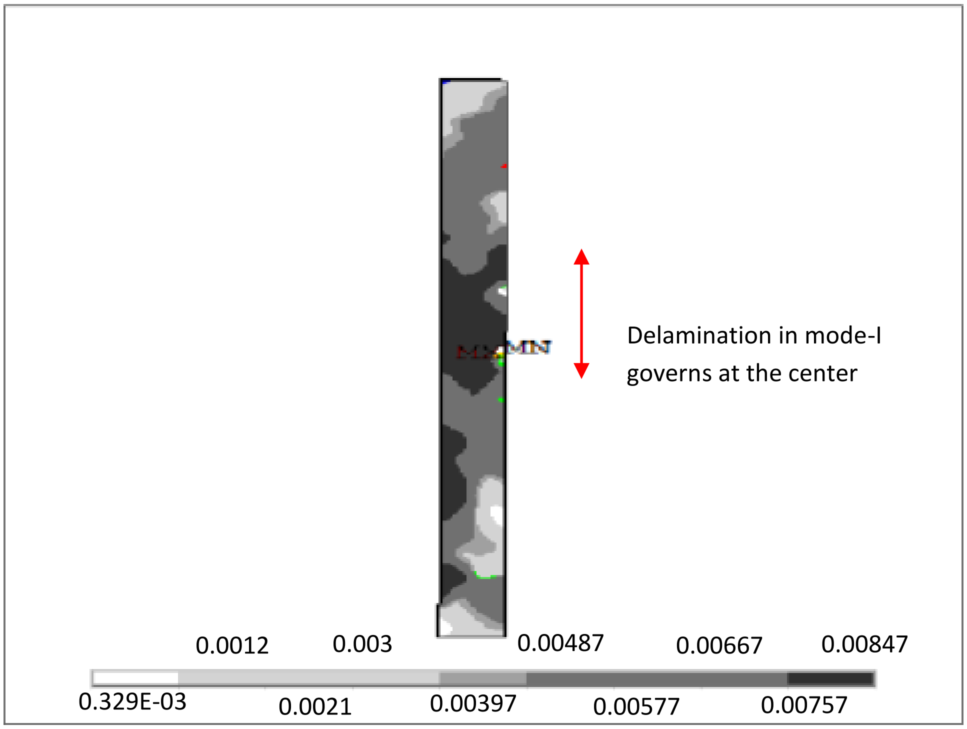

a) Mode-I energy release rate (G_n, N/mm)

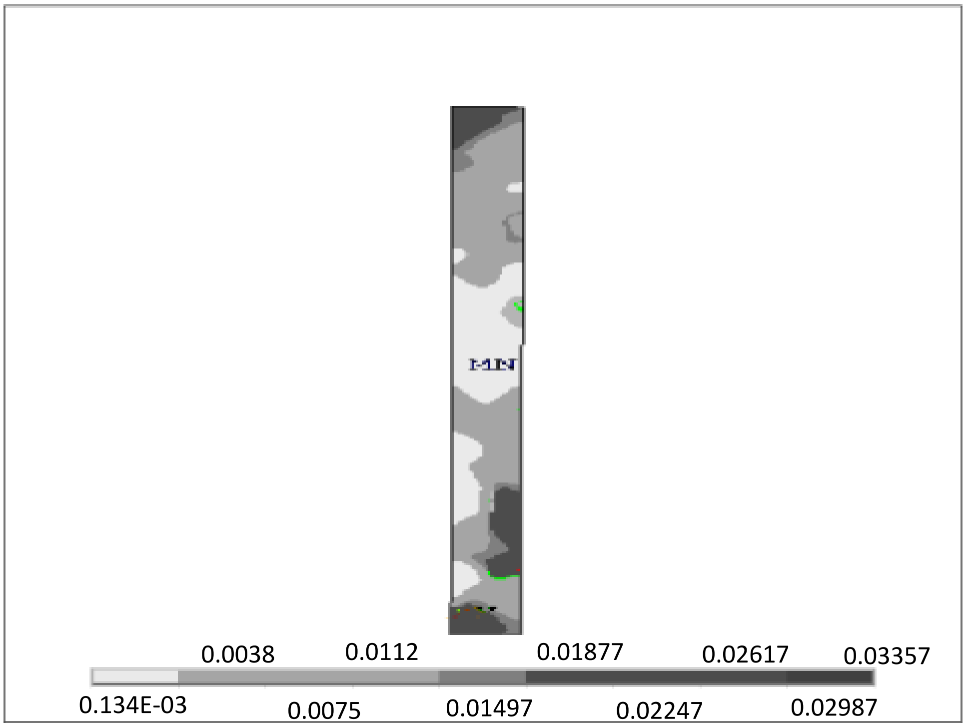

b) Mode-II energy release rate (G_t, N/mm)

Figure 5.5 Fracture energies released during delamination for gypsum

Numerical results presented in this section are based on average values obtained for cohesive zone parameters. To further prove the validity of interactions between previously mentioned factors, the effect of each critical factor is separately investigated in subsequent sections. Eventually, the interdependency of the critical factors is quantitatively represented through definition of a delamination characteristic parameter that incorporates all critical factors.

5.3.3 Effect of Variation in Cohesive Zone Parameters on Delamination

In this section, to explore the sensitivity of onset and completion of delamination of SFRM to cohesive zone parameters, a sensitivity study is carried out with respect to cohesive strength and fracture energy at both modes I and II. While keeping all other input parameters constant, the average value for chosen parameter is varied by ± 25 percentages to quantify its influence on steel strain ductility demand at initiation and completion of delamination. Note that, the chosen variation range covers the level of variation observed in experiments.

Figure 5.6 is self-explanatory in showing the analysis cases in the sensitivity study. It can be noticed that displacement ductility of cohesive zone is indirectly influenced when changing cohesive strength or fracture energy. In the case of constant cohesive strength (Figure 5.6a), the relationship among displacement ductility change and fracture energy change is direct. However, in the case of constant fracture energy (Figure 5.6b), the displacement ductility and cohesive strength change are inversely related. That is, by increasing the cohesive strength the displacement ductility is reduced and vice versa.

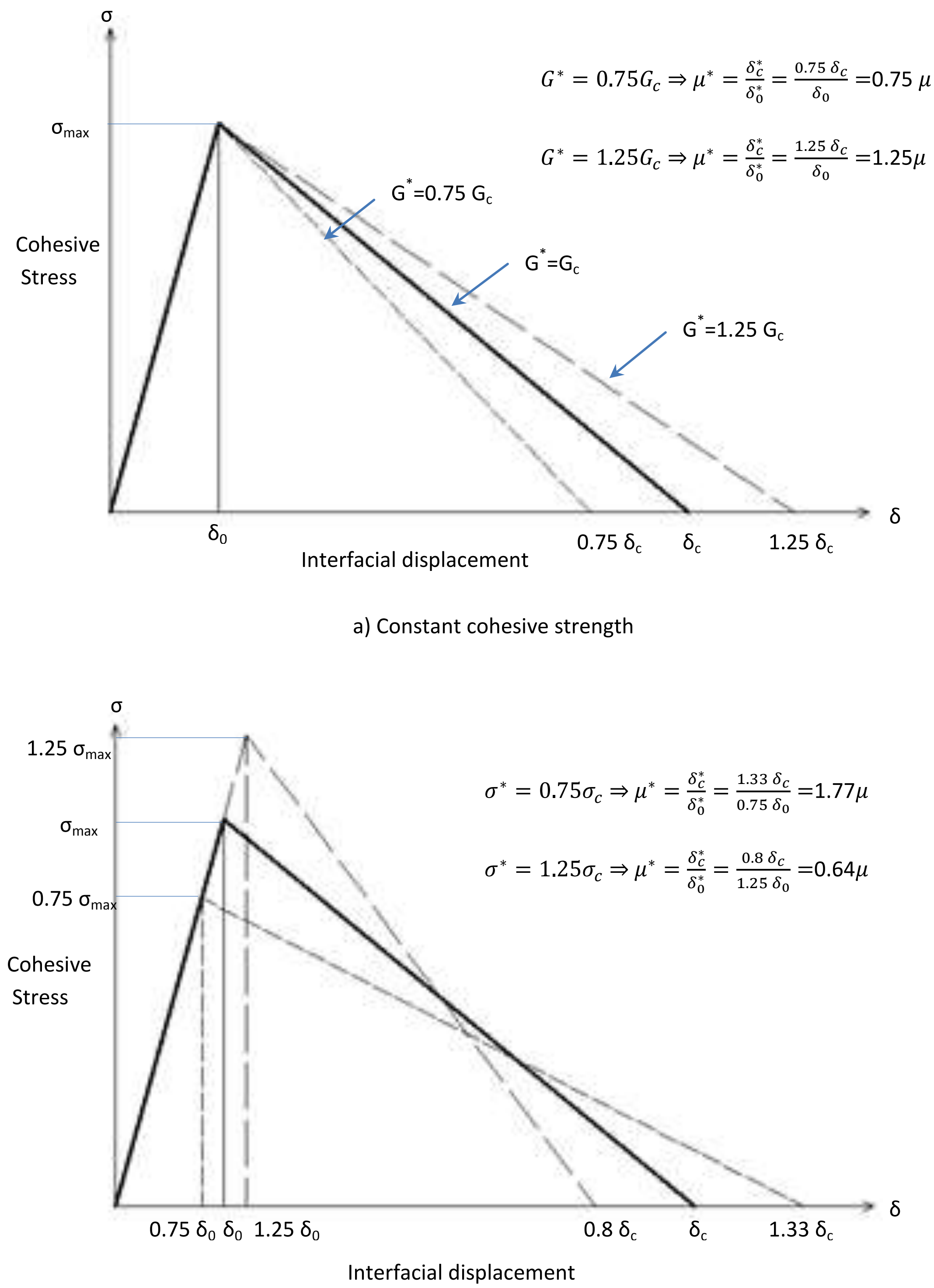

a) Constant cohesive strength

b) Constant fracture energy

Figure 5.6 Schematic view of various analyses cases for studying the sensitivity of delamination progression to CZM parameters

The results from sensitivity analysis with respect to fracture energy are depicted in Figure 5.7, Figure 5.8 and Figure 5.9, for gypsum-based SFRM, Portland cement-based SFRM and mineral fiber-based SFRM, respectively. It is noticed from above figures that delamination is delayed by increasing the fracture energy and accelerated by decreasing it for the three types of SFRM, as was expected. For instance, as a result of ± 25 percentage variation in fracture energy of gypsum-based SFRM, the steel strain at delamination onset changes by ± 10 percentages. However, once initiated, delamination is completed within a larger strain range, when the fracture energy is boosted. This can be attributed to the fact that, under constant cohesive stress, any increase in fracture energy enhances the displacement ductility of cohesive zone as well (as illustrated in Figure 5.6 a), thereby hampering the delamination propagation process.

The important role that displacement ductility of cohesive zone plays in SFRM delamination process is further revealed while assessing the effect of variation in cohesive strength on delamination. It is depicted in Figure 5.10, Figure 5.11 and Figure 5.12 that delamination onset is procrastinated when cohesive strength is decreased by 25 percentages, and on the contrary, delamination is accelerated by increasing the cohesive strength value. As shown in Figure 5.6b, 25 percentage decrease in cohesive strength leads to 77 percentage increase in displacement ductility of cohesive zone. Also, 25 percentage of rise in cohesive strength reduces ductility by 36 percentages. Therefore, it seems that influence of ductility change in consequence of cohesive strength change (under constant fracture energy) is predominant compared to effect of cohesive strength itself.

Therefore, by far, it can be concluded that strain ductility demand of steel at delamination onset and completion has a direct relationship with fracture energy release rate and displacement ductility of cohesive zone.

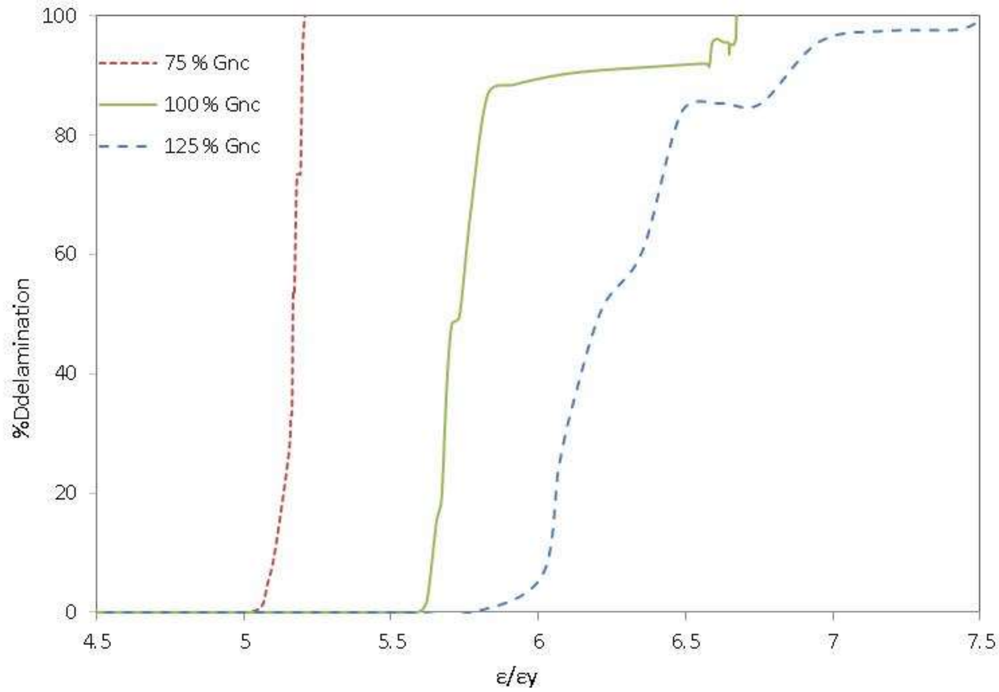

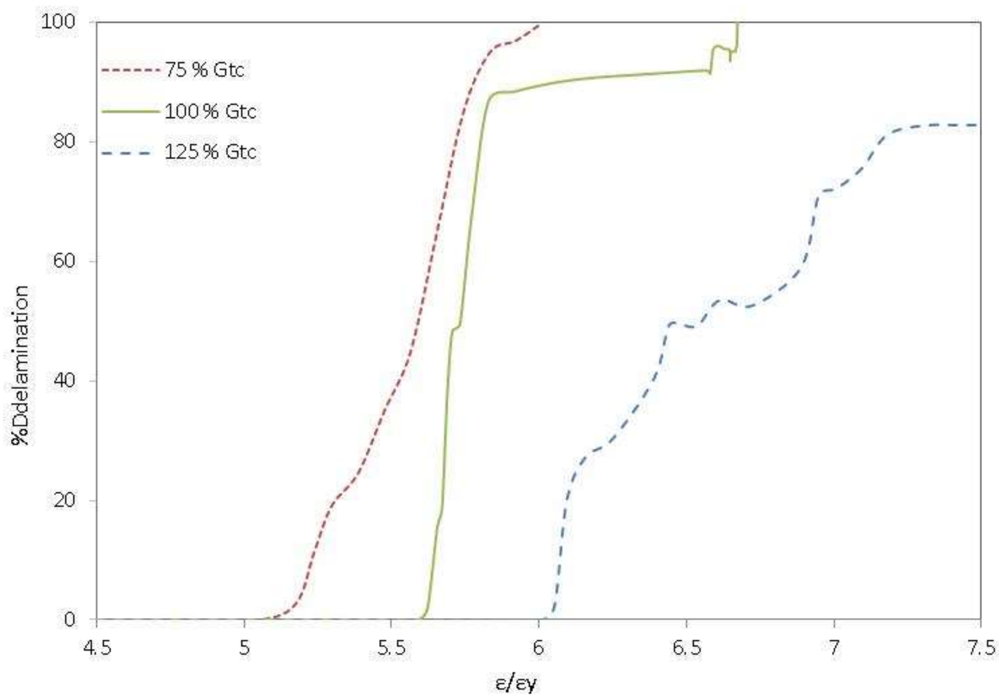

b) Effect of variation in mode-II fracture energy

Figure 5.7 Effect of fracture energy of gypsum-based SFRM on initiation and progression of delamination in truss member under tension

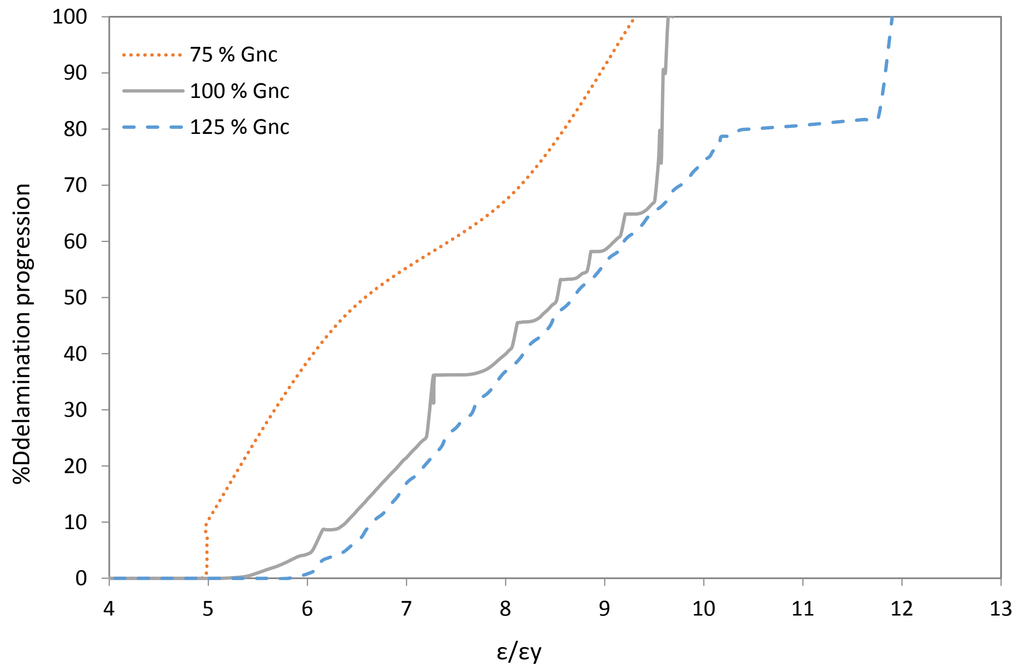

a) Effect of variation in mode-I fracture

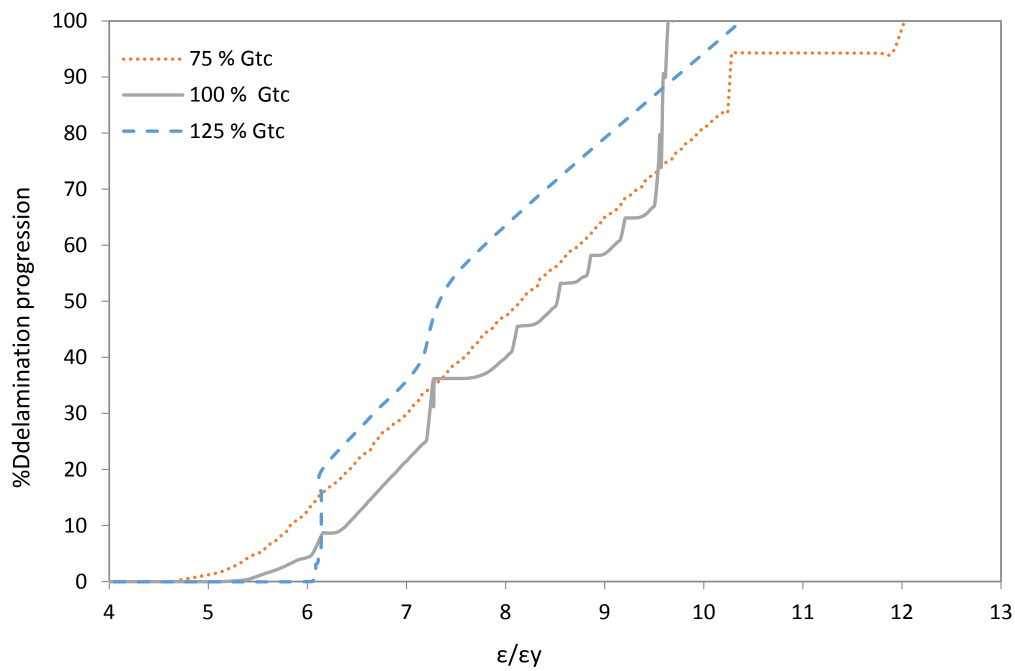

b) Effect of variation in mode-II fracture energy

Figure 5.8 Effect of fracture energy of Portland cement-based SFRM on initiation and progression of delamination in truss member under tension

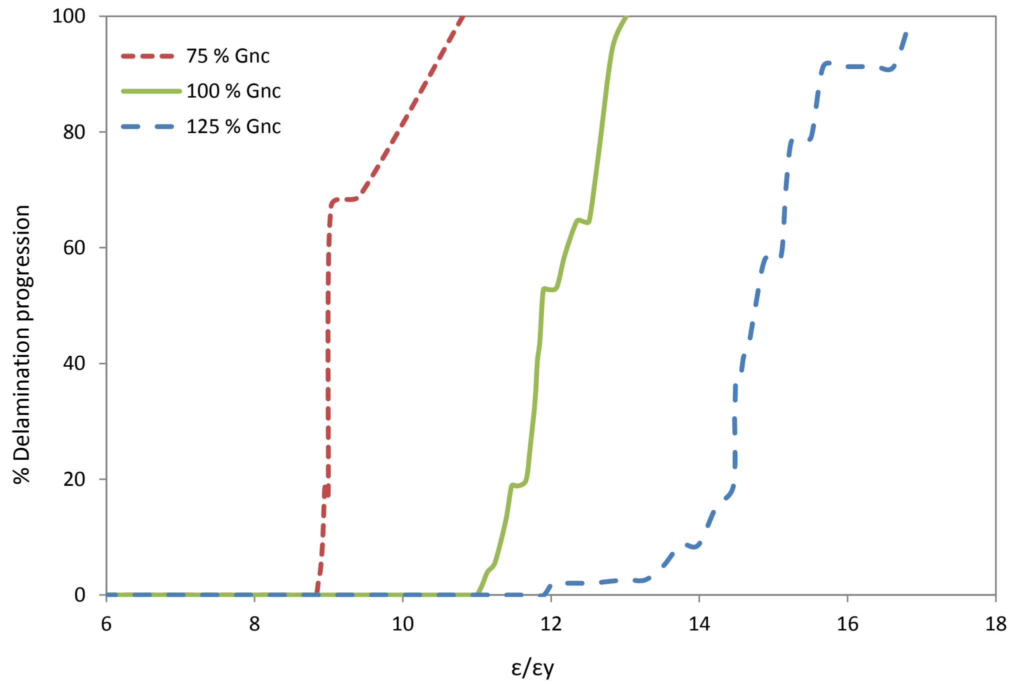

a) Effect of variation in mode-I fracture

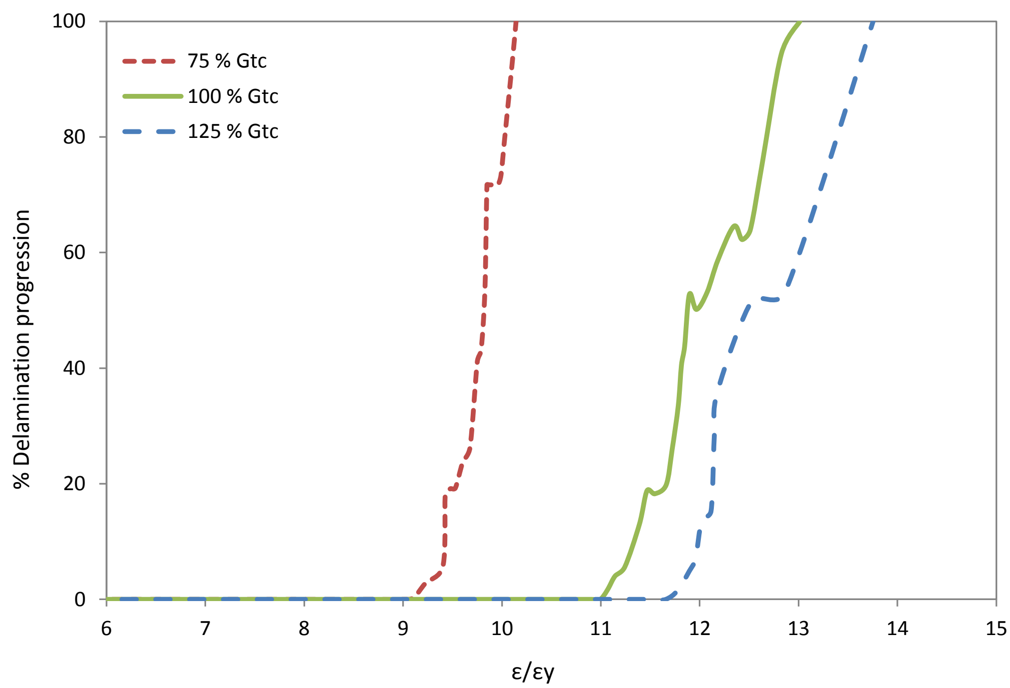

b) Effect of variation in mode-II fracture energy

Figure 5.9 Effect of fracture energy of Mineral fiber-based SFRM on initiation and progression of delamination in truss member under tension

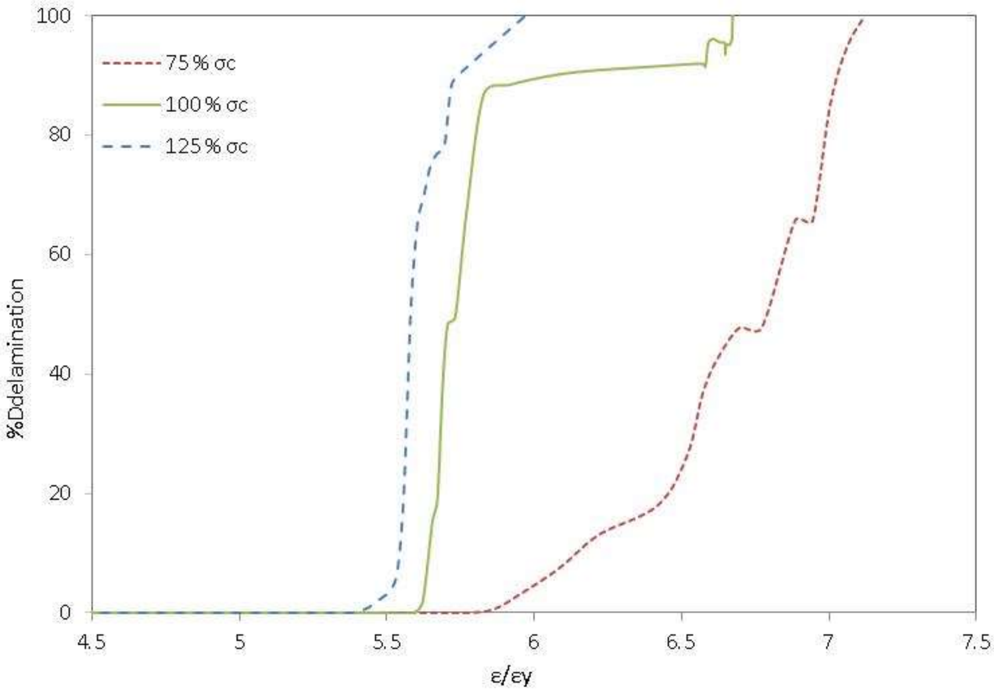

a) Effect of normal cohesive strength

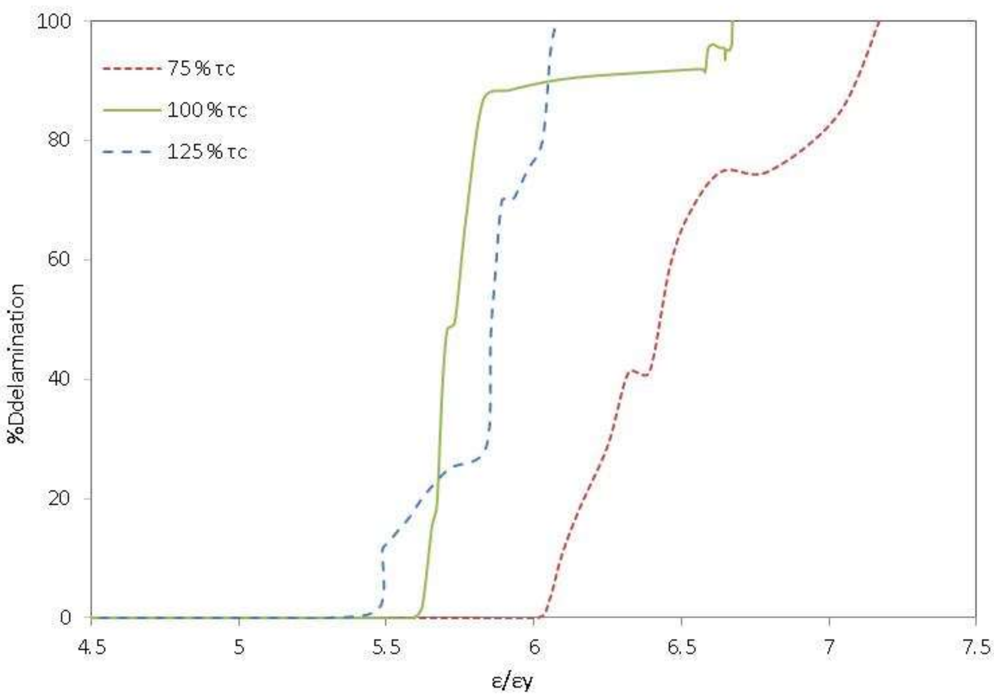

b) Effect of shear cohesive strength

Figure 5.10 Effect of cohesive strength of gypsum-based SFRM on initiation and progression of delamination in truss member under tension

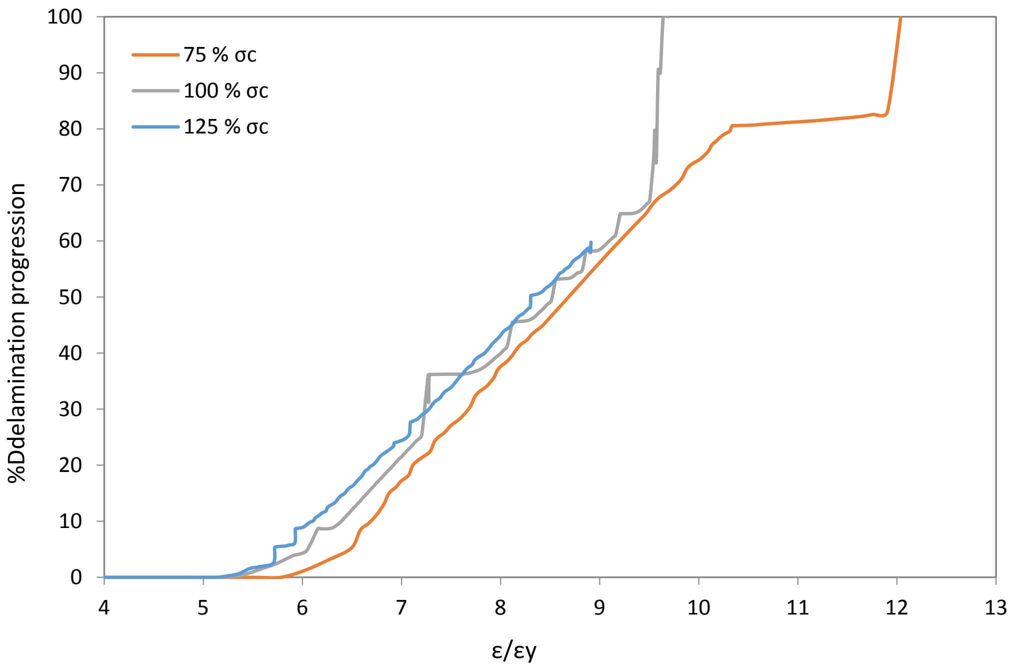

a) Effect of normal cohesive strength

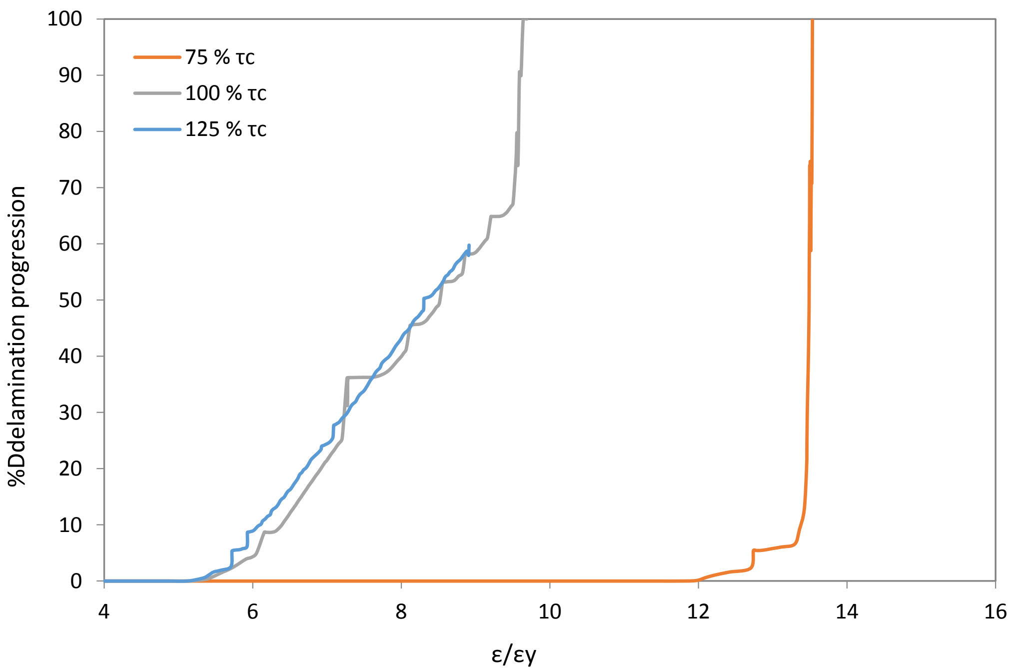

b) Effect of shear cohesive strength

Figure 5.11 Effect of cohesive strength of Portland cement-based SFRM on initiation and progression of delamination in truss member under tension

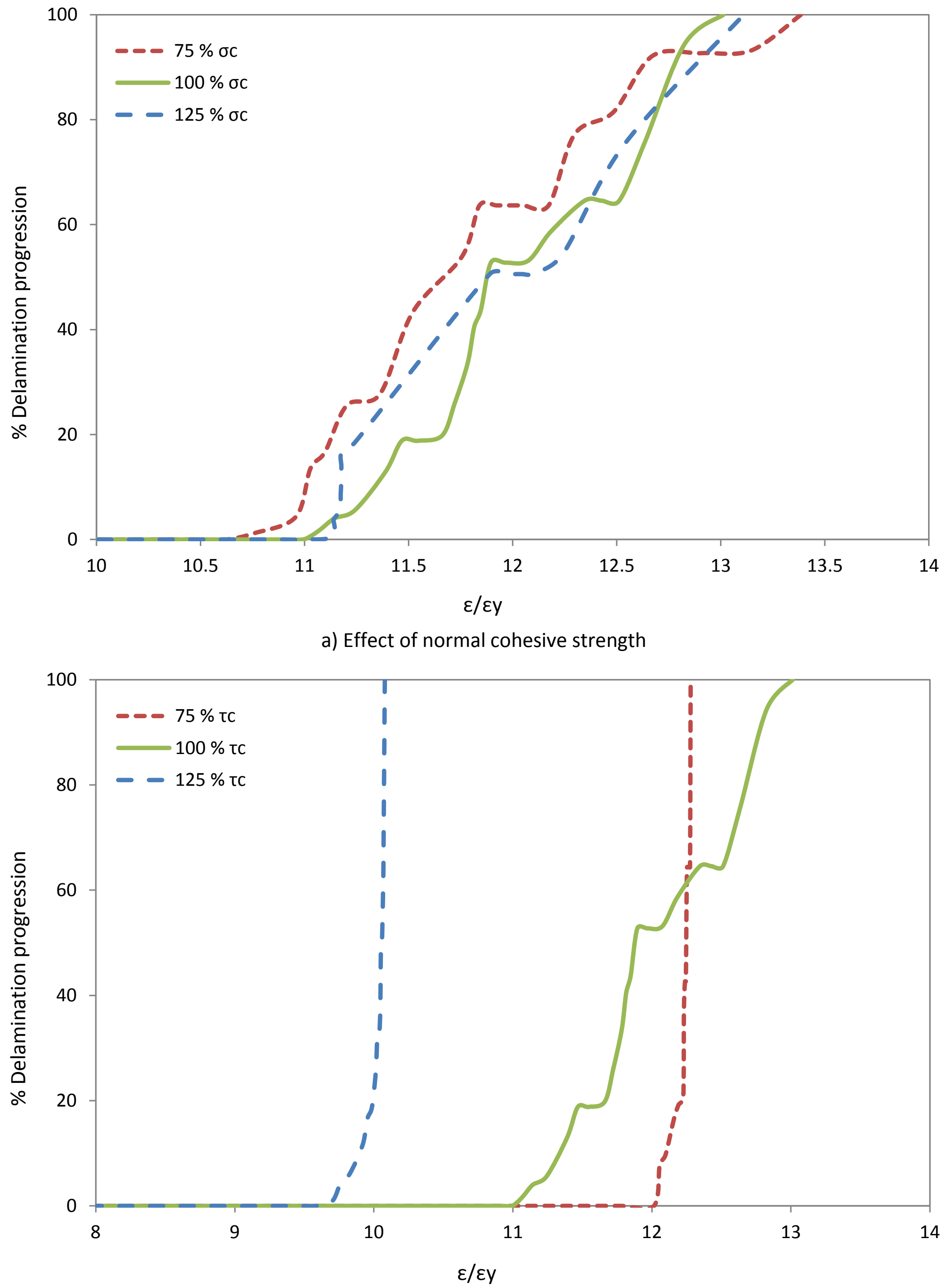

a) Effect of normal cohesive strength

b) Effect of shear cohesive strength

Figure 5.12 Effect of cohesive strength of Mineral fiber-based SFRM on initiation and progression of delamination in truss member under tension

5.3.4 Effect of Variation in SFRM Elastic Modulus

It was previously shown that mineral fiber-based SFRM, which possesses the least elastic modulus, demonstrated the most delayed fracture. To further prove the significant effect of elastic modulus of SFRM on delamination process, the average elastic modulus value is varied by ± 25 percentage and corresponding analyses are carried out. Figure 5.13, Figure 5.14 and Figure 5.15 show that, increasing the elastic modulus of SFRM leads to early delamination and vice versa. When the load is not directly applied on SFRM, but the load is carried through the steel substrate, increasing the flexibility of SFRM procrastinates the internal and interfacial fractures, thereby enhancing the performance of SFRM to great extent. The strain ductility demand of steel at delamination initiation and completion can therefore be inversely related to elastic modulus.

Higher tendency for delamination in stiffer SFRM can be attributed to the fact that when the elastic modulus of SFRM is increased it becomes harder for SFRM to maintain the strain compatibility at SFRM-steel interface and hence the interfacial delamination is expedited to accommodate large strains. In fact, by increasing modulus of elasticity, strain level decreases in SFRM, while the strain in steel remains at the same level. Consequently, higher differential strain develops at the steel-SFRM interface that results in premature delamination of SFRM from steel surface.

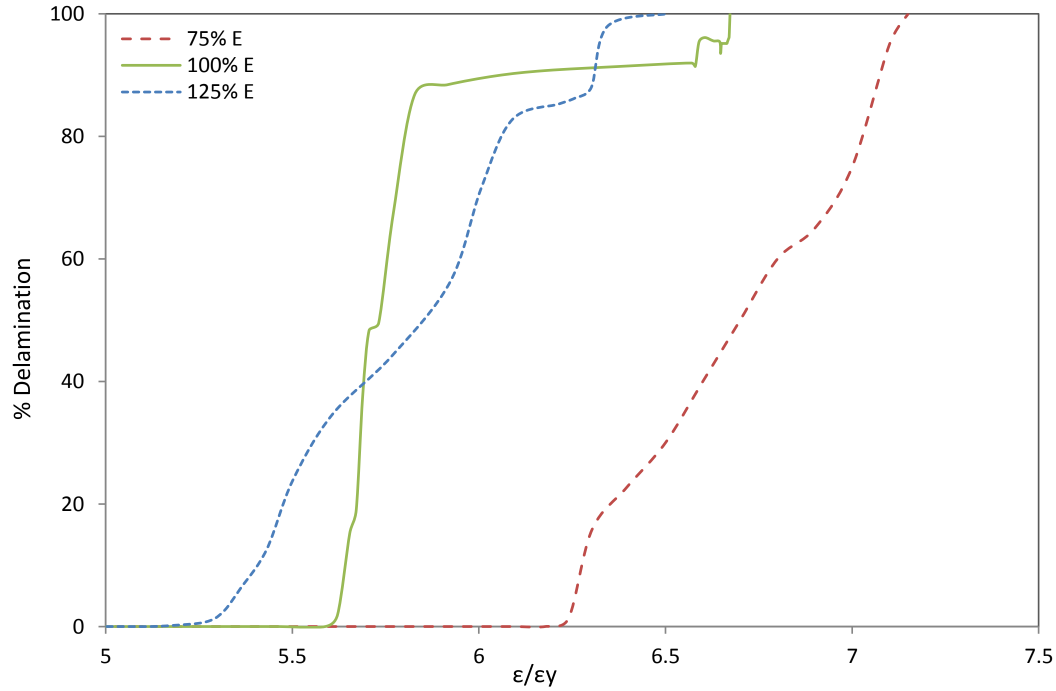

Figure 5.13 Effect of SFRM elastic modulus on initiation and progression of delamination in truss member under tension (Gypsum-based SFRM)

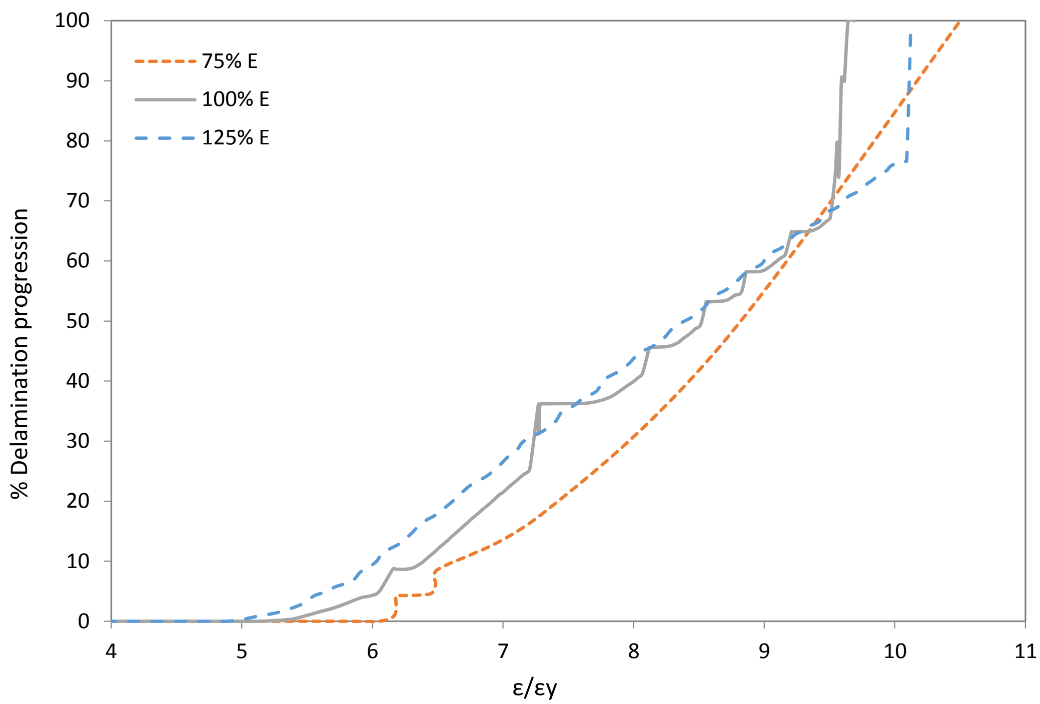

Figure 5.14 Effect of SFRM elastic modulus on initiation and progression of delamination in truss member under tension (Portland cement-based SFRM)

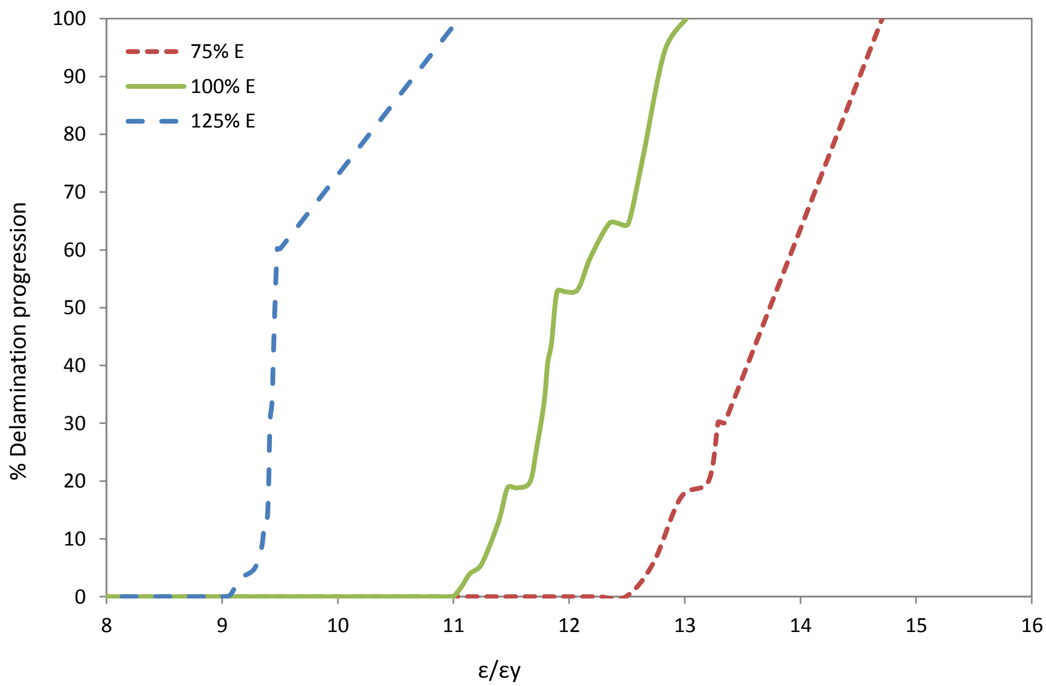

Figure 5.15 Effect of SFRM elastic modulus on initiation and progression of delamination in truss member under tension (Mineral fiber-based SFRM)

The variation of percentage of delamination versus strain ductility demand in steel is plotted in Figure 5.16, Figure 5.17 and Figure 5.18 for four incremental thicknesses. In above figures, increasing trend in strain ductility demand of steel at initiation and completion of delamination is noticeable as SFRM thickness decreases. However, this tendency is nonlinear. As such, in the case of gypsum-based SFRM, reducing thickness from 20 mm to 10 mm delays the delamination onset by 57 percentages. Whereas, increasing thickness from 20 mm to 30 mm accelerates delamination by only 16 percentages.

In essence, the higher the cross sectional area of insulation, the higher the amount of energy absorbed. While the absorbed energy needs to be mobilized at the interface of steel and SFRM, the critical fracture energy at the interface remains constant from thicker to thinner insulation. Hence, it is concluded that, strain ductility demand in steel at initiation and completion of delamination can be inversely related to thickness of SFRM.

5.3.5 Effect of Variation in SFRM Thickness

To quantify the effect of thickness of SFRM on delamination phenomenon, the thickness of SFRM applied on the truss chord is varied within a practical range of 10 mm to 40 mm, while average properties are used for other parameters.

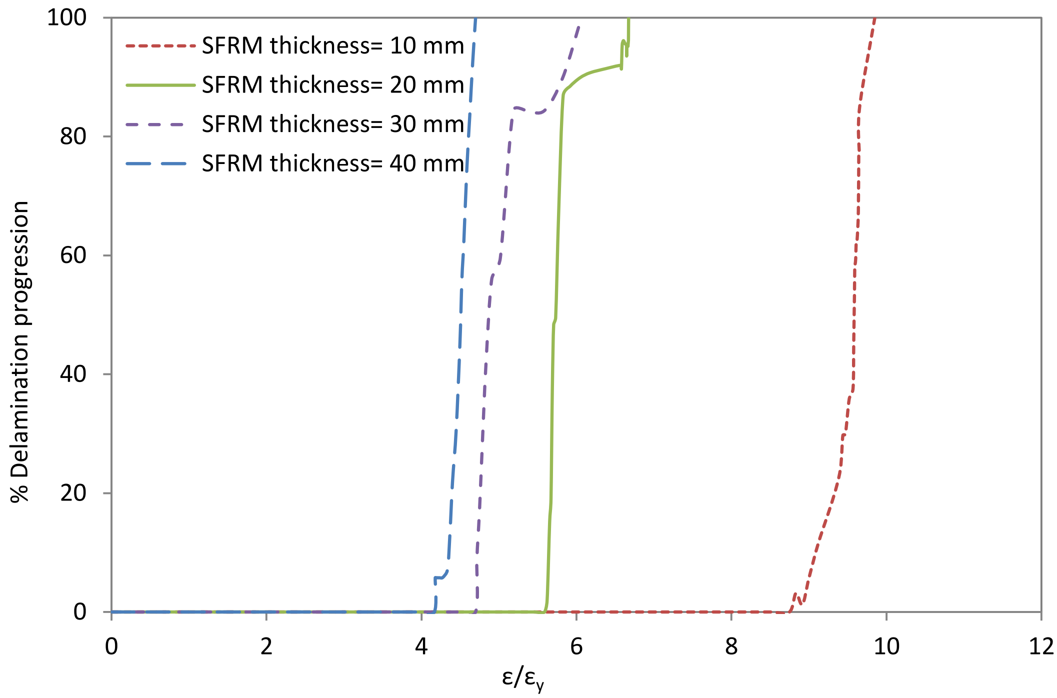

Figure 5.16 Effect of SFRM thickness on initiation and progression of delamination in truss member under tension (Gypsum-based SFRM)

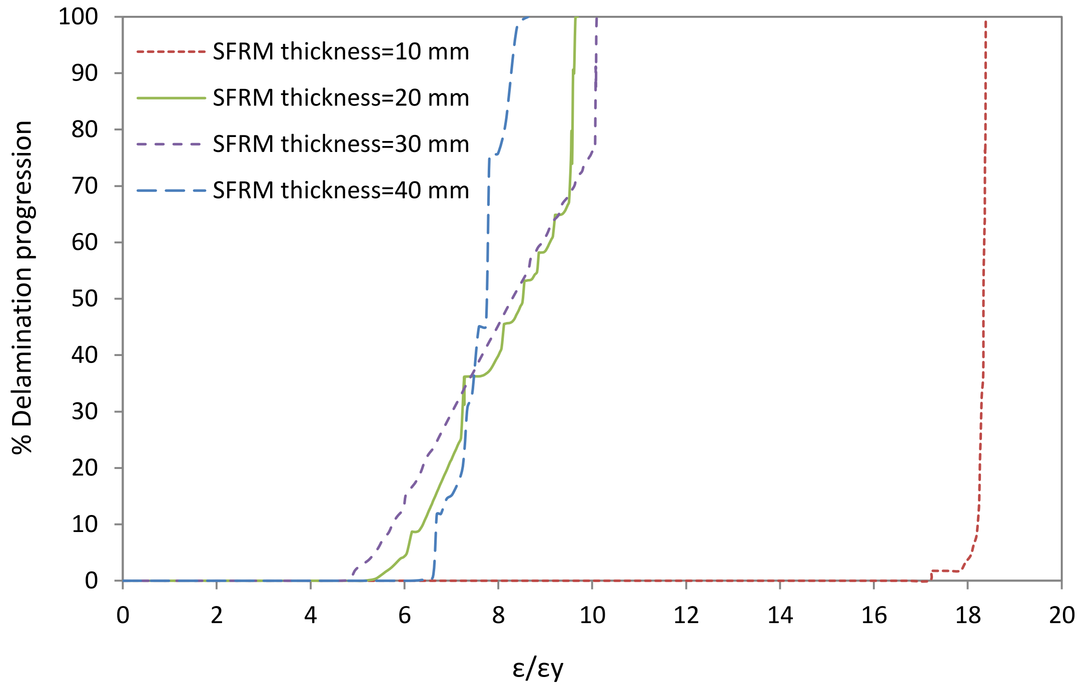

Figure 5.17 Effect of SFRM thickness on initiation and progression of delamination in truss member under tension (Portland cement-based SFRM)

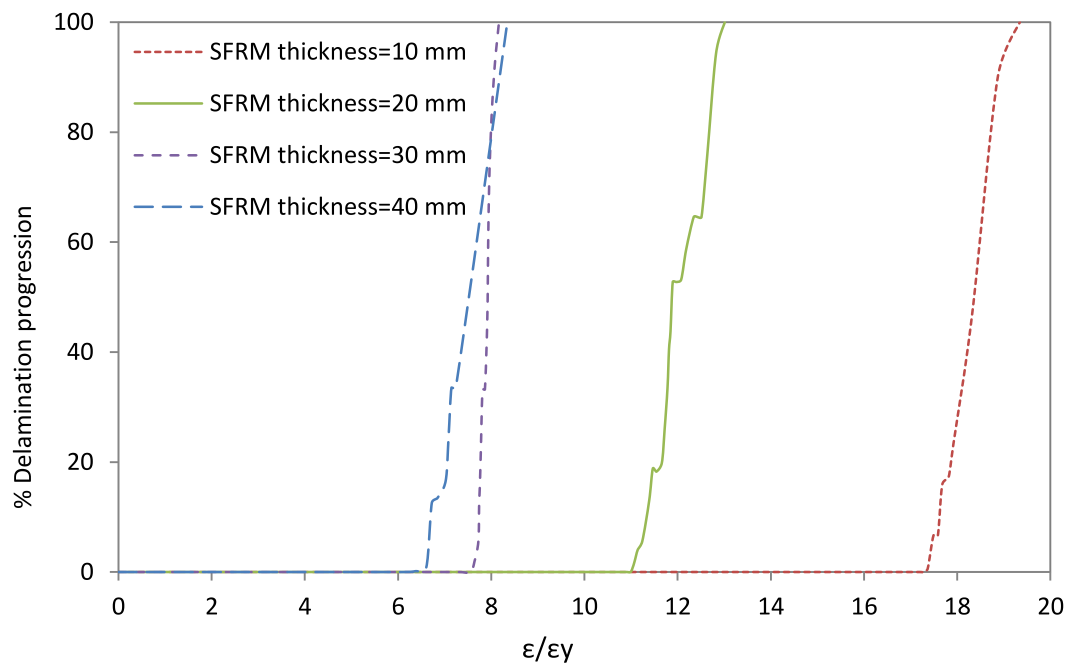

Figure 5.18 Effect of SFRM thickness on initiation and progression of delamination in truss member under tension (Mineral fiber-based SFRM)

5.3.6 Parameter for Characterizing Delamination of SFRM

Results of numerical simulations explained in preceding section suggests that, despite the current tendency, cohesive strength (or in other words bonding strength) alone cannot characterize the fracture performance of SFRM. Consequently, cohesive strength is not the only reliable parameter to distinguish the performance of SFRM with respect to delamination from steel surface. Definition of a characteristic parameter is therefore required to account for all critical factors influencing the delamination process, thereby quantifying the interdependency among them. In line with the conclusions made at the end of previously discussed sensitivity study, a delamination characteristic parameter is defined as:

$$d_{ch} = \frac{E.t}{\bar{\mu}\bar{G}_c} \tag{5.1}$$

where, E and t are elastic modulus and thickness of SFRM and $\bar{\mu}$ and $\bar{G}$ are equivalent displacement ductility of cohesive zone and fracture energy of SFRM, respectively. The parameter $\bar{\mu}$is expressed as:

$$\bar{\mu} = \sqrt{{\mu_n}^2 + {\mu_t}^2} \tag{5.2}$$

where, μ_n and μ_t are displacement ductility of cohesive zone for mode-I and Mode-II fracture, respectively and are computed as:

$$\mu_n = \frac{\delta_{n,c}}{\delta_{n,0}} \tag{5.3}$$

$$\mu_t = \frac{\delta_{t,c}}{\delta_{t,0}} \tag{5.4}$$

The term$\bar{G}_c$ is expressed as:

$$\bar{G}_c = \sqrt{G_{nc}{}^2 + G_{tc}{}^2} \tag{5.5}$$

where, G_{nc} and G_{tc} are fracture energy release rates for mode-I and Mode-II fracture, respectively. Note that cohesive strength is already embedded in $\bar{G}$value.

Results from previous analyses are compiled in one figure where strain ductility demand in steel at initiation of delamination ($\mu_{s,i} = \varepsilon_{s,i}/\varepsilon_y$) is plotted against the delamination characteristic parameter of SFRM (d_{ch}) in Figure 5.19. A curve fitting to the existing data reveals a power-law relationship between $\mu_{s,i}$ and d_{ch}, that is expressed as:

$$\mu_{s,i} = 8.1 \left(\frac{E.t}{\bar{\mu}.\bar{G}_c}\right)^{-0.37} \tag{5.6}$$

As it can be realized in Figure 5.19, for the practical range of d_{ch}, ductility demand in steel at which the delamination initiates falls between 4 and 18 depending on the SFRM characteristics. Obviously, fracture performance of SFRM improves as the d_{ch} value decreases. Further, while $\mu_{s,i}$ value is substantially sensitive to d_{ch} value less than 1, it remains almost constant for d_{ch} value beyond 2.

In Figure 5.20, strain ductility demand in steel at completion of delamination over the member length ($\mu_{s,f} = \varepsilon_{s,f}/\varepsilon_y$) is plotted against the delamination characteristic parameter of SFRM (d_{ch}). Again, power-law gives the best fit for the data. The associated relationship is expressed as:

$$\mu_{s,f} = 10.2 \left(\frac{E.t}{\bar{\mu}.\bar{G}_c}\right)^{-0.25} \tag{5.7}$$

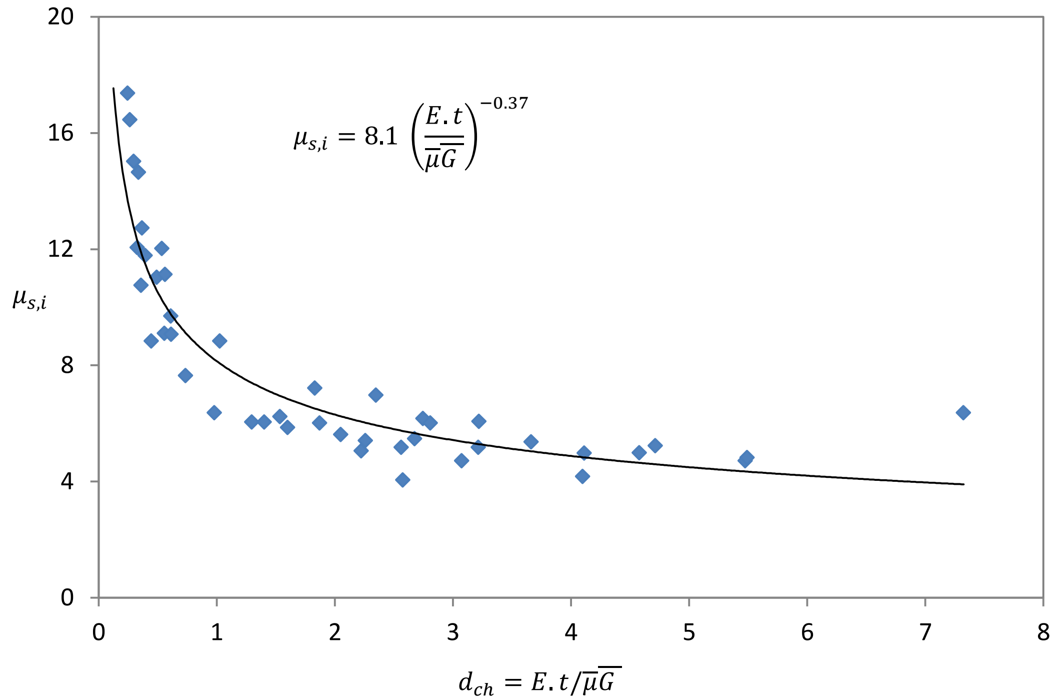

Figure 5.19 Strain ductility demand of steel at delamination initiation versus delamination parameter

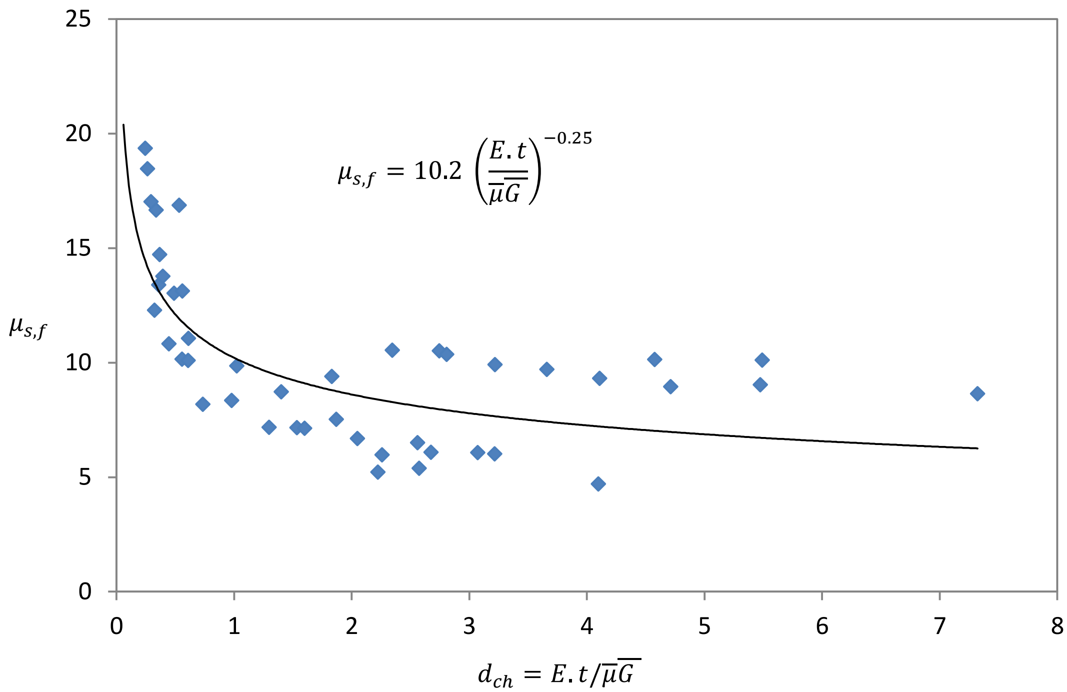

Figure 5.20 Strain ductility demand of steel at complete delamination versus delamination parameter

According to Figure 5.20, for practical range of mechanical properties of SFRM (reflected in d_{ch}), strain ductility demand in steel spans between 5 to 20 when SFRM is fully delaminated from truss chord. In addition, when d_{ch} value exceeds 2, $\mu_{s,f}$ becomes steady. It should be noted that, in the case of extreme loading events, strain ductility demands can reach a value of 20 or more depending on the severity of loading. Consequently, the full delamination of SFRM over critically loaded truss members can occur even for the SFRM with very low value of delamination characteristic parameter.

It should be noted that the above delamination characteristic parameter was defined based on the results obtained under quasi-static loading. As will be outlined in following sections, depending on the loading condition this parameter should be revised or modified to conform to the behavior of SFRM under a specific loading condition.

5.4 Delamination of Fire Insulation from Steel Beam-Column Assembly under Seismic Loading

A set of parametric studies are carried out to quantify critical parameters affecting delamination of SFRM from steel surface under the action of cyclic loading. The parametric study is carried out on a beam-column assembly tested by Braxtan and Pessiki (2011b), which was chosen for validating the numerical model in chapter 4 under different insulation configuration. The effect of cohesive strength and fracture energy at SFRM-steel interface, SFRM thickness and modulus of elasticity of SFRM is studied.

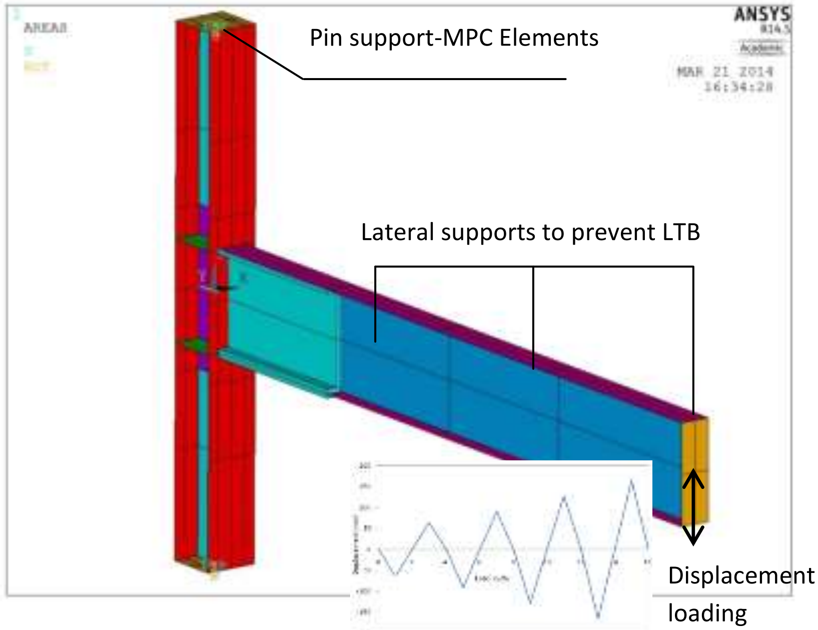

a) Loading and boundary condition

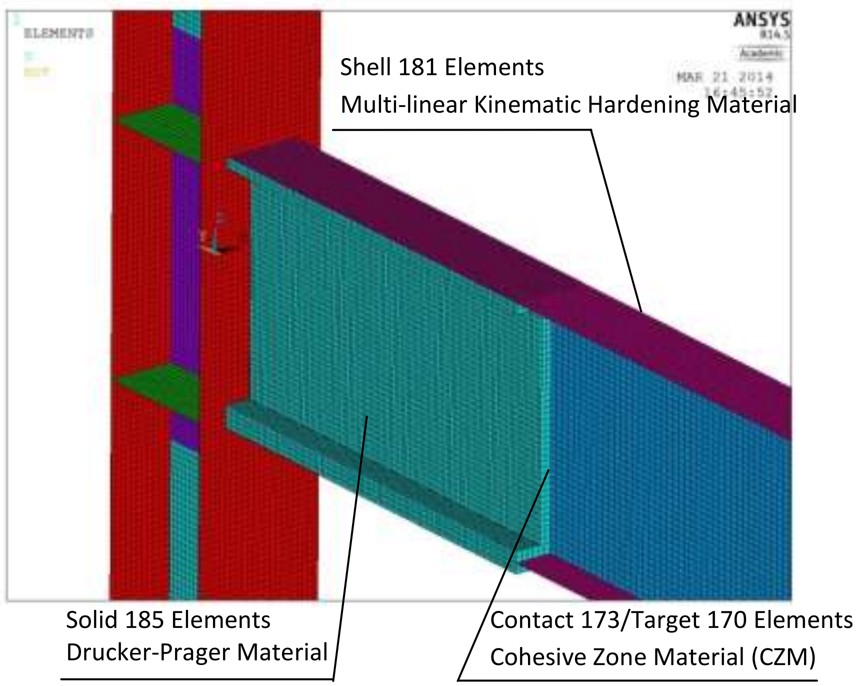

b) Element types and material models

Figure 5.21 Finite element model of beam-column assembly used for parametric study under seismic

5.4.1 Analysis Details

The finite element model of the beam-column assembly is illustrated in Figure 5.21. The beam-column assembly is discretized using shell elements (SHELL181) and SFRM is discretized using solid elements (SOLID185). The shell elements and solid elements which are interacting are bordered by contact and target (CONTACT173 and TARGET173) elements to establish the interaction between steel and SFRM. The contact elements follow the stress-displacement behavior defined as cohesive zone model, as shown in Figure 3.11.

A delamination problem in this scale entails tremendous amount of computational effort due to presence of contact interactions and material softening. With this in mind, and given the fact that initial cracks do not form until hitting a drift level of 1.53% (according to results from verification analyses), only last four steps of FEMA loading protocol was used in this parametric study. Also, the number of cycles is reduced to one at each load step to make computational time manageable. The displacement loading adopted in parametric studies is shown in Figure 5.22.

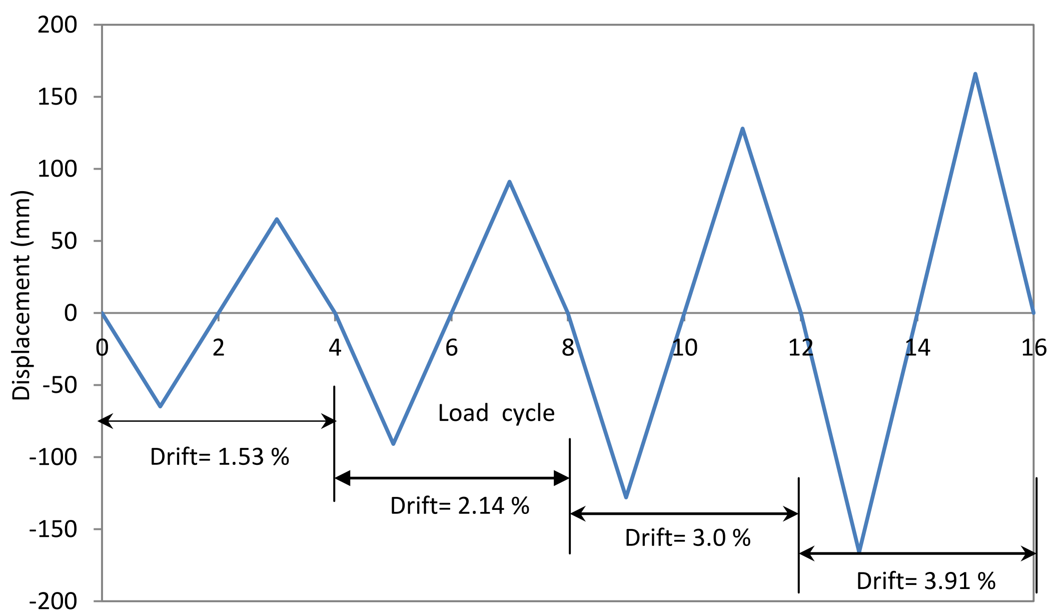

Figure 5.22 Cyclic displacements applied at beam tip for parametric study

During cyclic loading, beam flange is subjected to sequential compressive and tensile forces. In this event, flange local buckling can accelerate crack initiation at the interface of steel and SFRM. Further, the sequential loading and unloading cycles can result in damage accumulation at the interface of steel and SFRM. When the effect of flange local buckling is combined with the effect of SFRM damage accumulation, severe delamination can occur at SFRM-steel interface. Therefore, the beam flange is chosen as target surface over which extent of delamination is monitored.

5.4.2 Effect of Type of SFRM

The extent of delamination of three types of SFRM over bottom flange of the beam is plotted versus loading cycles in Figure 5.23. The crack initiation starts when drift level (displacement of tip of the beam divided by length of the beam) reaches to 3% in beam-column assembly insulated with gypsum-based SFRM and Portland cement-based SFRM. It is a point of interest, that only 20% of delamination occurs by downward movement of the beam when drift reaches to 3%. Subsequently, the crack progression continues during unloading phase which leads to complete separation over the plastic hinge region. However, in case of mineral fiber-based SFRM, cracks do not get opened until reaching to drift level of 3.91%. The delamination extends up to 40% of the insulated length on the bottom flange of the beam.

The above results pinpoint two important characteristics of SFRM behavior under seismic loading. First, despite the fact that fracture energy of Portland cement-based SFRM is higher than gypsum-based SFRM, upon reaching to a certain deformation level both material show a similar behavior. That means, for a specific range of material properties delamination under extreme seismic deformation is inevitable. Second, considerably lower level of extent of delamination in case of gypsum-based SFRM, in spite of its lower fracture energy compared to two other types of SFRM suggests that there is another parameter, i.e. elastic modulus of SFRM, which is playing an important role. The lesser amount of elastic modulus for gypsum-based SFRM makes it flexible helping this material to resist crack initiation and propagation under seismic loading. The reason for higher tendency of delamination in SFRM with higher elastic modulus was explained in section 5.3.4.

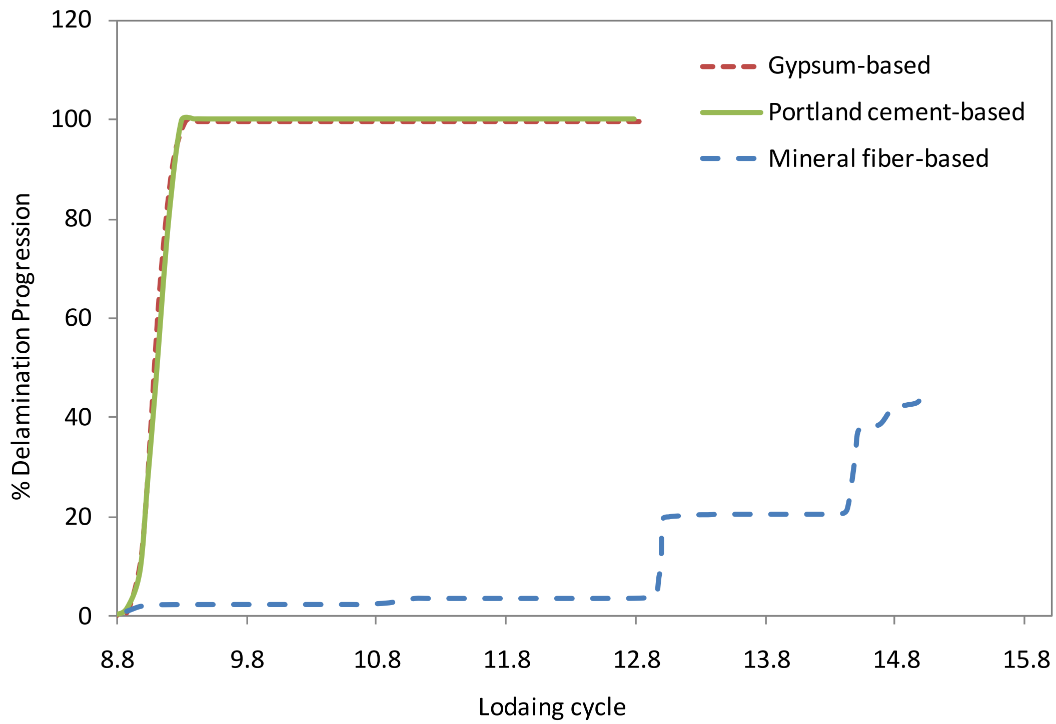

Figure 5.23 Percentage of delamination of three types of SFRM applied on the beam in a beam column assembly subjected to seismic loading

5.4.3 Effect of Cohesive Strength and Fracture Energy

The fracture tests conducted in this study shows that cohesive strength and fracture energy of SFRM can vary by 25%. To quantify the effect of uncertainties in cohesive zone properties, a set of parametric studies is carried out by varying the cohesive strength and fracture energy within a range of ±25%. This is undertaken for the three types of SFRM. The extent of delamination at bottom flange of steel beam is plotted against loading cycle in Figure 5.24, Figure 5.25 and Figure 5.26 for three types of SFRM to show the effect of variation in fracture energy on extent of delamination. The results in above figures include variation in both normal fracture energy and tangential fracture energy.

Figure 5.24a depicts that 25% variation in mode-I fracture energy of gypsum-based SFRM does not have substantial effect on the drift level at which crack initiation occurs. However, reduction in normal fracture energy leads to acceleration in fracture extension. For instance, at drift of 3% the percentage delamination increases from 20% to 40%. Subsequently, delamination is completed during unloading phase with higher speed. Further, it is clear that 25% enhancement in fracture energy cannot prevent complete delamination, since despite slight reduction in delamination percentage during the critical loading cycle (i.e. drift of 3%), 100% of SFRM ultimately detaches from steel surface.

As shown in Figure 5.24b, reducing mode-II fracture energy by 25% has negligible effect on initiation, progression speed and final extent of delamination. On the contrary, enhancement of mode-II fracture energy by 25%, though does not affect drift level at which crack formation starts, it dramatically hinders crack propagation. As such, full delamination does not occur during downward movement at drift of 3% and further crack propagation is postponed to upward movement at same drift level. This type of behavior implies that the reason why delamination extends during unloading phase of downward movement at drift of 3% is due to lower shear fracture resistance at the interface of SFRM and steel. When shear fracture resistance in boosted crack propagation is arrested.

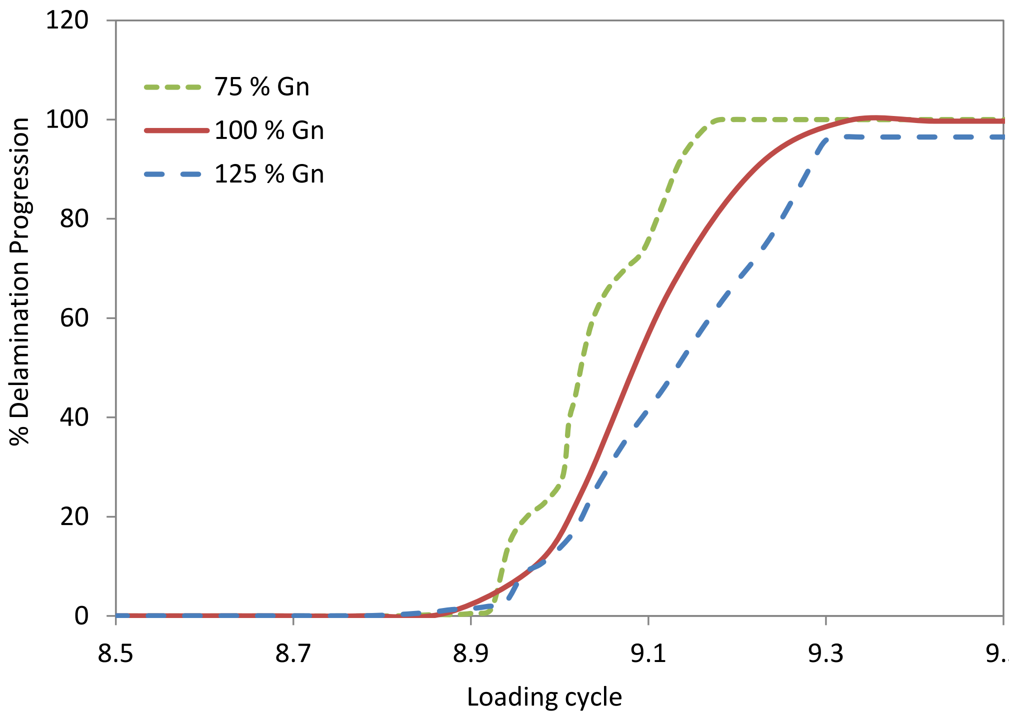

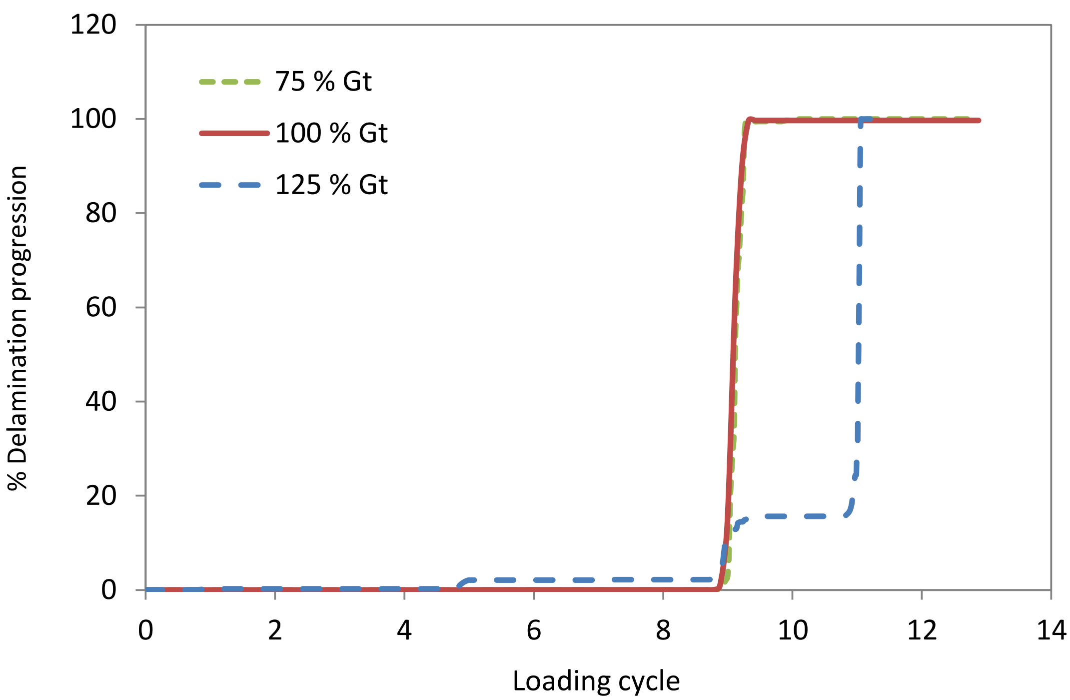

b) Effect of variation in mode-II fracture energy

Figure 5.24 Effect of fracture energy of gypsum-based SFRM on delamination progression on the beam of beam-column assembly subjected to seismic loading

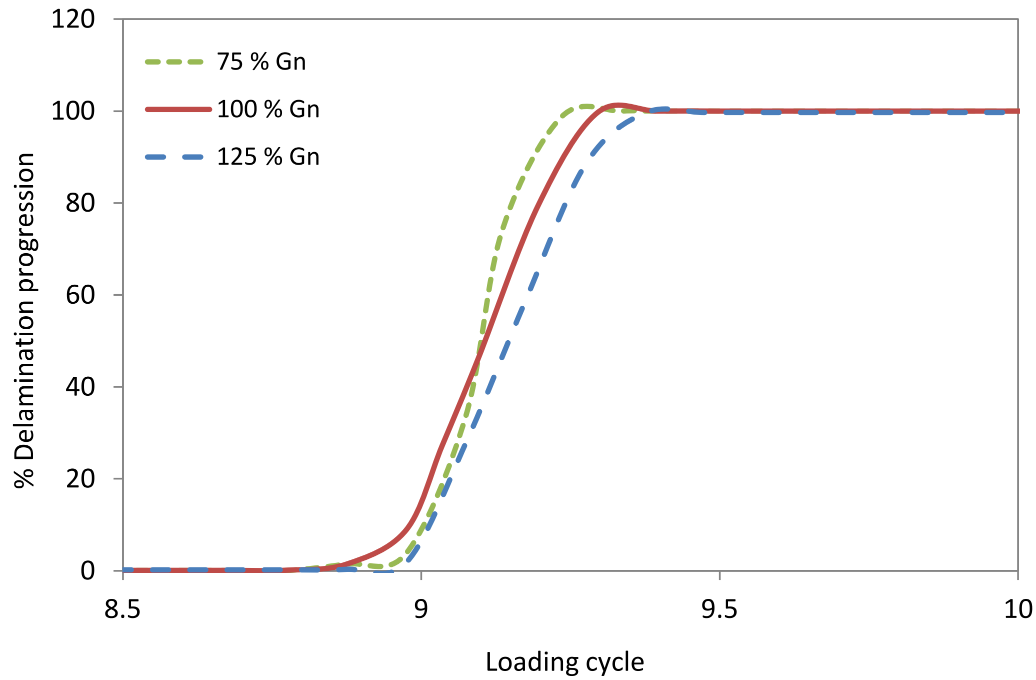

a) Effect of variation in mode-I fracture

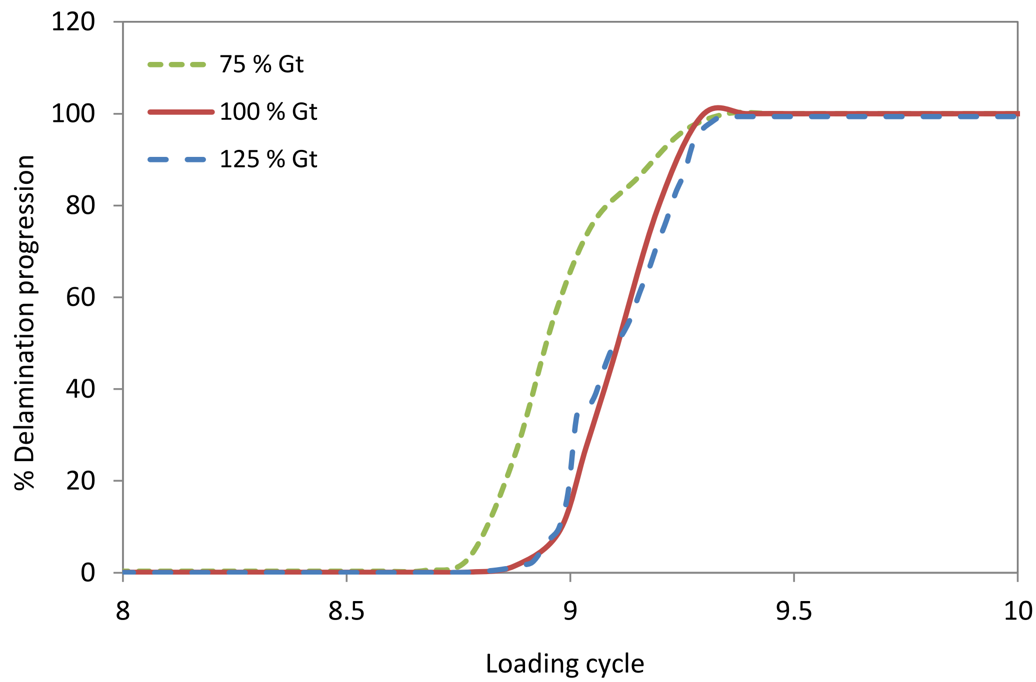

b) Effect of variation in mode-II fracture energy

Figure 5.25 Effect of fracture energy of Portland cement-based SFRM on delamination progression on the beam of beam-column assembly subjected to seismic loading

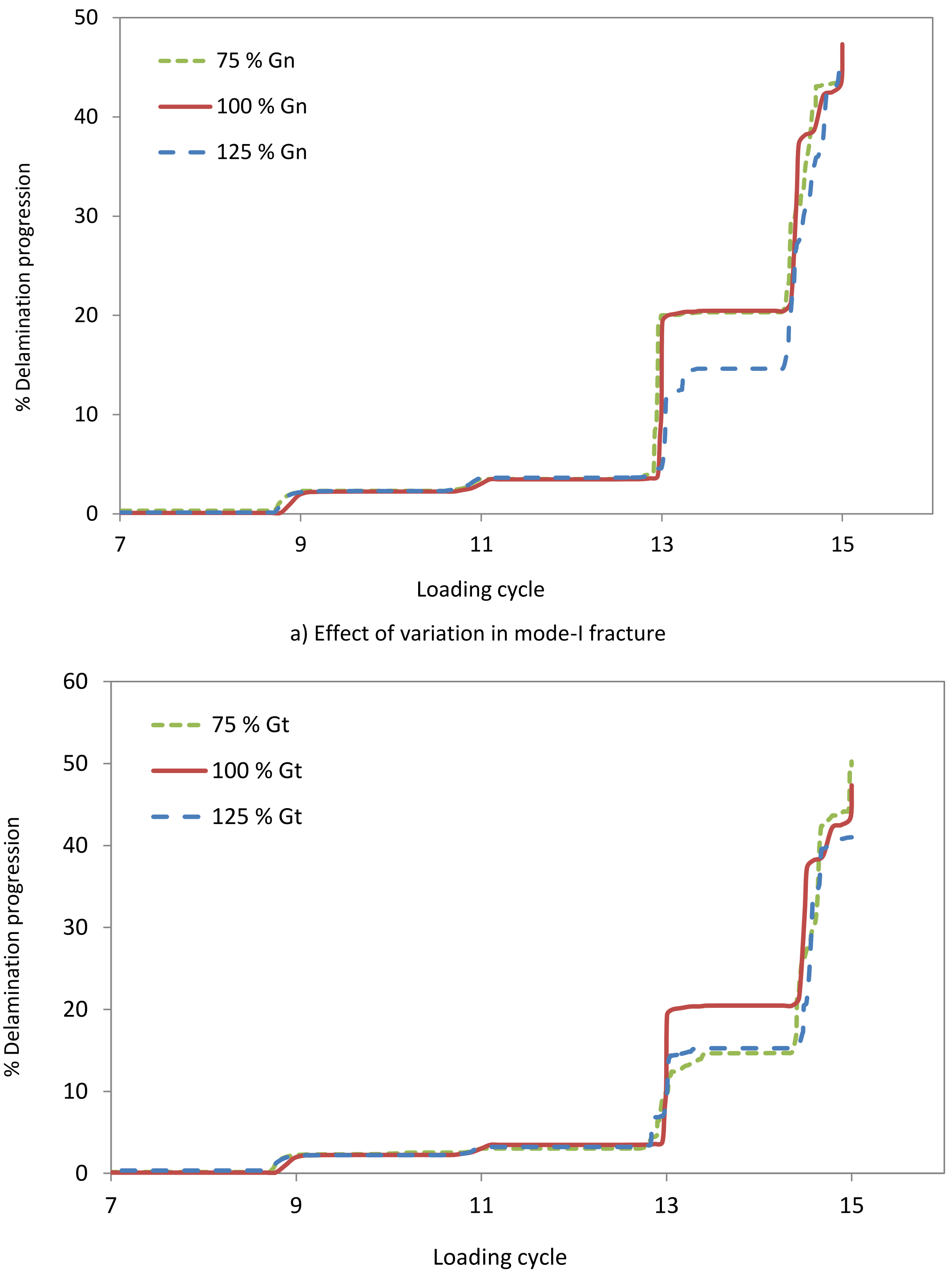

Figure 5.26 Effect of fracture energy of mineral fiber-based SFRM on delamination progression on the beam of beam-column assembly subjected to seismic loading

In case of beam-column assembly insulated with Portland cement-based SFRM, 25% variation in normal fracture energy does not have pronounced effect on crack initiation and propagation, as shown in Figure 5.25a. However, reduction in mode-II fracture energy reduces the drift level at which crack formation occurs, as depicted in Figure 5.25b. Cracks subsequently propagate with the same speed as in the case of average fracture energy (shown as 100%G_t in the legend of the figure) leading to complete delamination over the plastic hinge region. The drift level at which cracks open is 2.1% that is lesser than the drift of 2.14% which the beam-column assembly underwent before this loading cycle. In other words, even though the beam-column assembly experienced a higher drift level during previous cycle, cracks did not open. This is indicative of the fact that, damage has accumulated during previous loading cycles (second cycle) and finally fracture limit is reached during current loading cycle (third cycle) leading to crack opening.

According to Figure 5.26, when the beam-column assembly is insulated with mineral fiber-based SFRM, 25% variation in mode-I fracture energy and mode-II fracture energy does not noticeably influence drift level corresponding to crack initiation. However, final delamination extent is changed such that by decreasing fracture energy, extent of delamination is reduced by 5% and vice versa.

The effect of variation in normal cohesive strength of gypsum-based SFRM is shown in Figure 5.27a. The crack initiation is not accelerated by reducing normal cohesive strength by 25%. However, increasing normal cohesive strength by 25% hampers crack formation until end of downward movement of the beam during third loading cycle (i.e. drift of 3%). The cracks, formed at the end of this cycle, propagate during unloading leading to full delamination.

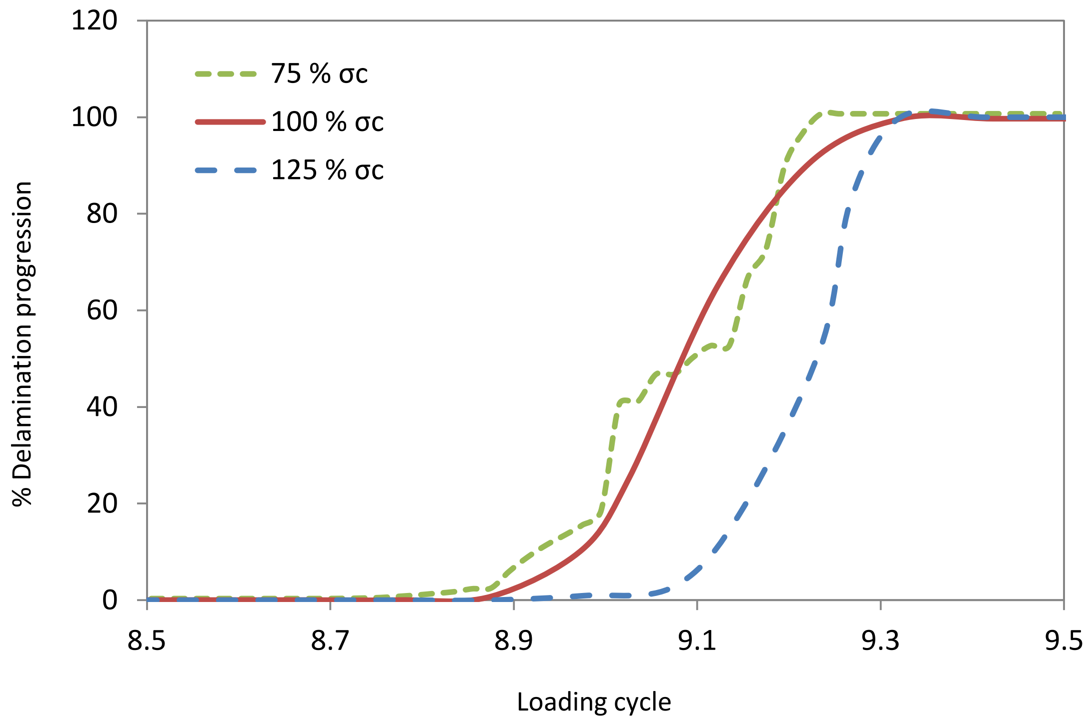

a) Effect of variation normal cohesive strength

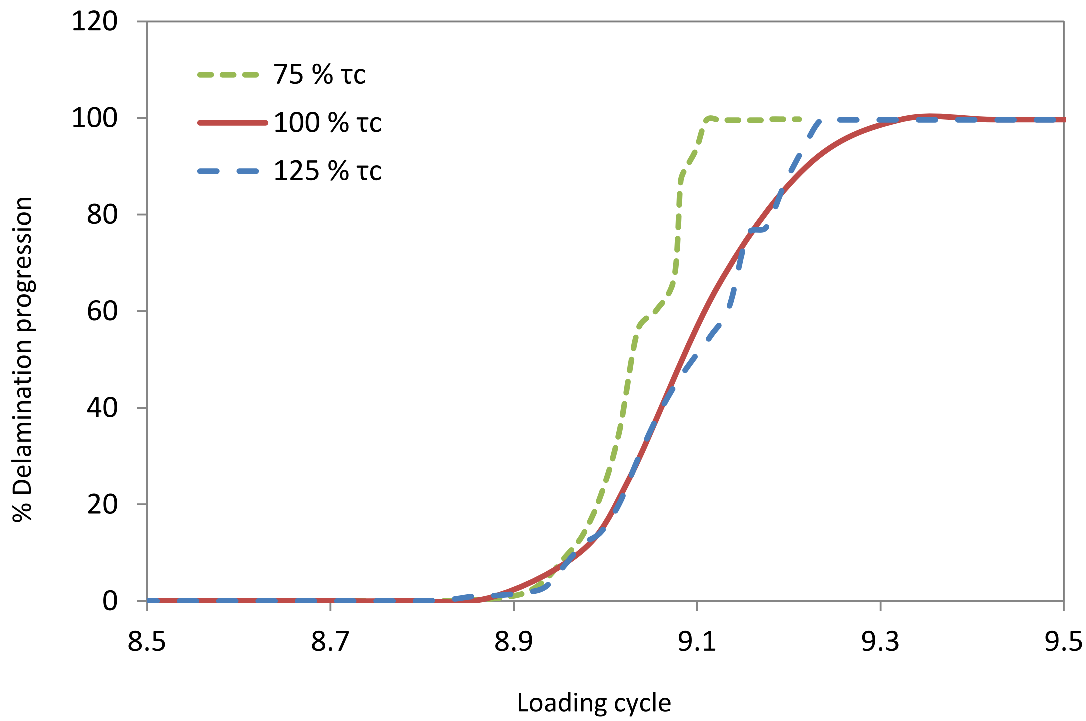

b) Effect of variation in tangential cohesive strength

Figure 5.27 Effect of cohesive strength of gypsum-based SFRM on delamination progression on the beam of beam-column assembly subjected to seismic loading

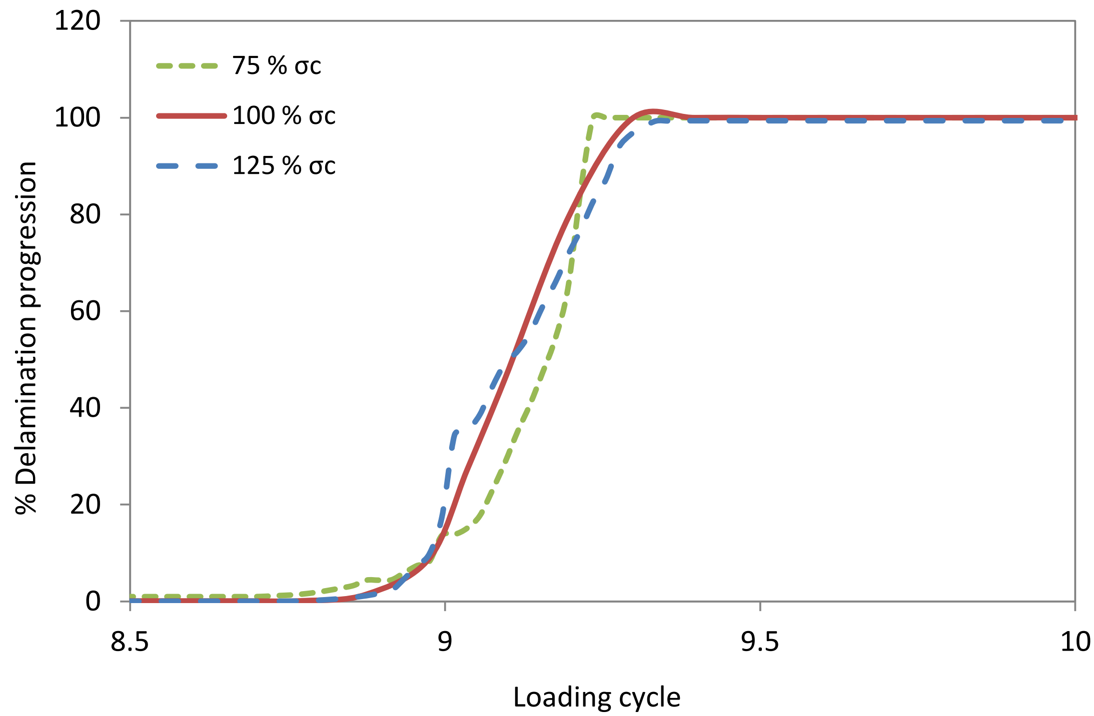

a) Effect of variation normal cohesive strength

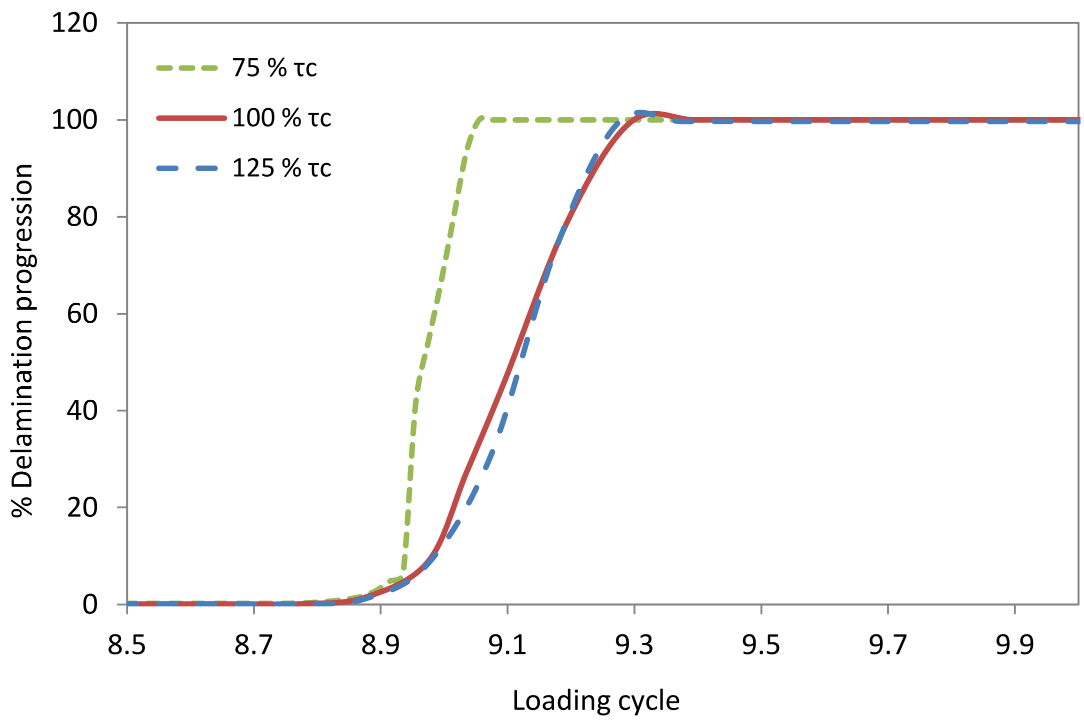

b) Effect of variation in tangential cohesive strength

Figure 5.28 Effect of cohesive strength of Portland cement-based SFRM on delamination progression on the beam of beam-column assembly subjected to seismic loading

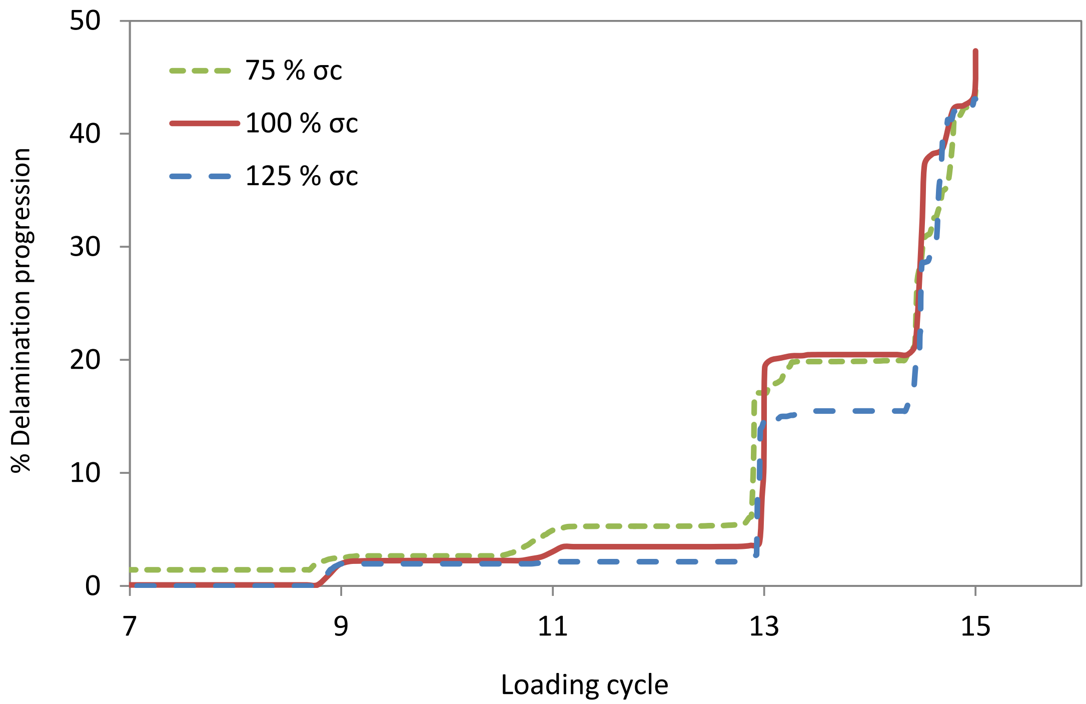

a) Effect of variation normal cohesive strength

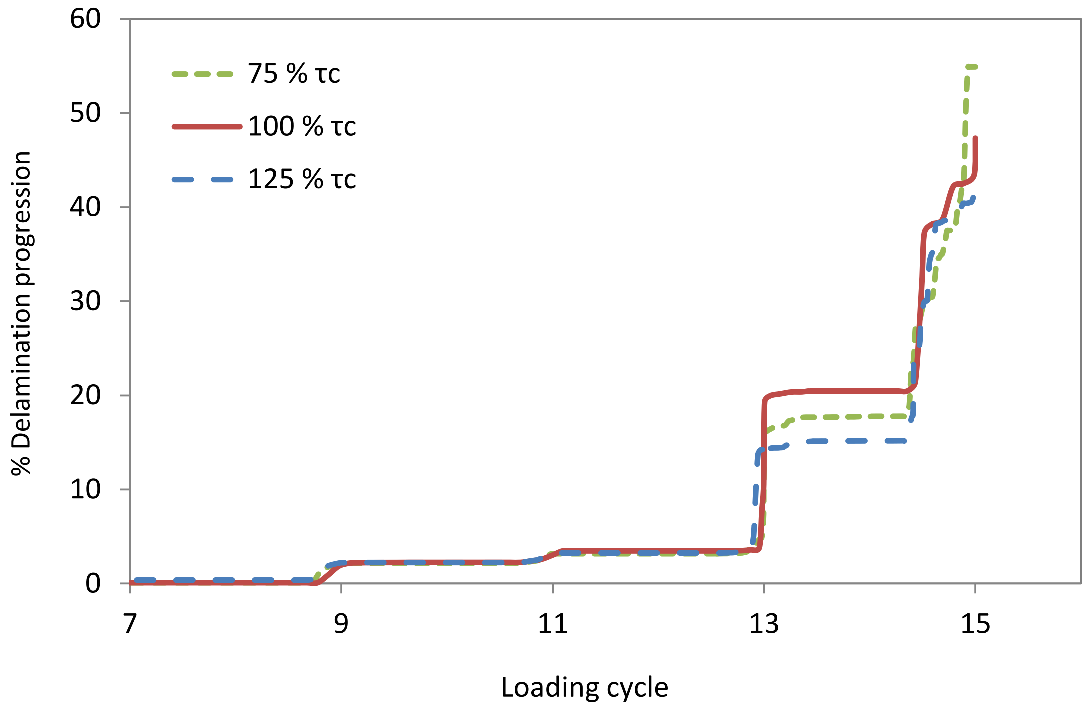

b) Effect of variation in tangential cohesive strength

Figure 5.29 Effect of cohesive strength of mineral fiber-based SFRM on delamination progression on the beam of beam-column assembly subjected to seismic loading

As depicted in Figure 5.27b, increasing shear cohesive strength by 25% has negligible influence on initiation and propagation of delamination. However, decreasing shear cohesive strength by 25%, though has no effect on damage initiation, it accelerates delamination propagation to considerable extent.

In case of Portland cement-based SFRM, as illustrated in Figure 5.28a, variation in normal cohesive strength does not have significant effect on drift at which delamination starts. When normal cohesive strength is decreased by 25%, crack propagation speed is not altered, while by increasing normal cohesive strength by 25% crack propagation speed is reduced. However, complete delamination occurs over the plastic hinge region despite variation in crack propagation pace. The effect of variation in shear cohesive strength is plotted in b and it is clear that enhancement in cohesive strength by 25% has almost no effect on both delamination initiation and propagation speed. The reduction in cohesive strength by 25%, however, increases crack propagation speed while it does not have any effect on drift level causing crack initiation.

Figure 5.29 plots effect of variation in normal and shear cohesive strength on delamination of mineral fiber-based SFRM from beam-column assembly. The drift level corresponding to initiation of cracks is not affected by variation in both normal and shear cohesive strength. Further, speed of delamination does not show noteworthy sensitivity to variation in normal cohesive strength. However, extent of delamination increases by 10% when shear cohesive strength is reduced by 25% and it reduces by 5% when shear cohesive strength is enhanced by 25%.

5.4.4 Effect of Elastic Modulus of Insulation

As pinpointed in section 5.4.2, the lower level of elastic modulus for mineral fiber-based SFRM is believed to be the reason for better performance of this type of SFRM during seismic loading despite its lower fracture energy compared to gypsum-based and Portland cement-based SFRM. However, it is also a point of interest to clarify the effect of variation of elastic modulus for each type of SFRM on its performance. To quantify the effect of elastic modulus for each type of SFRM, this parameter is varied by ±25% and the percentage of delamination in bottom flange of the beam is plotted in Figure 5.30, Figure 5.31and Figure 5.32 for three types of SFRM.

As shown in the above figures, delamination initiation is not affected by ±25% variation in elastic modulus of all three types of SFRM. The delamination propagation speed is increased when elastic modulus is boosted and vice versa. However, final delamination extent is not affected in case of gypsum-based and Portland cement-based SFRM and is slightly changed for mineral fiber-based SFRM. It should be noted that, as discussed in section 5.4.2, the effect of elastic modulus is pronounced when the variation is considerable as in the case of difference between mineral fiber-based SFRM and two other types. However, for a certain types of SFRM, ±25% variation in elastic modulus does not have significant effect on extent of delamination. Effect of significant change in elastic modulus along with variation in other influential parameters is presented in section 5.4.6.

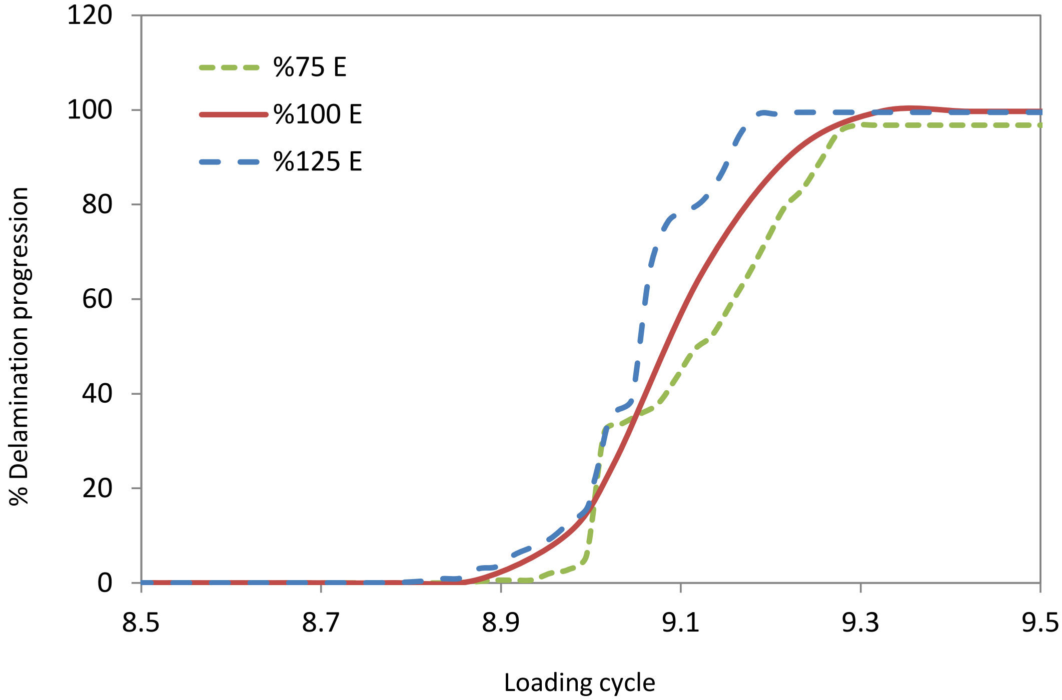

Figure 5.30 Effect of elastic modulus of gypsum-based SFRM on delamination progression on the beam of beam-column assembly subjected to seismic loading

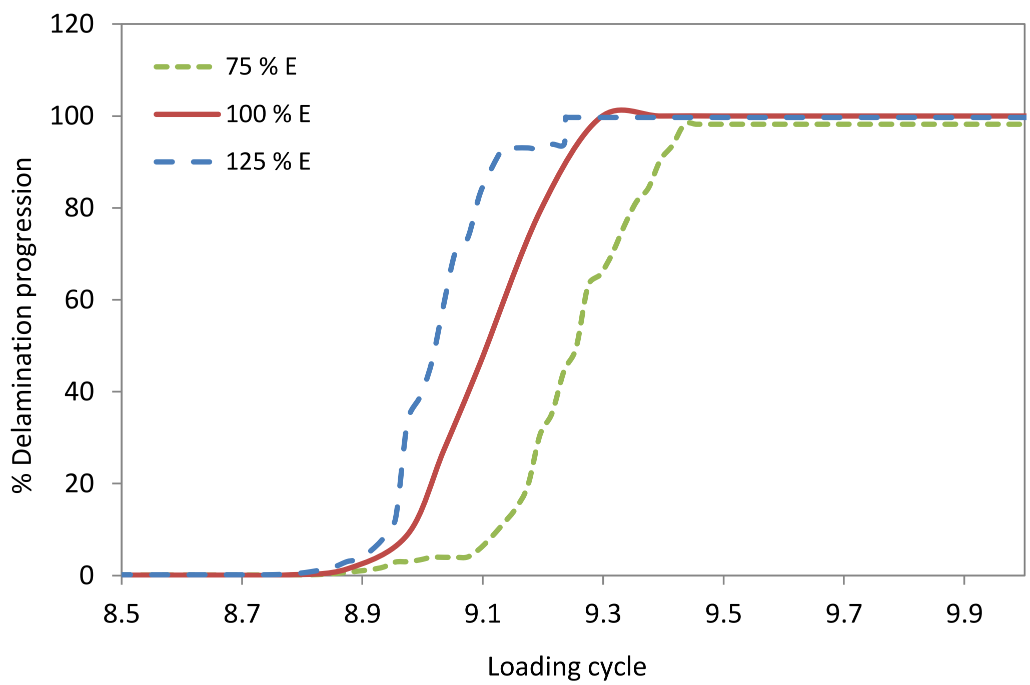

Figure 5.31 Effect of elastic modulus of Portland cement-based SFRM on delamination progression on the beam of beam-column assembly subjected to seismic loading

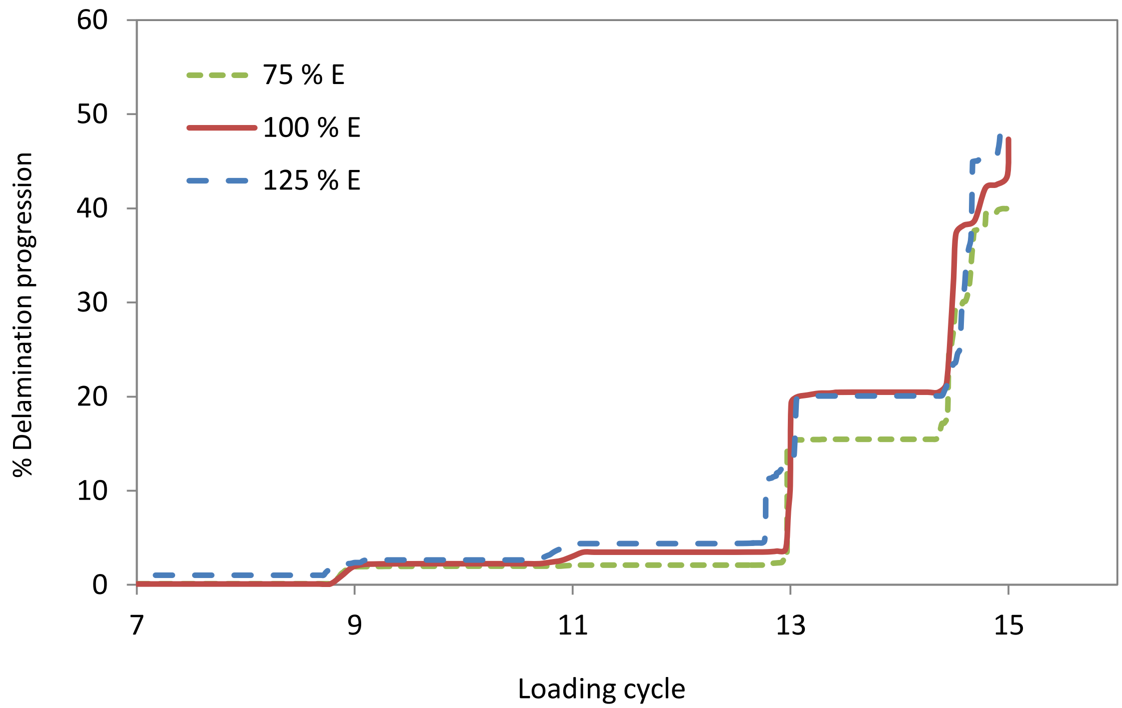

Figure 5.32 Effect of elastic modulus of mineral fiber-based SFRM on delamination progression on the beam of beam-column assembly subjected to seismic loading

5.4.5 Effect of Insulation Thickness

To quantify the effect of thickness for each types of SFRM, thickness is varied within a practical range of 12.5 mm to 50 mm, while all other parameters are kept constant. Resulted obtained from numerical simulations for three types of SFRM are depicted in Figure 5.33, Figure 5.34 and Figure 5.35. When thickness of gypsum-based SFRM is reduced from 25 mm to 12.5 mm delamination does not occur at drift level of 3% and it is delayed until drift reaches to 3.91% during next loading cycle, as illustrated in Figure 5.33.

The above results means that, an earthquake which does not push the structure beyond drift of 3% may not cause any damage to the SFRM with thickness of 12.5 mm. However, thickness of 12.5 mm does not usually provide fire endurance prescribed in the fire protection codes. Hence, thickness of SFRM may be chosen to be larger than 12.5 mm. As shown in Figure 5.33, increasing thickness does not change the drift level at which cracks get initiated. Therefore, increasing thickness up to 50 mm does not accelerate the crack formation which is beneficial from fire protection design stand point. That is to say, the thickness can be increased up to 50 mm to achieve desired fire protection provided that the expected drift does not reach to 3%.

The sensitivity of Portland cement-based SFRM to thickness variation is similar to gypsum-based SFRM, as shown in Figure 5.34. The SFRM with thickness of 25 mm to 50 mm show almost same delamination initiation drift and once initiated cracks develop throughout the plastic hinge region (i.e. 100% delamination). In case of 12.5 mm thickness, delamination starts at drift of 3.91%; however it is not completed during downward loading-unloading phase and is delayed until upward movement at this drift level. This indicates enhanced resiliency against delamination for Portland cement-based SFRM when thickness is reduced.

As shown in Figure 5.35, increasing thickness of mineral fiber-based SFRM to 37.5 mm and 50 mm leads to earlier delamination at drift of 3%. This clearly shows that providing higher thickness can be compromised during seismic loading since SFRM with thickness of 25 mm would not completely detach and would provide fire resistance to some extent whereas SFRM with thickness of 37.5 mm may no longer remain attached to steel surface to provide any fire resistance. Decreasing thickness of SFRM, from 25 mm to 12.5 mm, results in 66% reduction in extent of delamination, which occurs during upward movement at drift of 3.91%.

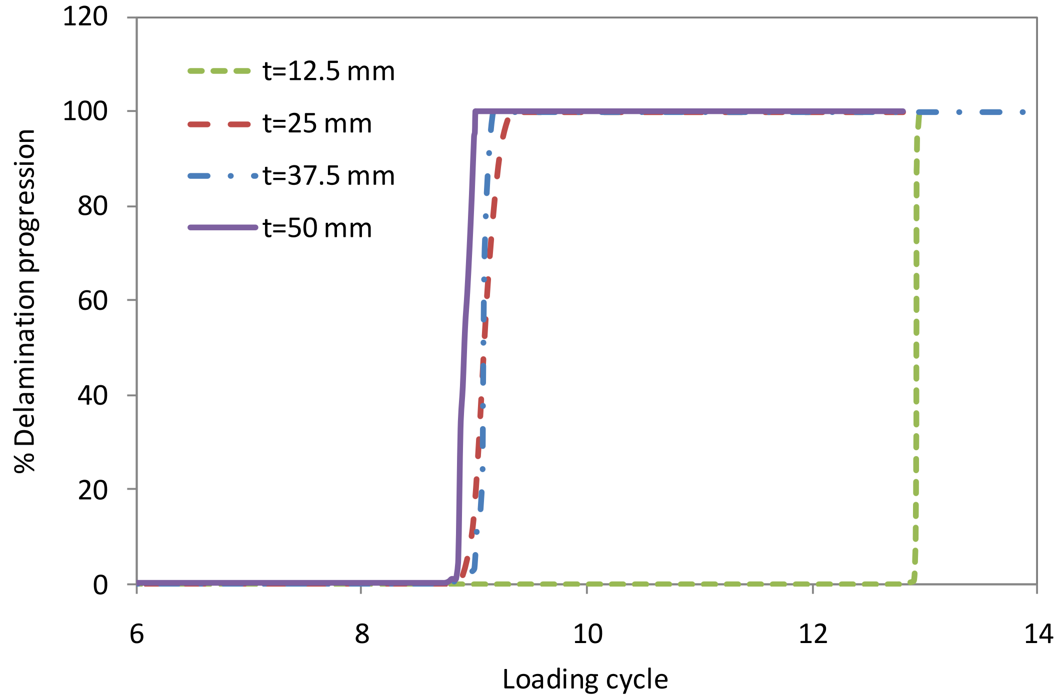

Figure 5.33 Effect of thickness of gypsum-based SFRM on delamination progression on the beam of beam-column assembly subjected to seismic loading

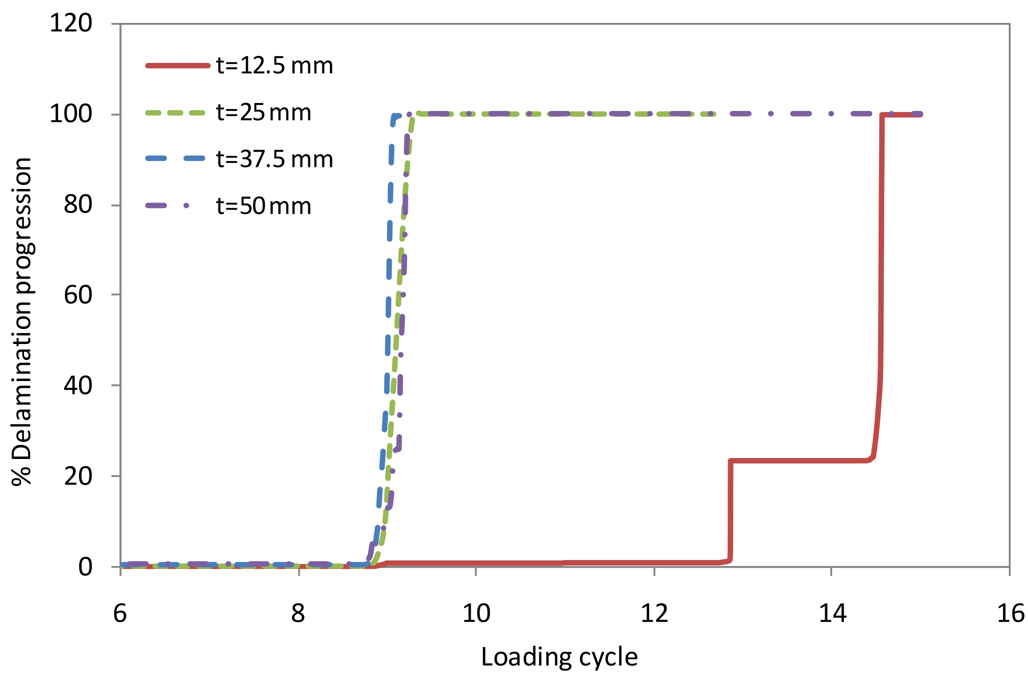

Figure 5.34 Effect of thickness of Portland cement-based SFRM on delamination progression on the beam of beam-column assembly subjected to seismic loading

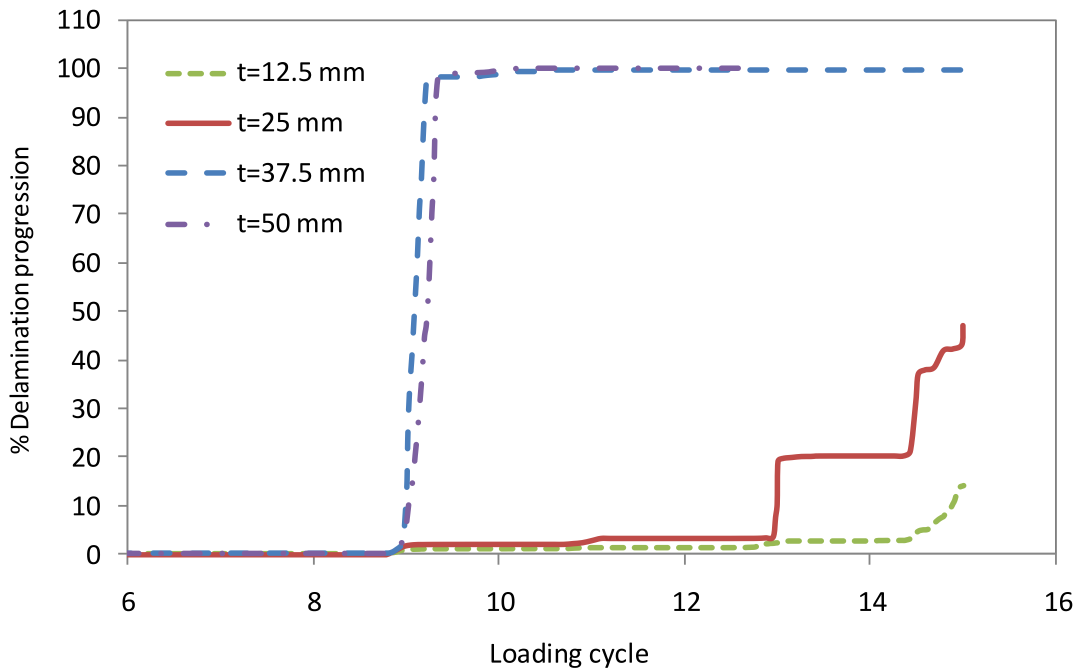

Figure 5.35 Effect of thickness of mineral fiber-based SFRM on delamination progression on the beam of beam-column assembly subjected to seismic loading

5.4.6 Additional Sensitivity Analysis

The above results with respect to sensitivity of delamination to cohesive zone properties, elastic modulus and thickness shows that despite some effects of variation in above parameters on crack initiation limits and propagation speed, full delamination cannot be prevented in case of gypsum-based and Portland cement-based SFRM. Therefore, additional parametric study is carried out to change above parameters simultaneously to quantify interdependency among the critical factors governing delamination.

The effect of variation in thickness, fracture energy and elastic modulus for gypsum-based SFRM is plotted in Figure 5.36 for three additional cases. The legend of this figure shows the variation in the parameters. The parameters not shown at legend of the figure are maintained constant. The maximum reduction in delamination extent is 60% which occurs when thickness is reduced to 12.5 mm and elastic modulus is reduced by 50%. Note that, delamination initiation is postponed to drift level of 3.91% for all three cases.

Figure 5.37 shows results from additional parametric study to quantify effect of variation in delamination governing factors for Portland cement-based SFRM. As can be seen, when elastic modulus is reduced by 75%, cracks do not form during loading cycle pertaining to 3% drift and crack initiation is delayed until downward movement at drift of 3.91%. Further, when thickness is reduced, along with decrease in elastic modulus or increase in fracture energy, crack initiation is postponed until upward movement at drift of 3.91%. However, extent of delamination in above three cases is diminished by 55% reduction.

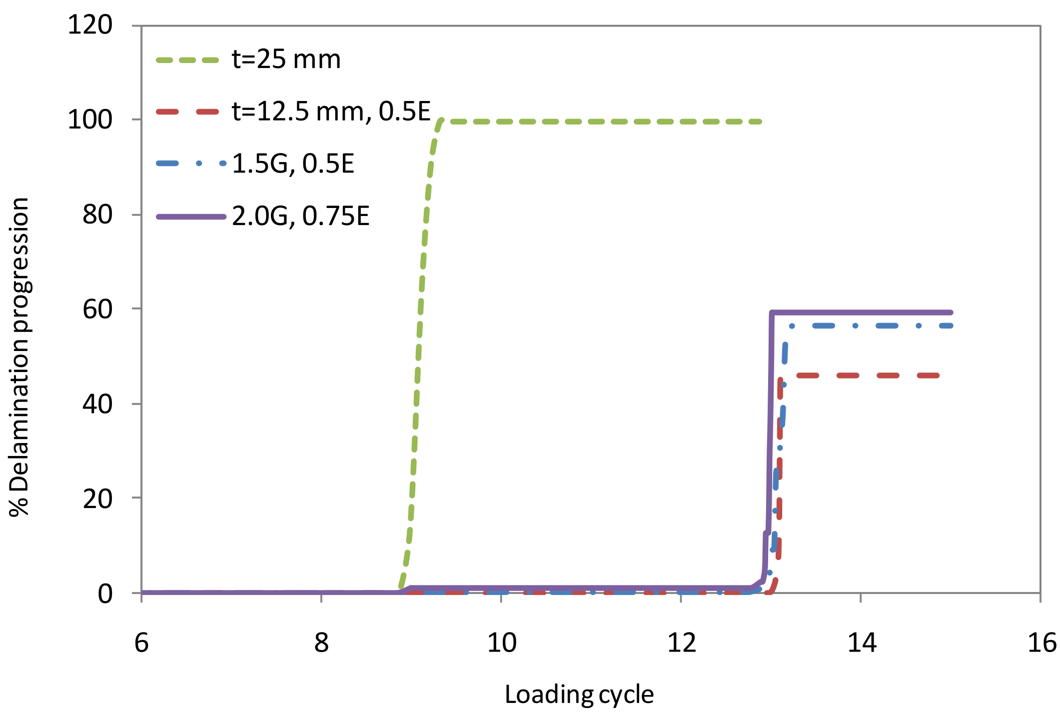

Figure 5.36 Effect of change in material properties of gypsum-based SFRM on delamination progression on the beam of beam-column assembly subjected to seismic loading

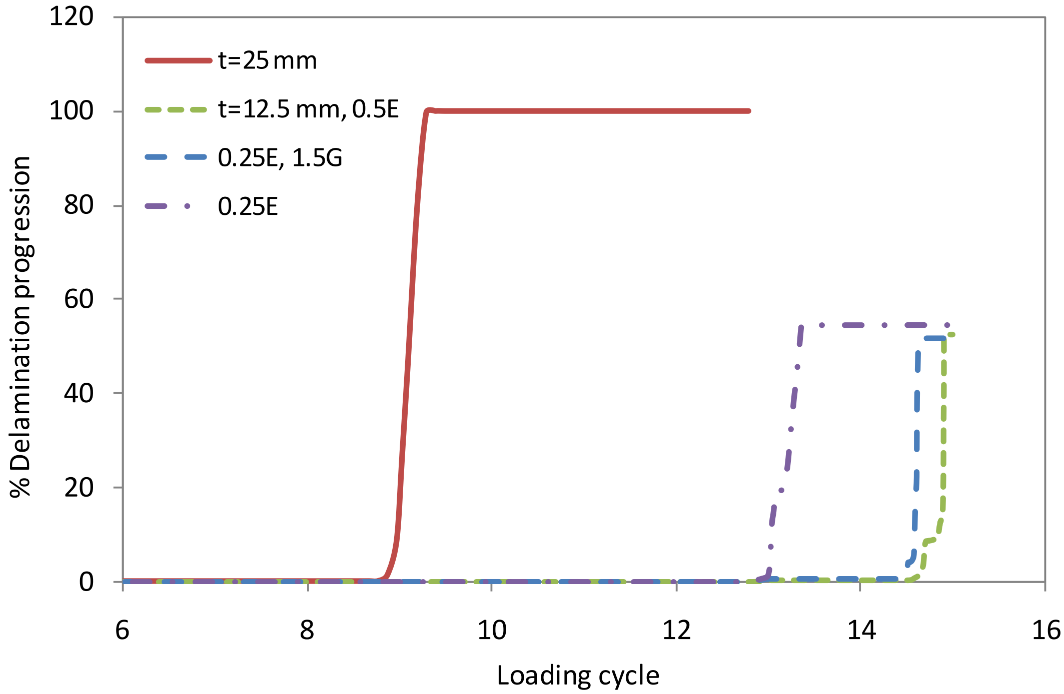

Figure 5.37 Effect of change in material properties of Portland cement-based SFRM on delamination progression on the beam of beam-column assembly subjected to seismic loading

5.4.7 Delamination Characteristic Parameter for Seismic Loading

Results from above explained parametric studies is assembled in Figure 5.38 where delamination percentage is plotted versus delamination characteristic parameter introduced in section 5.3.5 with slight change in the parameter. The cohesive zone displacement ductility, i.e. parameter $\bar{\mu}$ introduced in Equation (2) is eliminated from the characteristic parameter since under seismic loading this parameter did not show noticeable effect. This can be attributed to the fact that under quasi-static loading the cohesive stress-displacement curve is traced from beginning to end without any unloading, therefore, displacement ductility remains constant throughout the loading. However, under cyclic loading when cohesive strength is passed through and unloading occurs the displacement ductility is reduced during next loading cycle since the cohesive strength is plummeted, as shown in Figure 4.1. This may be the reason why the effect of displacement ductility is not important during cyclic loading. Hence, Equation (1) is rewritten for seismic loading:

$$d_{ch,seimic} = \frac{E.t}{\bar{G}_c} \tag{5.8}$$

As can be seen in Figure 5.38, delamination is inevitable in all types of SFRM having different combination of material properties and fire insulation thickness. Further, for $d_{ch,seimic}$ larger than 3.68, full delamination occurs over the plastic hinge region, while the least delamination (percentage) occurs for $d_{ch,seimic}$ of 1.23. This limit in $d_{ch,seimic}$ value of 3.68 is critical since a small variation leads to either complete delamination or reduction of delamination extent to 60%.

Subsequently, critical fracture energy, which is the most important parameter affecting the crack propagation at steel-SFRM interface is enhanced until the delamination is prevented. The analysis was performed for different levels of elastic modulus and thickness. Results from this parametric study are also shown in Figure 5.38. Results from this parametric study show that, in order to reduce the level of cracking and delamination over the plastic hinge region to 20%, $d_{ch,seimic}$ value should be decreased to 1.0.

Further, fracture energy should be significantly increased (up to 350 J/m^2 in normal mode) to completely eliminate the delamination of fire insulation from the bottom flange, such that for the $d_{ch,seimic}$ value less than 0.58 the crack propagation at steel-SFRM interface can be avoided. These results infer that, steel beams provided with higher fire-rating, which demand thicker insulation, need to be insulated with SFRM possessing higher fracture energy to prevent delamination. Further, fire insulation materials with high elastic modulus require higher fracture energy to assure that cracks will not advance at SFRM-steel interface.

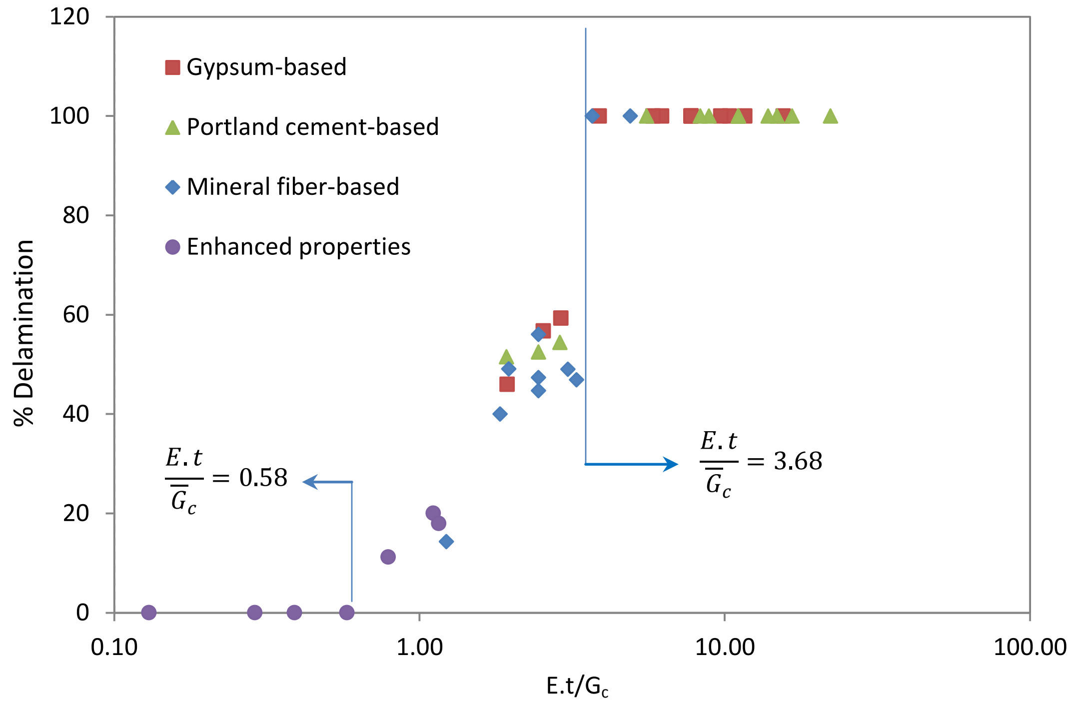

Figure 5.38 Extent of delamination as a function of parameter $E.t/G_c$

5.5 Delamination of Fire Insulation from a Beam under Impact Loading

Numerical modeling plays a crucial role in determining fracture properties when indirect fracture tests are utilized. In current practice, indirect test methods are widely adopted to determine the fracture energy as well as stress-displacement relationship over the fracture process zone (FPZ) developed at the interface of two materials (Sorensen and Jacobsen, 2003; Gordnian et al., 2008; Lee et al., 2010; Valoroso et al., 2013). In these test methods, such as double cantilever beam (ASTM D5528, 2013), end notched flexure (ASTM WK22949, 2009) and three point bending (RILEM, 1985), the only outcome from test is global load-displacement response of the specimen. The fracture energy is subsequently quantified using fracture mechanics-based analytical solutions which involve geometry of the specimen and the peak load recorded during tests.

However, the stress-displacement relationship over the fracture process zone, which is an essential input for cohesive zone model-based numerical approaches, can only be obtained utilizing numerical modeling. To extract theses parameters, an ideal stress-displacement curve is assumed and numerical simulation is carried out. The predicted overall load-displacement relationship is compared to the experimental behavior and this iterative process is repeated until the best agreement is obtained between experimental and simulation results.

5.5.1 Analysis Details

Finite element model of the insulated beam stricken by a mass was shown in Figure 4.31. The steel beam and SFRM are discretized using 8-noded solid elements with linear displacement interpolation functions and reduced integration. The plate stack in the hammer is also modeled using 8-noded solid elements. However, the indenter is discretized using 10-noded tetrahedron elements which use a quadratic displacement interpolation function with five point of integration.

The hammer is positioned at a distance of 2 mm above the flange of the beam, and an initial velocity calculated by energy conservation approach, is assigned to the hammer nodes. To simulate dynamic interaction between striking hammer and the flange of the steel beam, contact type “Automatic_One_Way_Surface_To_Surface” is used (LS-DYAN, 2014). The contact force developed between indenter tip and the flange of the beam is considered as impact force. The contact type “Automatic_One_Way_Surface_To_Surface_Tiebreak” in conjunction with cohesive zone model developed by Lemmen and Meijer, 2001is utilized to model delamination between fire insulation and steel.

5.5.2 Approach for Predicting Dynamic Increase Factor on Fracture Energy of SFRM

In this study, an approach, similar to the one as explained above, is adopted to estimate the dynamic increase factor (DIF) on traction-separation laws over FPZ at the interface of steel surface and fire insulation. However, the recorded global load-displacement relationship in the specimens, though is used to validate overall performance of numerical model, cannot be used as a reference curve for adjusting the assumed traction-separation law at the interface of steel and SFRM. This is due to the fact that, SFRM does not contribute to the structural performance of the fire insulated steel structures (E_{SFRM}=0.01GPa<<E_{steel}=200 GPa). Therefore, the cracking and delamination of SFRM cannot influence the global load-displacement relationship of steel structures.

As a substitute, the extent of delamination on the bottom flange is considered as the reference parameter for comparison of numerical predictions with experimental results leading to extraction of dynamic traction-separation laws at steel-SFRM interface. A cohesive zone approach is adopted to model the FPZ at the interface of steel and fire insulation. The traction-separation relationships determined using static direct fracture tests are utilized as initial interfacial cohesive laws. The predicted extent of delamination on bottom flange is compared to the one observed in the experiments. Subsequently, the cohesive properties, namely cohesive strength and cohesive fracture energy, are proportionally enhanced and the analysis is carried out again. This procedure is repeated until a good agreement is achieved between numerical results and experimental observation, which leads to estimation of DIF on fracture properties.

5.5.3 Numerical Predicaments

The validation of numerical model presented in Chapter 4 demonstrates that the numerical model adopted in this study is capable of simulating the behavior of insulated steel beam under the impact loading. Hence, it can be inferred that the predicted stresses at the interface of steel and SFRM are as accurate as the impact force and beam deformation. However, numerous numerical problems are encountered with, while modeling interaction between a very soft and quasi-brittle material such as fire insulation and a very stiff and ductile material such as steel.

Contact instability, resulting from excessive penetration, is the main issue in this type of contact modeling. Different solution strategies are therefore adopted to tackle the issues regarding contact modeling. The contact penalty stiffness is increased to ensure that early failure does not occur due to penetration. Increasing the contact penalty significantly increases the analysis time; therefore, the penalty stiffness is increased gradually until a rational value is achieved, that neither is too high to render the numerical solution so time-consuming, nor too low to jeopardize the accuracy of the solution. Further, vicious contact damping was assigned to the contact conditions to control the instability of contact interactions. The amount of damping coefficient was minimized (5%), thus it is not misinterpreted as rate-dependency of fracture toughness as will be outlined in below.

In the numerical model, the cohesive zone model determined through static fracture tests, shown in Figure 3.11, are initially utilized as the constitutive model at the interface of steel and SFRM. According to numerical results, a very good agreement with respect to extent of delamination in the bottom flange is obtained for the beams insulated with mineral fiber-based SFRM. However, the beams insulated with gypsum-based and Portland cement-based SFRM demonstrate excessive percentage of delamination on the bottom flange when compared to experimental results. The reason for such behavior is explored by evaluating three potential factors, namely, the mesh sensitivity of interfacial fracture, density of contact conditions in the numerical model and the rate-dependency of fracture properties for SFRM as a cementitious material.

The issue of mesh sensitivity is tackled by refining the mesh. The effect of density of contact conditions in the model is studied by increasing the density of contact condition until the solution stability and accuracy is not influenced as a whole. Results from numerical model shows that, the larger the distance between the contact surfaces is, the larger is the delamination area. The distance between contact conditions is kept constant at 22 mm since further reducing this distance does not significantly improve the results. Despite tackling the two former factors, the numerical model still predicts larger delamination percentage when using the fracture properties determined statically. Therefore, the discrepancy between the numerical and experimental delamination area on the bottom flange can be attributed to the latter factor, i.e., rate-dependency of cohesive zone properties at the interface of steel and SFRM.

5.5.4 Quantified Dynamic Increase Factors

To study the effect of high strain rate on the interfacial fracture properties, the cohesive strength and fracture energy is artificially and proportionally increased by a factor named dynamic increase factor (DIF) and the delamination percentage on the bottom flange is monitored. The percentage delamination on the bottom flange is plotted against the DIF in Figure 5.39, Figure 5.40 and Figure 5.41 for mineral fiber-based SFRM, gypsum-based SFRM and Portland cement-based SFRM, respectively. The experimentally observed delamination percentage is also superposed to these figures as a line. The parametric study in terms of DIF is carried out by assuming DIF=1.0, 2.0, 3.0 and 4.0. The DIF corresponding to the experiment is computed by finding the intersection of experimental line and the numerical curve using interpolation method and the computed values is shown in Figure 5.39, Figure 5.40 and Figure 4.41 for three types of SFRM.

Subsequently, a numerical analysis is carried out for that specific DIF. The results show a very good agreement between numerical results and experimental observation for the interpolated DIF. As is clear in Figure 5.39, mineral fiber-based SFRM does not exhibit rate-dependency, i.e. DIF=1.0.However, two other SFRM demonstrates different levels of rate-dependency. In the beams insulated with gypsum-based SFRM, as shown in Figure 5.40, the estimated DIF for the impact velocity (v) of 6.66 m/s and 8.05 m/s are 1.16 and 1.41, respectively. The Portland cement-based SFRM shows highest level of rate-dependency, such that DIF is computed as 2.32 for impact velocity of 8.05 m/s, as depicted in Figure 5.41. The DIF for impact velocity of 6.66 m/s cannot be quantified since the corresponding test was not carried out. The numerically predicted fracture and delamination of SFRM using the above estimated DIF are portrayed for three types of SFRM and compared to the experimental results in Figure 5.42, Figure 5.43 and Figure 5.44.

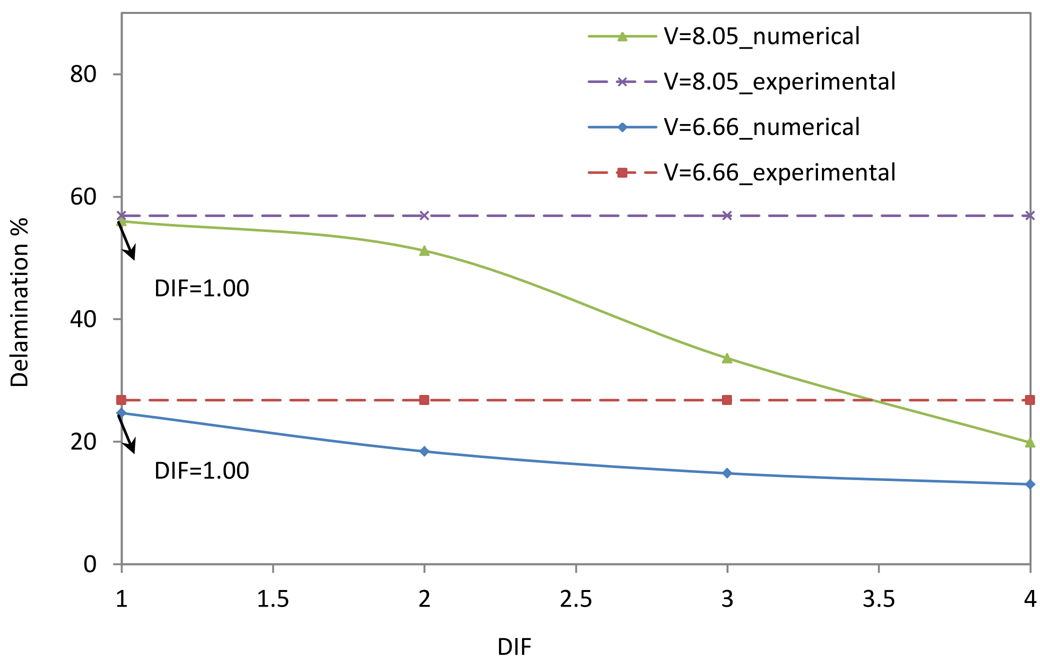

Figure 5.39 Extent of delamination ratio versus dynamic increase factor for CZM properties of mineral fiber-based SFRM

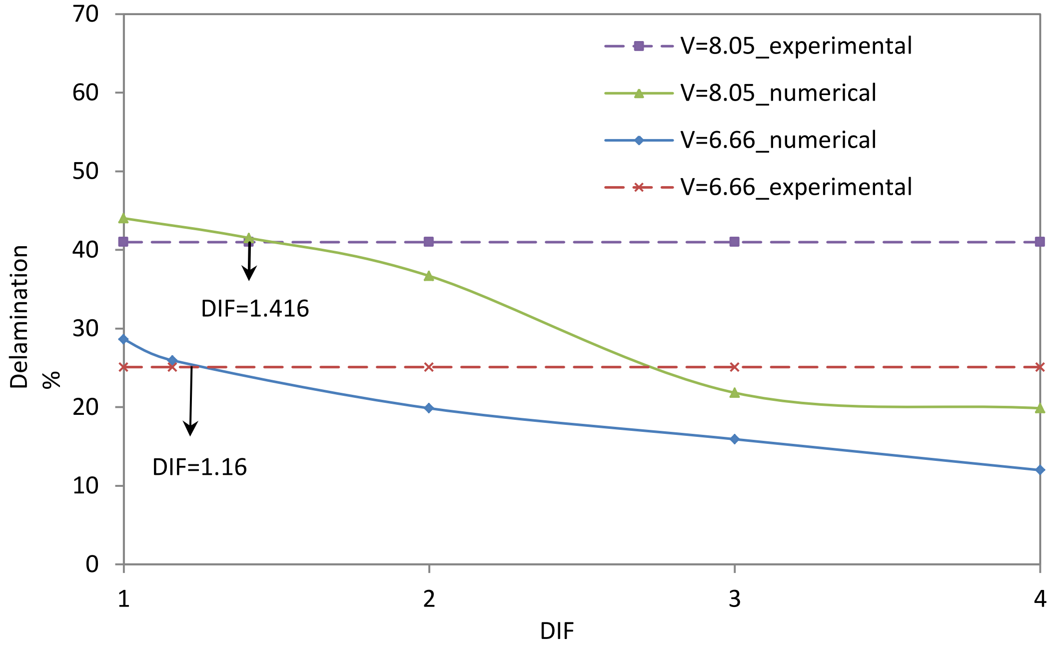

Figure 5.40 Extent of delamination ratio versus dynamic increase factor for CZM properties of gypsum-based SFRM

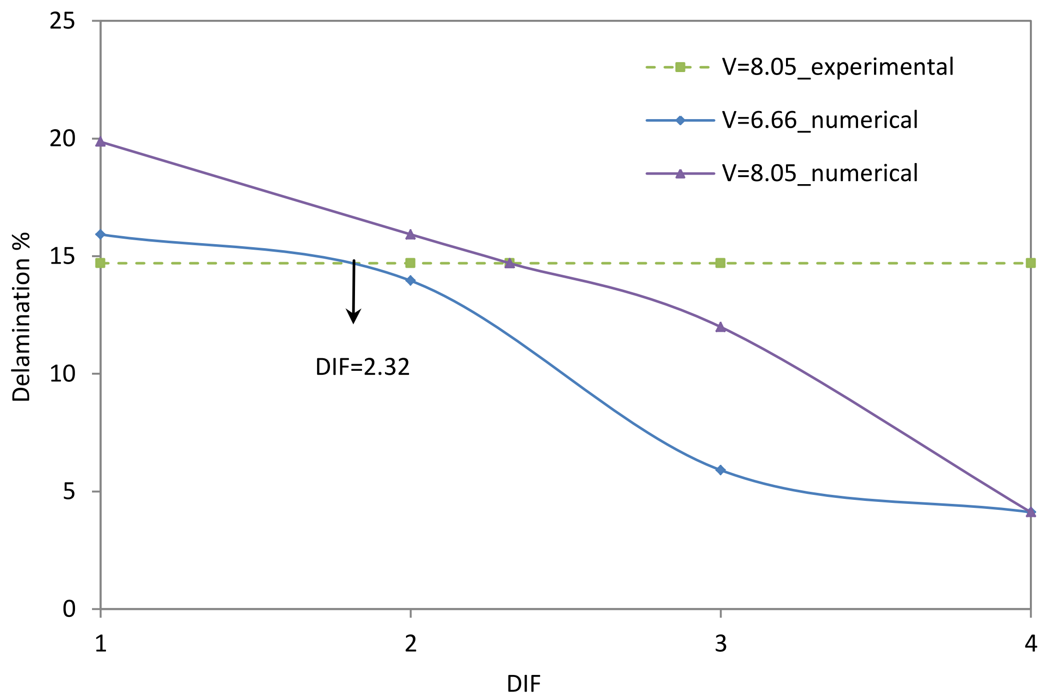

Figure 5.41 Extent of delamination ratio versus dynamic increase factor for CZM properties of Portland cement-based SFRM

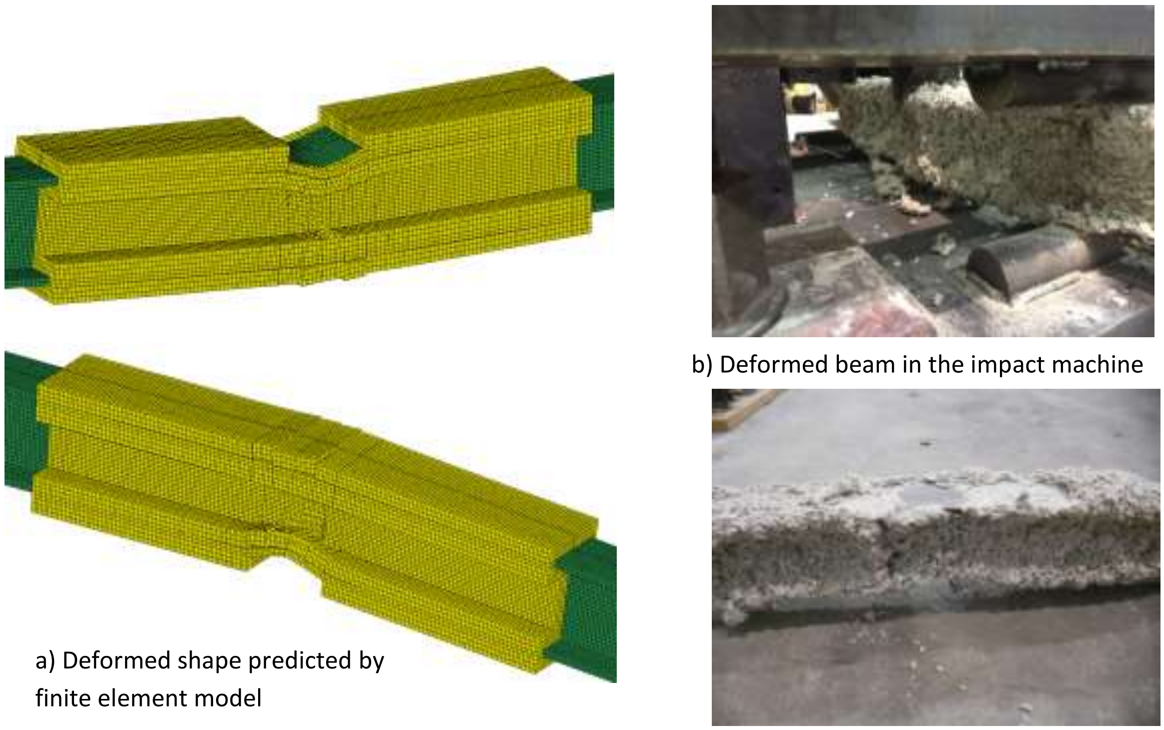

a) Deformed shape predicted by finite element model

b) Deformed beam in the impact machine

c) Delamination extent on the bottom flange

Figure 5.42 Numerical and experimental illustration of extent of delamination in beam insulated with Mineral fiber-based SFRM (DIF=1.00)

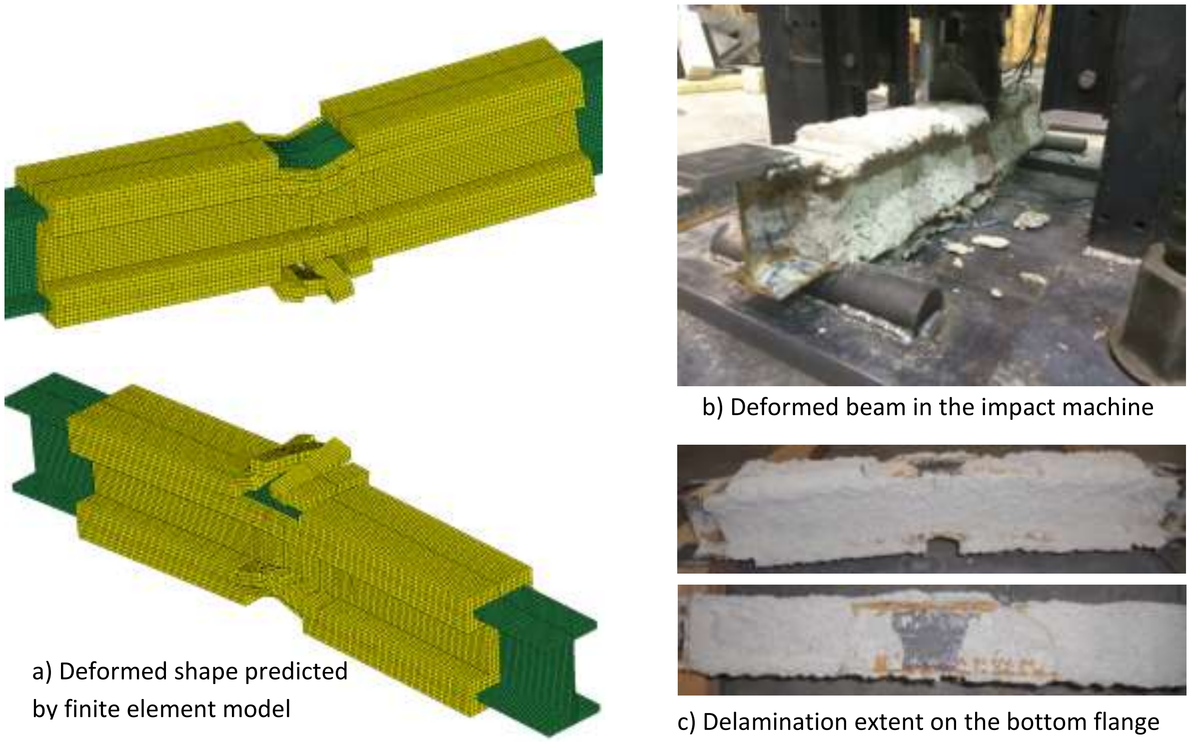

a) Deformed shape predicted by finite element model

b) Deformed beam in the impact machine

c) Delamination extent on the bottom flange

Figure 5.43 Numerical and experimental illustration of extent of delamination in beam insulated with Gypsum-based SFRM (DIF=1.41)

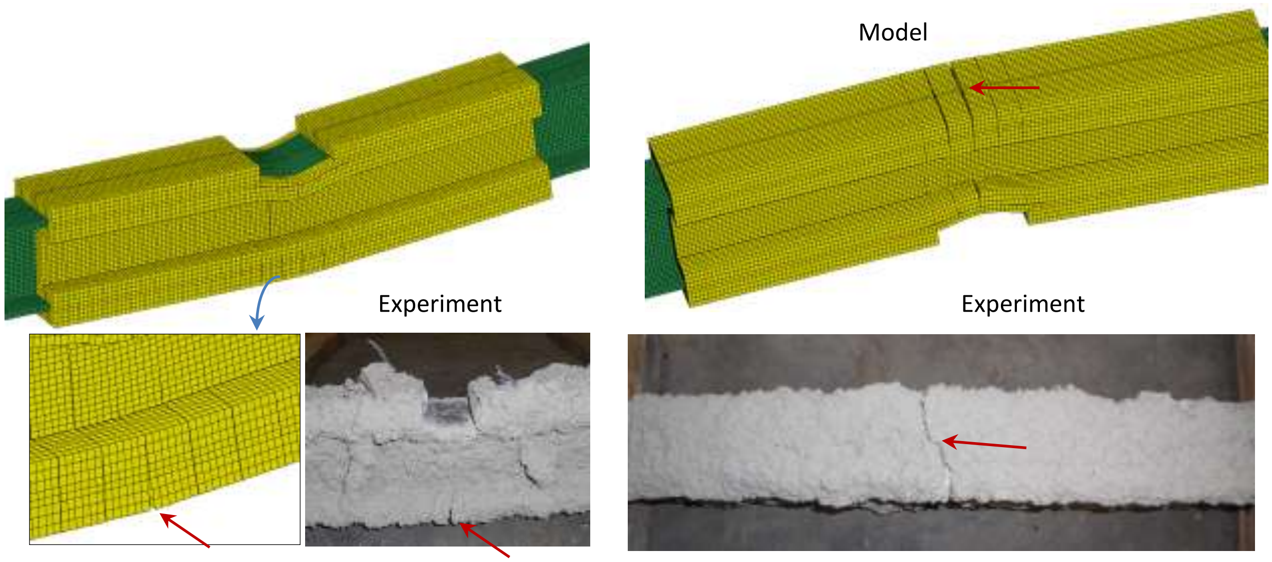

a) Deformed shape predicted by finite element model

b) Cracking on the bottom flange

Figure 5.44 Numerical and experimental illustration of extent of delamination in beam insulated with Portland cement-based SFRM (DIF=2.32)

As discussed in Chapter 4, in dynamic numerical modeling, the effect of rate-dependency of material is represented by material and interfacial constitutive laws. However, the influence of inertia forces is automatically accounted for through dynamic analysis where the material constitutive law interacts with structural inertia forces. Therefore, the dynamic increase in fracture properties explained above can only be attributed to rate-dependency of growing micro-cracks at the interface of steel and SFRM, which is considered as material property.

5.6 Delamination of Fire Insulation from Steel Beam-Column Assembly under Blast Loading

The validated numerical model is employed to carry out a set of parametric studies to evaluate the effect of most influential parameters that can affect the failure and delamination of fire insulation from steel beam-column under blast load. Under blast loading, blast overpressure is an additional parameter that can have important role on the delamination of SFRM from steel structures. In this parametric study, the focus is devoted towards the previously explained three important material properties of SFRM, namely fracture energy, elastic modulus and thickness along with blast overpressure. The axial force of the beam-column is maintained at 40 % of the axial capacity of the member, and duration of impact is retained at 10 ms.

5.6.1 Analysis Details

A typical insulated beam-column with height of 4880 mm and cross section of W14X193, which is made of ASTM A992- Gr.50 steel, is analyzed in the parametric study. Three types of SFRM namely Portland cement-based, gypsum-based and mineral fiber-based are considered in the analysis. The cohesive laws determined for the three types of SFRM, shown in Fig. 3.11, are utilized for modeling delamination between SFRM and steel. The finite element model of the beam-column insulated with SFRM is depicted in Figure 5.45.

To simulate delamination between SFRM and steel the cohesive zone model is employed in conjunction with contact type "Automatic_One_Way_Surface_To_Surface_Tiebreak" (LS-DYNA, 2014). The steel and SFRM is considered fully bonded at unstressed condition. Upon failure, the contact type is changed to "Surface_To_Surface". The contact formulation based on standard penalty method was not successful due to very low stiffness of SFRM. Consequently, soft constraint penalty formulation (LS-DYNA, 2014) is adopted to cope with excessive penetration as a result of low contact stiffness arising from very low stiffness of SFRM. In this formulation, the contact stiffness is no longer dependent on the stiffness of interacting bodies and the size of finite elements. Instead, it is determined based on stability of a local system composed of two masses connected by a spring. This stability contact stiffness ($K_{cs}(t)$) is computed as:

$$K_{cs}(t) = \frac{0.5\alpha M}{\Delta t_c(t)} \tag{5.9}$$

where, α is scale factor, M is a function of the mass of slave and master nodes, and $\Delta t_c(t)$ is the current stable solution time step (LS-DYNA, 2014).

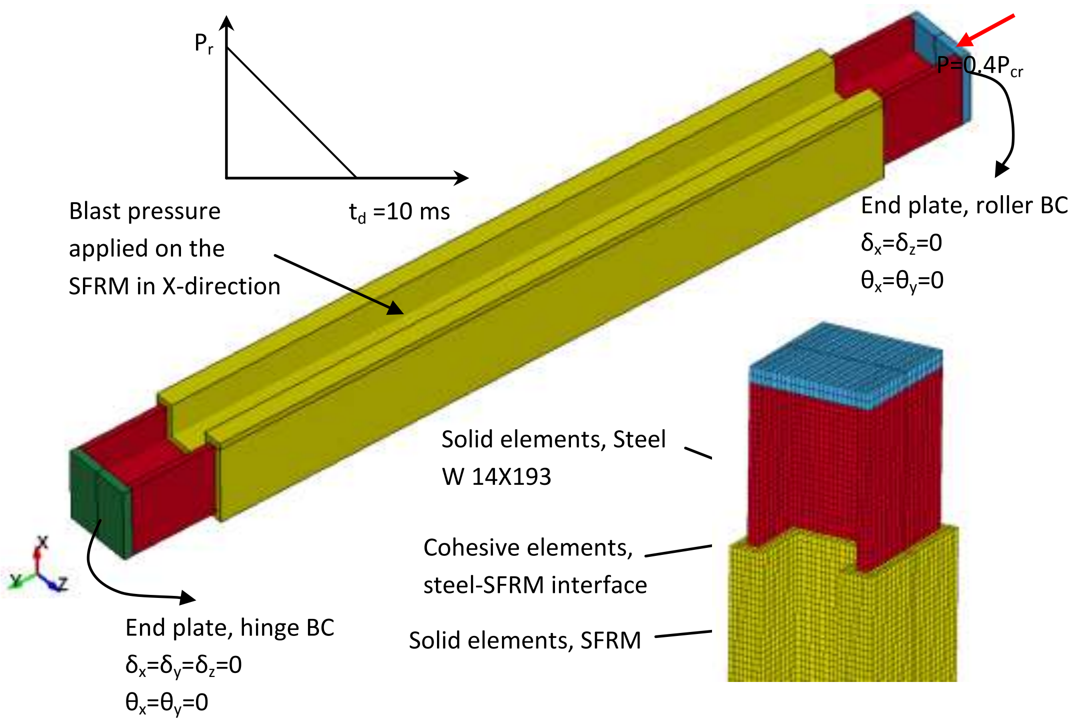

Figure 5.45 Finite element model of beam-column insulated with SFRM utilized in parametric study under blast loading

The two ends of the beam-column are modeled as hinge and roller boundary conditions, and an axial force up to 40% of the axial capacity of the beam-column is applied at the roller end. A triangular blast load with variable pressure and duration of 10 ms is applied in X-direction; therefore, the beam-column is loaded about its minor axis. The axial load is first applied slowly as nodal forces at the roller end of the beam-column and it is kept constant throughout the analysis. Subsequently, once the axial load reaches to its steady state, the blast pressure is applied.

5.6.2 Dynamic Response of the Beam-Column to Blast Load

The dynamic deformation of the beam-column depends on its natural frequency, current utilization factor under service loads, and characteristics of blast wave including blast overpressure and blast duration. In blast design, the energy-dissipation capacity of structural elements is engaged in order to reach a rational design. Consequently, the structural elements are expected to experience strain levels way higher than the yield strain that results in a large deformation. However, in case of beam-columns the level of inelastic energy dissipation cannot be allowed to be very high due to stability concern, and certain level of plastification occurs that can accelerate delamination of fire insulation from steel surface.

The first natural frequency of the beam-column is calculated using following expression for a simply supported beam-column (Bazant and Cedolin, 1991):

$$f = \frac{\pi}{2L^2}\sqrt{\frac{EI}{m}}\sqrt{1-\frac{P}{P_{cr}}} = 26.57\ Hz \tag{5.10}$$

where, L is the beam-column length, E is elastic modulus, I is moment inertia of the beam-column about minor axis and m is the mass per unit length of the beam-column. The natural period (T_n) of the beam is computed as T_n=37.63 ms (milliseconds) and duration of the blast load is t_d =10 ms. According to Baker et al. (1983), since $0.4 < \omega t_d = 1.67 < 40$ ($\omega=2\pi/T_n$), the loading regime is considered dynamic. Therefore, conducting dynamic analysis is necessary to accurately predict the response of the beam-column to blast load.

Figure 5.46 shows deflection time-history at mid-span of the beam-column under blast pressure varying between 200 to 1200 kPa. In all analyses, the beam-column undergoes a maximum deflection at around 11.6 ms and subsequently the beam-column rebounds and experiences a negative displacement at around 28 ms. The progressive delamination of mineral fiber-based SFRM from steel surface during the first 10 ms of the beam-column response is illustrated in Figure 5.47. The results presented in this figure are based on the model analyzed under blast overpressure of 500 kPa. The SFRM around the flange tips suffer severe cohesive failure during the first 2 ms of the blast load. Subsequently, interfacial cracks are initiated and the cracks propagate over the exterior surface of the flanges as well as the interior surface of the flanges exposed to the blast pressure. As can be seen in Figure 5.47, SFRM gets completely delaminated from flanges during first 10 ms of the response of the beam-column to blast load.

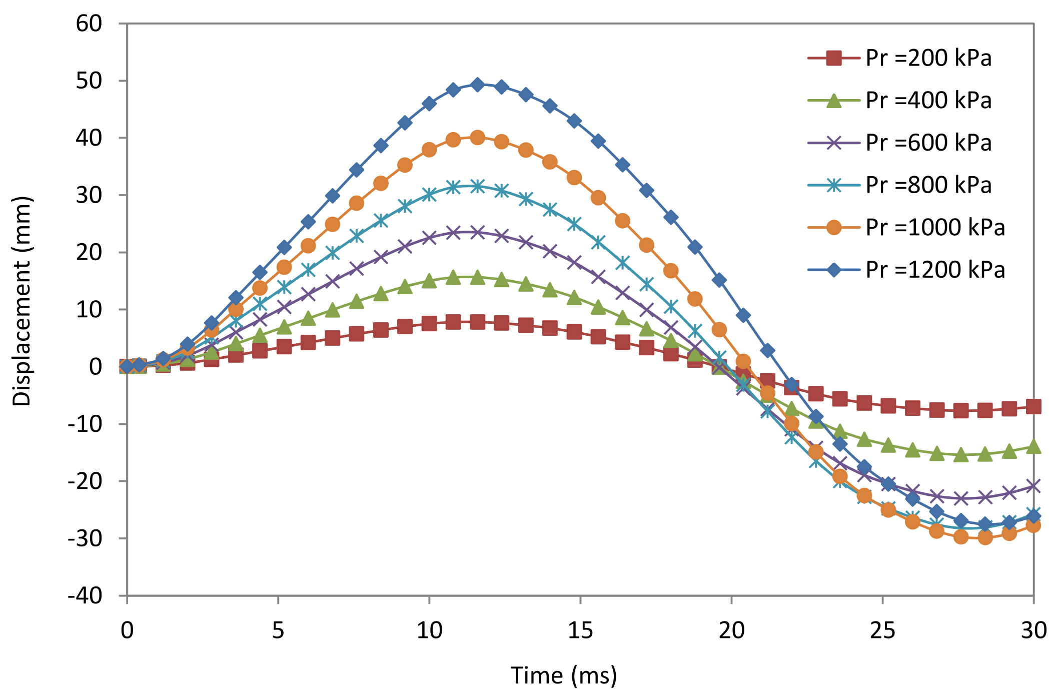

Figure 5.46 Mid-span deflection of the beam-column insulated with SFRM under different blast overpressure level

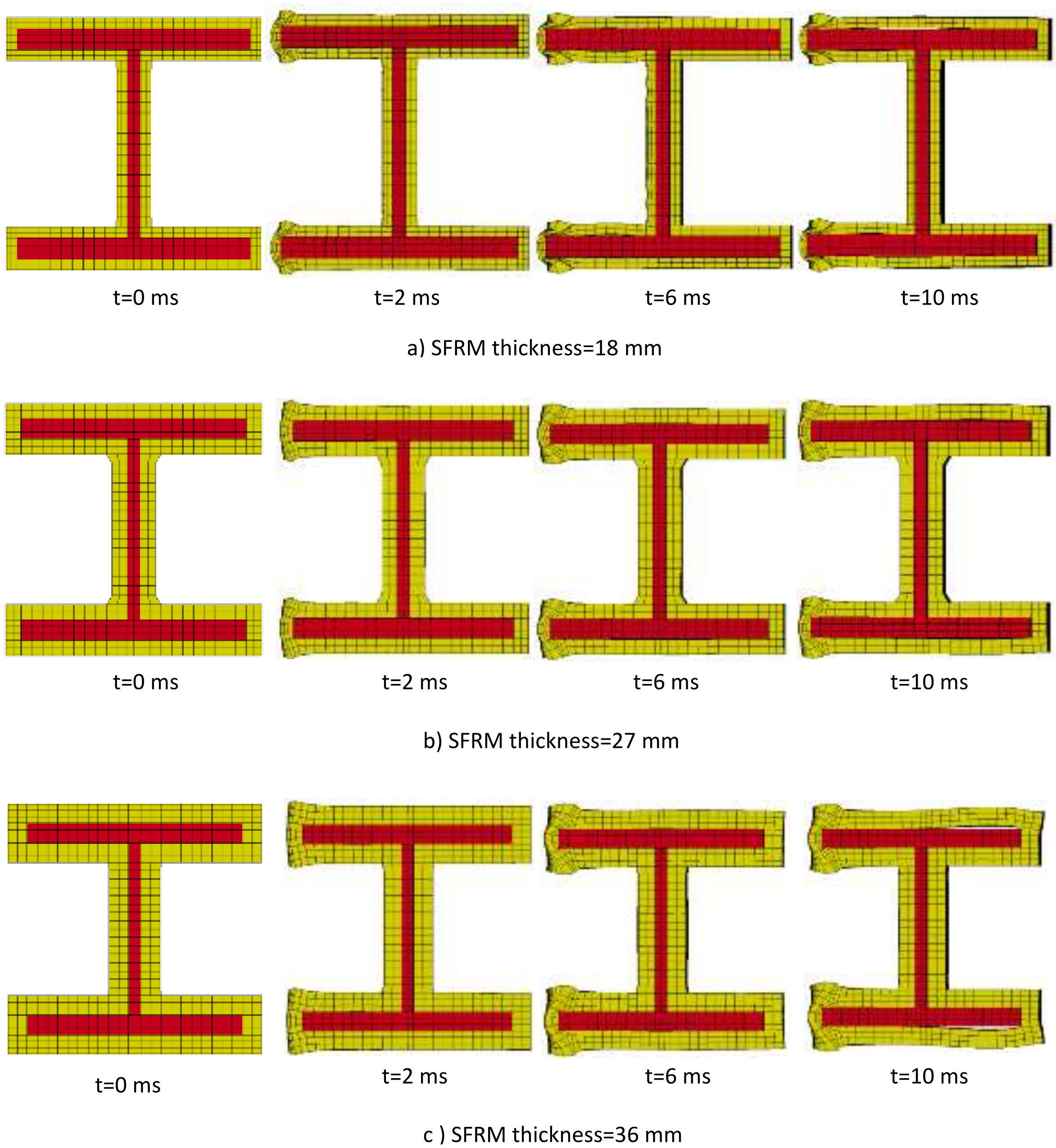

Figure 5.47 Illustration of delamination of mineral fiber-based SFRM from steel beam-column over the first 10 ms of the blast scenario

5.6.3 Effect of Blast Overpressure

For each type of SFRM and for three incremental thicknesses of 18 mm, 27 mm and 36 mm, the blast overpressure was incrementally applied until 100 % delamination occurred over the outer face of flanges and inner face of the flanges of beam-column exposed to blast overpressure.

Figure 5.48, Figure 5.49 and Figure 5.50 plot variation of delamination percentage with respect to blast overpressure for three types of SFRM and three thicknesses. The overall trend in all graphs is advancement of delamination by increasing the blast overpressure.

In addition, effect of thickness is pronounced, such that, the thicker the insulation, the earlier the delamination is completed. In other words, the thicker SFRM requires lesser overpressure to get fully detached from steel surface. The Portland cement-based SFRM shows a superior performance and gypsum-based SFRM has higher resiliency than mineral finer-based SFRM. For instance, Portland cement-based SFRM with thickness of 18 mm can survive a blast over pressure up to 500 kPa, whereas the gypsum-based and mineral fiber-based SFRM can only endure a blast overpressure of 200 kPa and 75 kPa, respectively.

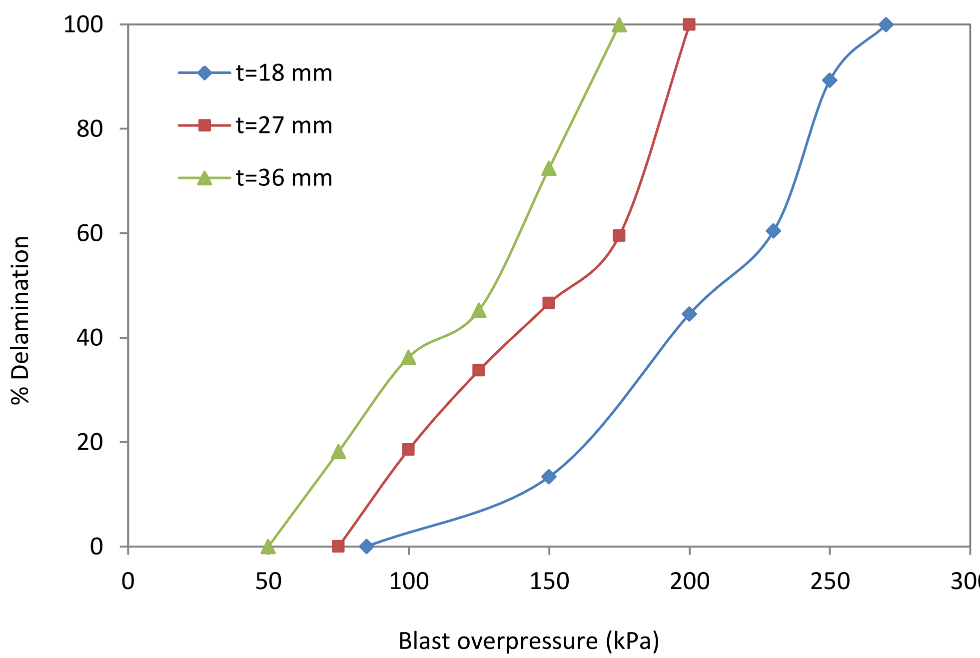

Figure 5.48 Extent of delamination on steel column as a function of blast overpressure for mineral fiber-based SFRM

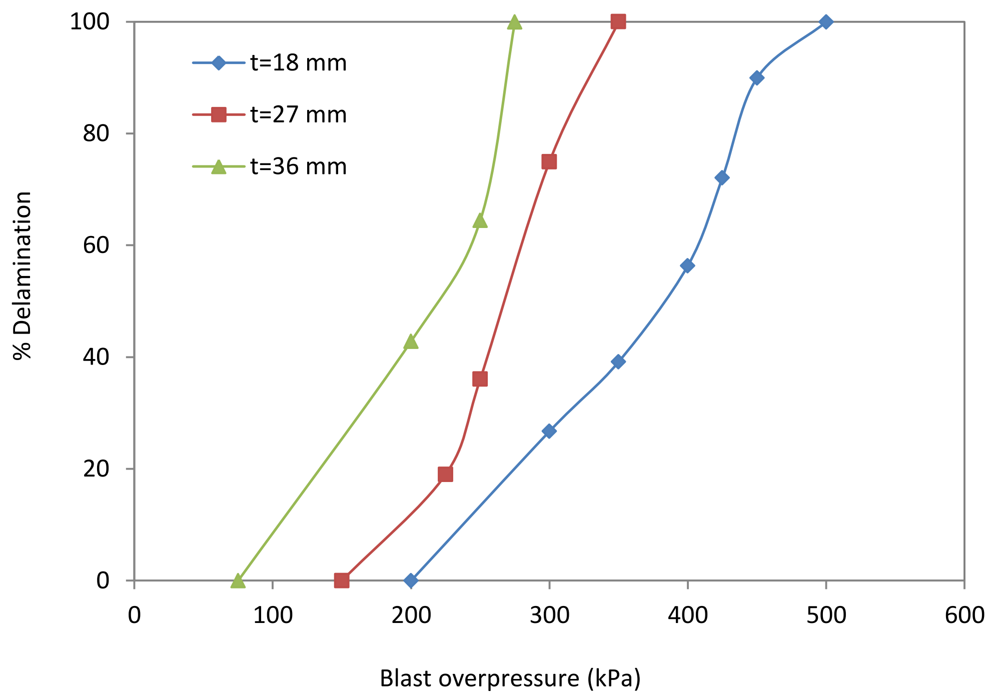

Figure 5.49 Extent of delamination on steel column as a function of blast overpressure for gypsum-based SFRM

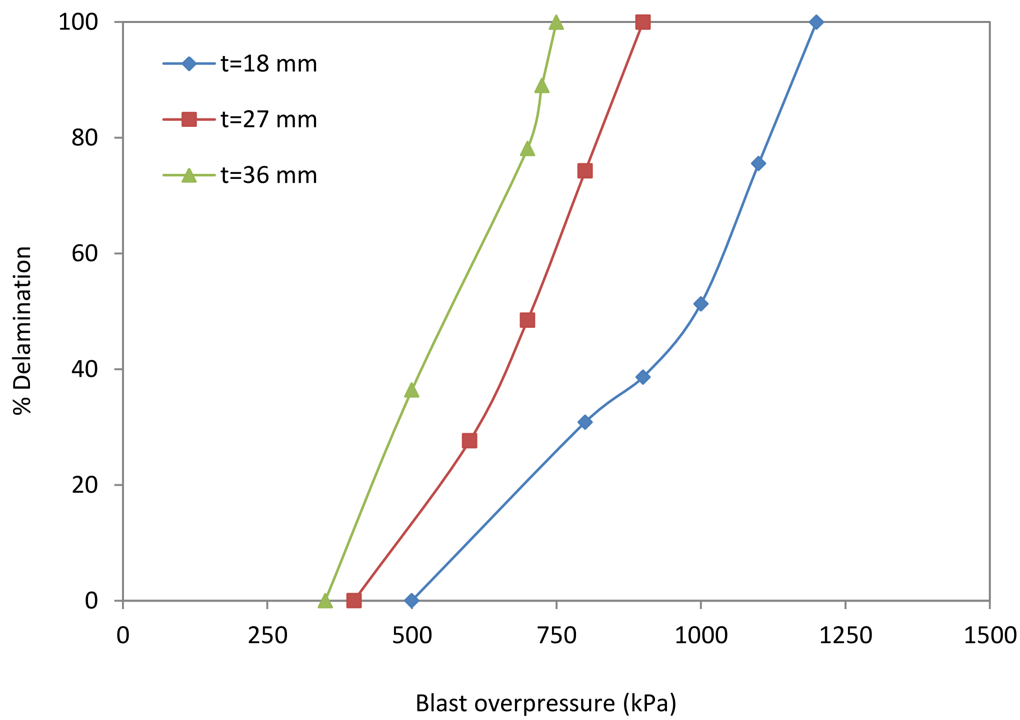

Figure 5.50 Extent of delamination on steel column as a function of blast overpressure for Portland cement-based SFRM

5.6.4 Effect of Elastic Modulus

To quantify the effect of variation in elastic modulus of SFRM on the extent of delamination, the elastic modulus (E) is enhanced incrementally while the fracture energy is kept constant. The blast overpressure is also maintained at the level that caused full delamination when elastic modulus had its normal value presented in Table 1 (E_0). It is shown in Figure 5.51, Figure 5.52 and Figure 5.53 that enhancing the stiffness of SFRM can considerably diminish the extent of delamination. However, the effect is more distinct when the elastic modulus is enhanced by 50%, such that the delamination extent plummets by 40%. Afterwards, increasing the elastic modulus reduces the extent of delamination, however with slower pace.

The exception for above explained behavior is the mineral fiber-based SFRM with thickness of 36 mm which can be noticed in Figure 5.51. The slower level of improvement in performance of mineral fiber-based SFRM with thickness of 36 mm may be attributed to its very low stiffness and also the fact that higher thickness absorbs more energy from blast that can dilute the effect of increasing the elastic modulus. Overall, the results obtained from parametric study with respect to elastic modulus reveals that enhancing the stiffness of SFRM can be very helpful in mitigating the delamination under blast load.

It should be highlighted here that the above results with respect to effect of elastic modulus in SFRM delamination is opposite to the one obtained under seismic loading. It was concluded in section 5.4.4 that increasing elastic modulus of SFRM has negative effect on its resiliency against delamination. This discrepancy can be attributed to the fact that the load is carried by steel substrate under seismic loading and straining in steel leads to delamination since SFRM cannot maintain compatibility at SFRM-steel interface. However, the load is directly applied on SFRM under blast loading and SFRM transfers the blast overpressure to the steel member.

Therefore, the stiffer the SFRM the faster the blast wave propagates through SFRM and less damage is incurred by SFRM. In contrast, flexible SFRM transmits the blast wave with less speed and hence undergoes higher damage.

It is noted that in this parametric study, the blast loading from internal explosion was considered. The external blast overpressure does not directly apply on the SFRM; instead, the blast pressure, applied on the exterior walls of the building, transfers the load to column (distributed load on the steel). In that case, the effect of elastic modulus will be similar to the one concluded under seismic loading. A different set of parametric study is thus to be carried out in order to quantify the effect of elastic modulus of SFRM under external blast.

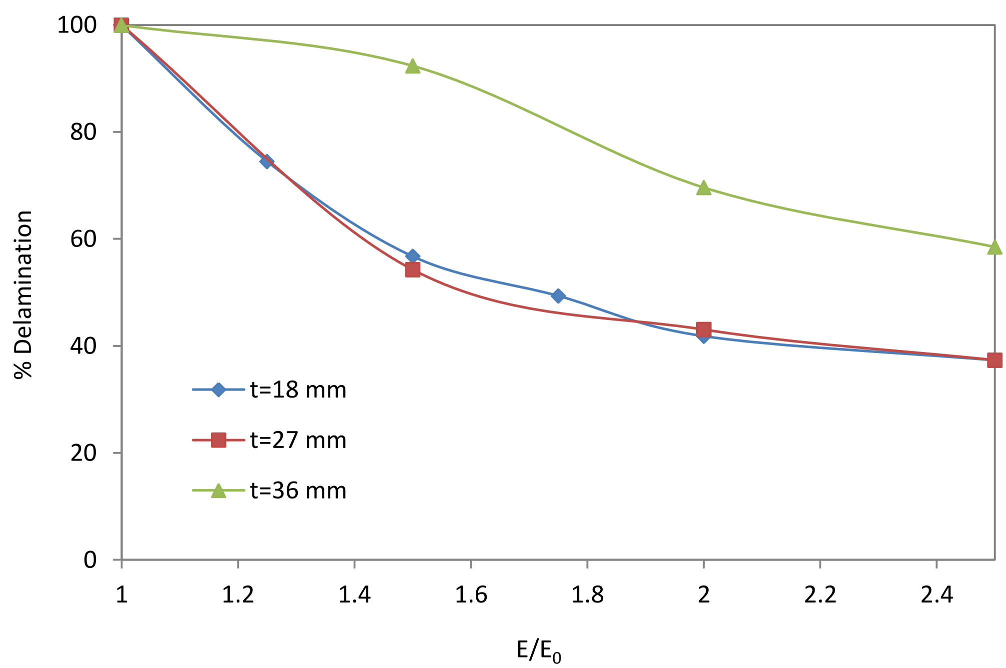

Figure 5.51 Extent of delamination on steel column as a function of elastic modulus for mineral fiber-based SFRM

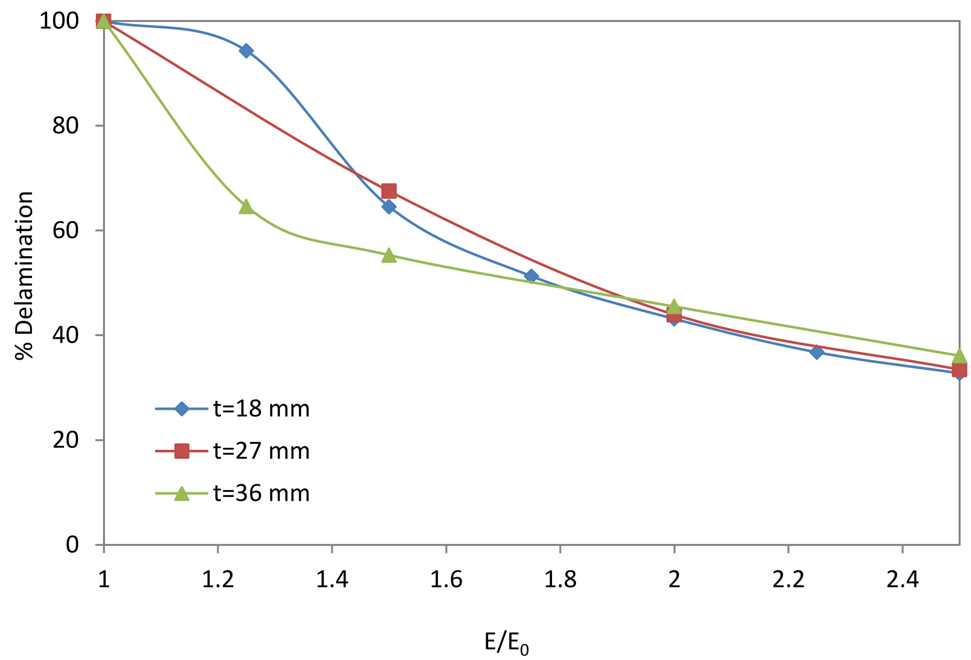

Figure 5.52 Extent of delamination on steel column as a function of elastic modulus for gypsum-based SFRM

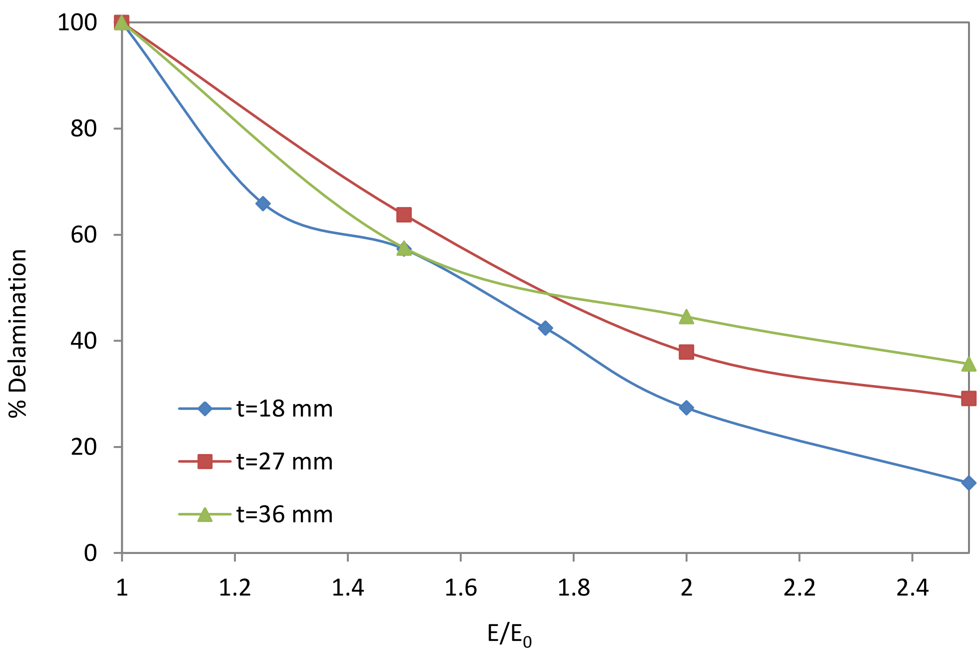

Figure 5.53 Extent of delamination on steel column as a function of elastic modulus for Portland cement-based SFRM

5.6.5 Effect of Fracture Energy

The crucial effect of fracture energy is quantified by increasing the amount of fracture energy (G) up to 2.5 times the average value measured in fracture experiments (G_0). The blast overpressure is maintained at the level that caused full delamination when fracture energy is not changed. The elastic modulus is also kept constant. Figure 5.54, Figure 5.55 and Figure 5.56 depict the variation of delamination extent with respect to the fracture energy increment factor between 1.0 and 2.5. The amount of reduction in extent of delamination is substantial (50%) when the fracture energy is enhanced by 50%. Subsequently, though the level of improvement gets slower, it is still significant. The extent of delamination can be reduced down to 20% when the fracture energy is boosted up to 250% of the normal value.

A very analogous trend is noticeable for all three types of SFRM with three levels of thickness, except in the case of mineral fiber-based SFRM with thickness of 36 mm. The enhancement pace is slower in this case presumably due to the fact that this type of SFRM possesses a very low level of fracture energy as compared to the other types of SFRM and also the higher thickness of SFRM is prone to higher force level exerted by blast overpressure that can partially suppress the positive effect of increasing fracture energy.

In general, results of this parametric study demonstrate that improving the fracture energy of SFRM is the dominant approach towards increasing the resiliency of SFRM when subjected to blast overpressure. It should be kept in mind that increasing the fracture energy of material can increase the elastic modulus as well, thereby substantially boosting the resiliency of SFRM to endure the blast loading.

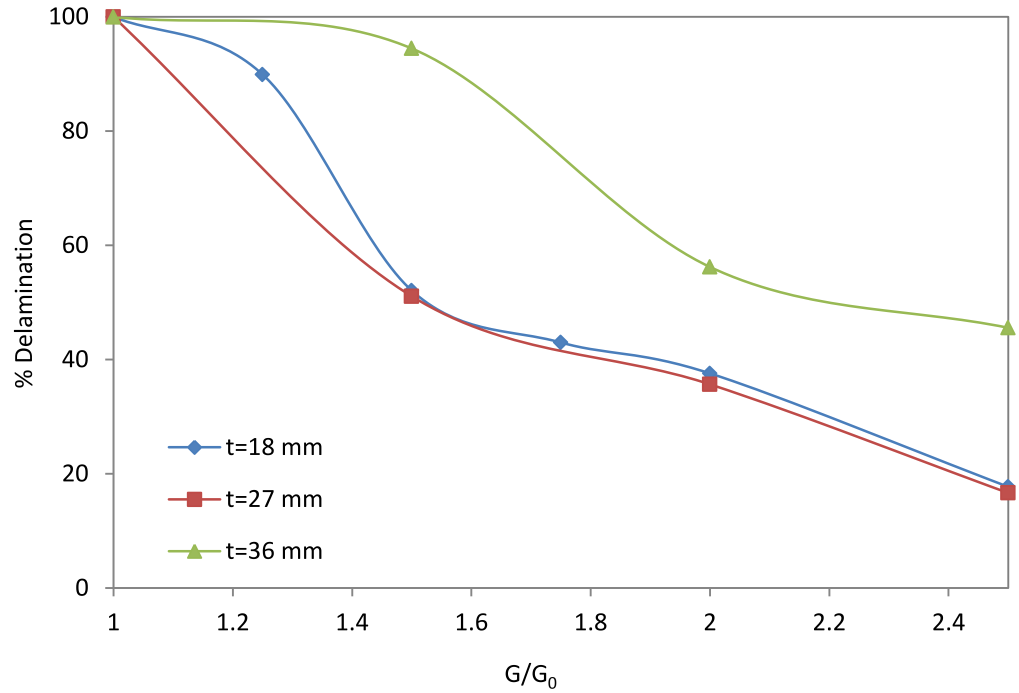

Figure 5.54 Extent of delamination on steel column as a function of fracture energy for mineral fiber-based SFRM

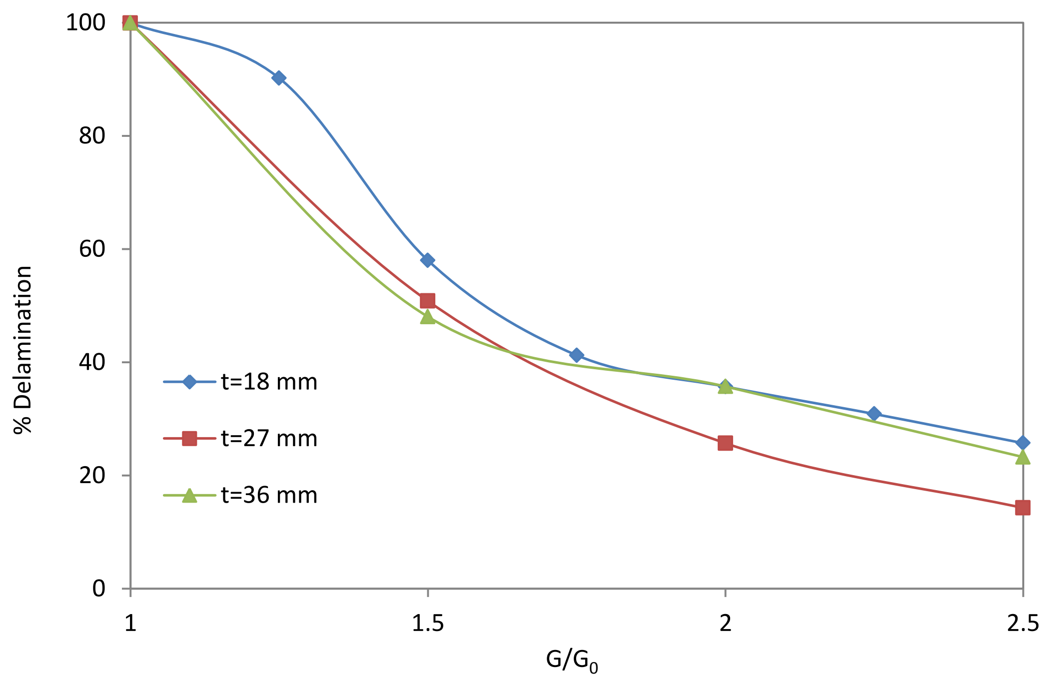

Figure 5.55 Extent of delamination on steel column as a function of fracture energy for gypsum-based SFRM

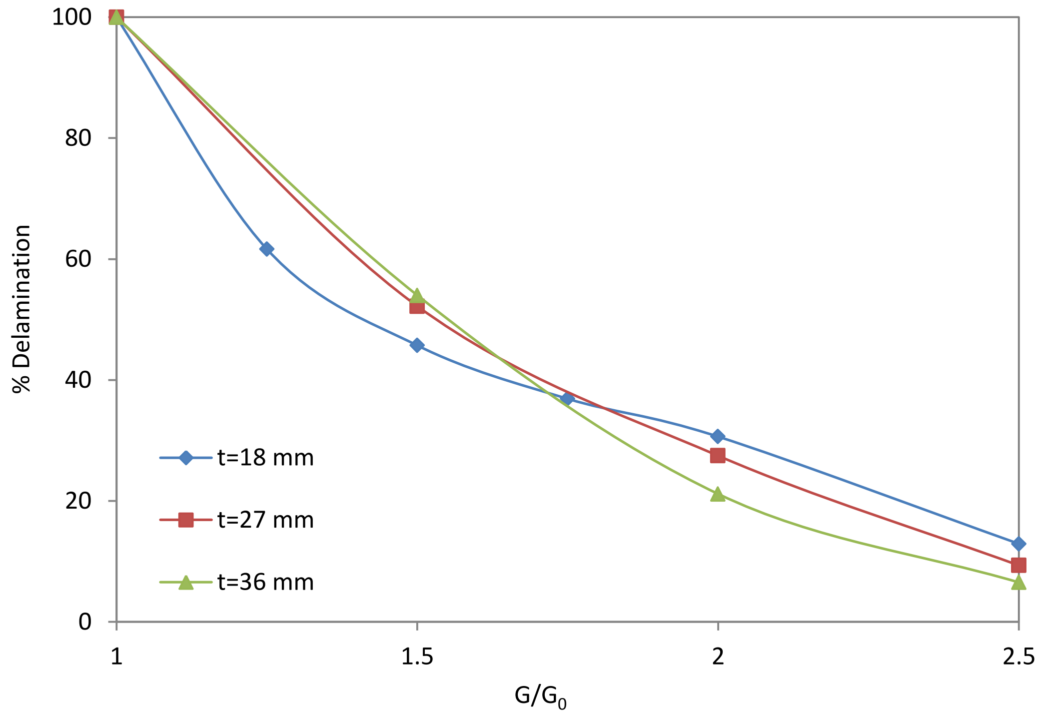

Figure 5.56 Extent of delamination on steel column as a function of fracture energy for Portland cement-based SFRM

5.6.6 Parameter for Characterizing Delamination of Fire Insulation under Blast Loading

Results obtained from the above presented parametric study are compiled in one place to explore the interdependency between the governing factors. The parametric study clarified that the extent of delamination has a direct relationship with blast overpressure and thickness of SFRM, while it has an inverse relationship with elastic modulus and fracture energy of SFRM. Therefore, a parameter ($d_{ch,blast}$) than can characterize the delamination of SFRM from steel structures under blast load by incorporating most of the governing factors, can be expressed as:

$$d_{ch,blast} = \frac{tP_r}{E\bar{G}_c} \tag{5.11}$$

where, P_r is the blast overpressure and t, E and G_c are thickness, elastic modulus and fracture energy of the SFRM, respectively. The fracture energy, G_c, is defined as:

$$\bar{G}_c = \sqrt{{G_{nc}}^2 + {G_{tc}}^2} \qquad (5.12)$$

where, G_{nc}, G_{tc}, are fracture energy at normal mode and fracture energy at tangential mode, respectively. Figure 5.57 plots percentage of delamination versus the delamination parameter ($d_{ch,blast}$) in a logarithmic scale. It is obvious that there are three distinct regions in the curve each one pertaining to a certain type of SFRM. The best fit to the data is a line representing delamination extent which is illustrated in the figure. The general equation for the lines in Fig. 5.57 can be written as:

$$l_d = \alpha . ln\left(\frac{tP_r}{E\bar{G}_c}\right) + \beta \qquad (5.13)$$

where, α and β are coefficients and *ln* returns natural logarithm. The coefficient α is equal to 73.5, 79.6, 85.1 and the coefficient β is equal to -232.6, -157.4, -80.6, for three types of SFRM namely mineral fiber-based, gypsum-based and Portland cement-based, respectively.

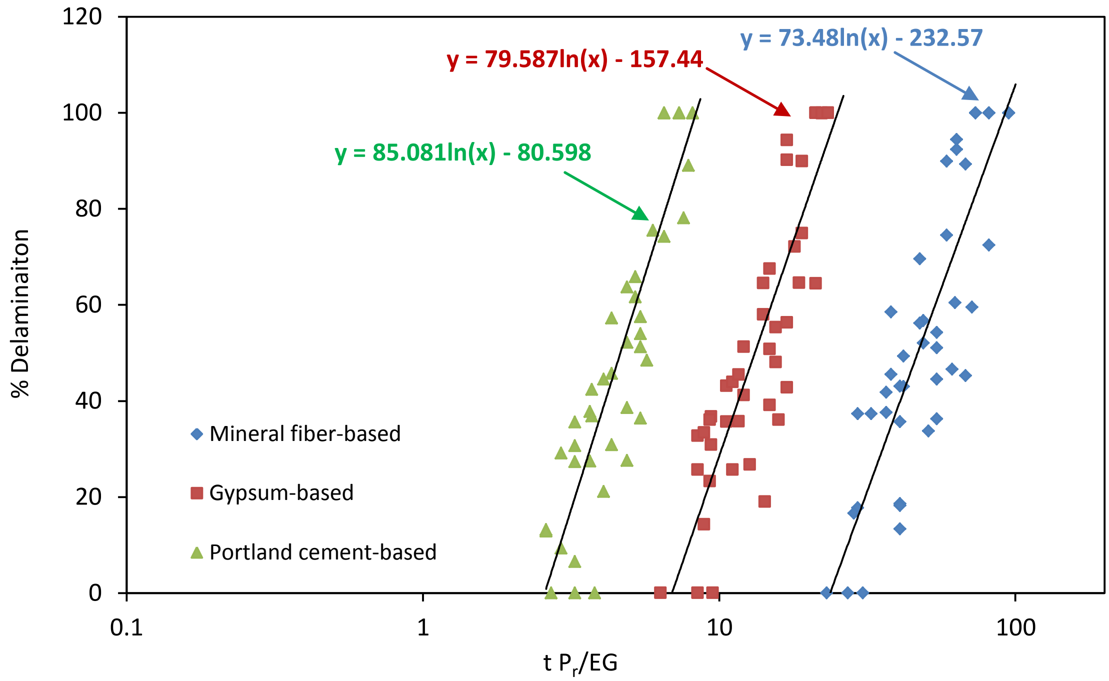

Figure 5.57 Extent of delamination on steel beam-column under blast loading as a function of delamination characteristic parameter

5.7 Summary

In this chapter, the numerical model developed and validated in chapter 4 was utilized to explore most effective parameters influencing delamination of fire insulation from steel structures under different loading conditions. The parametric study was started by modeling a flimsy truss member insulated with spray-applied fire-resistive material (SFRM) under quasi-static tensile deformation. Based on the results of first parametric study, a delamination characteristic parameter was defined that incorporates four material properties of SFRM namely fracture energy, elastic modulus, thickness and displacement ductility of the cohesive law over fracture process zone. Subsequently, strain level at steel corresponding to initiation of cracks at steel-SFRM interface and complete delamination was quantified and related to the delamination characteristic parameter.

The parametric study continued by investigating the factors governing delamination of SFRM from steel beam-column assembly subjected to seismic loading. Effect of above mentioned four parameters was quantified for three types of fire insulation namely gypsum-based, Portland cement-based and mineral fiber-based SFRM. Results from this parametric study revealed that among above four factors the effect of displacement ductility over fracture process zone is not pronounced under cyclic loading. Consequently, the delamination characteristic parameter, established in previous section, was revised by dropping the displacement ductility term. The extent of delamination over bottom flange of the beam near the column was quantified and related to the new delamination characteristic parameter redefined for seismic loading. Eventually, effective properties for SFRM to prevent delamination during seismic deformation were quantified.

The parametric study under impact loading was devoted to quantify effect of strain rate on fracture properties of three types of SFRM using an indirect method. The dynamic increase factor on the cohesive laws were estimated by comparing observed and numerically predicted values of the extent of delamination on bottom flange of an insulated beam subjected to drop mass impact. It was concluded that the level of strain rate dependency of fracture energy depends on the material constituents of fire insulation. The SFRM containing high amount of Portland cement showed higher sensitivity to strain rate while SFRM including gypsum demonstrated less strain-rate dependency. Further, strain rate showed no effect for SFRM composed of mineral fibers.

The chapter is closed by presenting the results of parametric study under blast loading. An additional parameter namely blast overpressure was included into parameters affecting delamination of fire insulation from a steel beam-column. Based on the results of numerical model, the delamination characteristic parameter, proposed in forgoing parametric studies, was further modified to capture performance of SFRM subjected to blast loading. Eventually, the extent of delamination over the steel beam-column was quantified and presented as a function of the new delamination characteristic parameter for three types of SFRM.

CHAPTER 6

6 CONSEQUENCES OF FIRE INSULATION DELAMINATION

6.1 General

In previous chapters the mechanisms of fracture and delamination of fire insulation from steel structures was outlined and the extent of delamination over the structural members was quantified. In this chapter, a numerical study is presented in which the consequences of loss of fire insulation from steel structures during fire following earthquake and blast are studied. To be consistent with the results presented in the forgoing chapters, the structural configurations used in this chapter are same as those used for modeling delamination. Two sets of analyses are performed; in the first set the consequence of loss of fire insulation from beam near the column during seismic loading is investigated, and in the second set of analysis effect of fire insulation delamination from a beam-column subjected to blast loading is studied.

In the both sets of analysis, only one type of fire insulation namely gypsum-based SFRM is considered since high temperature thermal properties are not available for two other types of SFRM namely Portland cement-based and mineral fiber-based SFRM (Kodur and Shakya, 2013). A sequential thermal-structural analysis is carried out using ANSYS program to compute the temperature time-history developed in the insulated beam and column during exposure to fire and its effect on structural softening and global and local behavior of structural elements. The numerical procedure outlined and verified in Chapter 5 is utilized in this chapter to quantify the time to failure of a moment frame and a beam-column during fire following earthquake and explosion, respectively.

6.2 Post-earthquake Fire Response of a Moment-Resisting Frame

To study effect of fire insulation delamination under seismic loading on structural integrity of steel moment frames during fire following earthquake two types of analysis are carried out. In the first type of analysis, the effect of delamination of fire insulation during earthquake is quantified in terms of softening occurred in the load-displacement relationship of a beam-column assembly. In the second type of analysis, the time to failure of a beam-column assembly under fire exposure following earthquake, which is sustaining gravity loading, is quantified.

6.2.1 Analysis Procedure to Obtain Load-Displacement Relationship

To obtain temperature-dependent load-displacement relationship during fire exposure, the beam-column assembly used for quantification of extent of delamination is subjected to sequential thermal and structural analysis. First, the temperature rise with time is predicted within the beam and column cross sections. Figure 6.1 shows the beam and column cross sections discretized for carrying out thermal analysis. According to results presented in Chapter 5, when delamination occurs over the plastic hinge region of a beam near the column, SFRM gets detached from both web and flanges, hence the beam cross section is left completely unprotected on this region. Consequently, the beam cross section is analyzed under fire condition for two cases; beam without SFRM and beam covered with SFRM. Given the fact that no delamination occurs in the column, the column cross section is confined with SFRM in the thermal analysis.

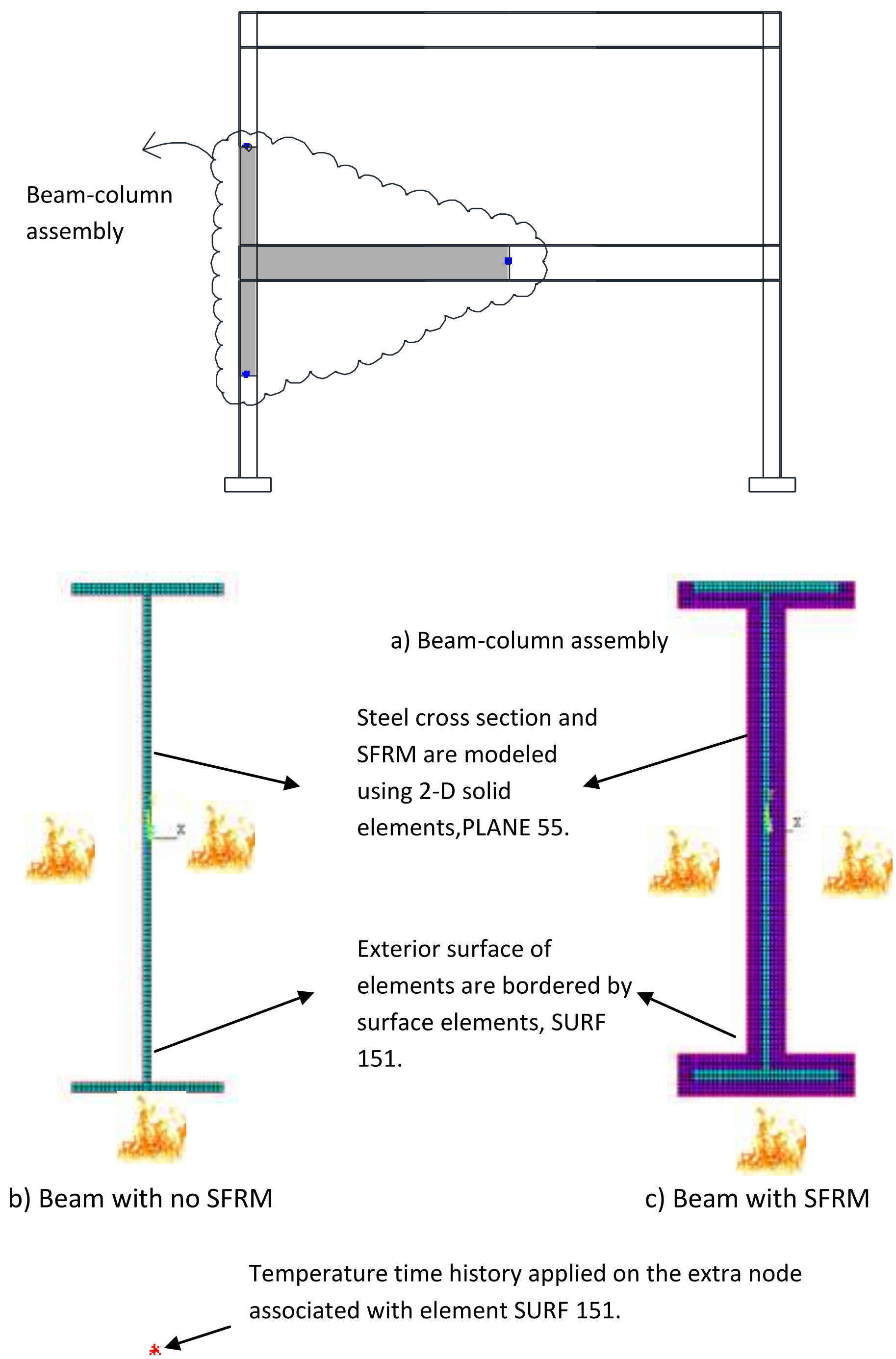

Figure 6.1 Finite element model of thermal analysis carried out to compute temperature time history of beam-column

Figure 6.1 (cont'd)

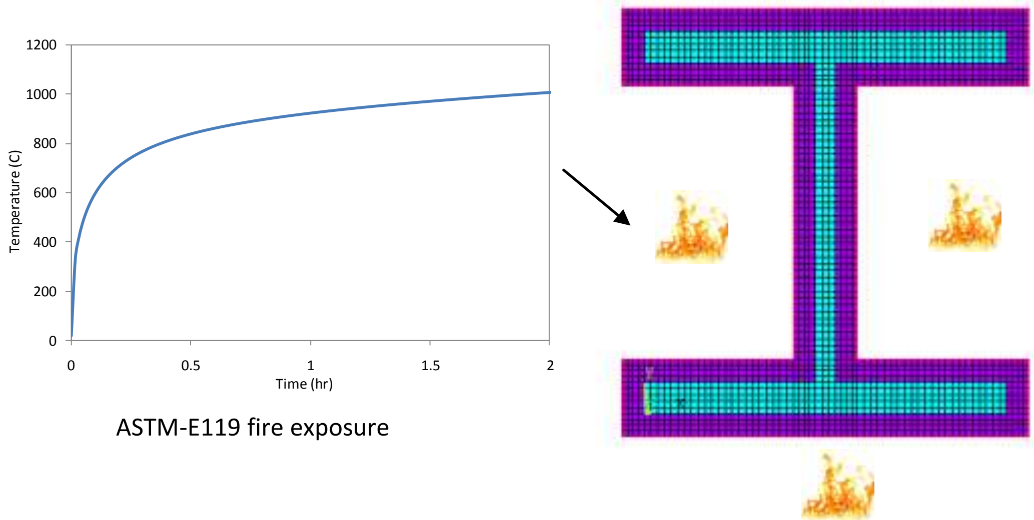

d) Column with SFRM

The steel cross section and SFRM are discretized using two dimensional plane elements (PLANE55) with temperature nodal variable. The SFRM type is gypsum-based with thickness of 20 mm (Braxtan and Pessiki, 2011b). The heat radiation is modeled by overlaying surface elements (SURF151) over the exterior edge of the elements exposed to fire. The temperature time history resulting from standard fire (ASTM E119) is applied to the nodes associated with the surface elements. Further, the convective fire loading is applied on three surfaces exposed to fire. The beam cross section is engulfed by fire from three sides due to presence of concrete floor over the top flange. The column cross section is however expected to be exposed to fire from all four faces.

Figure 6.2 illustrates the temperature distribution over the cross section of the beam insulated with gypsum-based SFRM after being exposed to standard fire for two hours. As can be seen, the entire section reaches to almost same temperature after two hours. The temperature evolution over the flange of the beam and column is plotted in Figure 6.3 in conjunction with the input fire temperature. The beam with no insulation can experience temperature up to 600°C within first 30 minute of the fire, while the temperature in the beam insulated with SFRM only reaches 200°C over the same duration. The column cross section develops considerably less temperature as compared to beam cross section due to thicker web and flanges which increase the thermal capacity of section and hence more energy is absorbed by the steel.

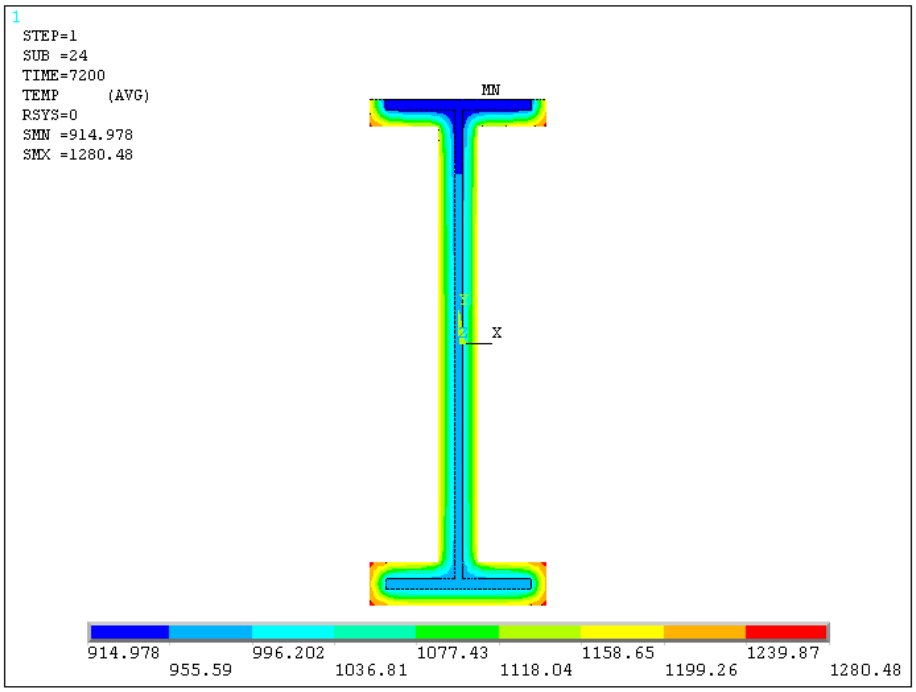

Figure 6.2 Temperature (K) distribution in the beam insulated with gypsum-based SFRM exposed to standard fire (ASTM E119)

The finite element model of the beam-column assembly is depicted in Figure 6.4. The model has been simplified compared to the one used for studying delamination to reduce the computation time. The beam and column sections in the vicinity of connection and plastic hinge region are discretized using shell elements (SHELL181) while the remained portion of the beam and column is discretized using nonlinear beam elements (BEAM188). A displacement-controlled loading is applied at the tip of the beam and reactions of the column are monitored. The analysis is performed at five incremental target temperature levels; i.e. 200°C, 400°C, 600°C, 800°C and 1000°C. The above target temperatures are applied to the region experiencing delamination and the corresponding temperature at column and insulated beam are applied at the same time. Subsequently, the beam is pushed downward to reach the target displacement (166 mm).

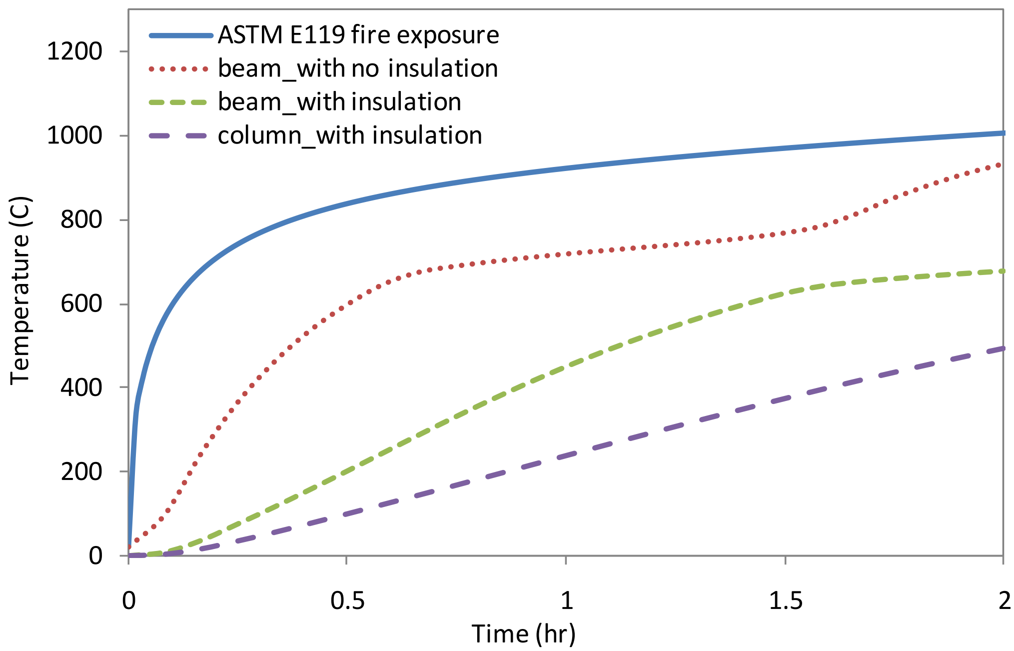

Figure 6.3 Temperature evolution in the beam and column subjected to standard fire (ASTM E119)

Figure 6.5, through Figure 6.8 show the load-displacement relationship under four incremental delamination scenarios, i.e. 25%, 50%, 75% and 100%, over the plastic hinge region. Note that plastic hinge region measures 1000 mm from face of the column. A dramatic reduction in the load carrying capacity of the system is noticeable when temperature reaches to 400 °C, which is due to considerable strength and modulus reduction of steel at this temperature. To better compare the effect of percentage of delamination on the capacity of the connection, the above results are presented in a different form by plotting load-displacement relationship for different levels of delamination at different temperatures. As is shown in Figure 6.9 through Figure 6.13, the larger the extent of the delamination, the larger the influence on the load-displacement response. Further, the effect of extent of delamination becomes more pronounced when temperature exceeds 200°C.

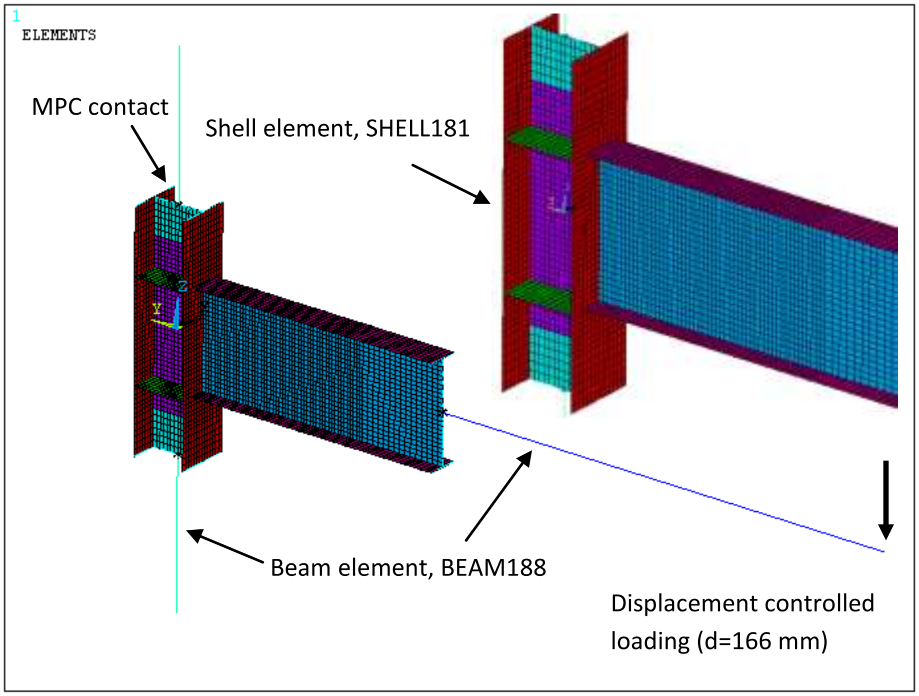

Figure 6.4 Finite element model of beam-column assembly used for studying effect of temperature rise on capacity reduction of moment connection due to loss of fire insulation during seismic loading

An interesting point in Figure 6.9 to Figure 6.13 is the softening occurred in load-displacement curve corresponding to 25% delamination of fire insulation. This softening is indicative of local instability in the bottom flange of the beam which is known as local buckling. By increasing temperature, the local buckling occurs faster and the amount of softening is increased. Figure 6.14 through Figure 6.17 clearly show that local distortion of the bottom flange only occurs when 25% of the plastic hinge of the beam is heated. This is presumably because of the fact that when the heated region is small, the tendency for expansion creates large compression stresses in the flange since the neighbor flange prevents expansion of the heated zone. However, when the heat-affected region is enlarged, the strains are relived and local buckling does not happen. For this reason, the load-displacement curves for temperatures above 200^{o}C do not show softening.

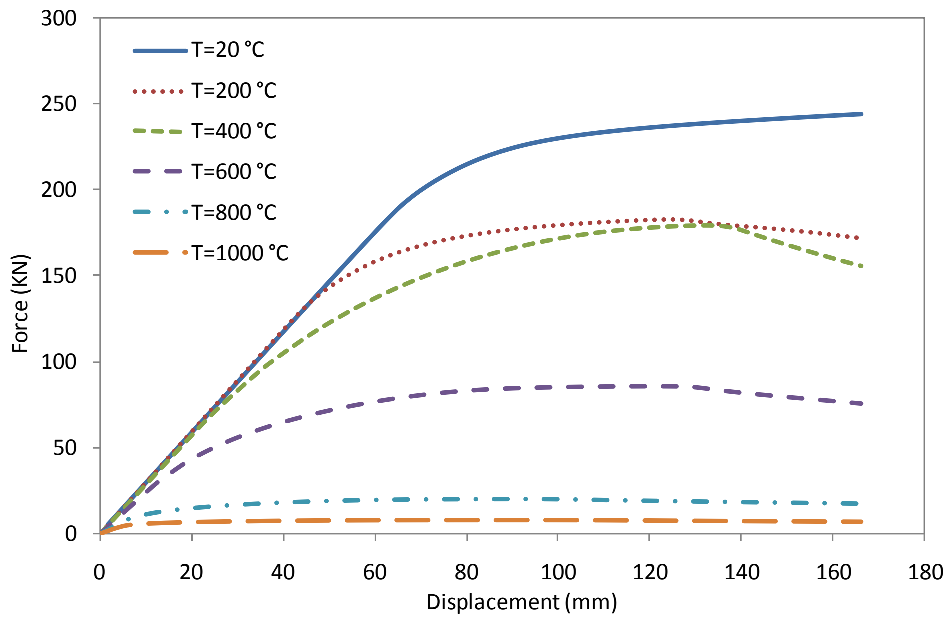

Figure 6.5 Effect of temperature on load-displacement relationship of beam-column assembly endured 25% delamination over the plastic hinge region on the beam

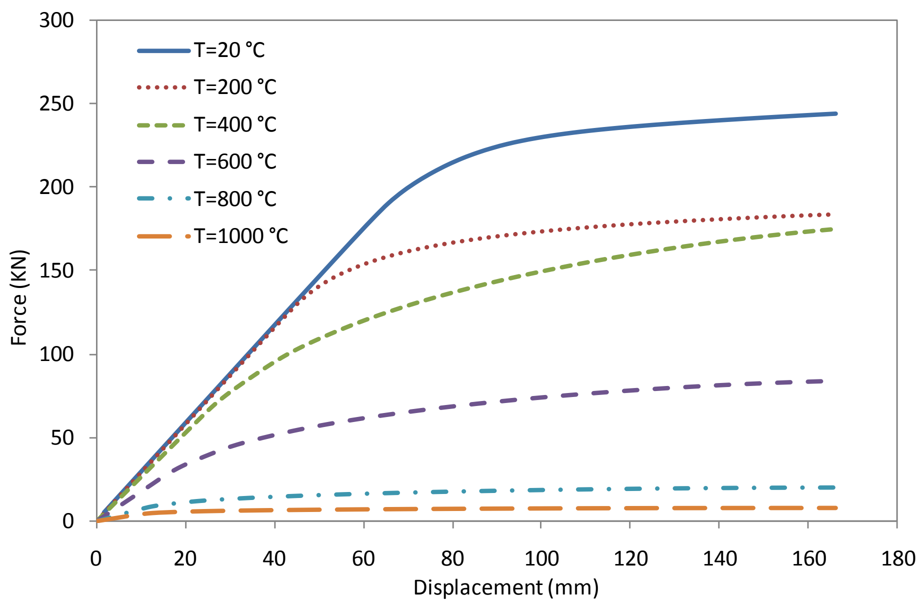

Figure 6.6 Effect of temperature on load-displacement relationship of beam-column assembly endured 50% delamination over the plastic hinge region on the beam

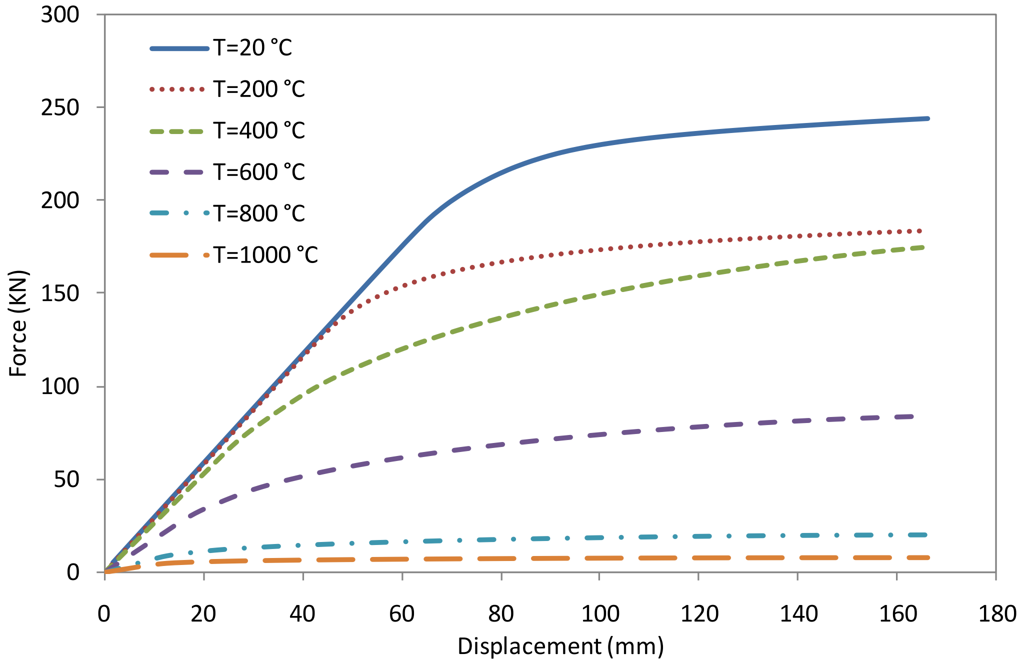

Figure 6.7 Effect of temperature on load-displacement relationship of beam-column assembly endured 75% delamination over the plastic hinge region on the beam

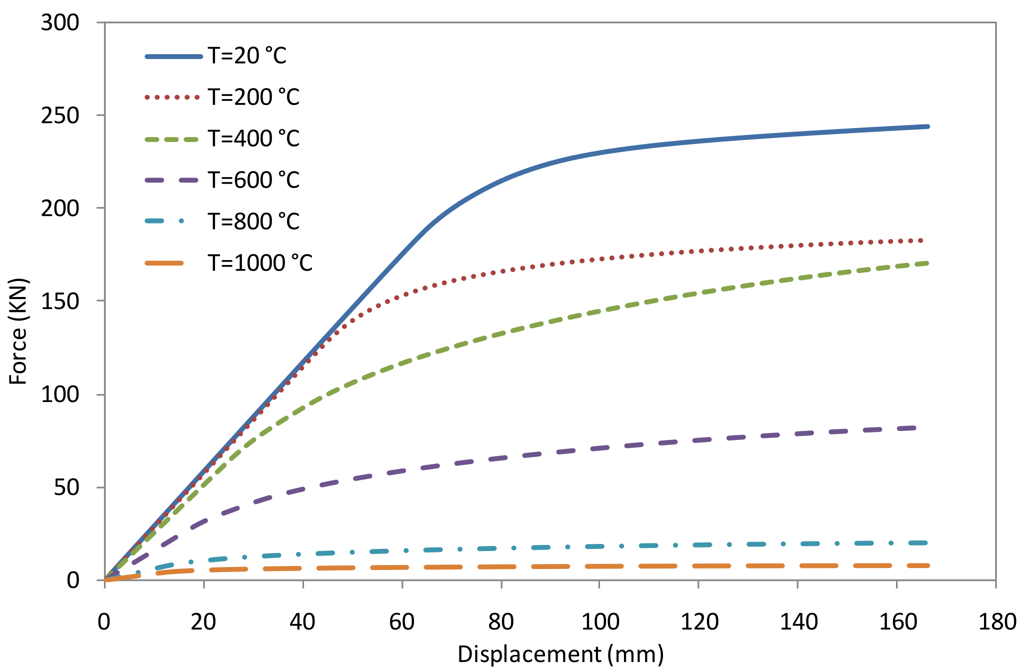

Figure 6.8 Effect of temperature on load-displacement relationship of beam-column assembly endured 100% delamination over the plastic hinge region on the beam

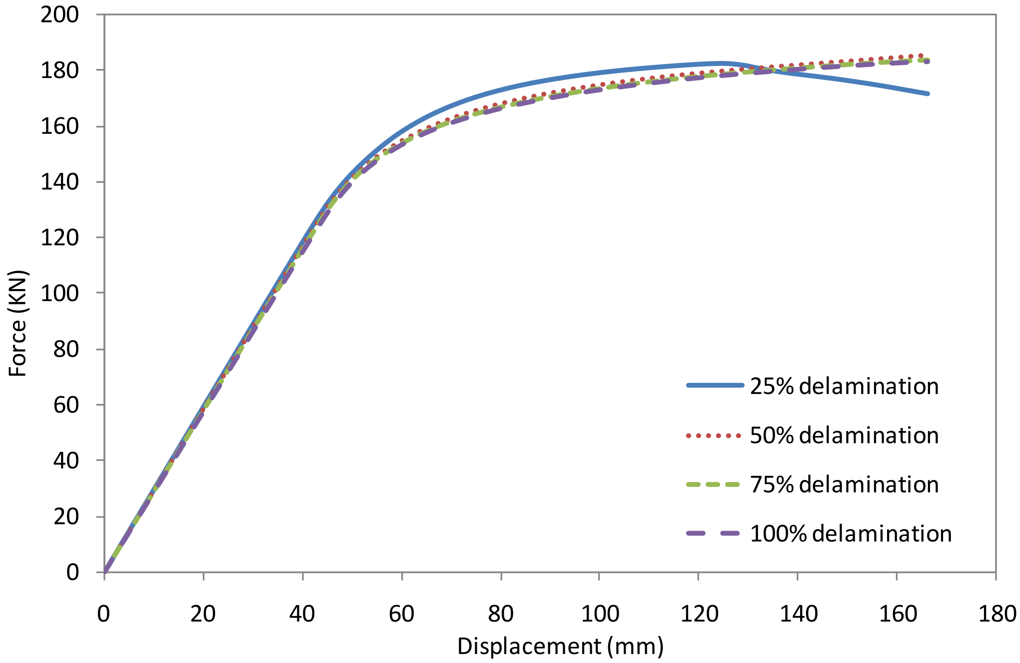

Figure 6.9 Effect of delamination percentage over the plastic hinge region of the beam on load-displacement relationship of beam-column assembly at temperature of 200 °C

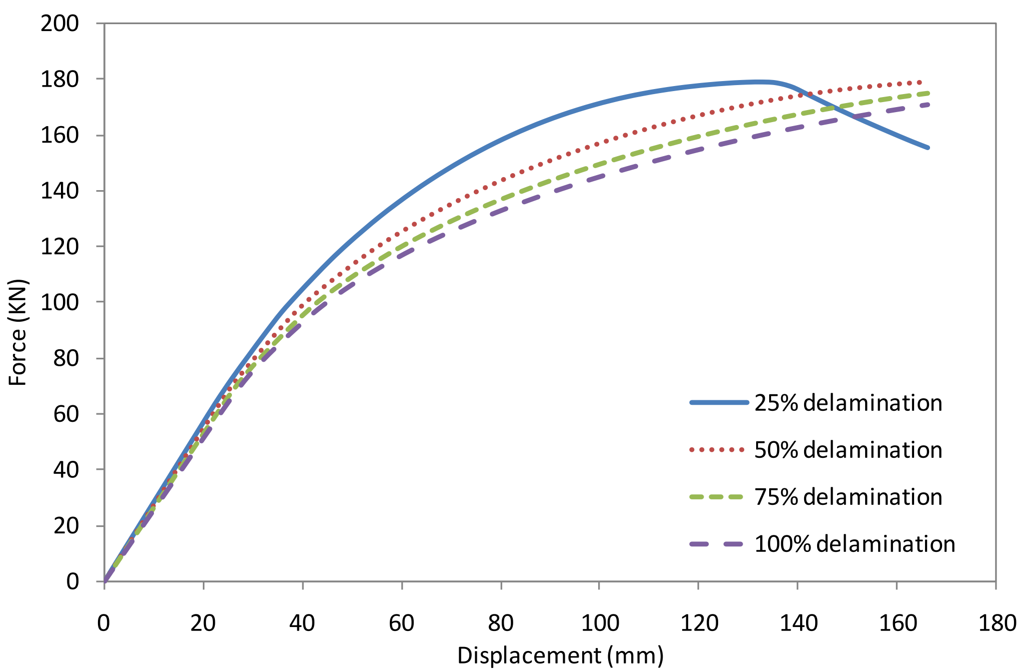

Figure 6.10 Effect of percentage of delamination over the plastic hinge region of the beam on load-displacement relationship of beam-column assembly at temperature of 400 °C

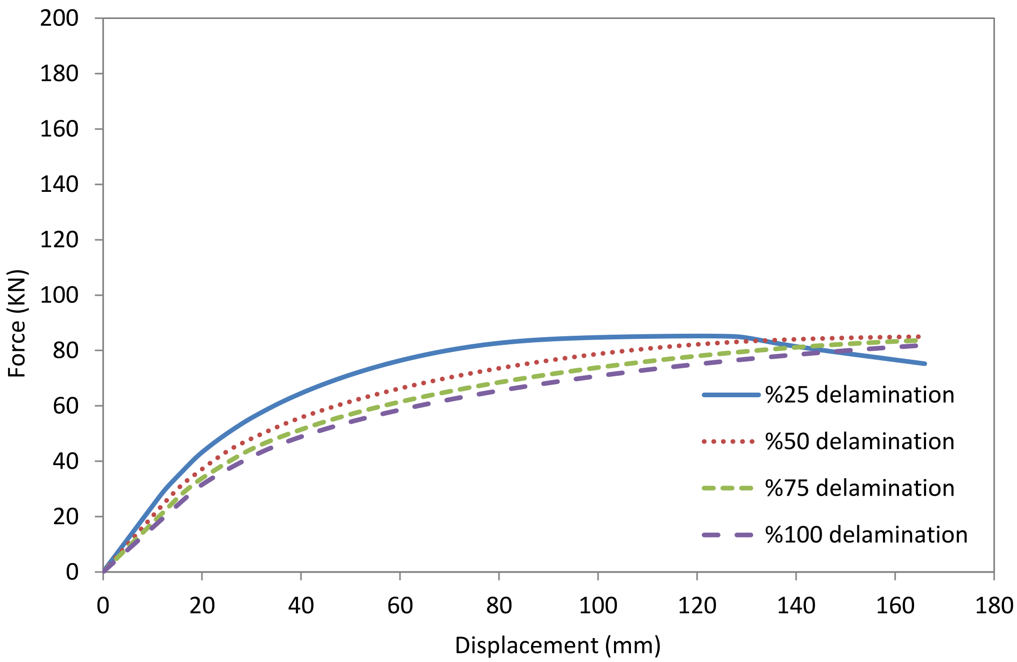

Figure 6.11 Effect of percentage of delamination over the plastic hinge region of the beam on load-displacement relationship of beam-column assembly at temperature of 600 °C

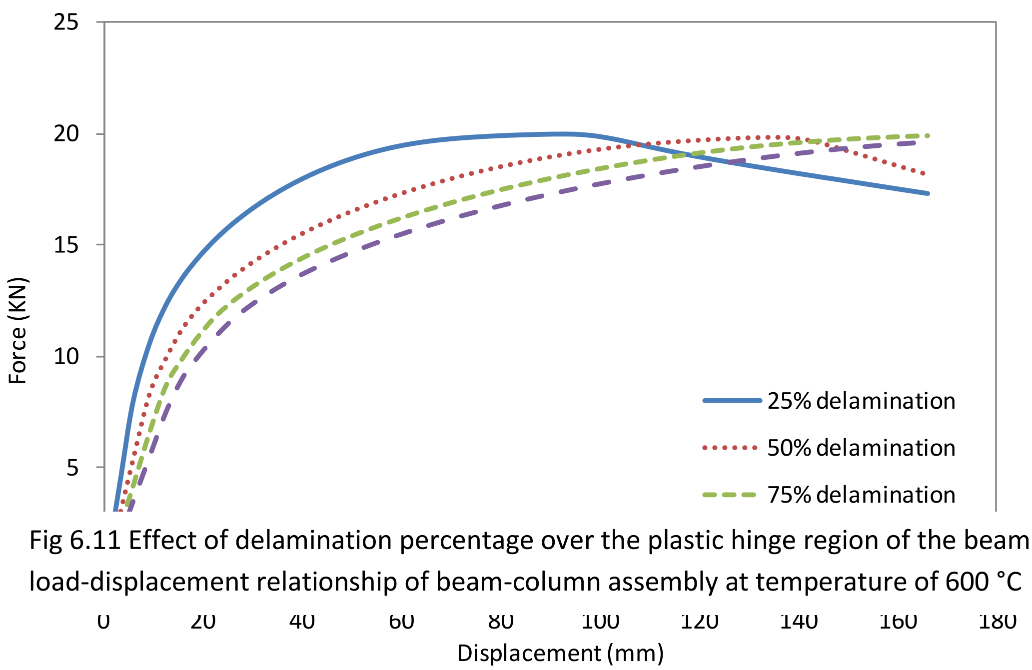

Figure 6.12 Effect of percentage of delamination over the plastic hinge region of the beam on load-displacement relationship of beam-column assembly at temperature of 800 °C

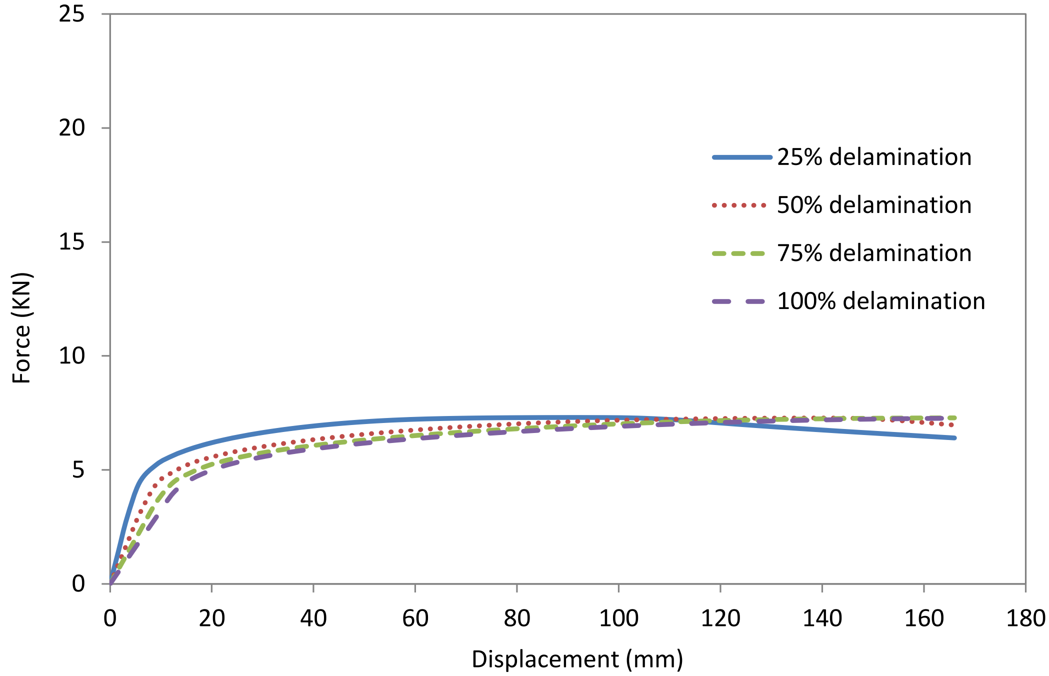

Figure 6.13 Effect of percentage of delamination over the plastic hinge region of the beam on load-displacement relationship of beam-column assembly at temperature of 1000 °C

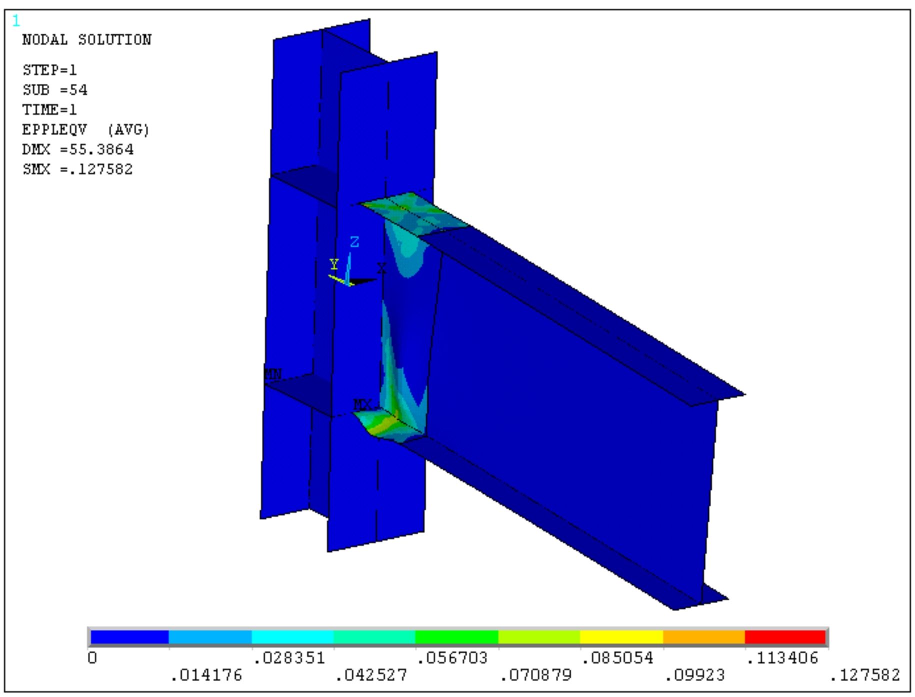

Figure 6.14 Plastic strain distribution in beam-column assembly at T=200 °C with 25% delamination over the plastic hinge region

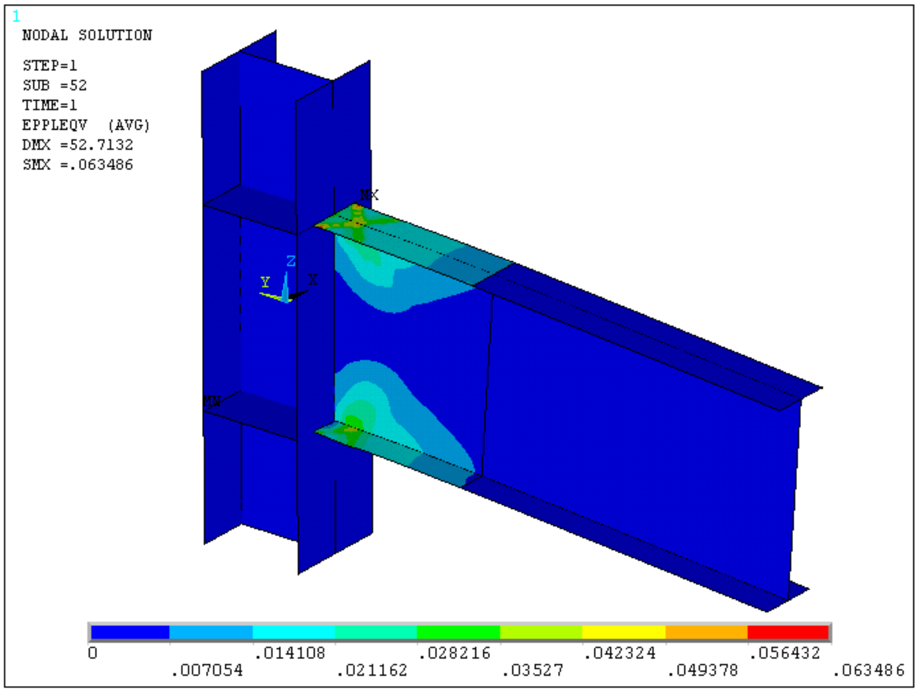

Figure 6.15 Plastic strain distribution in beam-column assembly at T=400 °C with 50% delamination over the plastic hinge region

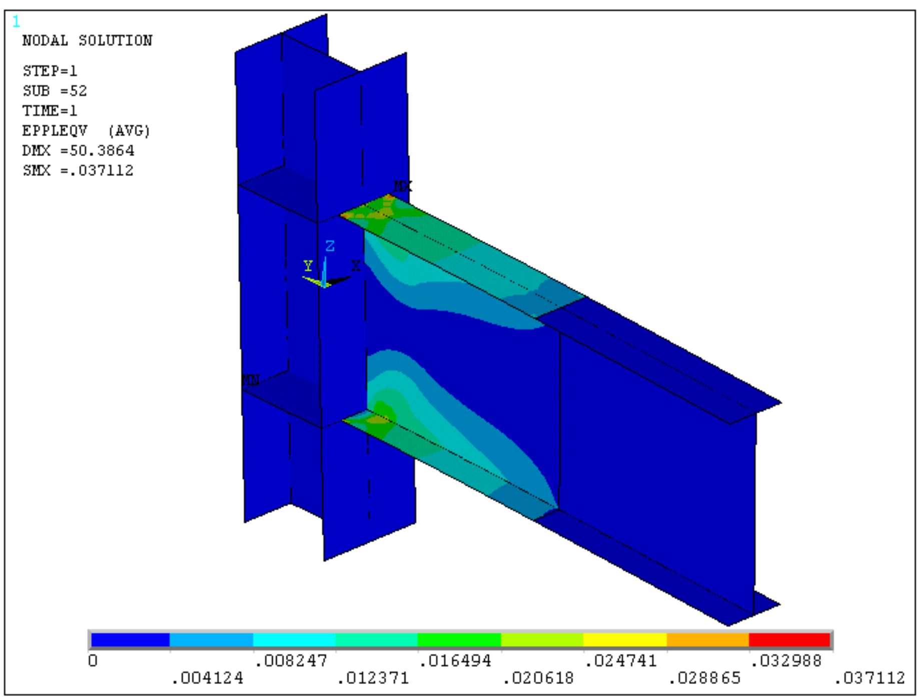

Figure 6.16 Plastic strain distribution in beam-column assembly at T=600 °C with 75% delamination over the plastic hinge region

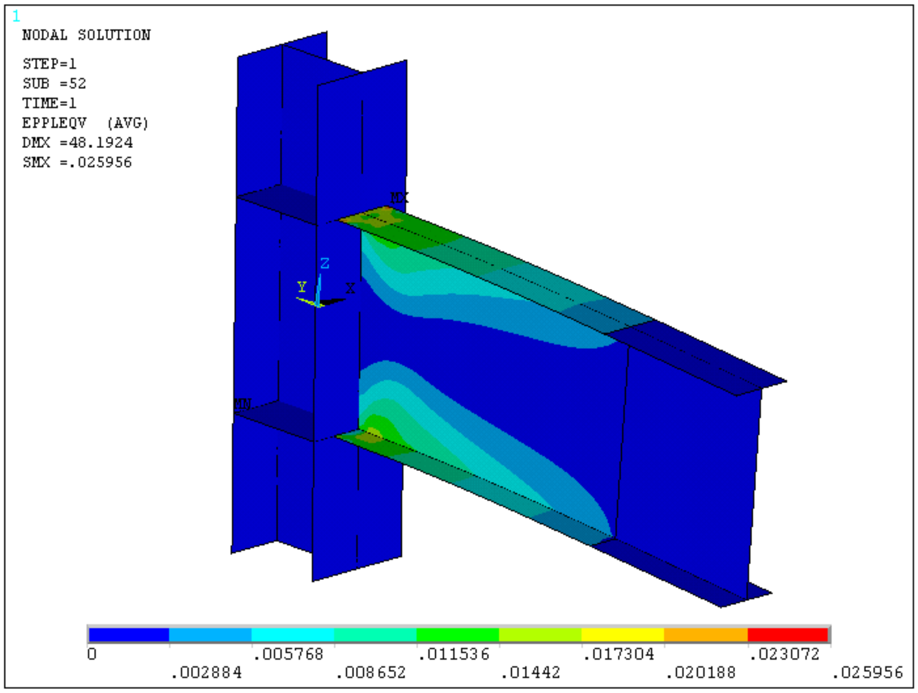

Figure 6.17 Plastic strain distribution in beam-column assembly at T=800 °C with 100% delamination over the plastic hinge region

6.2.2 Analysis Procedure to Quantify Time to Failure

The above presented analysis showed how delamination of fire insulation over the plastic hinge region developed in the beam under seismic loading, can reduce the capacity of beam-column assembly when subjected to elevated temperatures. In this section, a more rigorous analysis is performed in which the structural response of the beam-column assembly is traced throughout the fire exposure until complete collapse occurs. The time to failure of the beam-column assembly is recorded and compared for different levels of delamination.

The finite element model including loading and boundary condition is illustrated in Figure 6.18. A symmetric boundary condition is used in the mid-span of the beam. A distributed gravity load is applied on the beam representing dead and live loads of the floor system. A static analysis is carried out to establish the initial condition under gravity prior to fire exposure. Subsequently, the beam and column are subjected to the temperature time-history computed through the thermal analysis step which was explained in previous section.

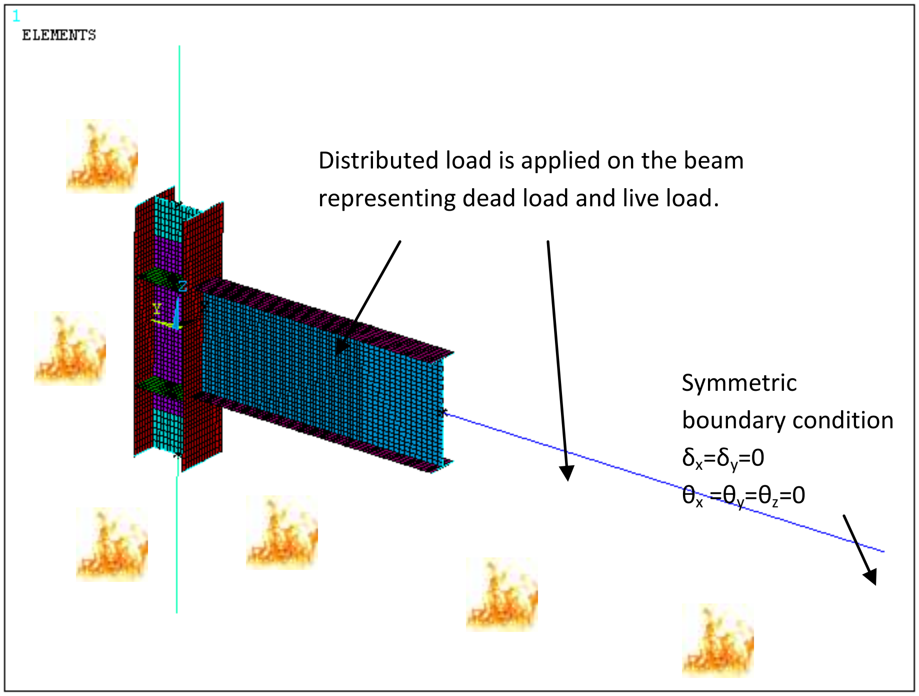

Figure 6.18 Finite element model of beam-column assembly used for quantifying failure time during fire following earthquake

Figure 6.19 plots vertical deflection of the beam mid-span (i.e. the symmetric boundary) for different levels of delamination percentage over the plastic hinge region of the beam. Figure 6.20 also shows time to failure versus percentage delamination. As depicted in Figure 6.19, the beam-column assembly without any delamination survives the standard fire for almost 100 minutes. However, 25% delamination of fire insulation reduced the time of failure to 64 minutes. Additional increase in extent of delamination up to 50% and 75% leads to further decline in failure time as low as 54 and 49 minutes respectively. However, an interesting response is obtained when the extent of delamination is increased from 75% to 100% (complete). Despite expanding the heat-affected zone, the failure time is procrastinated until 55 minutes, i.e. 6 minutes more loading carrying capacity is gained as to the case of 75% delamination.

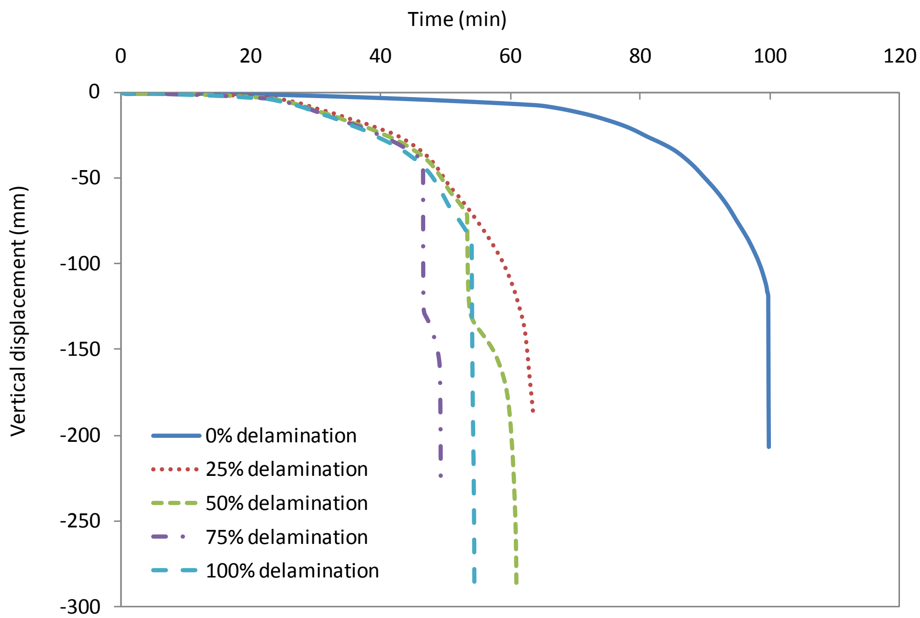

Figure 6.19 Displacement of the beam during fire following an earthquake that has undergone insulation damage during seismic loading

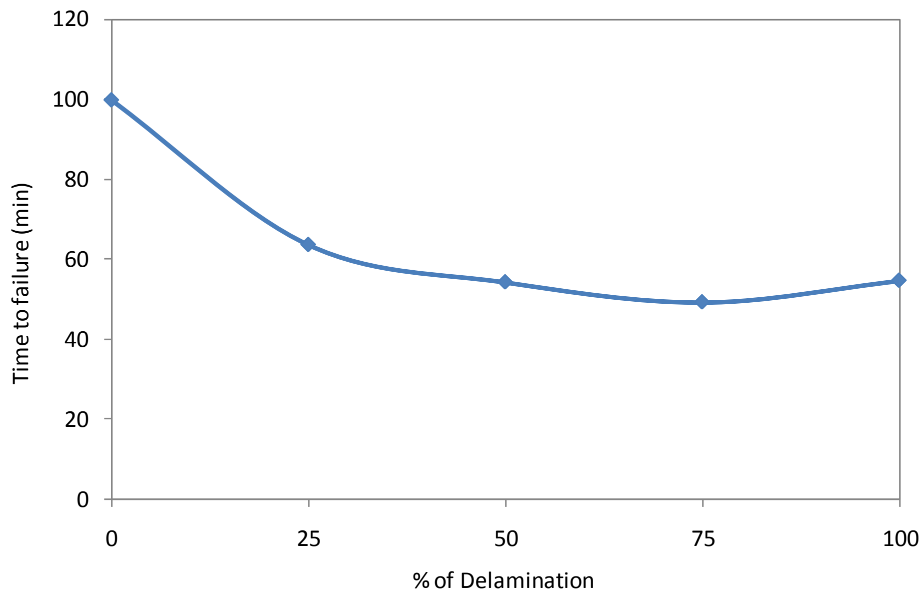

Figure 6.20 Displacement of the beam during fire following an earthquake that has undergone insulation damage during seismic loading

This behavior may be better explained by illustrating the deformed shape of the connection region and the failure mechanism occurred. Figure 6.21 through Figure 6.25 illustrate the failure pattern of the connection in conjunction with the true plastic strain distribution. When there is no insulation loss, failure is governed by inelastic local buckling of the web and the bottom flange of the beam, as shown in Figure 6.21. When 25% of the plastic hinge region gets delaminated and exposed to high temperature, shear failure occurs and top flange develops plastic strain as large as 0.63, as shown in Figure 6.22. Although the strain level has not reached to true fracture strain of 1.0 in the analysis due to convergence issues arisen in the implicit solution upon global instability of the structure, tensile fracture of top flange would happen if the beam moved further down and true plastic strain attained to 1.0 in reality.

By increasing the extent of the exposed area to 50%, the shear failure in the web is accompanied by formation a truss-like behavior in the web causing very large tensile stresses at the intersection of web and flanges. This leads to rupture at the top flange as the true plastic strain reaches to fracture strain limit (100%), as depicted in Figure 6.23. Further increase in extent of delamination up to 75% and 100% leads to more truss-like behavior of the heated zone, as clearly shown in Figure 6.24 and Figure 6.25. In both cases, stress concentration occurs at the intersection of web and flanges resulting in fracture at theses points. When delamination extent is 75%, failure initiates at top flange near the column, whereas, at 100% delamination fracture starts from bottom flange. The truss-like behavior is more pronounced in the case of full (100%) delamination of fire insulation which can increase the stiffness of the system and delay the collapse by 6 minutes, as compared to the case delamination extends to 75%.

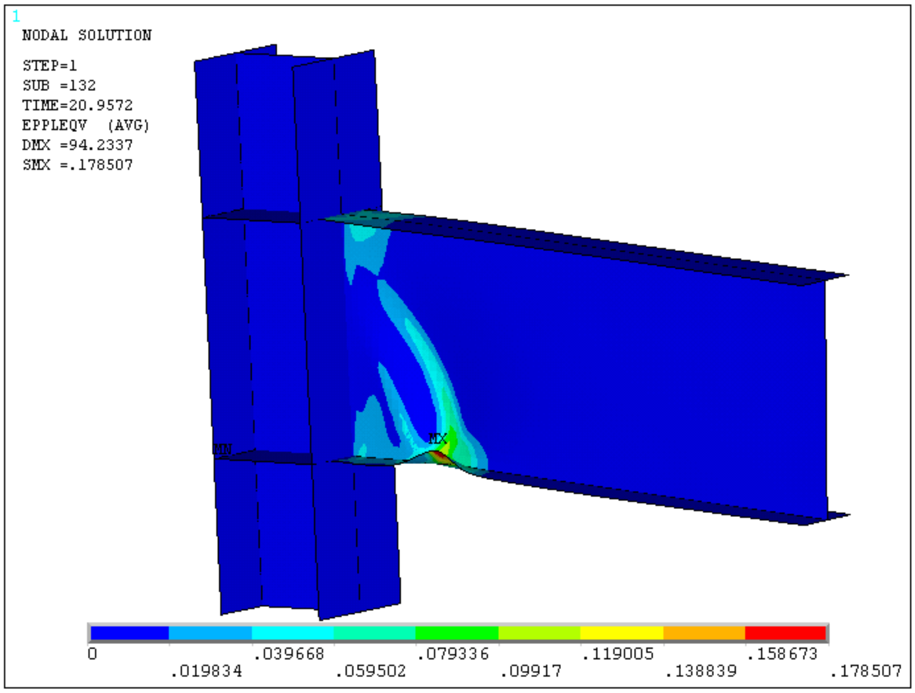

Figure 6.21 Plastic strain distribution in beam-column assembly at the time of failure (0% delamination of SFRM over the plastic hinge region)

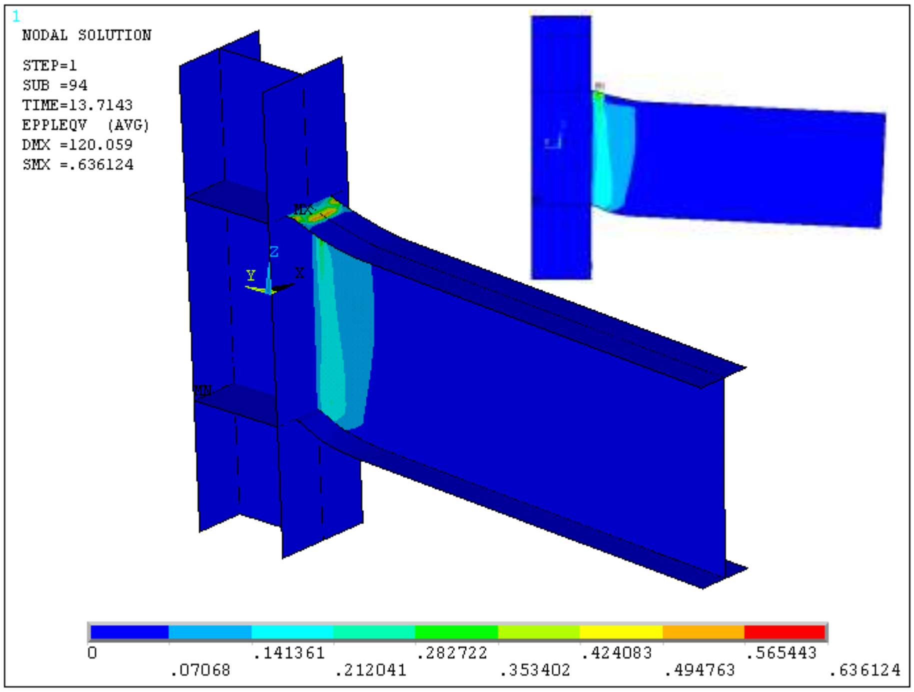

Figure 6.22 Plastic strain distribution in beam-column assembly at the time of failure (25% delamination of SFRM over the plastic hinge region)

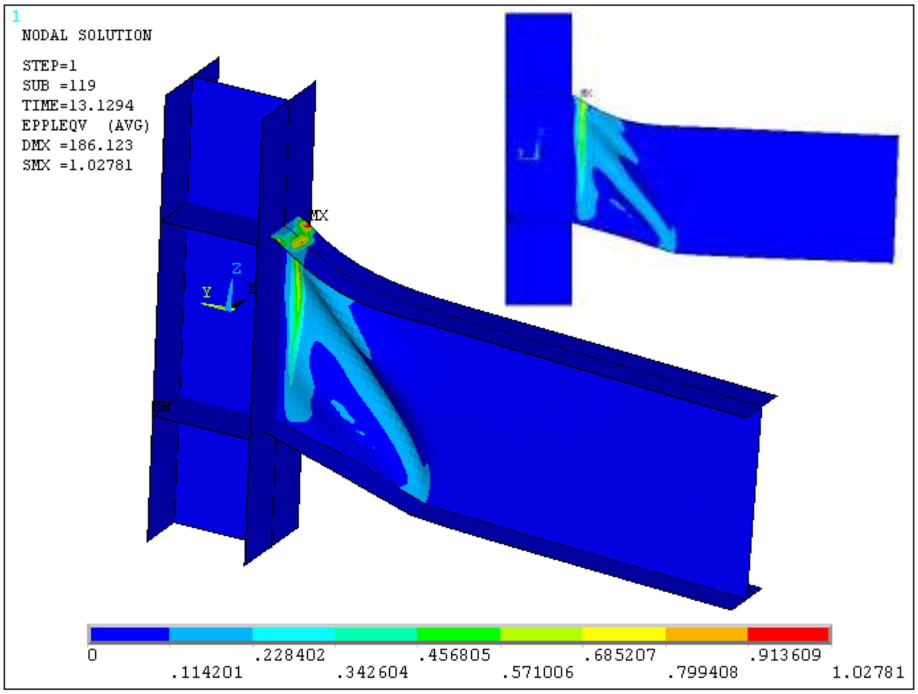

Figure 6.23 Plastic strain distribution in beam-column assembly at the time of failure (50% delamination of SFRM over the plastic hinge region)

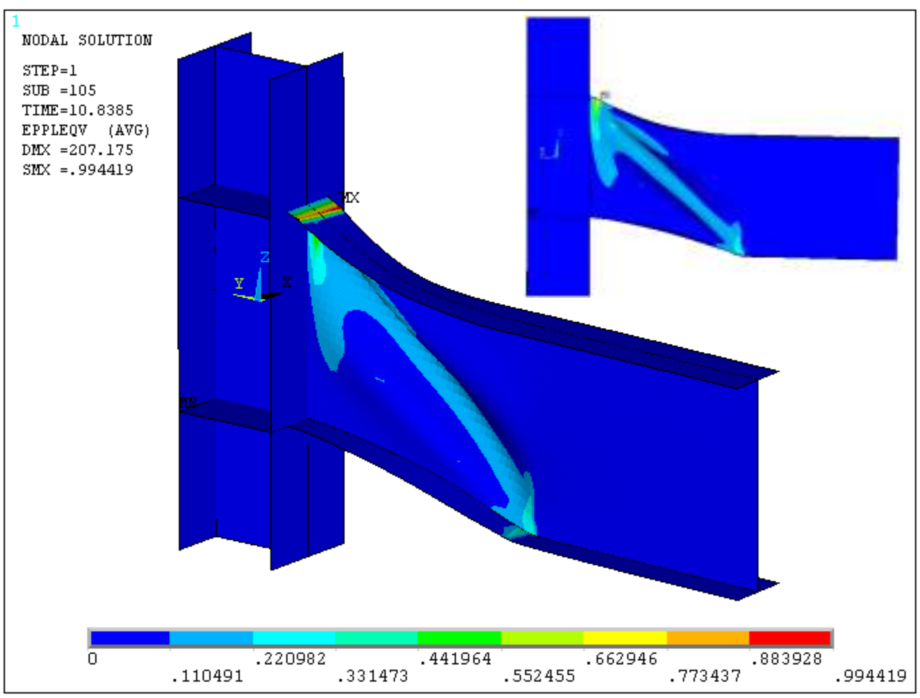

Figure 6.24 Plastic strain distribution in beam-column assembly at the time of failure (75% delamination of SFRM over the plastic hinge region)

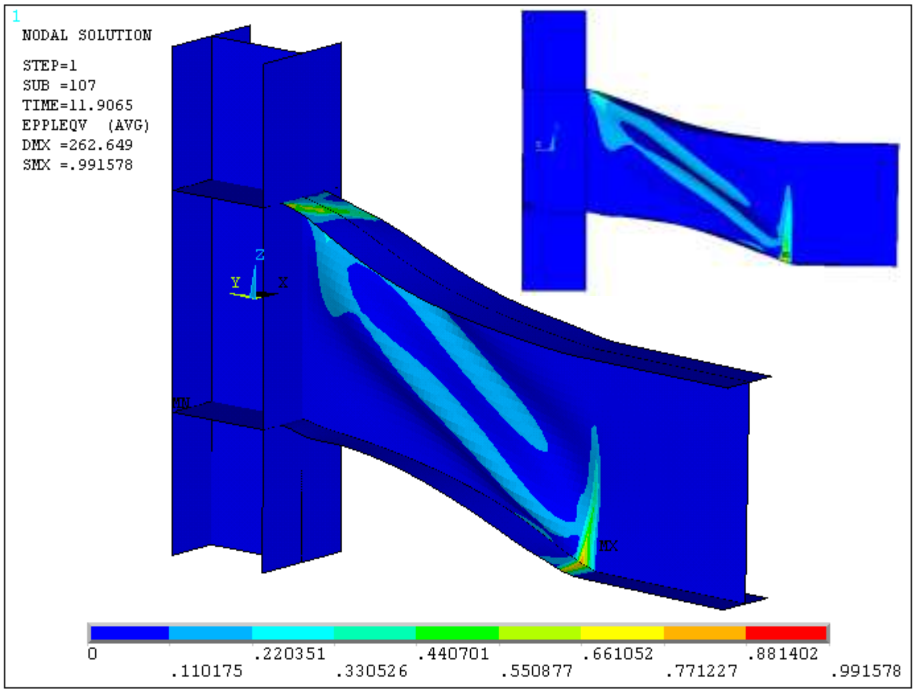

Figure 6.25 Plastic strain distribution in beam-column assembly at the time of failure (100% delamination of SFRM over the plastic hinge region)

6.3 Post-Blast Fire Response of a Beam-Column

To investigate performance of a beam-column supporting the heavy weight of above stories under fire following a blast event, a sequential thermal-structural analysis is carried out. The finite element model for thermal analysis is illustrated in Figure 6.26 where five cases of analysis are included. The fire insulation delamination pattern chosen in the analysis is based on the results of modeling of delamination under blast loading which was described in Chapter 5.

The steel cross section and SFRM are discretized using two dimensional elements (PLANE55) with temperature nodal variable. The SFRM type is gypsum-based with thickness of 27 mm. This thickness of insulation has been designed for achieving fire resistance of three hours under standard fire (UL, 2009).

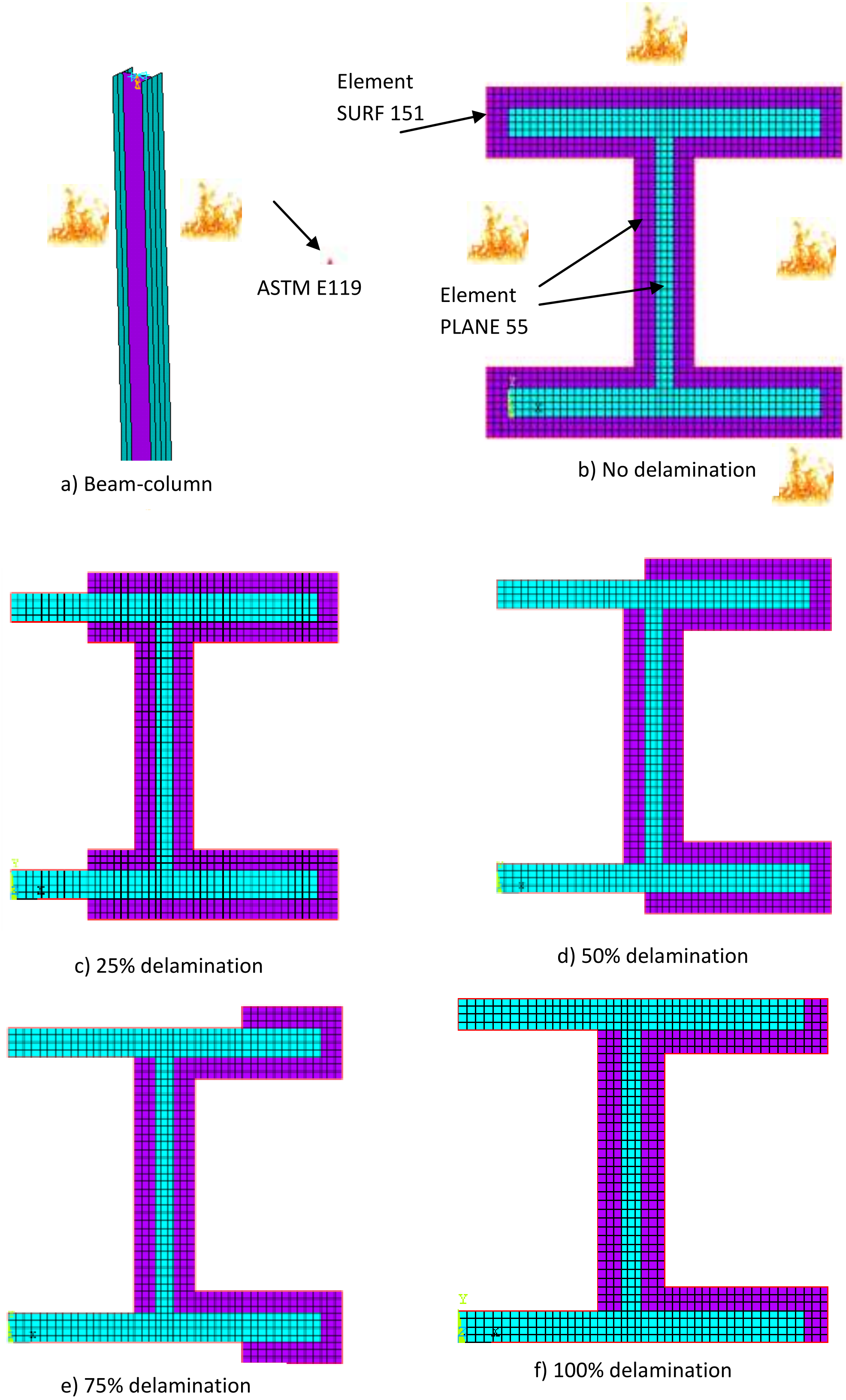

Figure 6.26 Finite element model of cross section of column for thermal analysis

The heat radiation is modeled by defining surface elements (SURF151) over the exterior edge of the elements exposed to fire. The temperature time history of standard fire (ASTM E119) is applied to the node associated with the surface elements. Further, the convective loading is applied on the surfaces exposed to fire. The column cross section is assumed to be engulfed by fire from all sides.

The temperature distribution over the insulated cross section, that suffered different levels of insulation delamination, is depicted in Figure 6.27 through Figure 6.31. It is clear that, the more insulation is delaminated, the higher temperature developed in the steel cross section. The presence of fire insulation can maintain temperature gradient of 600^{o}C through the thickness of SFRM. However, when the insulation is not in-place on some portions of the flange, the temperature not only rises very rapidly in the flange but also penetrates to the web even though the web insulation is in-place. Further, a dramatic increase in temperature evolution in the cross section is noticeable when 25% of SFRM gets delaminated when comparing to the case of no delamination of fire insulation. However, the variation of temperature is not substantial when delamination extent exceeds 25% and reaches to 100%.

Figure 6.32 shows the structural finite element model of the beam-column. The flanges and web of the beam-column are discretized using shell elements (SHEL181). The bottom boundary condition is hinge, i.e. three translational directions are restrained but two rotational (bending) degrees of freedom are free. Multiple point constraint (MPC) contact element are placed at the end boundaries to simulate the boundary conditions. The top boundary is restrained in lateral direction and is free in vertical direction and rotational directions. The vertical force as large as 45% of buckling capacity of the column ($0.45P_{cr}$) is applied at the top boundary condition.

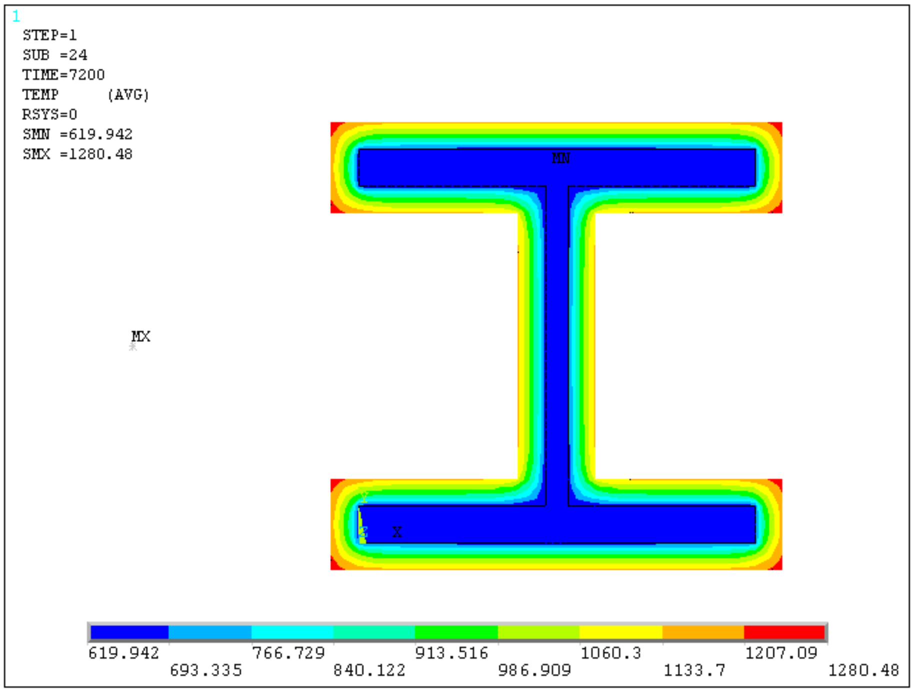

Figure 6.27 Temperature distribution (°K) in the cross section of column with full SFRM after 2 hours of exposure to standard fire (ASTM E119)

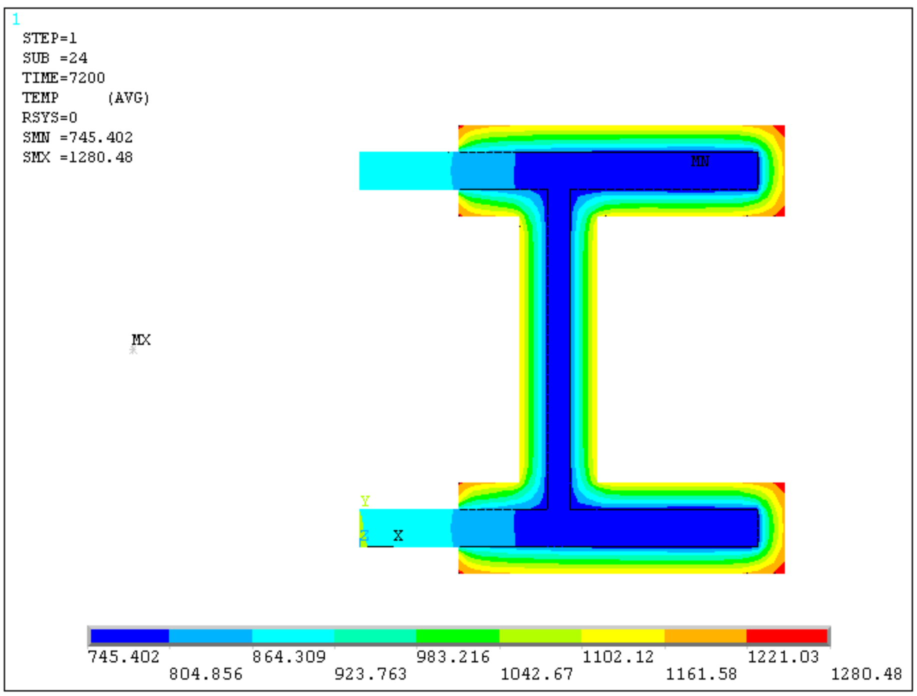

Figure 6.28 Temperature distribution (°K) in the cross section of column with 25% delamination of SFRM after 2 hours of exposure to standard fire (ASTM E119)

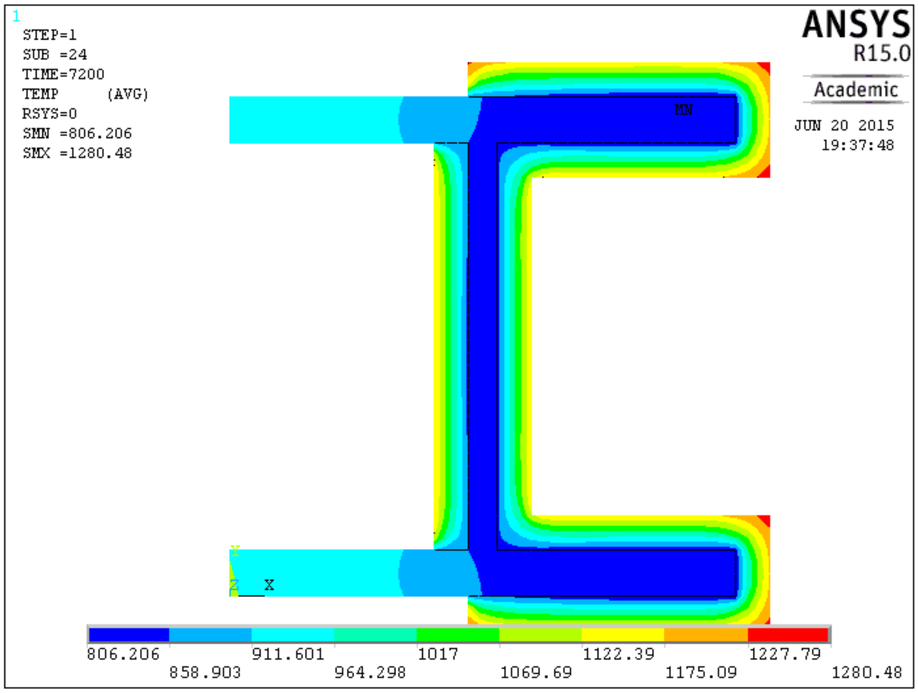

Figure 6.29 Temperature distribution (°K) in the cross section of column with 50% delamination of SFRM after 2 hours of exposure to standard fire (ASTM E119)

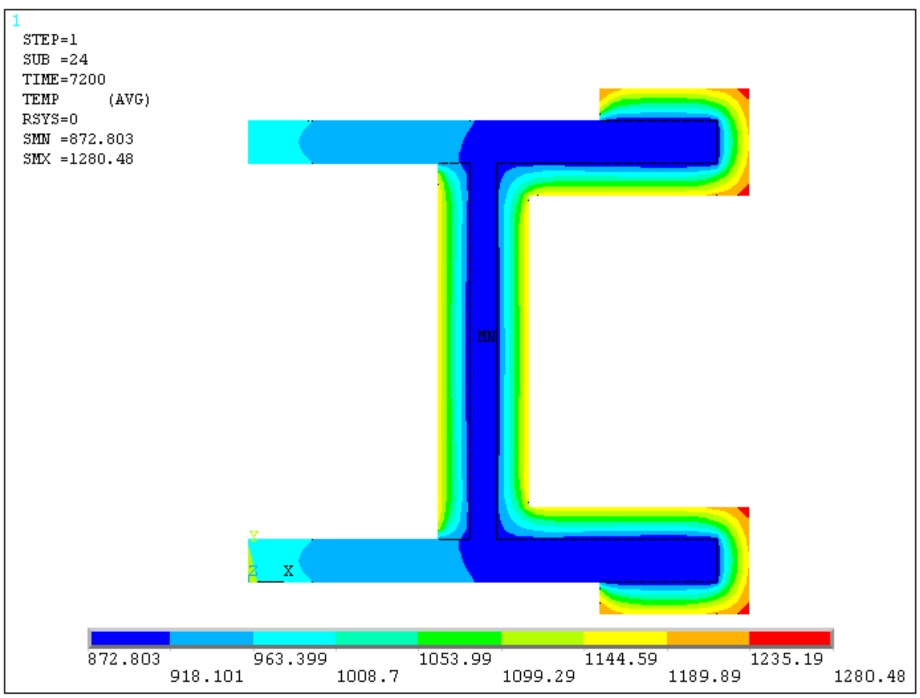

Figure 6.30 Temperature distribution (°K) in the cross section of column with 75% delamination of SFRM after 2 hours of exposure to standard fire (ASTM E119)

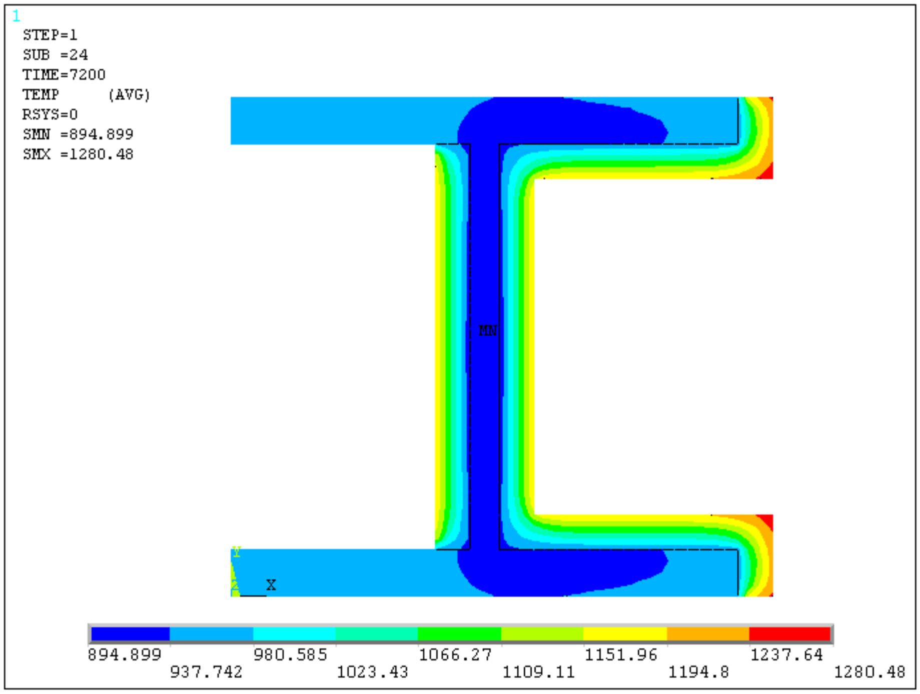

Figure 6.31 Temperature distribution (°K) in the cross section of column with 100% delamination of SFRM after 2 hours of exposure to standard fire (ASTM E119)

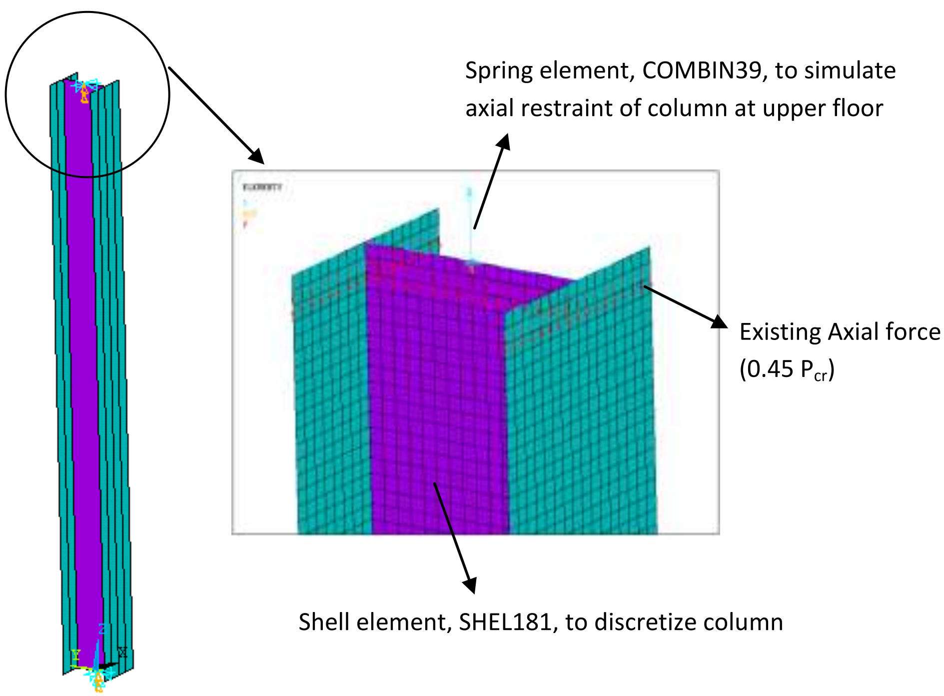

Figure 6.32 Finite element of the column to simulate effect of temperature rise after blast loading on structural response of the column

To simulate the axial restraint of the above stories, a nonlinear spring element (COMBIN39) is modeled at top boundary condition. The spring element consists of two nodes; the first node coincides with the column and the other node is fixed. The load-displacement of the spring element is defined such that it cannot carry tensile load. Hence, when the initial axial load is applied, which is representing the weight of above stories; the spring does not show any resistance. However, when the column expands the spring shows resistance against axial deformation. The axial stiffness of the beam-column is assigned to the spring which is a conservative assumption.

Figure 6.33 plots vertical displacement time-history of the column for all analysis cases. The beam-column assembly fully protected with SFRM, i.e. no delamination, survives two hours of exposure to standard fire. The beam-column assembly that undergoes fire insulation delamination up to 25%, however, experiences earlier loss of capacity around 85 minutes. Note that, for further extent of delamination up to 50% the global buckling of column happens after 62 minutes. In the cases of 75% and 100% of delamination, the failure time is around 55 minutes. In all cases, column expands up to 6 mm and then shrinks as a result of stiffness and strength loss until global buckling limit is attained. Figure 6.34 traces the variation of failure time versus delamination extent. The dramatic change between 0% and 25% delamination along with smooth variation beyond 25% delamination is clear in Figure 6.34.

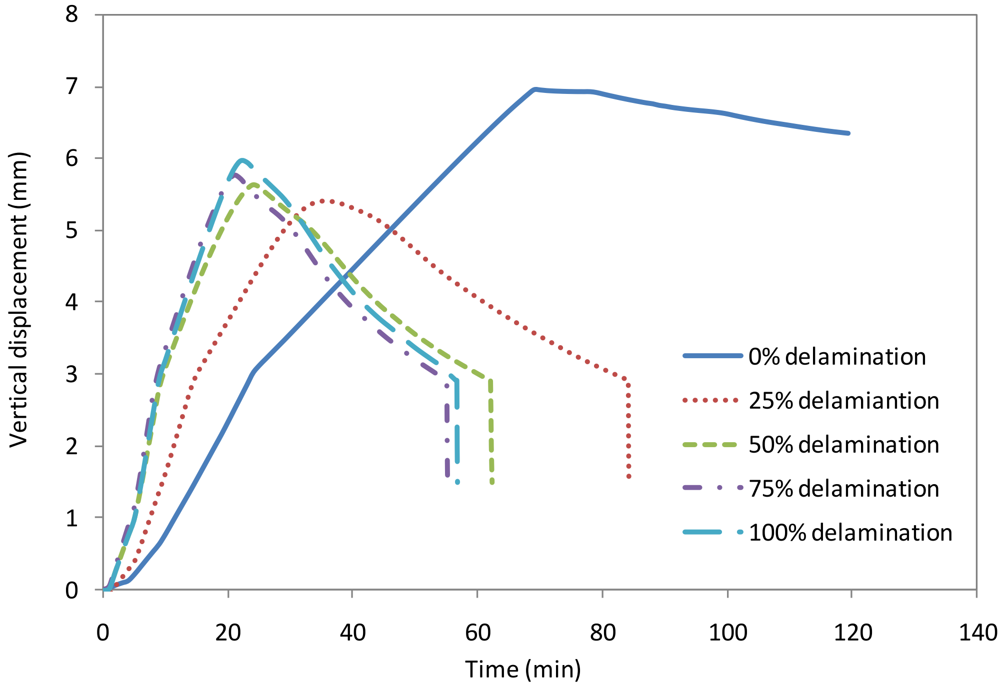

Figure 6.33 Vertical displacement of the column during fire following blast

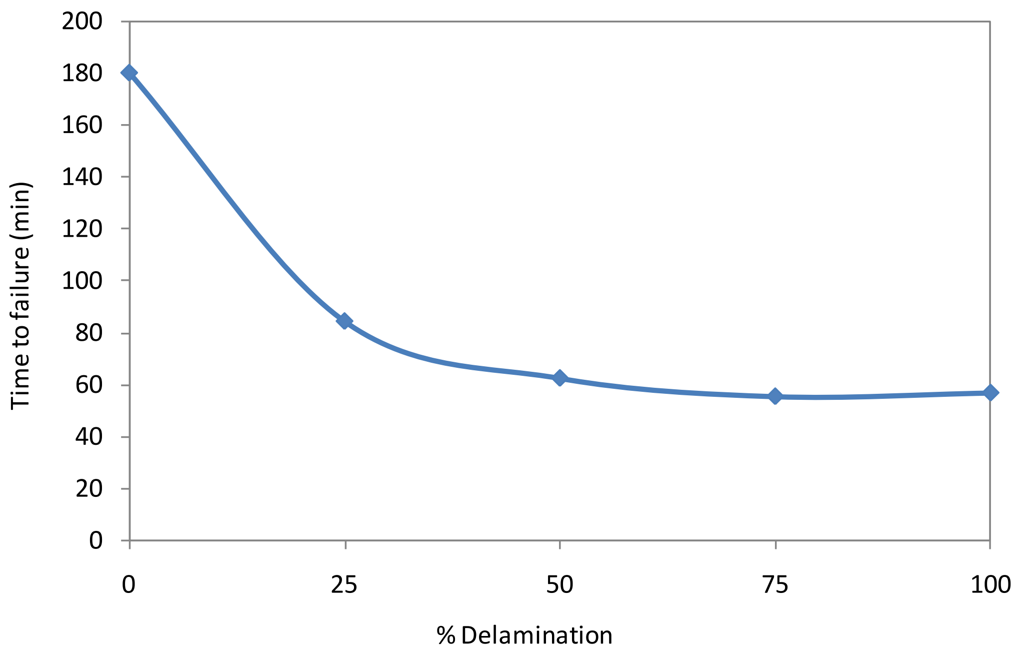

Figure 6.34 Time to failure of the column exposed to fire following blast as a function of percentage delamination occurred during blast loading

To better understand failure mechanism of the beam-column assembly, the axial force developed in the beam-column during fire due to presence of axial restrain from upper levels is depicted in Figure 6.35. The development of additional axial force is delayed until the deformation caused by existing axial force is recovered. When the beam-column is fully protected, the axial force increases up to 6000 KN and reduces afterwards, however, the load reduction is not dramatic and column remains stable for two hours as expected while designing the thickness of SFRM. When some portion of SFRM is missing, the beam-column expands up to certain limit when substantial material softening occurs and the load subsequently reduces until global buckling occurs.

To examine the effect of axial restraint on fire resistance of the beam-column assembly, an additional analysis is carried out for the case of 100% delamination of fire insulation, in which the axial spring is removed. Result of this analysis and the one including axial restrain effects is plotted in Figure 6.36. The column with no axial restraint expands considerably and then becomes unstable; however, the failure time increases to 79 minutes as compared to 55 minutes for the axially-restrained column. This result clearly shows the significance of fire-induced axial force developed in the beam-columns due to restraining effect of neighbor members.

Figure 6.37 through Figure 6.40 show deformed shaped of the beam-column upon instability point. As is clear, in all four cases, the d pattern is identical since irrespective of the history of deformation, the deformation level at which a column becomes instable is its property. The plastic strain developed in the column upon instability is shown in also Figure 6.41 through Figure 6.44. The plastic deformation is concentrated in the mid-height of the column where secondary order moment interacts with axial force. The plastic strain upon failure is 0.029 for all four cases.

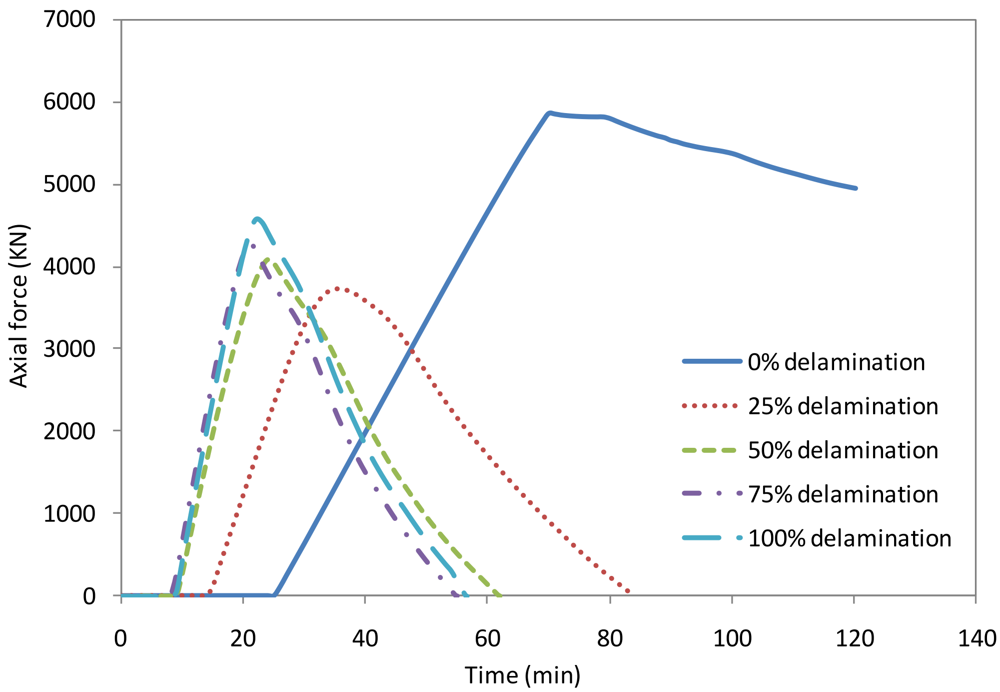

Figure 6.35 Axial force developed in the column during fire following blast

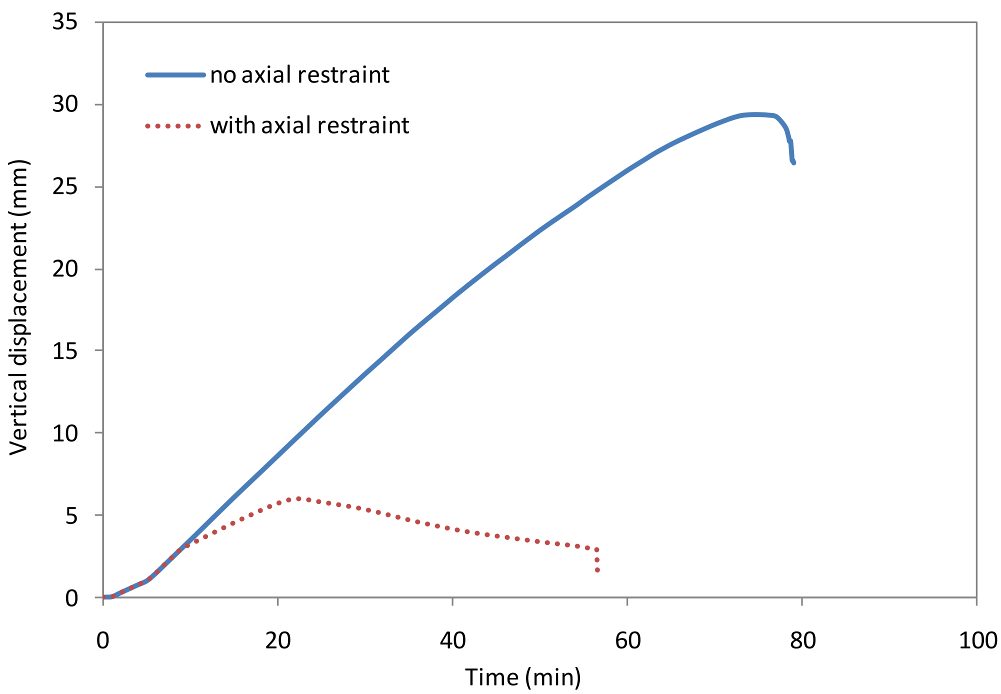

Figure 6.36 Effect of axial restraint on vertical expansion of column exposed to fire following blast (100% delamination)

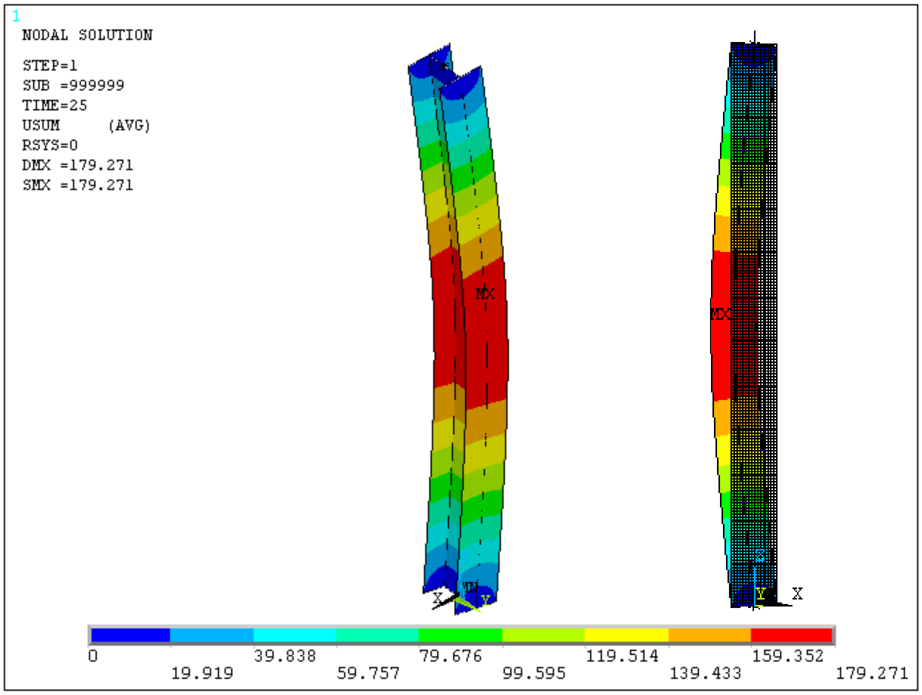

Figure 6.37 Displacement vector (mm) of column endured 25% delamination during fire following blast loading

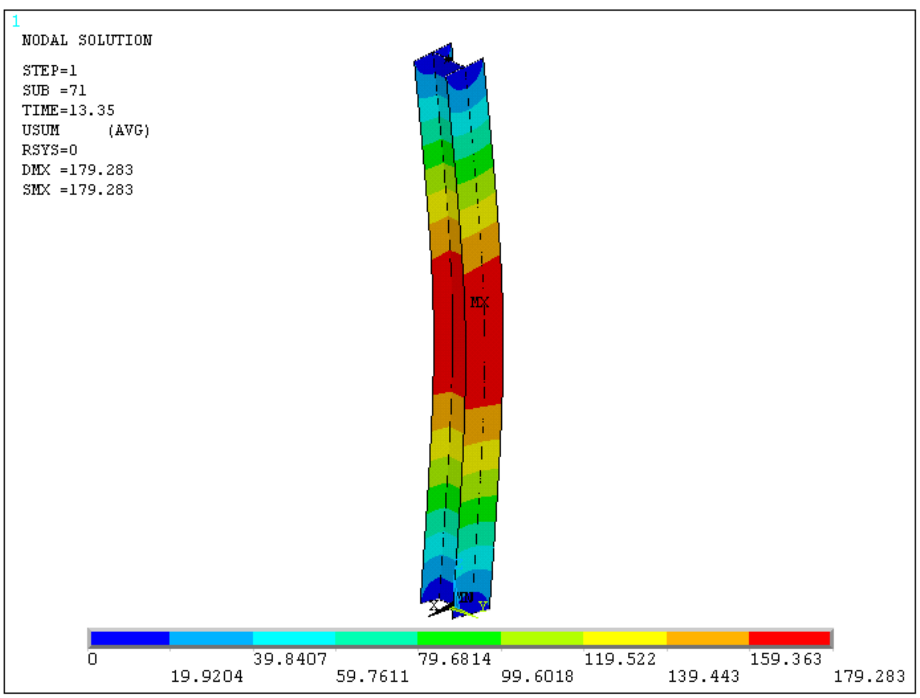

Figure 6.38 Displacement vector (mm) of column endured 50% delamination during fire following blast loading

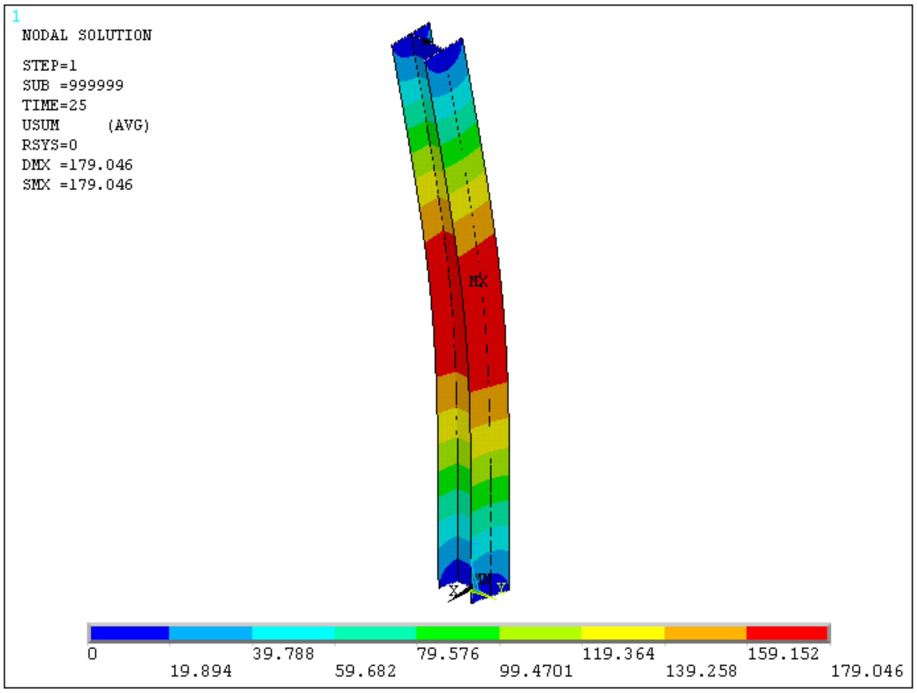

Figure 6.39 Displacement vector (mm) of column endured 75% delamination during fire following blast loading

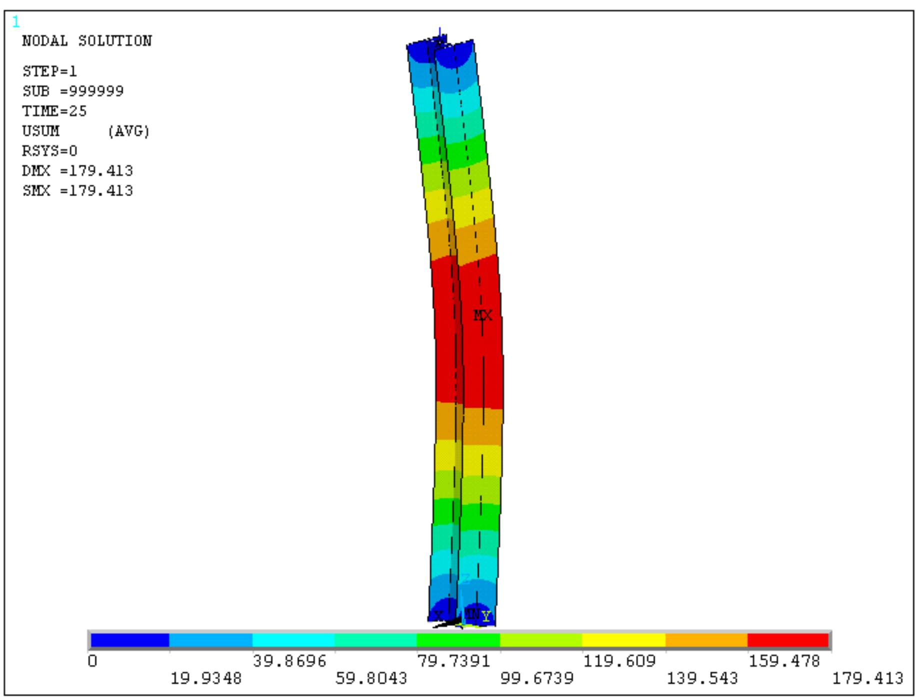

Figure 6.40 Displacement vector (mm) of column endured 100% delamination during fire following blast loading

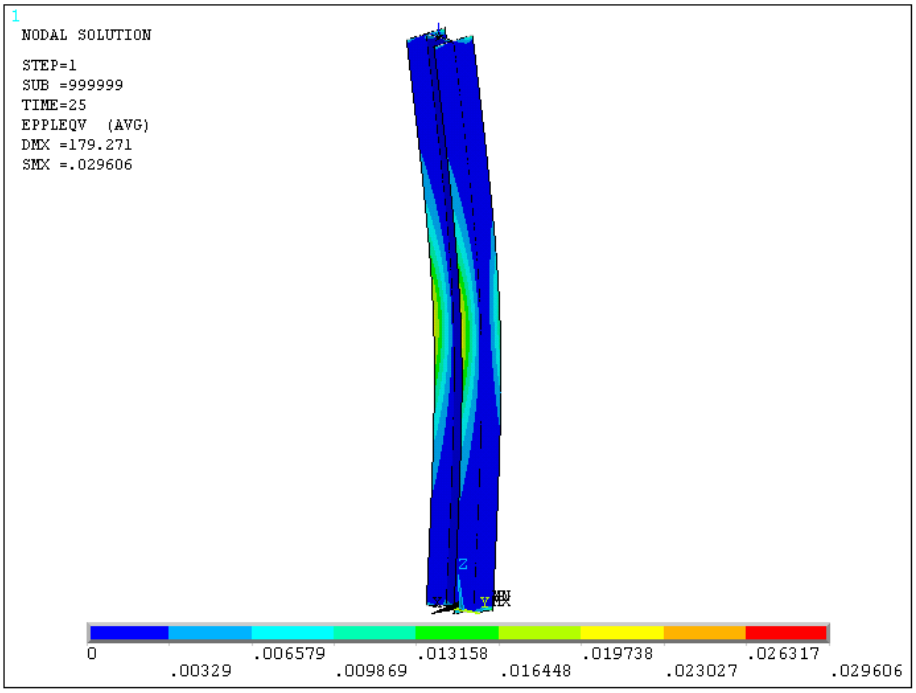

Figure 6.41 Plastic strain distribution over the column undergone 25% delamination of fire insulation and subjected to fire following blast loading

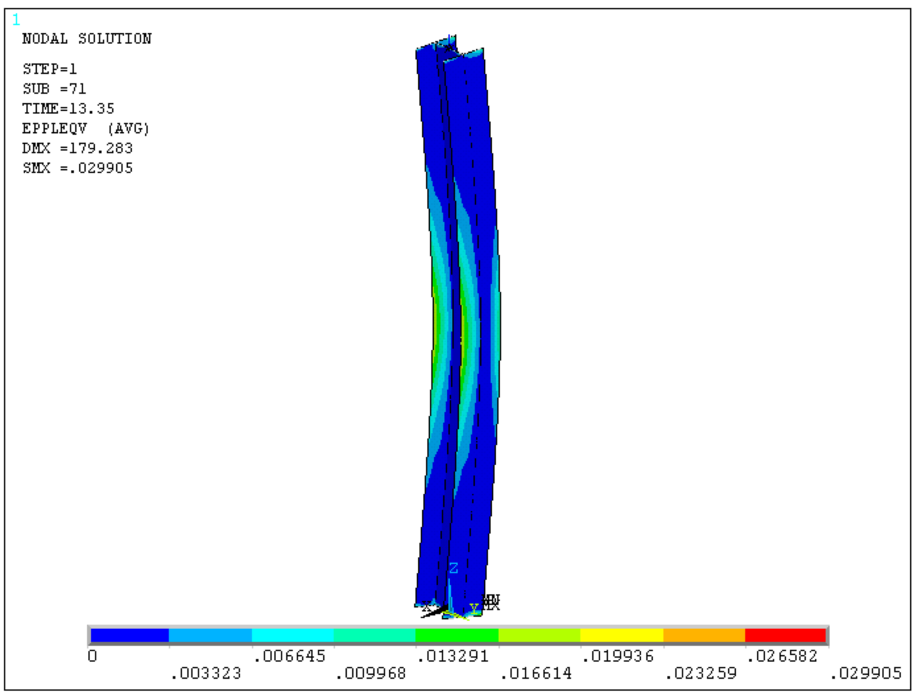

Figure 6.42 Plastic strain distribution over the column undergone 50% delamination of fire insulation and subjected to fire following blast loading

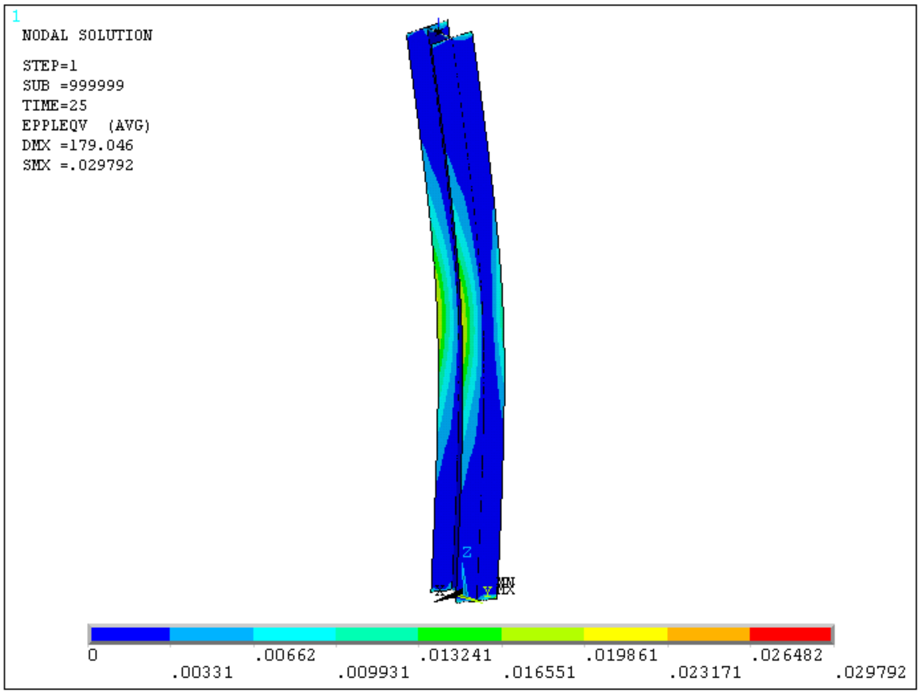

Figure 6.43 Plastic strain distribution over the column undergone 75% delamination of fire insulation and subjected to fire following blast loading

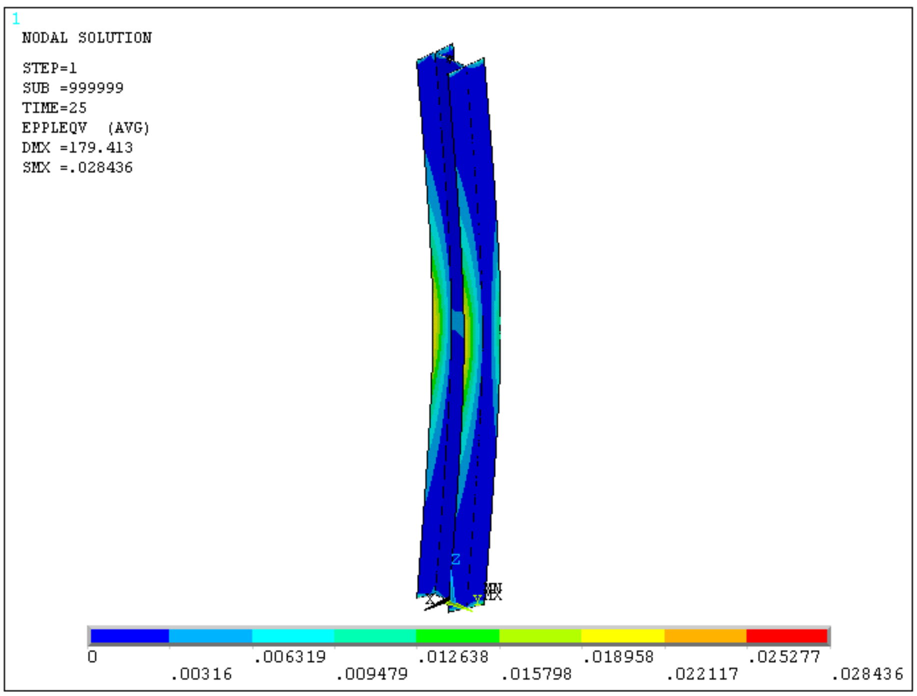

Figure 6.44 Plastic strain distribution over the column undergone 100% delamination of fire insulation and subjected to fire following blast loading

6.4 Strategies to Overcome Consequences of Delamination

As it was quantified through numerical modeling, the consequences of delamination of SFRM over the plastic hinge region can be quite significant. Hence, this region needs to be particularly protected. This may be achieved through utilizing a more resilient fire insulation material only over the plastic hinge regions. Intumescent fire insulation can be a practical replacement for SFRM over the plastic hinge region. As another alternative, SFRM can be applied using a special type of adhesive to enhance the interfacial fracture energy to the level quantified in this study, i.e. G_f=350 J/m^2. To protect the structure against fire following explosion, given the fact that the entire member is vulnerable for delamination of fire insulation, employing more resilient fire insulation materials such as intumescent fire insulation or concrete encasement seems feasible to deal with delamination issue.

6.5 Summary

In this chapter the ramification of fire insulation delamination from a steel moment-frame under seismic loading and a beam-column under blast loading was quantified by conducting thermal-structural analysis. The moment frame and beam-column was subjected to a fire scenario that engulfs the structure following a seismic and blast loading. Subsequently, the fire performance of the structure was evaluated for different levels of delamination.

It was found that even 25% delamination of fire insulation over the plastic hinge region of the beam near the column can significantly accelerate the failure of the beam subjected to fire following an earthquake. This level of delamination results in shear failure in the beam adjacent to the column. This result suggests that, in the moment frames under seismic loading, delamination of fire insulation over the plastic hinge regions of the beams should be prevented in order to protect the structure during fire following earthquake since the consequences may be heavy.

For fires occurring after blast events, it was concluded that consequences of 25% delamination of fire insulation from the flanges of the beam-column can be quite substantial. The failure time for the beam-column can diminish by 40%. It was also explored that effect of axial restraint is very crucial in fire response of beam-columns; hence a particular consideration should be given to this issue while quantifying capacity of beam-columns during fire.

Eventually, some strategies for overcoming consequences of delamination were outlined. To protect steel structures against fire following earthquake, it was proposed to utilize intumescent fire insulation over the plastic hinge region or use adhesive to increase the bond strength. To increase the resiliency of steel structures against fire following explosion, employing more resilient fire insulation materials such as intumescent fire insulation or concrete encasement was suggested.

CHAPTER 7

7 CONCLUSIONS AND RECOMMENDATIONS

7.1 General

In this research, an experimental-numerical approach was adopted to investigate delamination of fire insulation from steel structures subjected to extreme loading conditions such as seismic, impact and blast loading. The cohesive zone behavior at the interface of SFRM and steel was determined through static fracture tests for three types of SFRM namely, mineral fiber-based, gypsum-based and Portland cement-based SFRM. Subsequently, dynamic impact tests were carried out on beams insulated with above three types of SFRM to assess the performance of SFRM under dynamic loading and also to estimate the effect of strain rate on the cohesive zone properties. A numerical model was developed in ANSYS and LS-DYNA and validated against both material and structural level tests. The developed numerical model was subsequently applied to quantify the effect of critical factors governing delamination phenomenon namely, fracture energy, elastic modulus and thickness of SFRM. The parametric study was carried out on four types of representative structural components; a flimsy truss member subjected to static deformation, a beam-column assembly subjected to cyclic seismic loading, a beam subjected to impact loading and a beam-column subjected to blast pressure. Results from parametric studies under static loading were utilized to identify the critical factors governing delamination of fire insulation from steel structures. Data from parametric studies was utilized to define a delamination characteristic parameter that incorporates material-related governing factors in a single parameter and maintains interdependency between them. Results obtained from parametric study under impact loading was also utilized to estimate the dynamic increase factor (DIF) on fracture energy at the interface of steel and SFRM. Eventually, the delamination characteristic parameter was modified to capture the governing factors under seismic and blast loading conditions. In this chapter, the key findings from this study are summarized, the research impact and its practical implications are outlined and recommendations are lastly provided for future study.

7.2 Key Findings

The main conclusions drawn from this study is summarized in below:

- Strain-softening behavior of spray-applied fire-resistive material (SFRM) at steel-SFRM interface clearly infers that SFRM is not a purely brittle material; instead, it is a quasi-brittle material. Presence of considerable size of fracture process zone in SFRM infers that application of linear elastic fracture mechanics is not suited for characterizing fracture in quasi-brittle type of SFRM and more advanced approaches, such as cohesive zone model are to be applied to evaluate realistic response.
- Medium density Portland cement-based SFRM possesses the highest cohesive strength and fracture energy while having the least displacement ductility over the cohesive zone. Medium density gypsum-based SFRM possesses lower cohesive strength and fracture

energy, as compared to Portland-cement based SFRM, and has higher displacement ductility over the cohesive zone. Mineral fiber-based SFRM possesses the least cohesive strength and fracture energy but has the highest cohesive ductility. The proposed cohesive laws for three types of SFRM can be used for quantifying progressive delamination of SFRM from steel structures subjected to complex loading scenarios.

- Steel beams under impact loading such as drop mass, experience fracture and delamination that concentrates on the bottom flange with minor cracking extending to web, only at the mid-span. The fracture pattern infers that delamination does not only occur due to bending behavior of the beam, but also occurs as a consequence of rapid stress wave propagation in the beam, resulting in significant spalling of SFRM on the non-impacted flange. The delamination percentage on the bottom flange increases with decreasing critical fracture energy at the interface of steel member and fire insulation.
- Applying thicker fire insulation (SFRM) on steel structures is not necessarily the most efficient solution for increasing the resilience of steel structures against fire following seismic and blast loading conditions. Results from the analysis clearly indicate that, thicker insulation is more prone to develop premature fracture and delamination from steel surface.
- The effect of elastic modulus on delamination of SFRM depends on the loading type, especially strain rate. In the case of seismic loading, where no load is directly applied on fire insulation, increasing elastic modulus results in advancing extent of delamination of fire insulation from steel surface. On the contrary, under blast loading where the blast pressure is directly applied on fire insulation, increasing elastic modulus of SFRM enhances its resiliency against delamination.

- In slender truss members, even under static loading, delamination initiates at both ends of chord truss once strain level in steel reaches a certain value and this delamination subsequently propagates towards the center of the member. The progression of delamination is however very rapid, such that for gypsum-based SFRM, once initiated, delamination is completed within a strain range as low as ε_y (yield strain of steel).
- The proposed delamination characteristic parameter (d_{ch}) of SFRM, that incorporates fracture energy, displacement ductility over the cohesive zone, elastic modulus and thickness of SFRM into a single parameter, is an enhanced indicator of delamination since it accounts for all critical factors that affect delamination of SFRM from steel structures. Strain ductility demand of steel at the onset of delamination and its completion shows a power-law relationship with respect to delamination characteristic parameter (d_{ch}). By increasing the value of delamination characteristic parameter (d_{ch}) the strain ductility demand at delamination onset dramatically reduces; however, beyond d_{ch} value of 2, a steady trend can be noticed.
- In a beam column assembly subjected to seismic loading, the crack initiation starts when drift level (displacement of tip of the beam divided by length of the beam) reaches to 3% in beam-column assembly insulated with gypsum-based SFRM and Portland cement-based SFRM and the crack progression continues leading to complete separation over the plastic hinge region. However, in case of mineral fiber-based SFRM, cracks do not get opened until reaching to drift level of 3.91%. The delamination extends up to 40% of the insulated length on the bottom flange of the beam.
- In a beam-column assembly subjected to seismic loading, the interdependency of critical factors governing delamination, namely fracture energy, elastic modulus and thickness of

SFRM is established through the definition of delamination parameter, $d_{ch,seismic}$. When this parameter approaches 3.68, delamination occurs over 60 % of the plastic hinge region. However, a slight increase from 3.68 leads to complete delamination (100%) over the plastic hinge region. Therefore, the limiting value of 3.68 for $d_{ch,seismic}$ represents a combination of critical governing factors. Further, when $d_{ch,seismic}$ value is less than 0.58, crack initiation and propagation can completely be prevented.

- The dynamic increase factor (DIF) represents enhancement in material strength and fracture energy under high strain rate loading. The estimated DIF for mineral fiber based SFRM is 1.0, i.e., no increase in static fracture properties is required to acceptably predict the experimental behavior, hence, this material does not show any load rate-dependency effects. The Portland cement-based SFRM shows highest level of load rate-dependency, such that DIF is computed to be 2.32 for impact velocity of 8.05 m/s, whereas in the beams insulated with gypsum-based SFRM, the estimated DIF for the same impact velocity is 1.41.
- When a beam-column undergoes a blast overpressure perpendicular to its web, SFRM covering the flange tips can experience a severe cohesive failure over the first 2 ms of the blast duration. Consequently, cracks can form and progress at the interface of steel and SFRM leading to complete delamination of SFRM applied on exterior surface of the flanges, as well as the interior surface of the flanges exposed to blast overpressure.
- Based on the results of parametric study, a delamination characteristic parameter ($d_{ch,blast}$) is proposed for incorporating predominant factors influencing delamination of SFRM from steel beam-column under blast loading, namely, fracture energy of SFRM, elastic modulus of SFRM, thickness of SFRM and blast overpressure. The extent of

delamination shows a logarithmic relationship with the delamination characteristic parameter for three types of SFRM.

7.3 Research Impact and Practical Implications

The current design provisions is unable to rationally assess fire performance of steel structures subjected to extreme loading conditions, such as earthquake, impact and explosion, partly due to limited knowledge on delamination of fire insulation from steel structures subjected to such loading scenarios. The adhesion of fire insulation to the steel surface and its resiliency against delamination is characterized by normal bonding strength alone, which is determined using strength-based test methods prescribed in ASTM E736 (2011). However, results from this study clearly demonstrate that the delamination phenomenon at steel-fire insulation interface is governed by both geometrical (i.e. thickness of insulation) as well as material properties of SFRM (i.e., modulus of elasticity and fracture energy). Therefore the interdependency of these crucial factors should be given due consideration for mitigating delamination of SFRM from steel structures.

For instance, in addition to insulation thickness, interaction among the critical material properties of SFRM also need to be accounted for while designing the fire insulation thickness on steel structural elements. In fact, thicker insulation may not be the best solution for enhancing performance of steel structures during fire following an earthquake or blast. Further, while enhancing the critical fracture energy, it is important to not increase the elastic modulus proportionally, since it may not improve the delamination resistance as expected. The outcomes of this study suggest that the fire insulation properties, namely E, t and G_c, can be optimized in practical situations by accounting for all key factors influencing delamination.

The proposed delamination characteristic parameters can effectively be utilized in design of fire insulation for steel structural members designed to resist seismic, impact or blast loading and subsequent fire. In fact, these parameters take one step forward and provide a new perspective on design of fire insulation by accounting for the mechanical properties of fire insulation. Using these parameters can help designers to choose the proper type of fire insulation and also optimize its thickness.

This research aimed to produce two main results. First, the proposed numerical approach initiated the application of fracture mechanics principles in modeling delamination of fire insulation from steel structures on a practical scale. Second, since this study is aimed at identifying the critical factors governing delamination phenomenon at steel-SFRM interface, the outcomes of research can also be useful for those researchers who are attempting to rectify the drawbacks associated with current fire insulation by developing a new materials. Further, by relating the delamination initiation limits and extent of delamination over critical location over structural elements to the new parameters, a more rational way of differentiating among different fire insulation products and their application in different situations will be possible for practicing engineers.

7.4 Recommendations for Future Research

This study is the first research dedicated to determination of cohesive zone properties for fire insulation material and subsequently implementing the cohesive laws into a finite element model for quantifying the extent of delamination of fire insulation from steel structures under static and dynamic loading. However, there are many questions yet to be answered in order to comprehensively understand this complex phenomenon. Some of the potential research topics are recommended in below:

- Determine temperature-dependent cohesive laws at the interface of steel and SFRM, for use in numerical models to quantify delamination of fire insulation from steel structures during fire exposure. Subsequently, develop a numerical model that can simulate delamination of fire insulation from steel structures under the combined effect of structural loading and fire exposure.
- Carry out drop mass impact tests on insulated beams under various impact velocities to obtain a curve for dynamic increase factor as a function of strain rate. Perform blast tests on insulated beam-columns to study delamination of fire insulation under blast loading and thereby verify the numerical model with respect to prediction of fire insulation delamination.
- Develop cohesive laws for intumescent fire insulation material applied on steel structures. This type of fire insulation is very thin before being exposed to fire and can alternatively be utilized to protect plastic hinge regions in moment-resisting frames during post-earthquake fire when commonly used SFRM cannot withstand delamination under seismic loading.
- Conduct drop mass impact tests on beams insulated with intumescent fire insulation to study the strain rate dependency of fracture energy for this types of fire insulation material.
- Perform finite element analyses to predict the consequences of delamination of different types of SFRM from steel structures. In particular, adopt a numerical procedure that can model ductile and shear fracture of steel material at connection region by taking into account stress triaxiality and damage evolution into account. Also, carry out fire tests on

beam-column assembly that experiences fire insulation delamination over the plastic hinge region in the beam and monitor the connection behavior.

REFERENCES

REFERENCES

1. ANSYS Version 14.5 (2013), [Computer software]. ANSYS, Inc. Canonsburg, PA.

2. Arasaratnam, P., Sivakumaran, K., Tait, M., (2011). True stress-strain models for structural steel elements. International Scholarly Research Network, ISRN Civil Engineering, doi:10.5402/2011/656401.

3. Applied Fire Resistive Material. ATLSS Report No 06-25. Bethlehem, PA: Center for Advanced Technology of Large Structural Systems, Lehigh University, 120 pp.

4. ASTM D5528 (2013). Standard Test Method for Mode I Interlaminar Fracture Toughness of Unidirectional Fiber-Reinforced Polymer Matrix Composites.

5. ASTM WK22949 (2009). New Test Method for Determination of the Mode II Interlaminar Fracture Toughness of Unidirectional Fiber-Reinforced Polymer Matrix Composites Using the End-Notched Flexure (ENF) Test.

6. ASTM E736. (2010). “Standard test method for cohesion/adhesion of sprayed fire-resistive materials applied to structural members.” ASTM E736, West Conshohocken, PA.

7. ASTM E760-92(2011), Standard Test Method for Effect of Impact on Bonding of Sprayed Fire-Resistive Material Applied to Structural Members, ASTM International, West Conshohocken, PA, 2011.

8. ASTM E759-92(2011), Standard Test Method for Effect of Deflection on Sprayed Fire-Resistive Material Applied to Structural Members, ASTM International, West Conshohocken, PA, 2011.

9. ASTM E119 (2014). Standard Test Methods for Fire Tests of Building Construction and Materials, ASTM International, West Conshohocken, PA.

10. Applied Technology Council (ATC). (2007). Interim testing protocols for determining the seismic performance characteristics of structural and nonstructural components, FEMA 461, Washington, DC, 113.

11. Alfano, G. (2006). On the influence of the shape of the interface law on the application of cohesive-zone models. Composite Science and Technology; 66, 723-730.

12. Alfano, G., and Crisfield, M. A., (2001). Finite element interface models for the delamination analysis of laminated composites: mechanical and computational issues. International Journal for Numerical Methods in Engineering, 50(7), 1701–1736.

13. Alfano M, Furgiuele F, Leonardi A, Maletta C, Paulino GH.(2009). Mode I fracture of adhesive joints using tailored cohesive zone models. International Journal of Fracture; 157(1–2):193–204.

14. M. Alfano, G. Lubineau, F. Furgiuele, G. H. Paulino, (2011). On the enhancement of bond toughness for Al/epoxy T-peel joints with laser treated substrates. International Journal of Fracture; 171(2): 139-150.

15. Atas, A., Mohamed, G.F., Soutis, C., (2012). Modelling delamination onset and growth in pin loaded composite laminates. Composite Science and Technology; 72, 1096-1101.

16. Bazant, Z. P. (1984). Size effect in blunt fracture: Concrete, Rock, Metal. Journal of Engineering Mechnaics; 110 (4): 518-535.

17. Bazant, Z. P., Kazemi, M. T. (1990). Determination of fracture energy, process zone length and brittleness number from size effect, with application to rock and concrete. International Journal of Fracture; 44: 111-131.

18. Bazant, Z. P., Kazemi, M. T. (1991). Size dependence of concrete facture energy determined by RILEM work-of-fracture method. International Journal of Fracture; 51: 121-138.

19. Brara, A., Klepaczko, J., (2007). Fracture energy of concrete at high loading rates in tension. International Journal of Impact Engineering, 34, 424-435.

20. Barenblatt, G.I. (1962). Mathematical theory of equilibrium cracks in brittle failure, Advances in Applied Mechanics, 7.

21. Baker, W. E., Cox, P. A., Westine, P. S., Kulesz, J. J. and Strehlow, R. A. Explosion Hazards and Evaluation, 1983. Elsevier, NewYork.

22. Bazant, Z. P., Cedolin, L. (1991). Stability of structures: elastic, inelastic, fracture, and damage theories, Oxford University Press, New York.

23. Bažant, Z.P., Le, J.L., Greening; F.R., Benson, D.B. (2008). What Did and Did Not Cause Collapse of World Trade Center Twin Towers in New York?, ASCE Journal of Engineering Mechanics, 134(10), 892-906.

24. Bambach, M., Jama, H., Grzebieta, R., (2008). Hollow and concrete filled steel hollow sections under transverse impact loads. Engineering Structures, 30, 2859-2870.

25. Bentz DP, White CC, Prasad KR, Flynn DR, Hunston DL, Tan KT. A materials science-based approach to characterizing fire resistive materials. Journal of ASTM International 2009; 6(5).

26. Braxtan, N. L., and Pessiki, S. P. (2011a). "Bond performance of SFRM on steel plates subjected to tensile yielding." Journal of Fire Protection Engineering, 21, 37–55.

27. Braxtan, N. L., and Pessiki, S. P. (2011b)."Postearthquake fire performance of sprayed fire-resistive material on steel moment frames", ASCE Journal of Structural Engineering, 137 (9).

28. Camanho, P.P, Davila, C.G., and Moura, M.F. DE, (2003). Numerical simulation of mixed-mode progressive delamination in composite material, Journal of Composite Materials, 37 (1415-1438).

29. Chen, X., Wu, S., Zhou, J., (2013). Experimental and modeling study of dynamic mechanical properties of cement paste, mortar and concrete. Construction and building material, 47, 419-430.

30. Cotterell B, Mai YW., (1996). Fracture mechanics of cementitious materials. London, UK: Blackie Academic & Professional, an Imprint of Chapman and Hall.

31. Chen, S.-W., Chu, J., and Li, G.-Q. (2010). A study on damage mechanism of thick fireproof coating for steel member subjected to monotonic loading. Proceeding of 6th International Conference on Structures in Fire (SiF '10), Michigan State Univ., East Lansing, MI.

32. Crisfield, M.A., Hellweg, H.B. and Davies, G.A.O. (1994). Failure analysis of composite structures using interface elements, NAFEMS Conference on Application of Finite Elements to Composite Materials, London, UK.

33. Cowper, R., Symonds, P., (1957). Strain hardening and strain rate effects in the impact loading of cantilever beams, Brown University, Technical Report No. 28.

34. Dwaikat, MMS., Kodur, VKR. (2012). A simplified approach for predicting temperature profile in steel members with locally damaged fire protection. Fire technology 48 (2), 493-512.

35. Davila CG, Camanho PP, de Moura MFSF, (2001). Mixed-Mode decohesion elements for analyses of progressive delamination. In: Proceedings of the 42nd AIAA/ASME/ASCE/AHS/ASC structures. Structural dynamics and materials conference, Seattle, Washington; April 16–19.

36. Deng, Y., Tuan, C., Xiao, Y., (2012). Flexural behavior of concrete-filled circular steel tubes under high-strain rate loading. Journal of Structural Engineering. 138 (3), 449-456.

37. Drucker, D. C., and Prager,W. (1952). "Soil mechanics and plastic analysis for limit design." Quarterly of Applied Mathematics, 10(2), 157–165.

38. Dudgale, D.S. (1960). Yielding of steel sheets containing slits, Journal of Mechanics and Physics of Solids, 8:100–104.

39. Dwaikat, M.M.S., Kodur, V., (2012). A simplified approach for predicting temperature profile in steel members with locally damaged fire protection. Fire technology 48 (2), 493-512.

40. Eurocode 3 (2010) Design ofsteel structures. Part 1-2: General rules. Structural fire design.

41. Falk ML, Needleman A, Rice JR, (2001). A critical evaluation of cohesive zone models of dynamic fracture. J Phys IV, Proc: 543–50.

42. Faggiano B. Fire after earthquake. In: Proceedings from WG1 Meeting on Urban Habitat Constructions under Catastrophic Event, Prague, 30–31 March 2007.

43. FEMA P-750, (2009). NEHRP Recommended Seismic Provisions for New Buildings and Other Structures. Building Seismic Safety Council, Washington, D.C.

44. FEMA. (2002). "World Trade Center building performance study." FEMA Rep. No. 403, Washington, DC. Griffith AA. The phenomena of rupture and flow in solids. Philosophical Transactions of the Royal Society, London; Series A 1921; 221:163-198.

45. Fujikake, K., Bing, L., Soeun, S., (2009). Impact response of reinforced concrete beam and its analytical evaluation. ASCE Journal of Structural Engineering, 135(8), 938-950.

46. Gu, L., Kodur, V., (2011). "Role of Insulation Effectiveness on Fire Resistance of Steel Structures under Extreme Loading Events", J. Perform. Constr. Fac., 25 (4), p277-286.

47. GSA, 2010. Facilities Standards for the Public Buildings Service, Springfield, MA, USA.

48. Guo, Z.H., and Zhang, X.Q., "Investigation of complete stress-deformation curves for concrete in tension", ACI Materials Journal, 84 (4), 1987, 278-285.

49. Gordnian, K., Hadavinia, H., Mason, P.J., Madenic, E., (2008). Determination of fracture energy and tensile cohesive strength in Mode I delamination of angle-ply laminated composites, 82, 577-586.

50. Hu, X. Z., Wittmann, F.H., (1989). Fracture process zone and K_r curve of hardened cement paste and mortar, in Fracture of Concrete and Rock- Recent developments, Shah, S. P., Swartz, S.E. and Barr, B., Eds., Elsevier Applied Science, London, 307.

51. Hilleborg, A., Modeer, M., Peterson, PE., (1976). Analysis of crack formation and growth in concrete by means of fracture mechanics and finite elements, Cement and Concrete Research; 6:773-782.

52. Hordijk, D.A., Reinhardt, H.W., Cornelissen, H.A.W., (1987). Fracture mechanics parameters of concrete from uniaxial tensile tests as influenced by specimen length. Proceeding of international conference on Fracture Mechanics of Concrete and Rock, Houston (US), 138-149.

53. Hopkinson B., (1914). A method of measuring the pressure produced in the detonation of high explosives or by the impact of bullets, Phil. Trans Roy Soc Lond Ser A; 213(10);437-56.

54. Hofstetter, G., Meschke, G., (2011). Numerical modeling of concrete cracking. International Center for Mechanical Science. Courses and Lectures - No. 532. Springer Wien NewYork.

55. IBC 2012. International Building Code, Country Club Hills, IL, USA.

56. Irwin GR. Plastic zone near a crack and fracture toughness. Proceedings of the seventh Sagamore Ordnance materials conference, vol. IV. New York: Syracuse University; 1960. p. 63–78.

57. Jones, N., (2012). Structural impact. Cambridge University Press, Cambridge, New York.

58. Keller, W.J., Pessiki, S, (2012). "Effect of earthquake-induced damage to spray-applied fire-resistive insulation on the response of steel moment-frame beam-column connections during fire exposure", Journal of Fire Protection Engineering, 22(4), 271-299.

59. Khoo, A., H., 2000. Ductile fracture of steel, Ph.D. thesis, University of Alberta, Alberta, Canada, 2000.

60. Kodur, V.K.R., Shakya, A.M., (2013). Effect of temperature on thermal properties of spray applied fire resistive materials, Fire Safety Journal, 61, 314-323.

61. Kodur V., Lie TT., 1996, "Fire resistance of circular steel columns filled with fiber-reinforced concrete", Journal of Structural Engineering", 122(7), pp. 776-781.

62. Krausz AS, Krausz K. (1988). Fracture kinetics of crack growth. Dordrecht, Netherlands: Kluwer.

63. Kwon, K.H., Pessiki, S.P. & Lee, B.J. (2006). Fire Load Behavior of Steel Building Columns with Damaged Spray Applied Fire Resistive Material. ATLSS Report No 06-25. Bethlehem, PA: Center for Advanced Technology of Large Structural Systems, Lehigh University, 120 pp.

64. Kosloff, D., Frazier, G,A., (1978). Treatment of hourglass patterns in low order finite element codes. International Journal for Numerical and Analytical Methods in Geomechnaics, 2, 57-72.

65. Lemmen, P., Meijer, G., (2001). Failure Prediction Tool Theory and User Manual. TNO Building and Construction Research, Center for Maritime Engineering, Netherlands, Report 2000-CMC-R0018.

66. Lie, TT., Chabot, M., 1990, " A method to predict the fire resistance of circular concrete filled hollow steel columns", Journal of Fire Protection Engineering", 2(4), pp. 111-126.

67. Lie TT., Kodur V., 1996, "Fire resistance of steel columns filled with bar-reinforced concrete", Journal of Structural Engineering, 122(1), pp. 30-36.

68. Li, V.C. Chan, C.M. and Leung, C.K.Y. (1987). Experimental determination of the tension-softening curve in cementitious composites, Cement and Concrete Research, 17(3), 441-452.

69. Lee, M.J., Cho, T.M., Kim, W.S., Lee, B.C., Lee, J.J., (2010). Determination of cohesive parameters for a mixed-mode cohesive zone model. International Journal of Adhesion and Adhesives, 30, 322-328.

70. Liew, J., Sohel, K., Koh, C., (2009). Impact tests on steel-concrete-steel sandwich beams with lightweight concrete core. Engineering Structures, 31, 2045-2059.

71. LS-DYNA, (2014). User's manual, Version R7.1. Livermore Software Technology Corporation (LSTC).

72. Mi Y, Crisfield MA, Davies GAO, Hellweg HB. (1998). Progressive delamination using interface elements. Journal of Composite Materials; 32(14):1246–72.
73. Mousavi, S., Bagchi A., and Kodur, V.K.R., (2008). "Review of post-earthquake fire hazard to building structures", Canadian Journal of Civil Engineering, 35, 689-698.

74. Modeer, M. (1979).A fracture mechanics approach to failure analysis of concrete materials, University of Lund, Report TVBM-1001.

75. Moes N, Belytschko T., (2002). Extended finite element method for cohesive crack growth. Journal of Engineering Fracture Mechanics, 69, 813–833.

76. Nassr., A.A., Razaqpur, A.G., Tait, M.J., Campodelli, M., Foo., Simon., (2013). Dynamic response of steel columns subjected to blast loading. ASCE Journal of Structural Engineering, 04014036, 1-15.

77. NIST (National Institute of Standards and Technology), 2005, Final Report on the Collapse of the World Trade Center Towers, NIST NCSTAR1, Gaitherburge, MD, September.

78. Ozbolt, J., Sharma, A., Reinhardt. H., (2011). Dynamic fracture of concrete-compact tension specimen. International Journal of Impact Engineering, 48, 1534-1543.

79. Ozbolt, J., Sharma, A., Irhan, B., Sola, E., (2014). Tensile behavior of concrete under high loading rates. International Journal of Impact Engineering, 69, 55-68.

80. Park K, Paulino GH, Roesler JR, (2008). Determination of the kink point in the bilinear softening model for concrete. Engineering Fracture Mechanics. 75(13): 3806–3818.

81. Pate-Cornell, M., (1993). Learning from the Piper Alpha Accident: A Postmortem Analysis of Technical and Organizational Factors.Risk Analysis, 13(2), 215-232.

82. Petersson, P.E., (1985). Crack growth development of fracture zones in plain concrete and similar materials. Report No. TVBM-1006., Lund Institute of Technology, Sweden.

83. Rybicki, E.F. and Kanninen, M.F. (1977). A finite element calculation of stress intensity factors by a modified crack closure integral. Engineering Fracture Mechanics, 9: 931–938.

84. Reinhardt, H., Cornelissen, H., and Hordijk, D. (1986). Tensile Tests and Failure Analysis of Concrete. ASCE Journal of Structural Engineering. 112(11), 2462–2477.

85. Ryder, N. L.,Wolin, S. D., and Milke, J. A. (2002). "An investigation of the reduction in fire resistance of steel columns caused by loss of spray applied fire protection." Journal of Fire Protection Engineering, 12(1), 31–44.

86. Remennikov, A., Kong, S., Uy, B., (2013). The response of axially restrained non-composite steel-concrete-steel sandwich panels due to large impact loading. Engineering Structures, 49, 806-818.

87. Sorensen, B.F., Jacobsen, T.K., (2003). Determination of cohesive laws by the *J* integral approach. Journal of Engineering Fracture Mechanics. 70, 1841-1858.

88. Schuler, H., Mayrhofer, C., Thoma, K., (2006). Spall experiments for the measurement of the tensile strength and fracture energy of concrete at high strain rates. International Journal of Impact Engineering, 32, 1635-1650.

89. Scheider., I, Brocks., W., (2006). Cohesive elements for thin walled structures. Computational Material Science 37(1–2):101–109.

90. Stronge WJ, Yu TX. Dynamic models for structural plasticity. London, UK: Springer; 1993. p. 122–55.

91. Tvergaard V, Hutchinson JW., (1996). On the toughness of ductile adhesive joints. J Mechanics and Physics of Solids 44(5):789–800.

92. Tomecek, D.V., & Milke, J.A. (1993, March). Study of the Effect of Partial Loss of Protection on the Fire Resistance of Steel Columns. Fire Technology, 29, pp. 3-21.

93. Turon, A., Dávila, C. G., Camanho, P. P., and Costa, J., (2007). An Engineering Solution for Mesh Size Effects in the Simulation of Delamination Using Cohesive Zone Models. Engineering Fracture Mechanics, 74(10), 1665-1682.

94. Turon, A. Camanho, P. P., and Dávila, C. G., (2006). A Damage Model for the Simulation of Delamination in Advanced Composites under Variable-Mode Loading," Mechanics of Materials, Vol. 38(11), 1072-1089.

95. Tan, K. T., Christopher, C. W., and Hunston, D. L. (2011). An adhesion test method for spray-applied fire-resistive materials. Fire and Materials, 35(4), 245–259.

96. Valorson, N., Sesa, S., Lepore, M., Cricri, G., (2013). Identification of mode-I cohesive parameters for bonded interfaces based on DCB tests. Journal of Engineering Fracture Mechanics, 104, 56-79.

97. Wang, W-Y., Li, G-O., Kodur, V. (2013). An approach for modeling fire insulation damage in steel columns. ASCE Journal of Structural Engineering, 139(4), 491-503.

98. Wang, R., Han, L., Hou, C., (2013). Behavior of concrete filled steel tubular (CFST) members under lateral impact: Experiment and FEA model. Journal of Constructional Steel Research, 80, 188-201.

99. Xu, X.-P., and Needleman, A. (1994). Numerical simulations of fast crack growth in brittle solids. Journal of the Mechanics and Physics of Solids, 42(9), 1397–1434.

100. Ye, Q., Chen, P., (2011). Prediction of the cohesive strength for numerically simulating composite delamination via CZM-based FEM. Composites: Part B, 42, 1076-1083.

101. Zhang Z, Paulino GH (2005). Cohesive zone modeling of dynamic failure in homogeneous and functionally graded materials. International Journal of Plastics, 21(16):1195–1254.

102. Zhang, Q., Li, V. (2014). Adhesive bonding of fire-resistive engineered cementitious composites (ECC) to steel. Construction and Building Material, 64, 431-439.

103. Zhang, K., S., Li, H., Z., (1994). Numerical analysis of the stress-strain curve and fracture initiation for ductile material. Engineering Fracture Mechnaics, 49(2), 235-241.

104. Zhang, X., Ruiz, G., Yu, R., Tarifa, M., (2009). Fracture behavior of high-strength concrete at a wide range of loading rates. International Journal of Impact Engineering, 36, 1204-1209.

105. Zeinoddini GAR, Harding Parke JE. (2002). Axially pre-loaded steel tubes subjected to lateral impacts: an experimental study. International Journal of Impact Engineering; 27:669-90.